Probing Plasmonic Nanostructures with Electron Energy - Loss Spectroscopy

Raza, Søren

Publication date:
2014

Document Version
Publisher's PDF, also known as Version of record

DTU Fotonik
Institut for Fotonik

DTU

PROBING PLASMONIC NANOSTRUCTURES WITH ELECTRON ENERGY-LOSS SPECTROSCOPY

Supervised by

Prof. N. Asger Mortensen
Assoc. Prof. Martijn Wubs
Prof. Jakob Birkedal Wagner

Søren Raza

PhD Thesis
Department of Photonics Engineering
Technical University of Denmark
September 2014

Abstract

This thesis presents theoretical and experimental results on plasmonic phenomena in nanosized metallic structures. The theoretical aspect concerns the extension of the local-response approximation, which leads to a description of metals based on the classical dielectric function, to account for nonlocal response. The experimental work comprises the use of electron energy-loss spectroscopy (EELS) to excite and study both localized and propagating surface plasmons in metal structures.

Following a short introduction, we present the theoretical foundation to describe nonlocal response in Maxwell's equations for arbitrary geometries. We show that the key quantity which is modified by nonlocality is the induced charge in the metal. In particular, the induced surface charge is smeared over an Ångstrom length scale in contrast to the delta-function induced charge distribution in the local-response approximation. Irrespective of the microscopic origin, we find that nonlocal response modifies the electromagnetic wave equation by an additional Laplacian term. The hydrodynamic model, which includes nonlocal response through the Thomas–Fermi pressure of a free-electron gas, is discussed. We present also the generalized nonlocal optical response model, which expands the hydrodynamic model by taking into account the diffusion of free electrons in metals through Fick's law. We go on to consider the implications of these two nonlocal models in the following plasmonic geometries: metal-insulator interface, nanosphere, dimer with nanometer-sized gaps, core-shell nanowire with ultrathin metal shell, and a thin metal film. In all cases we compare the nonlocal models with the local-response approximation. Below the plasma frequency, we find that the distance between the induced positive and negative surface charges is the main indication for the importance of nonlocal response. Specifically, the mentioned distance in nanospheres translates into a size-dependent resonance energy and linewidth broadening of the surface plasmons, while in the dimer a gap-dependent resonance energy and linewidth broadening is observed. Above the plasma frequency, resonant excitations are supported by nonlocal theory due to the inclusion of curl-free waves.

The application of EELS to study surface plasmons in nanosized metallic systems is then presented. In particular, we discuss that EELS can provide important information on the optical response of plasmonic structures. We perform two separate EELS experiments and discuss their theoretical interpretations. The first experiment concerns the study of localized surface plasmon resonances of chemically prepared silver nanoparticles with diameter sizes down to 3.5 nm dispersed on a thin substrate. The second experiment is devoted to the investigation of propagating gap surface-plasmon modes in gold nanogrooves, which are experimentally observed to subsist in gaps of only 5 nm.

Resumé

Denne afhandling præsenterer teoretiske og eksperimentelle resultater af plasmoniske fænomener i metalstrukturer med dimensioner af nanometer størrelse. Det teoretiske aspekt omhandler udvidelsen af lokal respons approksimationen, som medfører en beskrivelse af metaller baseret på den dielektriske funktion, til at inkludere ikke-lokal respons. Det eksperimentelle arbejde omfatter brugen af elektron energitab spektroskopi (EELS) til at anslå og undersøge både lokaliseret og bevægende overfladeplasmoner i metalstrukturer.

Efter en kort introduktion præsenterer vi det teoretiske fundament for at beskrive ikke-lokal respons i Maxwells ligninger i arbitrære geometrier. Vi viser at hovedparameteren, der modificeres af ikke-lokalitet, er den induceret ladningsfordeling i metallet. Mere præcist så udsmøres den induceret overfladeladning over en Ångstrom længdeskala, hvilket er i modsætning til den delta funktion lignende induceret ladningsfordeling i lokal respons approksimationen. Uanset den mikroskopiske oprindelse finder vi at ikke-lokale respons modificerer den elektromagnetiske bølgeligning ved tilføjelsen af et Laplace-operator led. Den hydrodynamiske model, som inkluderer ikke-lokal respons via inkluderingen af Thomas–Fermi trykket af den frie elektrongas, diskuteres. Vi præsenterer også den generaliseret ikke-lokal optiske respons model, som udvider den hydrodynamiske model ved at tage hensyn til diffusion af de frie elektroner via Ficks lov. Vi fortsætter ved at undersøge konsekvenserne af disse to ikke-lokale modeller i de følgende plasmoniske systemer: metal-dielektrikum grænseflade, en nanokugle, en dimer med gab af nanometer størrelse, en kerne-skal nanotråd med en ultratynd metal skal og til sidst en tynd metalfilm. I alle tilfælde sammenligner vi de ikke-lokale modeller med lokal respons approksimationen. Under plasmafrekvensen finder vi at afstanden mellem den positive og negative induceret overfladeladning er hovedindikatoren for vigtigheden af ikke-lokal respons. Mere konkret så medfører den nævnte afstand en størrelsesafhængig resonansenergi og linjebredde af overfladeplasmonen, mens i dimeren observeres en gabafgængig resonansenergi og linjebrede. Over plasmafrekvensen er der resonante excitationer i den ikke-lokale teori på grund af inkluderingen af rotationsfrie bølger.

Anvendelsen af EELS til at studere overfladeplasmoner i metalsystemer af nanostørrelse præsenteres. Mere præcist så argumenteres der for at EELS kan fremskaffe vigtig information om den optiske respons af plasmoniske strukturer. Vi udfører to separate EELS forsøg og diskuterer deres teoretiske fortolkning. Det første forsøg omhandler studiet af lokaliseret overfladeplasmoner af kemiske produceret sølv nanopartikler med størrelser ned til 3.5 nm, som er fordelt på et tyndt substrat. Det andet forsøg er dedikeret til undersøgelsen af bevægende gab overfladeplasmoner i guld nanoriller, som observeres ekperimentelt stadig at eksistere i gab på kun 5 nm.

Preface and acknowledgments

This thesis is submitted in partial fulfillment of the requirements for obtaining the Philosophiae Doctor (PhD) degree at the Technical University of Denmark. The work presented here has been carried out at the Department of Photonics Engineering and at the Center for Electron Nanoscopy during the period September 2011 to September 2014. The PhD project has been supervised by Prof. N. Asger Mortensen and Assoc. Prof. Martijn Wubs. My initial third supervisor Andrew Burrows was in the second half of my PhD replaced by Prof. Jakob Birkedal Wagner.

I wish to first and foremost thank my daily supervisors Asger and Martijn for an outstanding working environment, invaluable discussions and always having time to talk about new and sometimes off-topic ideas. I cannot imagine having done my PhD in a better place. I would also like to thank Jakob for sharing his insight with me and providing an accessible environment for performing experiments. I thank Giuseppe Toscano for a fruitful collaboration on the theoretical aspects of this work. I am also truly grateful to Ass. Prof. Nicolas Stenger for kick-starting my experimental activities, and without whom, my experimental understanding would not have been the same. I thank Shima Kadkhodazadeh for great assistance with the experiments in this work and always having time to answer my many questions. I am grateful to Prof. Sergey I. Bozhevolnyi for great discussions and a rewarding collaboration. I thank my office mates Thomas Christensen and Jeppe Clausen for fun lunch and coffee breaks and interesting office discussions. Moreover, I thank Thomas for a great collaboration.

I am very grateful to Prof. Mark L. Brongersma for generously hosting my stay at Stanford University. In particular, I thank Majid Esfandyarpour and Ai Leen Koh for assisting me with my experiments during my stay.

I would like to thank Prof. Javier García de Abajo, Prof. Martin Wegener, and Prof. Jesper Mørk for taking time out of their activities to serve on the committee of my thesis. Additionally, I thank Andrew Burrows, Antti-Pekka Jauho, Wei Yan, Sanshui Xiao, Anders Pors, Tobias Holmgaard, Søren V. Fischer, Natalie Kostesha, Claus Jeppesen, Thomas Søndergaard, and Kjeld Pedersen for their productive collaboration.

Finally, I thank the apple of my eye Sophia for her love and encouragement, and my family and friends for their continuous support.

Søren Raza
September 2014

List of publications

Peer-reviewed journal publications

[A] **S. Raza**, M. Wubs, S. I. Bozhevolnyi, and N. A. Mortensen, 'Nonlocal study of ultimate plasmon hybridization', Opt. Lett. **40**, 839 (2015).

[B] **S. Raza**, N. Stenger, A. Pors, T. Holmgaard, S. Kadkhodazadeh, J. B. Wagner, K. Pedersen, M. Wubs, S. I. Bozhevolnyi, and N. A. Mortensen, 'Extremely confined gap surface-plasmon modes excited by electrons', Nat. Commun. **5**, 4125 (2014).

[C] N. A. Mortensen, **S. Raza**, M. Wubs, T. Søndergaard, and S. I. Bozhevolnyi, 'A generalized non-local optical response theory for plasmonic nanostructures', Nat. Commun. **5**, 3809 (2014).

[D] T. Christensen, W. Yan, **S. Raza**, A.-P. Jauho, N. A. Mortensen, and M. Wubs, 'Nonlocal response of metallic nanospheres probed by light, electrons, and atoms', ACS Nano **8**, 1745 (2014).

[E] **S. Raza**, W. Yan, N. Stenger, M. Wubs, and N. A. Mortensen, 'Blueshift of the surface plasmon resonance in silver nanoparticles: substrate effects', Opt. Express **21**, 27344 (2013).

[F] **S. Raza**, T. Christensen, M. Wubs, S. I. Bozhevolnyi, and N. A. Mortensen, 'Nonlocal response in thin-film waveguides: loss versus nonlocality and breaking of complementarity', Phys. Rev. B **88**, 115401 (2013).

[G] G. Toscano, **S. Raza**, W. Yan, C. Jeppesen, S. Xiao, M. Wubs, A.-P. Jauho, S. I. Bozhevolnyi, and N. A. Mortensen, 'Nonlocal response in plasmonic waveguiding with extreme light confinement', Nanophotonics **2**, 161 (2013).

[H] **S. Raza**, G. Toscano, A.-P. Jauho, N. A. Mortensen, and M. Wubs, 'Refractive-index sensing with ultrathin plasmonic nanotubes', Plasmonics **8**, 193 (2013).

[I] **S. Raza**, N. Stenger, S. Kadkhodazadeh, S. V. Fischer, N. Kostesha, A.-P. Jauho, A. Burrows, M. Wubs and N. A. Mortensen, 'Blueshift of the surface plasmon resonance in silver nanoparticles studied with EELS', Nanophotonics **2**, 131 (2013).

[J] G. Toscano, **S. Raza**, S. Xiao, M. Wubs, A.-P. Jauho, S. I. Bozhevolnyi, and N. A. Mortensen, 'Surface-enhanced Raman spectroscopy (SERS): nonlocal limitations', Opt. Lett. **37**, 2538 (2012).

[K] G. Toscano, **S. Raza**, A.-P. Jauho, N. A. Mortensen, and M. Wubs, 'Modified field enhancement and extinction by plasmonic nanowire dimers due to nonlocal response', Opt. Express **20**, 4176 (2011).

[L] **S. Raza**, G. Toscano, A.-P. Jauho, M. Wubs, and N. A. Mortensen, 'Unusual resonances in nanoplasmonic structures due to nonlocal response', Phys. Rev. B **84**, 121412(R) (2011).

Conference proceedings

[M] N. A. Mortensen, G. Toscano, **S. Raza**, N. Stenger, W. Yan, A.-P. Jauho, S. Xiao, and M. Wubs, 'Nanophotonics beyond Ohms law', AIP Conf. Proc. **1475**, 28 (2012).

[N] M. Wubs, **S. Raza**, G. Toscano, A.-P. Jauho, and N. A. Mortensen, 'Are there novel resonances in nanoplasmonic structures due to nonlocal response?', Proc. SPIE 8260, 82601E (2012).

All papers have been published during my PhD, except Paper L which was published during my Master's Thesis. Papers A, B, C, E, F, H, I and L are included and discussed in this PhD thesis.

Contents

Chapter 1

Introduction

The field of plasmonics focuses on the study of and the associated electromagnetic phenomena due to surface plasmons (SPs) [1], which in its simplest form can be described as the collective excitation of the conduction electrons bound to a metal-dielectric interface. The term surface plasmons comprises a large range of different types of electromagnetic excitations in metals, from *localized* surface plasmons (LSPs) in confined geometries (e.g., single particles) to *propagating* surface plasmons in extended geometries with translational invariance, i.e., waveguides. The modal spectrum becomes even more exciting when several closely-spaced metal particles interact electromagnetically, such that the SPs of the individual particle hybridize to form so-called bonding and antibonding plasmon modes [2]. Some of the most attractive properties of SPs are their ability to localize light on the subwavelength scale (i.e., beyond the diffraction limit) [3, 4] and produce large enhancements of the electric field on the nanoscale [5]. The properties of the SPs have found application in a wide variety of fields; from medical applications, such as bio-sensing [6] and cancer therapy [7], to plasmonic waveguiding [8] and on-chip circuitry [9].

The theoretical description of SPs is in most accounts based on classical electromagnetism governed by Maxwell's equations, although the use of quantum mechanical approaches, such as density-functional theory (DFT), has also been applied to describe simple extended geometries (e.g., metal-vacuum interfaces) and nanometer-sized confined geometries, mainly in the quasistatic limit [10]. The classical approach, which describes the optical properties of metals with the dielectric function, has been successful in describing the vast majority of effects related to SPs, in particular for systems with feature sizes above 10 nm [11, 12] and surprisingly even in some cases below this size limit [13]. Despite its huge success, the local-response approximation (LRA), which leads to the dielectric function description, has been challenged on a number of accounts. One example is the size-dependent SP linewidth broadening observed in metal clusters and small nanoparticles [14, 15], which has to be phenomenologically accounted for in the LRA [16]. Size-dependent resonance shifts of the SP in noble metal nanoparticles have also been observed [17, 18, 19, 20]. Another example is the multipole plasmon (sometimes also referred as the Bennet plasmon) which, besides the usual surface-plasmon polariton (SPP), can be supported by the simple geometry of a metal-vacuum interface [21] as a direct consequence of the spill-out of free electrons beyond the classical metal boundary [22, 23]. Thin metal films have also been shown to support resonant excitations above the plasma frequency due to confined longitudinal waves [24, 25], which are not taken into account in the LRA. More recently, advances in sample preparation and experimental techniques have led to several experiments on metal dimers in subnanometer proximity with plasmonic effects clearly going beyond the LRA [26, 27, 28, 29, 30, 31]. A theoretical description

of the metal based on ab initio approaches such as DFT can in principle account for all of the observed non-classical effects. However, due to the computational demand of such approaches, only very small system sizes (few nanometers) can be considered [32], which puts serious constraints on the feasibility of these approaches for a generic plasmonic system. Another simpler and computationally less demanding path is to go beyond the LRA by taking into account nonlocal response through a hydrodynamic approach [33]. The hydrodynamic approach has at least qualitatively been able to describe size-dependent resonance shifts of noble metal nanoparticles and resonant excitations above the plasma frequency in thin films, and can now with the inclusion of electron diffusion [34] also describe size-dependent damping and the optical spectra of closely-spaced dimers. Besides being physically transparent, significant analytical progress is also possible with the hydrodynamic approach. Many of these properties are beneficial in the theoretical studies of generic plasmonic systems with large (> 10 nm) feature sizes.

Experimental techniques to study plasmonic effects, both classical and those beyond the LRA, have been based on both photons and electrons as the excitation sources. Interestingly, the first prediction [1] and observation [35, 36] of SPs were based on electron excitation. Specifically, the experimental technique known as electron energy-loss spectroscopy (EELS) was utilized. EELS is performed in a transmission electron microscope and has due to the advances of electron microscopy become a very powerful spectroscopy technique to study surface plasmons [37]. With the aid of electron monochromators and abberation correction of the electromagnetic lenses [38], the simultaneous spatial and spectral resolution of EELS is unmatched [39]. EELS is now often being used to study and map the SP resonances of metallic nanostructures [40, 41], and thus constitutes an ideal tool for the study of both classical and non-classical nanoplasmonic phenomena.

1.1 Outline of this thesis

The build-up of this thesis is as follows. In Chapter 2 we study the general equations governing the electromagnetic response of metals in arbitrary geometries. We show how the commonly employed local-response approximation leads to the formalism based on the dielectric function. Afterwards, we go beyond the LRA to include nonlocal response in a phenomenological picture, leading to a generic real-space formulation of the governing equations. We then consider the governing equations of two specific nonlocal models: the hydrodynamic model and the generalized nonlocal optical response (GNOR) model.

Chapter 3 is devoted to comparing the nonlocal models (i.e., hydrodynamic and GNOR models) with the LRA in specific plasmonic systems. In particular, we study the popular systems mentioned in the introduction, e.g., the single metal-insulator interface, the metal sphere, the plasmonic dimer consisting of two infinite nanowires, the thin metal film, and additionally, the core-shell nanowire made of an insulating core with a thin metal shell.

Chapter 4 deals first with the experimental and theoretical descriptions of EELS. Afterwards, two EELS experiments and their theoretical interpretation are described. The first EELS experiment is described in Paper I (and its supplemental material) and further studied in Paper E. As the results of the first experiment are spread over two papers and one supplemental material, I have combined these into a single coherent section. Similarly, the second EELS experiment is described in Paper B and its even-longer supplemental material, which have been combined into a single section.

Finally, Chapter 5 concludes the thesis and presents possible future paths for both theory and experiments.

Chapter 2

Electromagnetism in metals

In this chapter we first discuss how metals are described in the framework of classical electromagnetism. We start with the general Maxwell's equations and first consider the commonly employed local-response approximation. We then go beyond the LRA and take into account nonlocal response in Sec. 2.2, although we at first do not specify a microscopic origin of the nonlocal response. Finally, we study two nonlocal models: the hydrodynamic model in Sec. 2.3 and the recently introduced generalized nonlocal optical response (GNOR) model in Sec. 2.4.

We begin our considerations with Maxwell's equations in matter. Disregarding magnetic effects since most plasmonic metals are non-magnetic, we can write Maxwell's equations in the frequency domain as (time convention: $e^{-i\omega t}$)

$$\nabla \cdot \mathbf{D}(\mathbf{r},\omega) = \rho(\mathbf{r},\omega) + \rho_{\text{ext}}(\mathbf{r},\omega), \tag{2.1a}$$
$$\nabla \cdot \mathbf{H}(\mathbf{r},\omega) = 0, \tag{2.1b}$$
$$\nabla \times \mathbf{E}(\mathbf{r},\omega) = i\omega\mu_0 \mathbf{H}(\mathbf{r},\omega), \tag{2.1c}$$
$$\nabla \times \mathbf{H}(\mathbf{r},\omega) = -i\omega \mathbf{D}(\mathbf{r},\omega) + \mathbf{J}(\mathbf{r},\omega) + \mathbf{J}_{\text{ext}}(\mathbf{r},\omega), \tag{2.1d}$$

where we have connected the magnetic flux density $\mathbf{B}(\mathbf{r},\omega)$ to the magnetic field $\mathbf{H}(\mathbf{r},\omega)$ through the non-magnetic constitutive relation $\mathbf{B}(\mathbf{r},\omega) = \mu_0 \mathbf{H}(\mathbf{r},\omega)$. Furthermore, we have split the free charges and currents into two contributions: one due to induced charges and currents inside the metal, denoted by the charge density $\rho(\mathbf{r},\omega)$ and current density $\mathbf{J}(\mathbf{r},\omega)$, respectively, and one due to external source charges and currents, given by $\rho_{\text{ext}}(\mathbf{r},\omega)$ and $\mathbf{J}_{\text{ext}}(\mathbf{r},\omega)$, respectively. Both the currents and charges satisfy continuity equations

$$\nabla \cdot \mathbf{J}(\mathbf{r},\omega) = i\omega\rho(\mathbf{r},\omega), \tag{2.2a}$$
$$\nabla \cdot \mathbf{J}_{\text{ext}}(\mathbf{r},\omega) = i\omega\rho_{\text{ext}}(\mathbf{r},\omega). \tag{2.2b}$$

The external contributions must only be taken into account when an external electromagnetic source such as a moving electron is present, as in the case of electron energy-loss calculations [1, 37], see Chapter 4 of this thesis. For plane-wave excitations, the external source is in general not needed. On the other hand the induced currents and charges stem from the (free) conduction band electrons in the metal and are therefore always present.

In the absence of any external currents and charges, the response of the metal due to an electric field $\mathbf{E}(\mathbf{r},\omega)$ is solely described by the displacement field $\mathbf{D}(\mathbf{r},\omega)$ and the induced current density $\mathbf{J}(\mathbf{r},\omega)$. The displacement field describes the response from

the bound charges of the metal, i.e., the metal ions and the tightly bound electrons, while the current density describes the response due to the conduction electrons of the metal. For linear and isotropic media, we can relate the displacement field and the current density to the electric field through the constitutive relations

$$\mathbf{D}(\mathbf{r},\omega) = \varepsilon_0 \int \mathrm{d}\mathbf{r}' \varepsilon(\mathbf{r},\mathbf{r}',\omega)\mathbf{E}(\mathbf{r}',\omega), \tag{2.3a}$$

$$\mathbf{J}(\mathbf{r},\omega) = \int \mathrm{d}\mathbf{r}' \sigma(\mathbf{r},\mathbf{r}',\omega)\mathbf{E}(\mathbf{r}',\omega), \tag{2.3b}$$

where ε_0 is the vacuum permittivity, and $\varepsilon(\mathbf{r},\mathbf{r}',\omega)$ and $\sigma(\mathbf{r},\mathbf{r}',\omega)$ denote the frequency-dependent nonlocal dielectric constant and conductivity, respectively. The nonlocal relations in Eq. (2.3) state that the response of the metal at a given point $\mathbf{r}$ may depend on the electric field at neighboring points $\mathbf{r}'$ through the nonlocal permittivity and conductivity, see Fig. 2.1(a) for a schematic illustration.

Since the bound charges inherently respond as an insulator, we can make the justifiable assumption that the bound charges are well described by the local-response approximation, which allows us to write $\varepsilon(\mathbf{r},\mathbf{r}',\omega) = \delta(\mathbf{r}-\mathbf{r}')\varepsilon_\infty(\omega)$ with $\delta(\mathbf{r})$ denoting the Dirac delta function. The integral in Eq. (2.3a) is then straightforwardly performed

$$\mathbf{D}(\mathbf{r},\omega) = \varepsilon_0\varepsilon_\infty(\omega)\mathbf{E}(\mathbf{r},\omega). \tag{2.4}$$

Here, $\varepsilon_\infty(\omega)$ takes into account all electric polarization effects due to the bound charges, or put in other words, the response not due to the free electrons. To proceed further we must now choose how to describe the conductivity $\sigma(\mathbf{r},\mathbf{r}',\omega)$ in Eq. (2.3b).

2.1 Local-response approximation

Before we delve into the study of nonlocal response, it is instructive to first revisit the description of metals and the derivation of the governing equations in the local-response approximation. This will allow us to clearly outline not only differences but also similarities between the LRA and nonlocal response. In addition, the importance of the LRA is further accentuated by its prevalence in the plasmonic community, being the most commonly applied constitutive description [11]. The LRA has successfully described a plethora of plasmonic phenomena and experiments, such as optical far-field measurements [42, 43, 44], electron energy-loss spectroscopy [1, 40, 41, 45, 46, 47], cathodoluminescence experiments [48, 49, 37], near-field microscopy [50], and surprisingly, even for the two-dimensional material graphene [51] and plasmonic particles with nanometer-sized gaps [13].

Our starting point will therefore be to assume that nonlocal effects due to the free electrons are negligible and apply the local-response approximation to the conductivity, i.e., $\sigma(\mathbf{r},\mathbf{r}',\omega) = \delta(\mathbf{r}-\mathbf{r}')\sigma(\omega)$. This simplifies Eq. (2.3b) to

$$\mathbf{J}(\mathbf{r},\omega) = \sigma(\omega)\mathbf{E}(\mathbf{r},\omega). \tag{2.5}$$

We now insert Eqs. (2.4-2.5) into Maxwell's equations [Eq. (2.1)] and find

$$\nabla\cdot\mathbf{E}(\mathbf{r},\omega) = \frac{\rho_{\mathrm{ext}}(\mathbf{r},\omega)}{\varepsilon_0\varepsilon(\omega)}, \tag{2.6a}$$

$$\nabla\cdot\mathbf{H}(\mathbf{r},\omega) = 0, \tag{2.6b}$$

$$\nabla\times\mathbf{E}(\mathbf{r},\omega) = i\omega\mu_0\mathbf{H}(\mathbf{r},\omega), \tag{2.6c}$$

$$\nabla\times\mathbf{H}(\mathbf{r},\omega) = -i\omega\varepsilon_0\varepsilon(\omega)\mathbf{E}(\mathbf{r},\omega) + \mathbf{J}_{\mathrm{ext}}(\mathbf{r},\omega), \tag{2.6d}$$

where we have defined the LRA dielectric constant $\varepsilon(\omega) \equiv \varepsilon_\infty(\omega) + i\sigma(\omega)/(\omega\varepsilon_0)$, which takes into account polarization effects due to both bound and free charges. We can also write up the LRA wave equation, by taking the curl of Eq. (2.6c) and using Eq. (2.6d)

$$\nabla \times \nabla \times \mathbf{E}(\mathbf{r},\omega) = \left(\frac{\omega}{c}\right)^2 \varepsilon(\omega)\mathbf{E}(\mathbf{r},\omega) + i\omega\mu_0 \mathbf{J}_{\text{ext}}(\mathbf{r},\omega). \tag{2.7}$$

We note that in the absence of external sources, the electric field within the LRA will always be divergence free, i.e., $\nabla \cdot \mathbf{E}(\mathbf{r},\omega) = 0$. This is an important point as this criterion gives rise to a specific class of solutions to Maxwell's equations. As we will see later, this property no longer holds when nonlocal response is taken into account.

The divergence-free property can be examined further if we consider a homogenous medium, where we can perform a spatial Fourier transform (space convention: $e^{i\mathbf{k}\cdot\mathbf{r}}$)

$$\mathbf{k} \cdot \mathbf{E}(\mathbf{k},\omega) = 0. \tag{2.8}$$

Thus, we see that in the LRA the electric field in the homogeneous metal is always transverse, i.e., the variations in the electric field occur perpendicular to the direction of propagation ($\mathbf{k}$-direction). Additionally, by spatially Fourier transforming Eq. (2.7), we can find the dispersion relation for the transverse field in homogeneous media as

$$k^2 = \left(\frac{\omega}{c}\right)^2 \varepsilon(\omega). \tag{2.9}$$

We remark that one should be very careful not to interchange the properties of divergence-free and transverse fields, as the divergence-free property is more general and applies in real space, while the transverse property strictly only applies in homogeneous media (where the spatial Fourier transform can be easily performed).

2.1.1 Drude model

Although the LRA conductivity is not limited to a specific type of function, the Drude model [11, 52] for the conductivity $\sigma_{\text{D}}(\omega)$ is commonly used to describe metals [53, 54, 55]

$$\sigma_{\text{D}}(\omega) = \frac{\varepsilon_0 i\omega_{\text{p}}^2}{\omega + i\gamma}. \tag{2.10}$$

Here, $\omega_{\text{p}}^2 = \frac{e^2 n_0}{\varepsilon_0 m}$ is the plasma frequency of the metal, given in terms of the free-electron density n_0 and effective electron mass m, and γ is the free-electron collision frequency, which phenomenologically accounts for collisions both with nuclei and other electrons. We can hereby write the dielectric function as

$$\varepsilon_{\text{D}}(\omega) = \varepsilon_\infty(\omega) - \frac{\omega_{\text{p}}^2}{\omega^2 + i\gamma\omega}, \tag{2.11}$$

which we denote the Drude dielectric function, even though the frequency-dependent term $\varepsilon_\infty(\omega)$, which is not due to the free electron gas, is present. Eq. (2.11) will be the main form for the dielectric constant used throughout this thesis, unless otherwise stated.

2.2 Nonlocal response

Now that we have studied the derivation of the governing equations in the local-response approximation, we are in a position to consider the implications of including nonlocal response. The derivation we present in this section will follow closely the

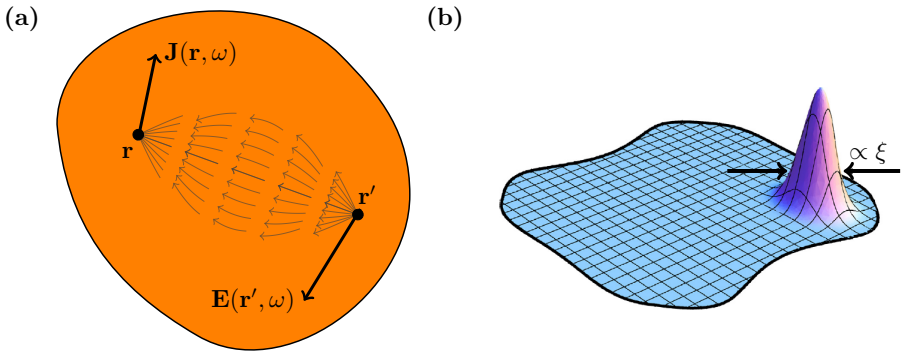

Figure 2.1: **(a)** Schematic illustration of the nonlocal relation between the current density (response of the material) and the electric field (driving field) in a metal, as described by Eq. (2.3). **(b)** Schematic illustration of the nonlocal response function $f(|\mathbf{r}-\mathbf{r}'|)$ with range proportional to ξ, which is centered around $\mathbf{r}$ and plotted as a function of $\mathbf{r}'$. Reproduced from Ref. [56].

approach in Ref. [56], which has been inspired by Ref. [57]. Our starting point is again the nonlocal relation between the current density and the electric field, given by Eq. (2.3b). As we recognize that the LRA accounts for many of the physical phenomena observed in studies involving metals, it seems reasonable to assume that nonlocal effects should only slightly correct the LRA Drude conductivity, which allows us to write for an isotropic medium

$$\sigma(\mathbf{r},\mathbf{r}',\omega) = \sigma_{\text{D}}(\omega)\delta(\mathbf{r}-\mathbf{r}') + f(|\mathbf{r}-\mathbf{r}'|,\omega), \tag{2.12}$$

where $f(|\mathbf{r}-\mathbf{r}'|,\omega)$ is the nonlocal response function associated with a homogenous medium. Insertion of Eq. (2.12) into the constitutive relation Eq. (2.3b) then gives

$$\mathbf{J}(\mathbf{r},\omega) = \sigma_{\text{D}}(\omega)\mathbf{E}(\mathbf{r},\omega) + \int \mathrm{d}\mathbf{r}' f(|\mathbf{r}-\mathbf{r}'|,\omega)\mathbf{E}(\mathbf{r}',\omega). \tag{2.13}$$

Besides assuming that $f(|\mathbf{r}-\mathbf{r}'|,\omega)$ is a small correction to the LRA conductivity $\sigma(\omega)\delta(\mathbf{r}-\mathbf{r}')$, we furthermore make the justifiable assumptions that $f(|\mathbf{r}-\mathbf{r}'|,\omega)$ should be symmetric and short-ranged. We can express these assumptions mathematically through the moments of the function [56]

$$\int f(\mathbf{r},\omega)\mathrm{d}\mathbf{r} \ll \sigma_{\text{D}}(\omega), \tag{2.14a}$$

$$\int \mathbf{r} f(\mathbf{r},\omega)\mathrm{d}\mathbf{r} = 0, \tag{2.14b}$$

$$\int \mathbf{r}^2 f(\mathbf{r},\omega)\mathrm{d}\mathbf{r} = -2i\omega\varepsilon_0\xi^2, \tag{2.14c}$$

where $\mathbf{r}^2 \equiv (x^2, y^2, z^2)$ and we have introduced the length scale ξ as the range of the nonlocal response function [see Fig. 2.1(b) for a schematic illustration]. The prefactor

$-2i\omega\varepsilon_0$ in Eq. (2.14c) has been conveniently introduced in anticipation of the final result. Since the response function $f(|\mathbf{r}-\mathbf{r}'|,\omega)$ is short-ranged, we Taylor expand the electric field in the integrand of Eq. (2.13) around $\mathbf{r}$. To second order we find

$$E_i(\mathbf{r}') \simeq E_i(\mathbf{r}) + [\nabla E_i(\mathbf{r})]\cdot(\mathbf{r}'-\mathbf{r}) + \frac{1}{2}(\mathbf{r}'-\mathbf{r})^T\cdot\left[\hat{\mathbf{H}}E_i(\mathbf{r})\right]\cdot(\mathbf{r}'-\mathbf{r}), \tag{2.15}$$

where we for clarity have omitted the frequency dependence of the electric field. The Hessian matrix $\hat{\mathbf{H}}$ has the elements $H_{ij} = \partial^2/(\partial_i\partial_j)$ with $i,j = x,y,z$. Now inserting the Taylor-expanded electric field, given by Eq. (2.15), into Eq. (2.13) and using the assumptions stated in Eq. (2.14), we find that only the diagonal elements of the Hessian matrix contribute to the general nonlocal constitutive relation

$$\mathbf{J}(\mathbf{r},\omega) = \sigma_{\text{D}}(\omega)\mathbf{E}(\mathbf{r},\omega) - i\omega\varepsilon_0\xi^2\nabla^2\mathbf{E}(\mathbf{r},\omega). \tag{2.16}$$

Before commenting on this crucial result, let us derive the nonlocal wave equation by applying the curl to Eq. (2.1c) and using Eqs. (2.1d), (2.4) and (2.16)

$$\nabla\times\nabla\times\mathbf{E}(\mathbf{r},\omega) = \left(\frac{\omega}{c}\right)^2\left[\varepsilon_{\text{D}}(\omega) + \xi^2\nabla^2\right]\mathbf{E}(\mathbf{r},\omega) + i\omega\mu_0\mathbf{J}_{\text{ext}}(\mathbf{r},\omega). \tag{2.17}$$

Here, we emphasize the important fact that nonlocal response to lowest order in field inhomogeneity manifests itself through the Laplacian term with a strength determined by the nonlocal length scale ξ. This result holds irrespectively of the microscopic origin of the nonlocal response, providing great insight into the mathematical form of any nonlocal model. At this stage, the nonlocal parameter ξ^2 is an unknown variable that must be determined either from a theoretical model, such as the hydrodynamic or GNOR models which are to be discussed in Secs. 2.3 and 2.4, respectively, or a more pragmatic approach can be taken, where ξ^2 is fitted using experimental observations. A combination of both approaches can also be utilized, as it is done with measurements of the dielectric constant from which the Drude parameters in Eq. (2.11) are extracted [53, 54].

We can simplify Eq. (2.17) by using the vector identity $\nabla^2 = \nabla(\nabla\cdot) - \nabla\times\nabla\times$ and rearranging the terms. We find

$$\begin{aligned}\left[1 + \left(\frac{\omega}{c}\right)^2\xi^2\right]\nabla\times\nabla\times\mathbf{E}(\mathbf{r},\omega) = \left(\frac{\omega}{c}\right)^2\left[\varepsilon_{\text{D}}(\omega) + \xi^2\nabla(\nabla\cdot)\right]\mathbf{E}(\mathbf{r},\omega)\\ + i\omega\mu_0\mathbf{J}_{\text{ext}}(\mathbf{r},\omega).\end{aligned} \tag{2.18}$$

Considering optical frequencies $\omega \approx 10^{15}$ rad/s and expecting the nonlocal length scale to be on the Ångstrom scale [58], i.e., $\xi \approx 10^{-10}$ m, we find that $(\omega/c)^2\xi^2 \approx 10^{-8}$ which is negligible compared to unity, allowing us to simplify Eq. (2.18) as

$$\nabla\times\nabla\times\mathbf{E}(\mathbf{r},\omega) = \left(\frac{\omega}{c}\right)^2\left[\varepsilon_{\text{D}}(\omega) + \xi^2\nabla(\nabla\cdot)\right]\mathbf{E}(\mathbf{r},\omega) + i\omega\mu_0\mathbf{J}_{\text{ext}}(\mathbf{r},\omega). \tag{2.19}$$

We prefer the formulation of Eq. (2.19) instead of Eq. (2.17) as nonlocal response then only alters the curl-free part of the electric field, while the divergence-free part of the electric field remains the same as in the LRA (to be shown in detail in the next section).

2.2.1 Helmholtz decomposition of electric field

Besides the nonlocal wave equation [Eq. (2.19)], there is another enlightening way to write the governing nonlocal equations for the electric field. Inspired by the approach

used for the nonlocal hydrodynamic model [59, 60, 33, 61, 62], we write two differential equations, one for $\nabla \cdot \mathbf{E}(\mathbf{r},\omega)$ and one for $\nabla \times \mathbf{E}(\mathbf{r},\omega)$ as

$$\left(\nabla^2 + k_{\mathrm{nl}}^2\right) \nabla \cdot \mathbf{E}(\mathbf{r},\omega) = \frac{\nabla \cdot \mathbf{J}_{\mathrm{ext}}(\mathbf{r},\omega)}{i\omega\varepsilon_0\xi^2}, \tag{2.20a}$$

$$\left(\nabla^2 + k^2\right) \nabla \times \mathbf{E}(\mathbf{r},\omega) = -i\omega\mu_0 \nabla \times \mathbf{J}_{\mathrm{ext}}(\mathbf{r},\omega), \tag{2.20b}$$

where $k_{\mathrm{nl}}^2 = \varepsilon_{\mathrm{D}}/\xi^2$ is the nonlocal wave vector and $k^2 = (\omega/c)^2\varepsilon_{\mathrm{D}}$ is the usual LRA wave vector, associated with the divergence-free electric field [Eq. (2.9)]. The result in Eq. (2.20a) is derived by inserting Eq. (2.16) into Gauss' equation [Eq. (2.1a)] and rearranging the terms, while the starting point for Eq. (2.20b) is Eq. (2.19). Here we first use the vector identity $\nabla \times \nabla \times = \nabla(\nabla\cdot) - \nabla^2$, and then apply the curl operator. Exploiting that the curl of a gradient is zero and that the curl and Laplacian commute, we finally arrive at Eq. (2.20b).

Considering for clarity the case where no sources are present, we use the Helmholtz decomposition to write the electric field as

$$\mathbf{E}(\mathbf{r},\omega) = \mathbf{E}_{\mathrm{DF}}(\mathbf{r},\omega) + \mathbf{E}_{\mathrm{CF}}(\mathbf{r},\omega), \tag{2.21}$$

where $\mathbf{E}_{\mathrm{DF}}(\mathbf{r},\omega)$ and $\mathbf{E}_{\mathrm{CF}}(\mathbf{r},\omega)$ have the properties of being divergence free $\nabla \cdot \mathbf{E}_{\mathrm{DF}} = 0$ and curl free $\nabla \times \mathbf{E}_{\mathrm{CF}} = 0$, respectively. In the Fourier domain ($\mathbf{k}$-space), the divergence-free field is a transverse field, as discussed in the context of the LRA (see Sec. 2.1), while the curl-free field corresponds to a longitudinal field, where the propagation direction ($\mathbf{k}$-direction) is parallel to the electric field. Thus, these two properties constitute two different types of electric fields, which in a homogeneous medium are uncoupled, but in the presence of an interface can be coupled by means of the electromagnetic boundary conditions. We stress that the difference between the LRA and the inclusion of nonlocal response is the presence of the curl-free (or longitudinal) wave, which will be responsible for all nonlocal effects. By inserting Eq. (2.21) into Eq. (2.20), we can derive the governing equations for the divergence-free and curl-free fields, which in the absence of any sources is given by

$$\left(\nabla^2 + k_{\mathrm{nl}}^2\right) \nabla \cdot \mathbf{E}_{\mathrm{CF}}(\mathbf{r},\omega) = 0, \tag{2.22a}$$

$$\left(\nabla^2 + k^2\right) \nabla \times \mathbf{E}_{\mathrm{DF}}(\mathbf{r},\omega) = 0. \tag{2.22b}$$

We now clearly see that the divergence-free wave $\mathbf{E}_{\mathrm{DF}}$ has the same wave vector as in the LRA, i.e. determined by the relation $k^2 = (\omega/c)^2\varepsilon_{\mathrm{D}}(\omega)$, while the curl-free wave $\mathbf{E}_{\mathrm{CF}}$ is described by the nonlocal wave vector $k_{\mathrm{nl}}^2 = \varepsilon_{\mathrm{D}}(\omega)/\xi(\omega)^2$. In other words, nonlocal response does not directly affect the divergence-free (transverse) wave (cf. BCs), but only the curl-free (longitudinal) wave.

Lastly, we point out that we could also have performed the Helmholtz decomposition on the external current density $\mathbf{J}_{\mathrm{ext}}$ as well to show that the divergence-free (curl-free) part of the source contributes solely to the divergence-free (curl-free) part of the electric field.

2.2.2 Additional boundary condition

Within the LRA, Maxwell's boundary conditions, which are derived using pill-box and current loop arguments [63], are sufficient to determine the amplitudes of the divergence-free electric and magnetic fields. However, the presence of an additional wave due to nonlocal response will require an additional boundary condition (ABC) to determine the amplitude of the curl-free wave [64]. As the inclusion of nonlocal response alters Gauss' law [compare Eq. (2.6a) with Eq. (2.20a)], we focus on the

boundary condition which is derived from this equation. In the following derivation, we consider any interface between a metal and a dielectric, where relevant fields and parameters are subscripted with m and d, respectively. For the metal we can write up Gauss' law [Eq. (2.1a)] as

$$\nabla \cdot \left(\mathbf{D}_{\mathrm{m}} + \frac{i}{\omega} \mathbf{J}_{\mathrm{m}} \right) = \rho_{\mathrm{ext}}, \tag{2.23}$$

where we have used the continuity equation [Eq. (2.2a)]. In the dielectric, Gauss' law reads

$$\nabla \cdot \mathbf{D}_{\mathrm{d}} = \rho_{\mathrm{ext}}, \tag{2.24}$$

since there are no free electrons in an dielectric to conduct a current ($\mathbf{J}_{\mathrm{d}} = 0$). Using the standard approach of rewriting Eqs. (2.23) and (2.24) into their integral forms and then considering a pill-box with vanishing height [63], we find

$$\left(\varepsilon_\infty \mathbf{E}_{\mathrm{m}} + \frac{i}{\varepsilon_0 \omega} \mathbf{J}_{\mathrm{m}} - \varepsilon_{\mathrm{d}} \mathbf{E}_{\mathrm{d}} \right) \cdot \hat{\mathbf{n}} = 0, \tag{2.25}$$

where we have removed the contribution from any surface charge density due to the external source and introduced the unit vector perpendicular to the interface $\hat{\mathbf{n}}$. Furthermore, we have used the relations given by Eq. (2.4) and $\mathbf{D}_{\mathrm{d}} = \varepsilon_{\mathrm{d}} \mathbf{E}_{\mathrm{d}}$, where ε_{d} is the dielectric constant of the insulator.

In the LRA, we know that the current density is connected to the electric field through the simple relation given by Eq. (2.5), thus allowing us to write the usual LRA boundary condition

$$(\varepsilon_{\mathrm{D}} \mathbf{E}_{\mathrm{m}} - \varepsilon_{\mathrm{d}} \mathbf{E}_{\mathrm{d}}) \cdot \hat{\mathbf{n}} = 0, \tag{2.26}$$

which states the normal component of the electric field is discontinuous across a metal-dielectric interface. Here, ε_{D} is again the Drude permittivity given by Eq. (2.11). However, with the inclusion of nonlocal response, an additional assumption must be made to determine the boundary condition. Inspired by the many discussions on the appropriate boundary conditions in the nonlocal hydrodynamic model [33, 64, 65, 66, 67, 68], we will assume that the static equilibrium free-electron density n_0 has a step profile, i.e., n_0 is constant inside the metal and abruptly drops to zero at the metal-dielectric interface. The consequence of this assumption is that the induced charge density ρ will vanish at the metal-dielectric boundary, at which a pill-box argument on the continuity equation [Eq. (2.2a)] reveals the additional boundary condition

$$\mathbf{J}_{\mathrm{m}} \cdot \hat{\mathbf{n}} = 0, \tag{2.27}$$

stating that the normal component of the current density vanishes at the metal boundary. We note that this additional boundary condition will not allow us to include the quantum mechanical effect of spill-out of electrons occurring due to the finite potential difference at the metal-dielectric interface. In fact, the ABC prompts the metal to have an infinite work function. We can rewrite this ABC by using Eq. (2.25), from which we find

$$(\varepsilon_\infty \mathbf{E}_{\mathrm{m}} - \varepsilon_{\mathrm{d}} \mathbf{E}_{\mathrm{d}}) \cdot \hat{\mathbf{n}} = 0. \tag{2.28}$$

Thus, even with the inclusion of nonlocal response, the normal component of the electric field is still discontinuous, however with a different amount compared to the LRA, as one can appreciate by comparing Eqs. (2.26) and (2.28).

For completeness, we also mention the remaining Maxwell's boundary conditions for the electric and magnetic fields [63]

$$(\mathbf{H}_{\mathrm{m}} - \mathbf{H}_{\mathrm{d}}) \cdot \hat{\mathbf{n}} = 0, \tag{2.29a}$$

$$(\mathbf{H}_{\mathrm{m}} - \mathbf{H}_{\mathrm{d}}) \times \hat{\mathbf{n}} = 0, \tag{2.29b}$$

$$(\mathbf{E}_{\mathrm{m}} - \mathbf{E}_{\mathrm{d}}) \times \hat{\mathbf{n}} = 0, \tag{2.29c}$$

which state that the parallel components of the electric field and all of the components of the magnetic field are continuous across the metal-insulator interface. The continuity of all of the components of the magnetic field is a consequence of the assumption of the metal being non-magnetic.

2.3 Hydrodynamic theory of free-electron gas

We consider now a specific nonlocal model, known as the hydrodynamic model, for the free-electron gas, which will allow us to determine the nonlocal length scale ξ, or equivalently the nonlocal wave vector k_{nl}, introduced in the previous section in Eqs. (2.16) and (2.20a), respectively. The hydrodynamic model has been examined extensively in the past, and has in the last few years seen a rebirth both due to numerical implementations allowing to study non-trivial structures [69, 70, 71], and to advances in fabrication [72] and experimental techniques, allowing to measure the signatures of nonlocality [26, 20].

2.3.1 Overview

The idea of modeling the electron gas in a continuum-field formulation was first introduced by Bloch in a seminal paper in 1933 [73]. It was considered a dynamic generalization of the static Thomas–Fermi theory [74, 75]. The hydrodynamic approach was further discussed by Jensen [76] in 1937 in the context of a spherically restricted electron gas. Initially, the hydrodynamic approach was mostly applied in the fields of atomic and nuclear physics, and with considerable success [77]. Due to the prevalence of more detailed microscopic theories, the hydrodynamic approach seemed less useful in solid-state physics until the beginning of 1970, where Bennett [22] applied the hydrodynamic model to study the effect of surface inhomogeneity in the electron gas, by considering the electron density to decrease linearly at the surface and not as a sudden step. In contrast to the microscopic theories, the hydrodynamic model allowed for incorporating inhomogeneity and spatial dispersion with a clear discussion of the physical principles involved. In 1974, Ying [77] extended Bloch's non-retarded approach to a more general density-functional formalism, allowing to go beyond the Thomas-Fermi ground state, which lacked information about the correlation and exchange energies of the electron gas. Shortly after Eguiluz and Quinn [78] included retardation effects. In the 1970s and the beginning of the 1980s the hydrodynamic model was extensively used in the field of solid-state physics. The effect of inhomogeneity and spatial dispersion in planar interfaces [23, 59, 64, 79], spherical particles [60, 80, 81] and voids [82], and cylindrical particles [83, 84] was given a considerable amount of attention. Especially, the results obtained for homogeneous planar surfaces are in excellent agreement with experiment [33]. Furthermore, confusion arose about the additional boundary conditions that are needed to solve the hydrodynamic equations. Discussions regarding the physically correct and the number of additional boundary conditions went back and forth [23, 66, 85, 67] and was finally thoroughly discussed and clarified by Jewsbury [68].

Recently, interest in the hydrodynamic model was rekindled when McMahon et al. introduced a finite-element time-domain numerical implementation of the hydrodynamic equations [69, 86], allowing them to calculate plasmon modes and extinction cross-sections of plasmonic dimers and core-shell structures [87, 88]. However, as afterwards shown in Paper L, the governing equations and the ABCs that McMahon et al. implemented were inconsistent with the hydrodynamic model [33], and instead gave rise to unphysical new plasmonic resonances below the plasma frequency. Shortly after, the correct hydrodynamic equations and corresponding ABC were implemented using a frequency-domain finite-element solver [70], which was utilized to study the

plasmonic cylindrical dimer [70], surface-enhanced Raman spectroscopy [89], and waveguiding in metallic nanostructures [90]. Simultaneously, application of transformation optics to the hydrodynamic model allowed for analytical solutions of several non-trivial plasmonic structures, even some containing singular geometric features [91, 92, 93]. Additionally, a plethora of metallic nanostructures and plasmonic effects have been studied using the hydrodynamic model, such as scattering and mode analysis of cylindrical structures, including nanotubes [94, 61, 95, 90, 96, 97], roughness effects on plasmonic tips [98, 99], nonlinear effects in nonlocal media [100, 101], scattering of light off three-dimensional nanostructures [102, 26, 103], surface plasmon propagation in metal-insulator, metal-insulator-metal (MIM), insulator-metal-insulator (IMI), and hourglass waveguides [104, 62, 105], epsilon-near-zero (ENZ) effects [106, 107], influence of nonlocal response on the Casimir force [108], studies of hyperbolic metamaterials and periodic media [109, 110, 111], and investigations of nonlocal effects in electron energy-loss spectroscopy [112, 113]. Finally, theoretical work has also been done to compare the hydrodynamic approach with more advanced approaches such as density-functional theory [114, 115, 116].

2.3.2 Governing equations

The derivation and discussion in this section are based on the work in Paper L. We will not go through a detailed derivation of the hydrodynamic model, as this has been reported before [33, 73, 78, 117]. Instead we go through the most important steps of the derivation and extract the essential physics of the hydrodynamic model. We begin by expressing the collective motion of the electrons in an inhomogeneous medium in terms of the electron density $n(\mathbf{r},t)$ and the hydrodynamic velocity $\mathbf{v}(\mathbf{r},t)$. Under the influence of macroscopic electromagnetic fields $\mathbf{E}(\mathbf{r},t)$ and $\mathbf{B}(\mathbf{r},t)$, the hydrodynamic model is defined via [33]

$$\left[\partial_t + \mathbf{v}\cdot\nabla\right]\mathbf{v} = -\gamma\mathbf{v} - \frac{e}{m}\left[\mathbf{E} + \mathbf{v}\times\mathbf{B}\right] - \nabla\frac{\delta G[n]}{\delta n}, \tag{2.30}$$

along with the continuity equation

$$\partial_t n = -\nabla\cdot(n\mathbf{v}), \tag{2.31}$$

expressing charge conservation. In the right-hand side of Eq. (2.30), the γ-term represents bulk damping, the second term is the Lorentz force, while the third term can take into account the correlation, exchange and the internal kinetic energy of the electron gas, if an appropriate functional $G[n]$ is chosen [77]. Finally, $\delta G[n]/\delta n$ denotes the functional derivative.

The most common, and also the simplest, approach [33, 22] is to use the Thomas-Fermi model for the functional $G[n]$, given as

$$G[n(\mathbf{r},t)] = \int \frac{3h^2}{10m}\left(\frac{3}{8\pi}\right)^{\frac{2}{3}} n^{\frac{5}{3}}(\mathbf{r},t)\mathrm{d}\mathbf{r}, \tag{2.32}$$

which describes only the internal kinetic energy of the electron gas. For completeness, we note that the Thomas–Fermi model has been shown to be the zeroth-order term in the gradient of the density $\nabla n(\mathbf{r},t)$ of a more general expansion of the functional $G[n]$ [118], where the next higher-order term, proportional to $\nabla^2 n(\mathbf{r},t)$, is given by the Weizsäcker correction [119]. The functional derivative of Eq. (2.32) can now be performed

$$\frac{\delta G[n]}{\delta n} = \frac{h^2}{2m}\left(\frac{3}{8\pi}\right)^{\frac{2}{3}} n^{\frac{2}{3}}(\mathbf{r},t), \tag{2.33}$$

which upon insertion in Eq. (2.30) finally gives

$$[\partial_t + \mathbf{v}\cdot\nabla]\,\mathbf{v} = -\gamma\mathbf{v} - \frac{e}{m}\left[\mathbf{E} + \mathbf{v}\times\mathbf{B}\right] - \frac{\beta^2}{n}\nabla n. \tag{2.34}$$

In analogy with fluid hydrodynamics [120], the third term represents a pressure that gives rise to a nonlocal permittivity. The pressure term is proportional to $\beta^2 = 3/5v_{\text{F}}^2$ with v_{F} denoting the Fermi velocity and describes a force that will act to homogenize any inhomogeneity in the electron density.

In the spirit of linear-response theory, we now follow the usual approach [33, 117] to solve Eq. (2.34) and the continuity equation [Eq. (2.31)], by expanding the physical fields in a static term (e.g., n_0 is the homogeneous static electron density), and a small (by assumption) first-order dynamic term, akin to perturbation theory, thereby linearizing the equations of motion. In the frequency domain, we obtain for a homogeneous medium [61, 70]

$$\frac{\beta^2}{\omega\,(\omega + i\gamma)}\nabla\left[\nabla\cdot\mathbf{J}(\mathbf{r},\omega)\right] + \mathbf{J}(\mathbf{r},\omega) = \sigma_{\text{D}}(\omega)\mathbf{E}(\mathbf{r},\omega), \tag{2.35}$$

where $\mathbf{J}(\mathbf{r},\omega) = -en_0\mathbf{v}(\mathbf{r},\omega)$ is the induced current density, and $\sigma_{\text{D}}(\omega)$ is the Drude conductivity given by Eq. (2.10). We see that in the limit of $\beta \to 0$, Eq. (2.35) reduces to Ohm's law [Eq. (2.5)]. Now, by combining Eq. (2.35) with Maxwell's equations [Eqs. (2.1) and (2.4)], we can rewrite the governing equations in the hydrodynamic model in the same form as Eq. (2.20). Thereby, we determine the nonlocal wave vector in the hydrodynamic model to be [62]

$$k_{\text{nl}}^2 = \frac{\omega^2 + i\gamma\omega - \omega_{\text{p}}^2/\varepsilon_\infty(\omega)}{\beta^2}, \tag{2.36}$$

from which we find the hydrodynamic nonlocal parameter ξ_{H} to be [90, 34]

$$\xi_{\text{H}}^2 = \frac{\varepsilon_\infty(\omega)\beta^2}{\omega^2 + i\gamma\omega}. \tag{2.37}$$

In the absence of interband effects and bulk damping mechanisms ($\varepsilon_\infty = 1, \gamma = 0$), the nonlocal parameter is simply $\xi_{\text{H}} = \beta/\omega$, which is a purely real-valued quantity. We also see that the nonlocal strength increases with the Fermi velocity (through β) and decreases with frequency. Since we consider optical frequencies ($\omega \approx 10^{15}$ rad/s) and since the Fermi velocity of most metals is on the order of 10^6 m/s, we see that ξ_{H} is on the nanometer scale, in agreement with our expectations from deriving Eq. (2.19). In general, the presence of interband effects and damping will render the nonlocal parameter ξ_{H} complex-valued.

Figure 2.2 displays the real and imaginary parts of ξ_{H} (blue lines) for sodium (Na), a simple metal which is well-described as a pure free-electron gas, and for silver (Ag), a noble metal with significant contributions to the permittivity from interband transitions. For Na [Fig. 2.2(a-b)], we see that both the real and imaginary parts of ξ_{H} increase in magnitude for decreasing energy, as expected from the previous discussion. Furthermore, the presence of a weak damping rate γ gives rise to an imaginary part to ξ_{H}, although the imaginary part is numerically almost one order smaller than the real part. Thus for Na, the hydrodynamic nonlocal parameter is mainly characterized by its real part. For the case of Ag [Fig. 2.2(c-d)], the picture is significantly more complicated since effects not due to the free-electron gas are present, i.e., those described by $\varepsilon_\infty(\omega)$. While the trend for the real and imaginary parts of ξ_{H} is quite different in Ag than Na, the magnitudes are on the same order for the two metals, and the real part still contributes more than the imaginary part.

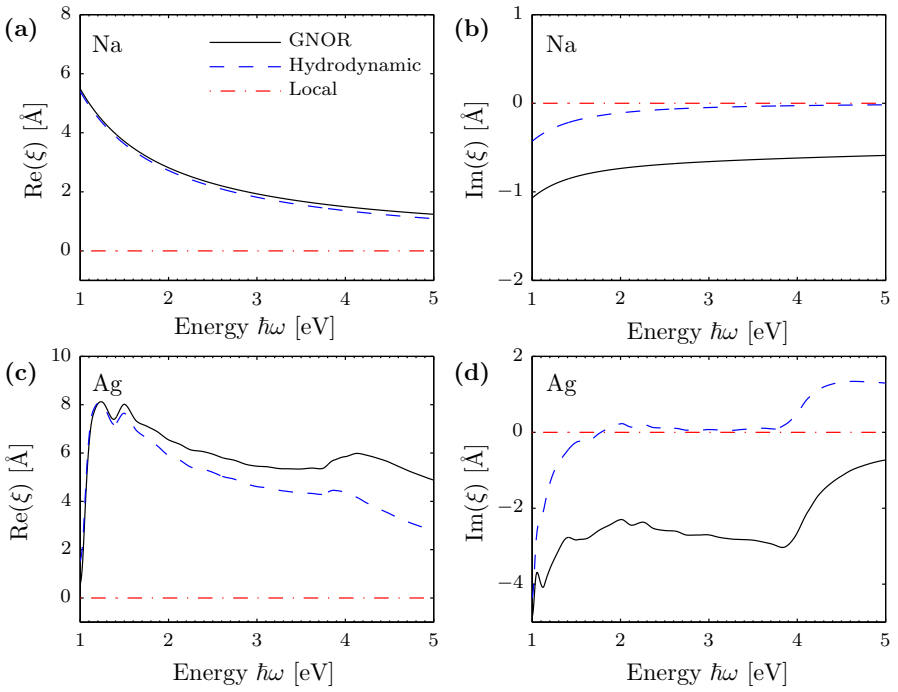

Figure 2.2: Real and imaginary parts of the nonlocal length scale ξ in the GNOR theory (black line) and hydrodynamic model (blue dashed line) as a function of energy $\hbar\omega$ for **(a-b)** Na and **(c-d)** Ag. For reference, the red dash-dotted line displays the LRA ($\xi = 0$). Material parameters for Na (Paper A): $\hbar\omega_\mathrm{p} = 6.04$ eV, $\hbar\gamma = 0.16$ eV, $\varepsilon_\infty = 1$, $v_\mathrm{F} = 1.07 \times 10^6$ m/s, and $D = 1.08 \times 10^{-4}$ m^2/s. Material parameters for Ag (Paper A): $\hbar\omega_\mathrm{p} = 8.99$ eV, $\hbar\gamma = 0.025$ eV, $v_\mathrm{F} = 1.39 \times 10^6$ m/s, and $D = 3.61 \times 10^{-4}$ m^2/s. Due to the interband transitions in Ag, we determine ε_∞ using the recipe $\varepsilon_\infty = \varepsilon_\mathrm{exp} + \omega_\mathrm{p}^2/(\omega^2 + i\gamma\omega)$ [121], where ε_exp is the experimentally measured bulk dielectric function for Ag, taken from Ref. [54].

2.4 Generalized nonlocal optical response

This section describes the recently introduced GNOR model, which is presented in Paper C. A hitherto disregarded effect in the discussion of metallic nanostructures and nonlocal response is the classical phenomenon of movement of electrons due to diffusive currents [122]. While the hydrodynamic model incorporates the convective current due to the pressure term in Eq. (2.34), it completely neglects any currents due to diffusion. The GNOR model expands the hydrodynamic theory to also take into account electron diffusion. We now consider the mathematical description of this effect. The inclusion of electron diffusion alters the continuity equation, which in its linearized form now reads

$$-i\omega en(\mathbf{r},\omega) = D\nabla^2[en(\mathbf{r},\omega)] + \nabla\cdot[-en_0\mathbf{v}(\mathbf{r},\omega)] = \nabla\cdot\mathbf{J}(\mathbf{r},\omega), \tag{2.38}$$

also known as the convection-diffusion equation. Here, D is the diffusion constant, and the induced current density, given by Fick's law, now has a diffusive contribution

$$\mathbf{J}(\mathbf{r},\omega) = -en_0\mathbf{v}(\mathbf{r},\omega) + D\nabla[en(\mathbf{r},\omega)]. \tag{2.39}$$

Combining the convection-diffusion equation and Fick's law for the current density with the linearized hydrodynamic equation (see Supplemental Material of Paper C), we eventually arrive at the following constitutive relation for the current density

$$\left[\frac{\beta^2}{\omega(\omega+i\gamma)}+\frac{D}{i\omega}\right]\nabla[\nabla\cdot\mathbf{J}(\mathbf{r},\omega)]+\mathbf{J}(\mathbf{r},\omega)=\sigma_{\text{D}}(\omega)\mathbf{E}(\mathbf{r},\omega), \tag{2.40}$$

which we immediately recognize to have the same form as the hydrodynamic constitutive relation, given by Eq. (2.35). The difference lies in the prefactor of the first term, which we can rewrite as

$$\frac{\beta^2}{\omega(\omega+i\gamma)}+\frac{D}{i\omega}=\frac{\beta^2+D(\gamma-i\omega)}{\omega(\omega+i\gamma)}\equiv\frac{\eta^2}{\omega(\omega+i\gamma)}, \tag{2.41}$$

where we have defined the parameter

$$\eta^2\equiv\beta^2+D(\gamma-i\omega). \tag{2.42}$$

Comparing Eq. (2.40) with Eq. (2.35), we see that the mathematical considerations from the hydrodynamic model can be mapped directly to the GNOR model using the simple substitution $\beta^2\to\eta^2$. Thus, we straightforwardly find the nonlocal GNOR wave vector to be

$$k_{\text{nl}}^2=\frac{\omega^2+i\gamma\omega-\omega_{\text{p}}^2/\varepsilon_\infty(\omega)}{\eta^2}=\frac{\omega^2+i\gamma\omega-\omega_{\text{p}}^2/\varepsilon_\infty(\omega)}{\beta^2+D(\gamma-i\omega)}, \tag{2.43}$$

and similarly, the GNOR nonlocal parameter ξ_{GNOR} is given by the relation

$$\xi_{\text{GNOR}}^2=\frac{\varepsilon_\infty(\omega)[\beta^2+D(\gamma-i\omega)]}{\omega^2+i\gamma\omega}. \tag{2.44}$$

Considering the case with no interband effects and no bulk damping, we see that the diffusion constant only contributes to the imaginary part of ξ_{GNOR}^2, making the nonlocal parameter complex-valued (in contrast to the hydrodynamic model). In the general case, the parameters β and D will contribute to both the real and imaginary parts of the nonlocal parameter.

For a more quantitative comparison with the hydrodynamic length scale ξ_{H}, given by Eq. (2.37), we show in Fig. 2.2 also the real and imaginary parts of the GNOR length scale ξ_{GNOR} (black lines) for Na [Fig. 2.2(a-b)] and Ag [Fig. 2.2(c-d)]. The main difference, when comparing the GNOR and hydrodynamic length scales, is that the inclusion of diffusion makes the imaginary part comparable in magnitude to the real part. For Na, we see that the presence of diffusion almost exclusively only changes the imaginary part of ξ, while for Ag diffusion also slightly alters the real part. However, as a general rule of thumb, one can think of the hydrodynamic parameter $\beta\propto v_{\text{F}}$ (or the convective current) as the main contributor to the real part of ξ, while the imaginary part of ξ is characterized by the diffusion constant D (or the diffusive current).

Chapter 3

Nonlocal effects in plasmonic nanostructures

With the governing equations for the nonlocal GNOR and hydrodynamic models in place from the last chapter, we are now in a position to solve the equations in specific systems. This chapter is therefore devoted to studying some of the relevant plasmonic systems, which exhibit strong features due to nonlocal response. We begin in Sec. 3.1 by considering the most fundamental plasmonic system, the simple metal-insulator interface and its surface plasmon polariton mode. Then in Sec. 3.2 we study the optical spectrum of a single spherical nanoparticle, where the important length scale is the particle size. Next in Sec. 3.3 we consider the plasmonic dimer, consisting in this case of two infinitely long cylinders, and study the dependence of the optical spectrum on the gap size. Finally in Sec. 3.4, we also take a look at the interesting properties of a core-shell nanowire, consisting of an insulating core and a nanometer-sized metallic shell. We will compare the GNOR model with the hydrodynamic model and the LRA, and, whenever possible, with more advanced calculations based on approaches such as density-functional theory and the random-phase approximation (RPA).

3.1 Metal-insulator interface

The support of SPP at the interface between a metal and an insulator represents perhaps the most generic theoretical electromagnetic problem in the LRA in plasmonics [11, 123] and for good reasons. Many important properties of the surface-bound plasma wave can be extracted in this simple system, such as e.g. the propagation length, the decay length (i.e., a measure of the confinement to the metal surface) and the surface plasmon wavelength. Thus, the metal-insulator system is a natural starting point for investigating and discussing the implications of nonlocal response. However, before considering the SPP mode in a nonlocal framework, we first study the Feibelman parameter [124], which is a function defined from examining the planar metal-insulator interface and provides great insight to the features of nonlocal response. Although these features are determined from studying the metal-insulator system, it turns out that they are more general and in fact be mapped to more complicated geometries, see Refs. [125, 114] and Paper A.

3.1.1 Feibelman parameter

The Feibelman parameter, denoted by $d(\omega)$ and with unit length, has a relatively intuitive definition, which, in the nonlocal framework developed in Chapter 2, can be

calculated analytically. In the many recent studies of nonlocal response, the parameter has unfortunately been overlooked (besides a few publications, see Refs. [114, 115] and Paper A), despite the fact that some of the major effects of nonlocal response can be understood from this parameter. The real and imaginary part of $d(\omega)$ have distinctive interpretations. As shown by Feibelman, the real part of $d(\omega)$ measures the position of the centroid of induced charges at the surface, while the imaginary part of $d(\omega)$ is related to the power absorption at the surface [124]. In fact, the sign of $\mathrm{Re}[d(\omega)]$ can be directly related to size-dependent shifts of the resonance energy of the localized surface plasmon in confined geometries [126, 125, 127, 114, 128], where $\mathrm{Re}[d(\omega)] > 0$ corresponds to the situation where the free electrons spill in and produce a blueshift of the surface plasmon resonance energy (compared to its LRA value), while a redshift occurs due to spill-out, i.e., $\mathrm{Re}[d(\omega)] < 0$. Due to the relation of $\mathrm{Im}[d(\omega)]$ to surface absorption, the presence of a finite value for $\mathrm{Im}[d(\omega)]$ will be connected to a size-dependent linewidth of the LSP resonance (LSPR).

With the coordinate system shown in Fig. 3.1(a), the Feibelman parameter is defined as [124]

$$d(\omega) = \frac{\int_{-\infty}^{\infty} z\rho(z,\omega)\mathrm{d}z}{\int_{-\infty}^{\infty} \rho(z,\omega)\mathrm{d}z}, \tag{3.1}$$

where $\rho(z,\omega)$ still denotes the induced charge density, however, only a z-dependence is present due to the one-dimensional nature of the metal-insulator geometry. In general, $d(\omega)$ will be complex-valued due to $\rho(z,\omega)$. Within the general nonlocal framework of Sec. 2.2, the integrals can be straightforwardly performed to find

$$d(\omega) = \frac{i}{k_{\mathrm{nl}}} = \frac{i\xi}{\sqrt{\varepsilon_{\mathrm{D}}}}, \tag{3.2}$$

where the additional boundary condition $\mathbf{J} \cdot \hat{\mathbf{n}} = 0$ has been used to cut off the integrals in Eq. (3.1) at the metal-insulator interface ($z = 0$). Furthermore, k_{nl} again denotes the nonlocal wave vector, describing the curl-free (longitudinal) wave present in any nonlocal theory. With the simple relation of Eq. (3.2), we can calculate the Feibelman parameter in the LRA, the hydrodynamic model as well as in the GNOR theory. The results for Na and Ag are shown in Figs. 3.1(b-c) and 3.1(d-e), respectively. In the LRA, we find $d(\omega) = 0$, which means that the induced surface charges are situated exactly at the metal-interface interface without any absorption. The picture is significantly different in the hydrodynamic and GNOR models. Here, $d(\omega)$ is finite, with both a real and imaginary part. Considering first $\mathrm{Re}[d(\omega)]$ of Na (presented in Fig. 3.1(b)], we see that the hydrodynamic and GNOR models show similar trends, with an always positive value for $\mathrm{Re}[d(\omega)]$, which grows for increasing energy and peaks at the plasma frequency $\hbar\omega_{\mathrm{p}} = 6.04$ eV, whereafter it drops. The always positive value for $\mathrm{Re}[d(\omega)]$ is a direct consequence of the ABC, which forces the induced charges to reside inside the metal. It should be added that the GNOR model shows a slightly larger positive value for $\mathrm{Re}[d(\omega)]$ due to the additional contribution from diffusion. The peak at the plasma frequency can be understood from Eq. (3.2), which displays a pole at $\mathrm{Re}[\varepsilon_{\mathrm{D}}(\omega)] = 0$, which for a simple metal as Na occurs at the plasma frequency (actually, due to a finite-valued loss rate γ a negligible redshift of the pole compared to the ω_{p} is observed). In Fig. 3.1(c), we consider $\mathrm{Im}[d(\omega)]$, which in the hydrodynamic model is zero for most energies except around the aforementioned pole, while the GNOR model displays a finite value in the same energy range.

The trend of $d(\omega)$ in the hydrodynamic and GNOR models for Ag [shown in Fig. 3.1(d-e)] is very similar to that of Na, despite the strong interband contributions present only in Ag. The main consequence of the interband contribution in Ag is that the peak observed in the real part of $d(\omega)$ occurs at the screened plasma frequency

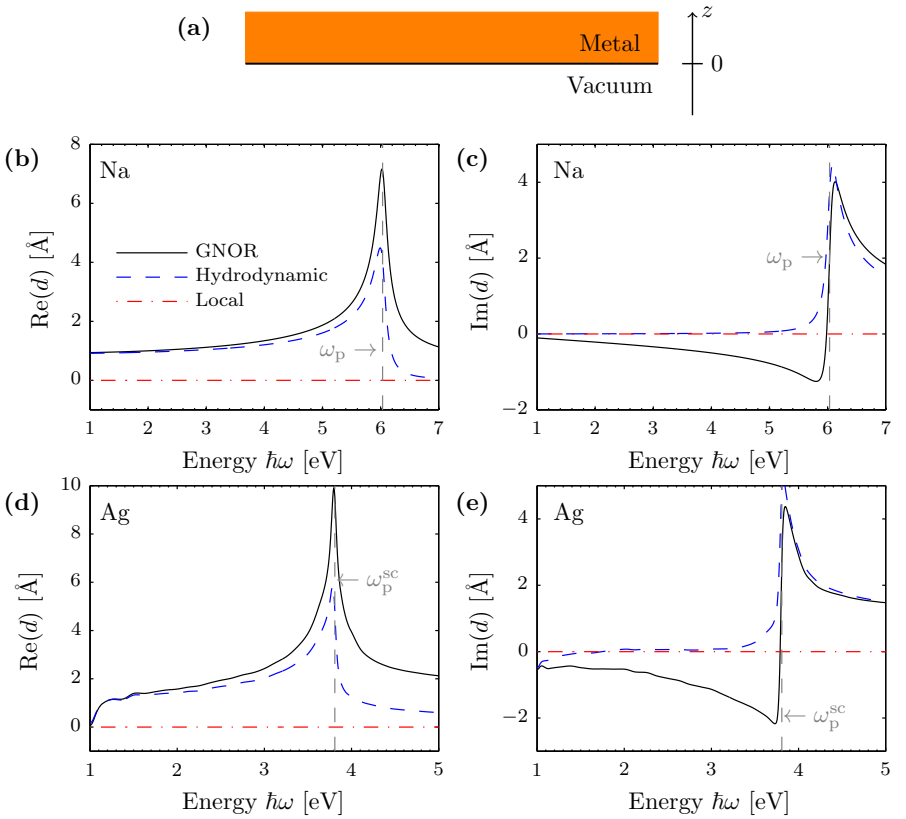

Figure 3.1: **(a)** Schematic illustration of metal-vacuum interface with coordinate system, where positive values of z indicate positions inside the metal. Real and imaginary parts of the Feibelman parameter $d(\omega)$ in the GNOR theory (black line) and hydrodynamic model (blue dashed line) as a function of energy $\hbar\omega$ for **(b-c)** Na and **(e-f)** Ag. The red dash-dotted line displays the LRA ($d = 0$). The grey vertical dashed lines display the screened plasma frequencies, determined from the relation $\mathrm{Re}[\varepsilon(\omega)] = 0$, which for Na is similar to the plasma frequency $\hbar\omega_\mathrm{p} = 6.04$ eV, while for Ag is significantly lower than the free-electron plasma frequency and measures $\hbar\omega_\mathrm{p}^\mathrm{sc} = 3.81$ eV. Material parameters for Na and Ag as in Fig. 2.2.

$\hbar\omega_\mathrm{p}^\mathrm{sc} = 3.81$ eV, which is much lower than the free-electron plasma frequency $\hbar\omega_\mathrm{p} = 8.99$ eV.

From the analysis of $d(\omega)$ in the LRA, hydrodynamic and GNOR models, we can expect the following properties of the LSPR in confined geometries:

- In the LRA, we expect no size-dependent shifts or broadening of the LSPR since $d(\omega) = 0$.
- In the hydrodynamic model, we expect a size-dependent blueshift of the LSPR (compared to the LRA value) since $\mathrm{Re}[d(\omega)] > 0$ for all energies considered, while a negligible size-dependent broadening of the LSPR is expected due to $\mathrm{Im}[d(\omega)] \approx 0$ for most energies below the plasma frequency.

- In the GNOR model, we expect both a size-dependent blueshift and size-dependent broadening of the LSPR (compared to the LRA value), since $\mathrm{Re}[d(\omega)] > 0$ and $\mathrm{Im}[d(\omega)] \neq 0$, respectively.

Finally, we can add that upon comparison of the calculations of Ag and Na, we find that the hydrodynamic and GNOR models treat the two different metals quite similarly, despite the interband contributions present in Ag.

Comparison with RPA

We can compare $\mathrm{Re}[d(\omega)]$ from the previous section with more advanced calculations performed by Feibelman [124]. Feibelman has used the jellium model within the RPA to calculate the surface properties of the metal-vacuum geometry. In Fig. 3.2, we display $\mathrm{Re}[d(\omega)]$ as a function of frequency for metals with varying conduction electron density, quantified by the Wigner–Seitz radius r_s. For Na, $r_\mathrm{s}/a_0 = 3.93$ [52], where a_0 is the Bohr radius, so we can with good approximation compare our calculations of $\mathrm{Re}[d(\omega)]$ on Na [Fig. 3.1(b)] with the curve for $r_\mathrm{s} = 4$ in Fig. 3.2. We see that the nonlocal calculations based on the hydrodynamic and GNOR models show a similar trend as the jellium calculations, with an increasing value for $\mathrm{Re}[d(\omega)]$ for increasing frequency which peaks at ω_p, whereafter it drops again. Furthermore, the length scale of $\mathrm{Re}[d(\omega)]$ is for both the nonlocal models and the jellium model on the same order. However, the difference lies in the fact that $\mathrm{Re}[d(\omega)]$ is negative for most frequencies below the plasma frequency in the jellium model, meaning that the centroid of induced charges is in fact positioned outside the metal, i.e., in the vacuum. This is possible due to the fact that the conduction electrons are allowed to spill-out through the finite energy barrier at the metal-vacuum interface in the jellium model. As mentioned in the discussion of the ABC, this is not possible in the nonlocal models due to the requirement of vanishing normal component of the current density. Thus, the jellium calculations give rise to redshift of the LSPR [114, 129, 130], which is different than the expected blueshift occurring in nonlocal calculations. For simple metals such as Na, the jellium model has been shown to be quite accurate [131], so we can unfortunately not expect the nonlocal models to represent such metals precisely, at least not for effects based on $\mathrm{Re}[d(\omega)]$, i.e., shifts of LSPR. However, it remains unclear if effects on the optical spectrum dominated by $\mathrm{Im}[d(\omega)]$, i.e., linewidth broadening, which are seen in dimer spectra (see Papers A and C), can be accurately captured by the nonlocal GNOR model (the nonlocal hydrodynamic model does not give rise to linewidth broadening, see Sec. 3.1.1). With these considerations in mind, studies of Na in the nonlocal models can still be valuable, as they illustrate effects solely due the free-electron gas and are not clouded by e.g. interband transitions (as in noble metals).

3.1.2 Surface plasmon polariton

The dispersion relation for the SPP mode supported at the metal-dielectric interface has been determined by Boardman et al. [59] in the absence of losses and interband effects, and later generalized to include such contributions in Ref. [104] and Paper F. The nonlocal retarded dispersion relation is given as

$$1 = -\frac{\varepsilon_\mathrm{D}\kappa_\mathrm{d}}{\varepsilon_\mathrm{d}\kappa_\mathrm{D}} - \delta_\mathrm{nl}, \tag{3.3a}$$

with

$$\delta_\mathrm{nl} = \frac{k^2}{\kappa_\mathrm{nl}\kappa_\mathrm{D}} \frac{\varepsilon_\mathrm{D} - \varepsilon_\infty}{\varepsilon_\infty}, \tag{3.3b}$$

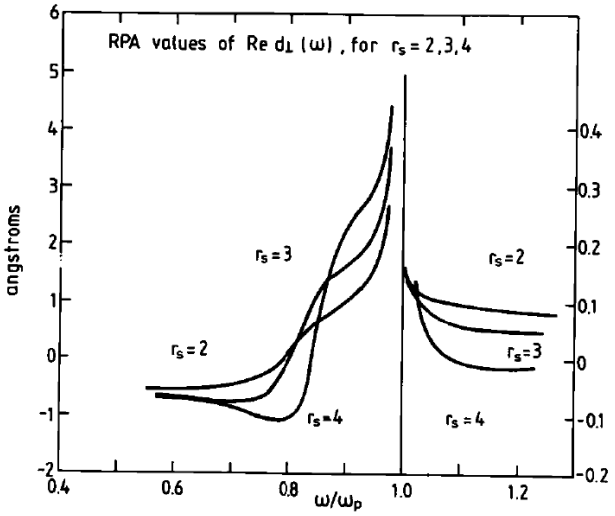

Figure 3.2: The real part of $d(\omega)$ as a function of frequency normalized to the plasma frequency $\omega/\omega_{\rm p}$, calculated using a jellium model within the random-phase approximation. Three different values for the Wigner–Seitz radius $r_{\rm s} = [3/(4\pi n_0)]^{\frac{1}{3}}$ in units of the Bohr radius a_0 are considered. Here, n_0 denotes the static equilibrium density of conduction electrons. Reproduced from Ref. [124].

where k is the SPP propagation constant, $\varepsilon_{\rm D}$ is the Drude permittivity of the metal [as given by Eq. (2.11)], $\varepsilon_{\rm d}$ is the permittivity of the insulator, and $\kappa_{\rm d}^2 = k^2 - (\omega/c)^2\varepsilon_{\rm d}$, $\kappa_{\rm D}^2 = k^2 - (\omega/c)^2\varepsilon_{\rm D}$, and $\kappa_{\rm nl}^2 = k^2 - k_{\rm nl}^2$ are propagation constants normal to the interface. The important nonlocal correction $\delta_{\rm nl}$ vanishes in the LRA. In the non-retarded limit $c \to \infty$, Eq. (3.3) simplifies to

$$1 = -\frac{\varepsilon_{\rm D}}{\varepsilon_{\rm d}} - \delta_{\rm nl}^{\rm nr}, \tag{3.4a}$$

with

$$\delta_{\rm nl}^{\rm nr} = \lim_{c\to\infty} \delta_{\rm nl} = \frac{k}{\kappa_{\rm nl}} \frac{\varepsilon_{\rm D} - \varepsilon_\infty}{\varepsilon_\infty}. \tag{3.4b}$$

As a first consideration, we solve Eq. (3.3) for the case of an ideal lossless metal with no interband effects, i.e., $\gamma = 0$ and $\varepsilon_\infty = 1$, interfaced with vacuum ($\varepsilon_{\rm d} = 1$). In Fig. 3.3 we display the dispersion relation for a lossless metal computed within the LRA (red line), the hydrodynamic model (blue line), and the GNOR model (black line). Considering first the LRA, we see that in the lossless case, the SPP propagation constant has no imaginary part, making the propagation length infinitely long. The real part of the propagation constant is always larger than the light line, which signifies that the SPP is a non-radiative bound mode. Finally, we note that as the $\mathrm{Re}(k)$ grows to infinity, an asymptotic frequency is reached, determined from the relation $\mathrm{Re}(\varepsilon_{\rm D}) = -1$, which for a lossless Drude metal corresponds to $\omega_{\rm sp} = \omega_{\rm p}/\sqrt{2}$, also known as the surface plasmon frequency. At the SP frequency, the group velocity $v_{\rm g} = \mathrm{Re}(\partial\omega/\partial k)$ of the SPP mode vanishes. In the nonlocal hydrodynamic model, the main difference is observed for large $\mathrm{Re}(k)$ where no asymptotic frequency is

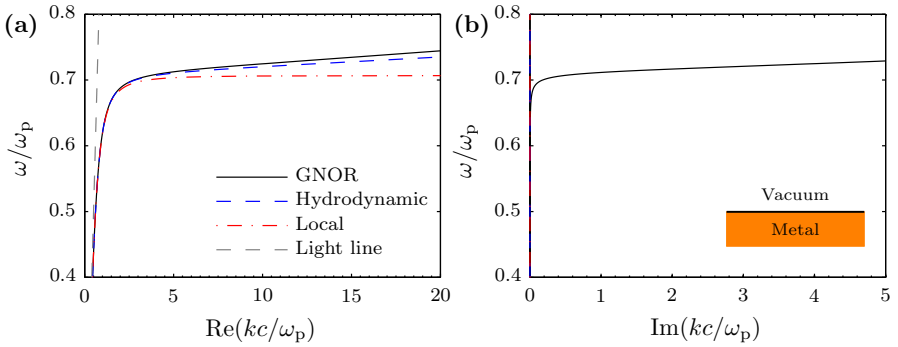

Figure 3.3: Normalized frequency ω/ω_p as a function of the real and imaginary parts of the normalized SPP propagation constant kc/ω_p in **(a)** and **(b)**, respectively, for a lossless metal-vacuum interface in the LRA (red dash-dotted line), hydrodynamic model (blue dashed line) and GNOR model (black solid line). The metal-vacuum interface is sketched as an inset in **(b)**. Material parameters correspond to Na but without losses ($\gamma = 0$).

encountered. In fact, the group velocity is bound by the relation $v_g \geq \beta$ for large $\mathrm{Re}(k)$ as a consequence of the nonlocal curl-free (longitudinal) wave. In the GNOR model, we find, quite interestingly and novel, a finite $\mathrm{Im}(k)$ with a similar frequency dependence as $\mathrm{Re}(k)$, despite the metal being lossless. This means that the diffusive currents present in the GNOR model set a fundamental limit to the SPP propagation length $l_{spp} = 1/[2\mathrm{Im}(k)]$. Quantitatively, we find that the group velocity is bound by the relation $v_g \geq \mathrm{Re}(\eta) = \mathrm{Re}(\sqrt{\beta^2 - iD\omega})$, while the slope for the curve in the $\omega - \mathrm{Im}(k)$ plot is determined from the relation $\mathrm{Im}(\partial\omega/\partial k) \geq \mathrm{Im}(\eta) = \mathrm{Im}(\sqrt{\beta^2 - iD\omega})$. From these relations we can see that the nonlocal parameters β and D contribute to both the real and imaginary parts of the SPP propagation constant. However, β [D] will be the main cause for the value of $\mathrm{Re}(k)$ [$\mathrm{Im}(k)$].

Having discussed the ideal case of a lossless metal interfaced with vacuum, we now turn our attention to realistic metals. In Fig. 3.4 we display the dispersion relations for Na and Ag, which differ markedly in comparison with the lossless case. Interestingly, the LRA and nonlocal models show identical dispersion relations for both Na and Ag. Furthermore, all models display a finite $\mathrm{Im}(k)$, i.e., a finite propagation SPP length, as a consequence of the presence of losses in realistic metals. The SPP propagation length is especially short at the surface plasmon energy $\hbar\omega_{sp}$ due to the decrease in SPP group velocity, which serves to amplify the material losses experienced by the SPP mode. Finally, above $\hbar\omega_{sp}$ the SPP mode bends back and even crosses the light line (grey dashed line), where the SPP mode becomes radiative and unbound to the surface. Thus, we see that material losses play a critical role in understanding the properties of the SPP mode. As we will discuss in detail in the next section, the presence of material losses is in fact the reason why there are no significant signs of nonlocal response in this geometry.

3.1.3 Interplay between losses and nonlocality

In this section, we will in detail examine what happens to nonlocal effects in the metal-vacuum geometry, when we start from an ideal lossless metal and gradually increase the material losses, which is quantified by the normalized Drude damping parameter $\Gamma = \gamma/\omega_p$. The following numerical analysis is based on the hydrodynamic

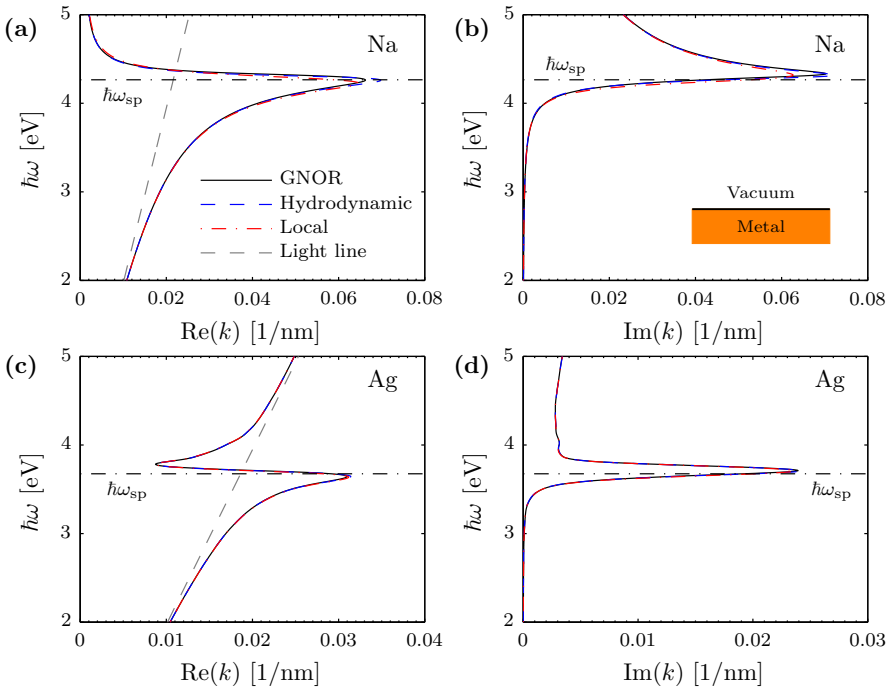

Figure 3.4: Energy $\hbar\omega$ as a function of the real and imaginary parts of the SPP propagation constant k for Na **(a-b)** and Ag **(c-d)** in the LRA (red dash-dotted line), hydrodynamic model (blue dashed line) and GNOR model (black solid line). The horizontal dashed lines correspond to the SP energy, determined from the relation $\mathrm{Re}[\varepsilon_{\mathrm{D}}(\omega_{\mathrm{sp}})] = -1$. The metal-vacuum interface is sketched as an inset in **(b)**. Material parameters for Na and Ag as in Fig. 2.2.

model, but is also valid for the GNOR model. This section outlines part of the work in Paper F.

Due to the absence of length scales associated with the geometry, the MI waveguide is an ideal system to study, when considering the interplay between losses and nonlocality of the SPP mode. In this subsection, we therefore focus on how the presence of absorption losses in the metal, i.e. a finite-valued Γ, affects the nonlocal and local retarded modes of the MI waveguide, as described by Eq. (3.3) with and without δ_{nl}, respectively.

The interplay between losses and nonlocality in the MI waveguide is seen in Fig. 3.5, where we display the effect of increasing the metal losses on the local and nonlocal hydrodynamic dispersion relations of the SPP mode, given by Eq. (3.3) with $\beta/c = 5 \times 10^{-3}$. In the lossless case ($\Gamma = 0$), the local dispersion relation converges towards the well-known surface plasmon energy limit for large k values, while the nonlocal dispersion relation increases in frequency without bound, as discussed in Sec. 2.1 and in agreement with earlier results [59]. However, in the presence of very weak losses ($\Gamma = 10^{-3}$) the infinite k values at the SP frequency ω_{sp} in the LRA are removed and the SPP mode bends back. This back-bending effect is a well-known textbook result [11], which occurs for any positive value for Γ in the LRA. The extreme sensitivity to even minute losses in the LRA is due to the vanishing group

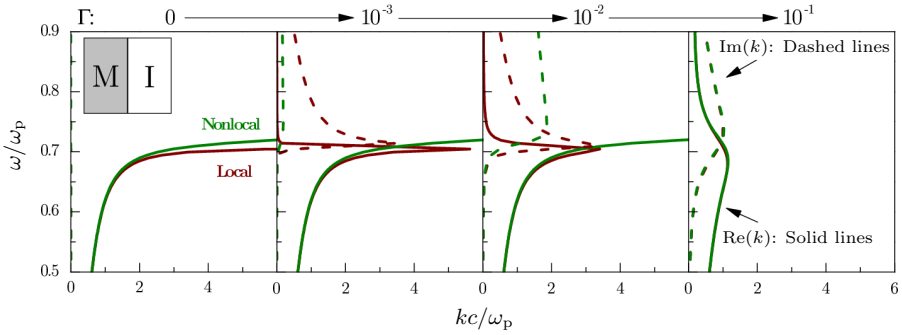

Figure 3.5: Local (red lines) and nonlocal (green lines) complex dispersion relations of the SPP mode of the MI waveguide, with $\varepsilon_{\mathrm{d}} = 1$ and metal losses increasing from $\Gamma = 0$ to $\Gamma = 10^{-1}$. Solid lines display the real part of the propagation constant, $\mathrm{Re}(k)$, while the dashed lines display the imaginary part of the propagation constant, $\mathrm{Im}(k)$. The value $\beta/c = 5 \times 10^{-3}$ suitable for noble metals, such as Ag and Au, has been used.

velocity at ω_{sp} [132]. In striking contrast, the nonlocal SPP mode [i.e., $\mathrm{Re}(k)$] is robust due to the finite group velocity $v_{\mathrm{g}} \geq \beta$. Consequently, no pronounced slow-light enhancement of weak losses takes place and the nonlocal SPP mode does not bend back until the losses of the system start to dominate. Although non-zero $\mathrm{Im}(k)$ is generated for the nonlocal SPP mode for $\Gamma \neq 0$, the real part of the propagation constant $\mathrm{Re}(k)$ remains largely unaffected. It is also interesting to note that the behaviour of $\mathrm{Im}(k)$, which is related to the SPP propagation length l_{spp}, changes drastically from $\Gamma = 10^{-3}$ to $\Gamma = 10^{-2}$. For $\Gamma = 10^{-3}$ the nonlocal SPP mode propagates longer than the local one in the frequency region $\omega > \omega_{\mathrm{sp}}$, while the opposite result is seen for $\Gamma = 10^{-2}$. At the same time $\mathrm{Re}(k)$ for the nonlocal mode is unchanged and substantially larger than in the LRA, resulting in shorter wavelengths and thereby stronger confinement of the SPP mode at the MI surface. Not until $\Gamma = 10^{-1}$, which is significantly larger than the normalized hydrodynamic parameter β/c, do the losses in the metal dominate over nonlocality and force the nonlocal SPP mode to bend back. At such losses, the local and nonlocal models result in almost identical solutions. Intuitively, we may understand this result by recalling that the influence of nonlocal effects is related to the free movement of the electron gas, which can be significantly impaired in the case of large losses, i.e., high collision frequencies.

The transition of the nonlocal mode from being dominated primarily by nonlocality to being dominated by losses (i.e. $\Gamma = 10^{-2} \rightarrow 10^{-1}$ in Fig. 3.5) is investigated in more detail in Fig. 3.6. To explain the transition we must also consider the presence of the high-energy branch known as the Brewster mode [12] (for clarity not shown in Fig. 3.5) and not only the SPP mode. The Brewster mode, which is also a solution emerging from Eq. (3.3), does not correspond to a true surface wave, since, in the lossless case, the wave is unbound and radiative. In fact the Brewster mode corresponds to a zero-valued reflection coefficient, which for a lossless Drude metal can be satisfied only in the transparency window $\omega > \omega_{\mathrm{p}}$. In Fig. 3.6 we see the merging of two separated modes, plotted as red and blue lines. For the lowest loss of $\log(\Gamma) = -1.7$, the red line corresponds to the continuation of the Brewster mode to frequencies lower than ω_{p} (see inset of Fig. 3.6), which in the lossless case would be a forbidden region (i.e., only purely lossy solutions exist) [12]. The blue line represents the standard, low-loss,

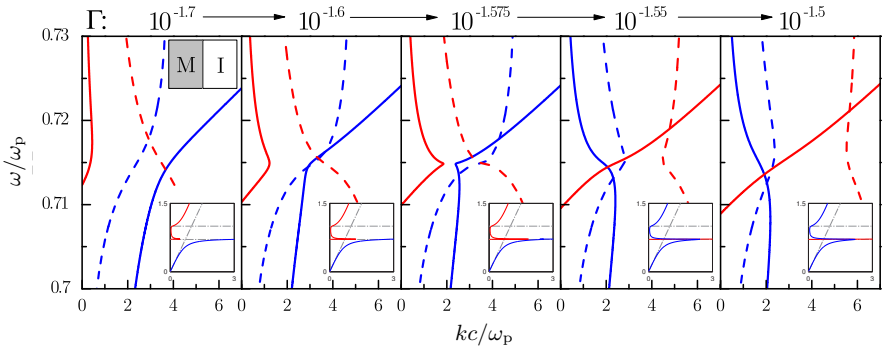

Figure 3.6: Nonlocal complex dispersion relations of the SPP and Brewster modes of the MI waveguide, both attained from solution of Eq. (3.3), with $\varepsilon_{\rm d} = 1$ and metal losses increasing from $\Gamma = 10^{-1.7}$ to $\Gamma = 10^{-1.5}$. Solid lines display the real part of the propagation constant, $\mathrm{Re}(k)$, while the dashed lines display the imaginary part of the propagation constant, $\mathrm{Im}(k)$. The insets show zoom-outs of the real dispersion relation and illustrate more clearly the Brewster mode. The transition and mode-evolution from nonlocality to loss-dominated behavior is explored. The value $\beta/c = 5 \times 10^{-3}$ suitable for noble metals, such as Ag and Au, has been used.

nonlocal SPP mode. As the losses increase [$\log(\Gamma) = -1.6 \to -1.575$], the real parts of the dispersion of the Brewster mode and SPP mode begin to merge [133]. At approximately $\log(\Gamma) = -1.55$ the mode-appearance has qualitatively changed, with the appearance of the usual well-known loss-dominated SPP mode (in blue), which is also present in LRA, as well as the emergence of a relatively flat-band, nonlocal surface plasmon mode (in red) near the surface plasmon resonance $\omega_{\rm sp}$ [33]. We notice that the nonlocal flat-band mode is significantly damped in comparison with the usual SPP mode, and that the damping increases drastically with increased material loss. In contrast, the usual SPP mode is not nearly so sensitive to the small change in material loss from $\log(\Gamma) = -1.55$ to $\log(\Gamma) = -1.5$.

We now present a simple analysis to understand when the metal losses dominate nonlocal effects in the MI waveguide. The back-bending occurs at the SP frequency $\omega_{\rm sp}$, where the propagation constant is significantly larger than the free-space propagation constant. We can therefore justify to examine the simpler non-retarded dispersion relation given by Eq. (3.4) instead of the retarded dispersion relation [Eq. (3.3)]. From Eq. (3.4), we see that nonlocality becomes negligible when $|\delta_{\rm nl}^{\rm nr}| \ll |1 + \varepsilon_{\rm D}/\varepsilon_{\rm d}|$. Evaluating this condition at the SPP frequency with $\varepsilon_{\rm d} = 1$ (as in Fig. 3.5) for small Γ leads to the simple condition for loss-dominated behavior

$$\frac{\gamma}{\omega_{\rm p}} \gg \frac{|\eta|}{c}, \tag{3.5}$$

where η is given by Eq. (2.42). In the hydrodynamic model, where $\eta = \beta$, we find Eq. (3.5) to be consistent with the numerical analysis of this section. We point out that the loss parameter Γ is just one of several options for introducing an imaginary part to the metal permittivity. An alternative approach to introducing losses is by simply adding a constant imaginary part to the lossless free-electron Drude model. In either case, the metal permittivity becomes complex-valued. To bridge these different approaches, we can relate the condition in Eq. (3.5) to the imaginary part of the

metal permittivity by noting that $\mathrm{Im}\left[\varepsilon_{\mathrm{D}}\left(\omega=\omega_{\mathrm{sp}}\right)\right]=2\sqrt{2}\gamma\omega_{\mathrm{p}}/\left(\omega_{\mathrm{p}}^{2}+2\gamma^{2}\right)$ in which case Eq. (3.5) can be rewritten as

$$\mathrm{Im}(\varepsilon_{\mathrm{D}})\gg\frac{|\eta|}{c}. \tag{3.6}$$

In noble metals the nonlocal parameter is of the order $|\eta|/c\approx10^{-3}$ and the losses are of the order $\mathrm{Im}(\varepsilon_{\mathrm{m}})\approx10^{0}$, which in general means that metal losses largely dominate nonlocal effects in the SPP mode of the MI waveguide [53]. In other words, in the MI waveguide the spatial dispersion of the metal becomes invisible to the SPP mode in the limit of infinitely high absorption losses.

Due to the absence of any geometric length scales in the MI waveguide, it is difficult to unmask nonlocal effects from material losses. However, introducing a length scale to enhance the nonlocal influence on the SPP mode can be achieved by considering the SPP modes of the insulator-metal-insulator (IMI) waveguide or the gap-SPP modes of a metal-insulator-metal (MIM) waveguide, where the relevant length scales are the thicknesses of the metal and insulator layers, respectively. For sufficiently thin layers (<10 nm), nonlocal effects manifest themselves in the dispersion relation diagrams, see Refs. [105, 107, 134, 135] and Paper F.

3.2 Sphere

The metallic spherical particle represents another archetypical geometry studied in plasmonics due to the support of localized surface plasmons and the presence of analytical solutions. The electromagnetic scattering problem of a metal sphere of radius R and Drude permittivity $\varepsilon_{\mathrm{D}}(\omega)$, which is excited by a plane monochromatic wave and homogeneously embedded in a material with dielectric constant ε_{B}, was first analytically solved by Mie in the LRA [136]. The exact solution provided by Mie is commonly named Mie theory [137, 138] and takes into account retardation effects. Later, Ruppin [80, 81] extended the Mie theory to include nonlocal response in the metallic sphere by taking into account the curl-free wave that Mie neglected by employing the LRA. In the simpler non-retarded limit, the multipolar polarizability of the metal sphere was extended to include nonlocal effects [126, 125, 139, 140, 141] and used to study the optical properties of very small particles $R<10$ nm, where retardation effects can be safely neglected. Finally, a quantum mechanical jellium model for spherical particles has also been presented in a series of papers by Ekardt [129, 142, 143, 144].

In this section, we derive the nonlocal dipolar polarizability, which in the LRA is described by the Clausius–Mossotti factor [11], to study the optical properties of spheres with diameters below 20 nm. In this size range and under the excitation of a plane wave, the effect of retardation is small and the response of the metal sphere is dominated by the dipolar mode, as we will see in the comparison with fully retarded calculations. By considering the poles of the nonlocal dipolar polarizability, we directly show that the nonlocal parameters β and D relate to the SP resonance energy and linewidth, respectively, as anticipated in our discussion on the Feibelman parameter in Sec. 3.1.1.

3.2.1 Nonlocal Clausius–Mossotti factor

The derivation of the nonlocal Clausius–Mossotti factor presented here is based on the work in Paper E. We consider a small isotropic metal sphere of radius R embedded in a homogeneous dielectric environment with permittivity ε_{B}. The polarizability α

of this sphere is a well-known result in the LRA [11, 145] and is given by

$$\alpha_{\text{L}} = 4\pi R^3 \frac{\varepsilon_{\text{D}} - \varepsilon_{\text{B}}}{\varepsilon_{\text{D}} + 2\varepsilon_{\text{B}}}, \tag{3.7}$$

where ε_{D} is the classical Drude permittivity. The factor $(\varepsilon_{\text{D}}-\varepsilon_{\text{B}})/(\varepsilon_{\text{D}}+2\varepsilon_{\text{B}})$ is called the Clausius–Mossotti factor and notice that it is independent of the sphere radius [146]. The polarizability is derived in the quasistatic approximation under the assumption of a static surrounding electric field, thus neglecting spatial variations in the exciting electric field. Our goal is now to derive a generalization to this formula, taking nonlocal response of the sphere into account. We begin by introducing the electric and current scalar potentials ϕ and ψ, respectively, defined as

$$\mathbf{E}(\mathbf{r},\omega) = -\nabla\phi(\mathbf{r},\omega), \qquad \mathbf{J}(\mathbf{r},\omega) = -\nabla\psi(\mathbf{r},\omega). \tag{3.8}$$

By inserting Eq. (3.8) into the nonlocal equations described in Sec. 2.2, it can straightforwardly be shown that the scalar potentials inside the metal sphere are governed by the equations

$$\left(\nabla^2 + k_{\text{nl}}^2\right) n(\mathbf{r},\omega) = 0, \tag{3.9a}$$

$$\nabla^2\phi(\mathbf{r},\omega) = \frac{e}{\varepsilon_0\varepsilon_\infty(\omega)} n(\mathbf{r},\omega), \tag{3.9b}$$

$$\psi(\mathbf{r},\omega) = \frac{1}{\gamma - i\omega}\left[\varepsilon_0\omega_{\text{p}}^2\phi(\mathbf{r},\omega) - e\eta^2 n(\mathbf{r},\omega)\right], \tag{3.9c}$$

where we have introduced the induced electron density $n(\mathbf{r},\omega)$, which relates to the induced charge density as $\rho(\mathbf{r},\omega) = -en(\mathbf{r},\omega)$. In the surrounding dielectric, the current density $\mathbf{J}$ and electron density n vanish, and the electric scalar potential must instead satisfy the usual Laplace equation $\nabla^2\phi(\mathbf{r},\omega) = 0$. Finally, Maxwell's BCs and the ABC for the scalar potentials translate into

$$\phi^{\text{in}} = \phi^{\text{out}}, \qquad \varepsilon_\infty \frac{\partial\phi^{\text{in}}}{\partial r} = \varepsilon_{\text{B}} \frac{\partial\phi^{\text{out}}}{\partial r}, \qquad \frac{\partial\psi^{\text{in}}}{\partial r} = 0, \tag{3.10}$$

where *in* and *out* refers to inside and outside the metal, respectively. The general solutions to the electric scalar potential and free-electron density inside and outside the sphere are

$$n^{\text{in}} = \sum_{l,m} A_l j_l(k_{\text{nl}} r) Y_{lm}(\theta,\phi), \qquad n^{\text{out}} = 0, \tag{3.11a}$$

$$\phi^{\text{in}} = \sum_{l,m} \left[D_l r^l - A_l \frac{e}{\varepsilon_0\varepsilon_\infty k_{\text{nl}}^2} j_l(k_{\text{nl}} r)\right] Y_{lm}(\theta,\phi), \tag{3.11b}$$

$$\phi^{\text{out}} = \sum_{l,m} \left[B_l r^l + C_l r^{-(l+1)}\right] Y_{lm}(\theta,\phi). \tag{3.11c}$$

Here, j_l and Y_{lm} are the spherical Bessel function of the first kind and the spherical harmonics, respectively. The current scalar potential ψ can be determined from Eq. (3.9c). We neglect variations in the exciting electric field and thus assume a constant electric field surrounding the sphere, here directed in the $\hat{\mathbf{z}}$ direction i.e. $\mathbf{E}^{\text{out}} = E_0\hat{\mathbf{z}}$. Thus, this poses the requirement that $\lim_{r\to\infty}\phi^{\text{out}} = -E_0 z = -E_0 r\cos(\theta)$, which excludes all orders of (l,m) in the sums in Eq. (3.11) except $(l,m) = (1,0)$.

Applying the BCs from Eq. (3.10) and following the usual approach to introduce the polarizability [11], we determine the nonlocal polarizability α_{NL} to be

$$\alpha_{\text{NL}} = 4\pi R^3 \frac{\varepsilon_{\text{D}} - \varepsilon_{\text{B}}\left(1+\delta_{\text{nl}}^{\text{sph}}\right)}{\varepsilon_{\text{D}} + 2\varepsilon_{\text{B}}\left(1+\delta_{\text{nl}}^{\text{sph}}\right)}, \tag{3.12a}$$

where

$$\delta_{\text{nl}}^{\text{sph}} = \frac{\varepsilon_{\text{D}} - \varepsilon_{\infty}}{\varepsilon_{\infty}} \frac{j_1(k_{\text{nl}}R)}{k_{\text{nl}}Rj_1'(k_{\text{nl}}R)}, \tag{3.12b}$$

and where the prime denotes differentiation with respect to the argument. These results constitute our nonlocal-response generalization of the Clausius–Mossotti factor of classical optics. We note that nonlocal effects enter the Clausius–Mossotti factor as an elegant and simple rescaling of either the metal permittivity from ε_{D} to $\tilde{\varepsilon}_{\text{D}} = \varepsilon_{\text{D}}\left(1+\delta_{\text{nl}}^{\text{sph}}\right)^{-1}$ [147] or of the background permittivity from ε_{B} to $\tilde{\varepsilon}_{\text{B}} = \varepsilon_{\text{B}}(1+\delta_{\text{nl}}^{\text{sph}})$ [148]. We point out that the rescaled metal permittivity $\tilde{\varepsilon}_{\text{D}}(\omega, R)$ is now both frequency- and size-dependent. Finally, we note that when $\eta \to 0$ then $\delta_{\text{nl}}^{\text{sph}} \to 0$ in Eq. (3.12) and the classical size-independent Clausius–Mossotti factor is retrieved.

The SP resonance energy follows theoretically from the Fröhlich condition, i.e., we must consider the poles of Eq. (3.12)

$$\varepsilon_{\text{D}} + 2\varepsilon_{\text{B}}\left(1+\delta_{\text{nl}}^{\text{sph}}\right) = 0, \tag{3.13}$$

which will be given by a complex-valued resonance frequency $\omega = \omega' + i\omega''$ (Paper C). The real part ω' gives the SP resonance frequency, while the imaginary part ω'' is related to the SP resonance linewidth. In the following analytical analysis based on the GNOR model, we consider for simplicity the case of a particle in vacuum ($\varepsilon_{\text{B}} = 1$) with no interband effects ($\varepsilon_{\infty} = 1$) and find (to second order in 1/R)

$$\omega' \simeq \frac{\omega_{\text{p}}}{3} + \frac{\sqrt{2}\beta}{2R}, \tag{3.14a}$$

$$\omega'' \simeq -\frac{\gamma}{2} - \frac{\sqrt{6}}{12}\frac{D\omega_{\text{p}}}{\beta R}. \tag{3.14b}$$

In Eq. (3.14a), the first term is the common size-independent local-response Drude result for the SP resonance that also follows from the poles of Eq. (3.7), and the second term gives the size-dependent blueshift due to the hydrodynamic pressure. In Eq. 3.14b, we have again the size-independent LRA term, while the second term shows a size-dependent linewidth due to diffusion. We can also clearly see that only a size-dependent blueshift is present in the hydrodynamic model, while the GNOR also accounts for a size-dependent SP linewidth, both results which are in concordance with our discussion of the Feibelman parameter in Sec. 3.1.1. With the inclusion of interband effects, this distinction becomes blurred, since the hydrodynamic model will also show an extremely weak size-dependent linewidth. At this stage, we note that a $1/R$ dependence on the blueshift and the linewidth of the SP resonance energy of small Ag nanoparticles has been experimentally observed in Refs. [16, 149, 150, 151, 18, 14, 17] using optical spectroscopy.

With the nonlocal polarizability we can determine the extinction cross section σ_{ext} [138] of a metal sphere using the relation [11]

$$\sigma_{\text{ext}} = \frac{k_{\text{B}}^4}{6\pi}|\alpha_{\text{NL}}|^2 + k_{\text{B}}\text{Im}(\alpha_{\text{NL}}), \tag{3.15}$$

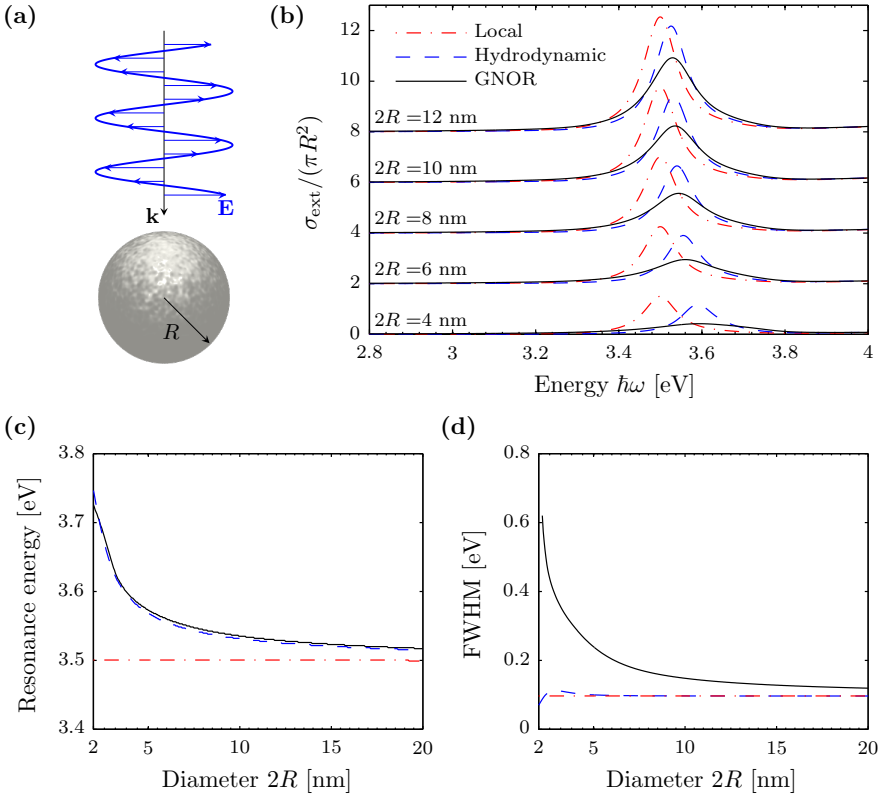

Figure 3.7: **(a)** Sketch of monochromatic plane wave impinging on small Ag nanoparticle. Material parameters for Ag as in Fig. 2.2. **(b)** Extinction cross section, in units of geometric cross section πR^2, as a function of energy $\hbar\omega$ for 5 different particle diameters in the GNOR theory (black solid line), hydrodynamic model (blue dashed line) and LRA (red dash-dotted line). Each spectrum is vertically displaced with 2 normalized units. Resonance energy **(c)** and linewidth **(d)** of the dipolar surface plasmon mode as a function of particle diameter $2R$.

where $k_B = (\omega/c)\sqrt{\varepsilon_B}$ is the wave vector in the background dielectric medium. Equation (3.15) allows for a more quantitative assessment of the size-dependent blueshift and linewidth broadening of the dipolar SP resonance anticipated from the approximate analytical relations in Eq. (3.14). In Fig. 3.7(b) we show the extinction cross section of a small Ag sphere, sketched in Fig. 3.7(a), with diameter varying from 4 nm to 12 nm, calculated in the GNOR theory (black line), hydrodynamic model (blue line) and LRA (red line). As expected, the LRA shows no change in resonance energy or linewidth of the dipolar SP with size. The hydrodynamic model shows a blueshift of the SP with decreasing diameter and a slightly smaller SP amplitude as a consequence of small, but finite, surface absorption due to bulk material losses and interband transitions, see Fig. 3.1(d). The GNOR model shows both blueshift and linewidth broadening of the SP resonance with decreasing particle size. Quantitatively, we see in Figs. 3.7(c) and (d) that a blueshift of ~ 0.2 eV and an increased

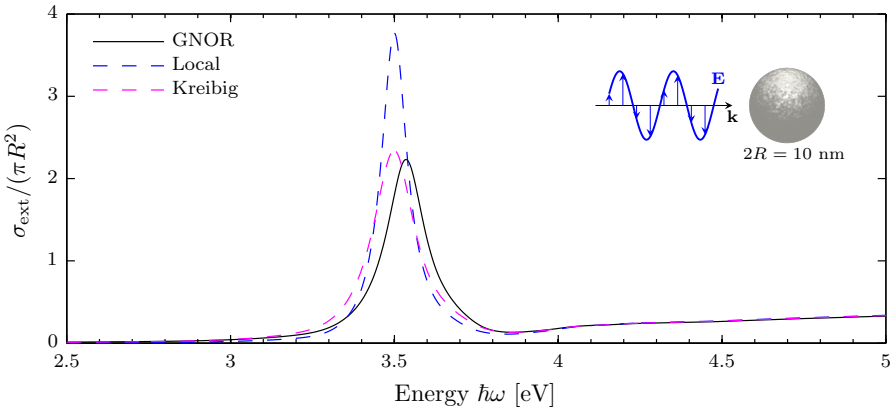

Figure 3.8: Extinction cross section, in units of geometric cross section πR^2, of Ag sphere with diameter $2R = 10$ nm as a function of energy $\hbar\omega$, calculated within the GNOR (black solid line), LRA (blue dashed line), and Kreibig (magenta dashed line) approaches, see Sec. 3.2.2. The value $A = 0.5$ has been used for the Kreibig calculation.

linewidth broadening of ~ 0.5 eV is seen when the sphere diameter decreases from 20 nm to 2 nm. We note that the size-dependent blueshift and linewidth exceeds the $1/R$-dependency, given by the analytical relations in Eq. (3.14), for diameters below 10 nm (Paper I) and higher-order terms become important. The hydrodynamic model shows the same blueshift of the SP as the GNOR model, but no significant increase in linewidth. In particular, a weak size-dependent linewidth in the hydrodynamic model can be seen in Fig. 3.7(d) for diameters below 5 nm, which is due to the inclusion of bulk losses (i.e., $\gamma \neq 0$) and interband effects.

3.2.2 Size-dependent damping

The phenomenon of size-dependent damping in metal nanoparticles has been extensively observed in experiments [16, 14, 15, 152, 153, 154]. The theoretical approach to account for this effect in the LRA, proposed by Kreibig [16] and adopted widely by researchers in the field, has been to phenomenologically modify the Drude bulk damping parameter γ as

$$\gamma \to \gamma + A\frac{v_{\mathrm{F}}}{R}, \tag{3.16}$$

which only applies for spherical particles of radius R. Here, A denotes a constant, which is related to the probability of the free electrons scattering off the surface of the particle. Both experimental data and more advanced theoretical calculations have been compared to this approach, resulting in a robust value for A close to unity for different metals [15, 147, 155, 156]. In the following, we denote the method described in Eq. (3.16) as the Kreibig approach. In Fig. 3.8, we compare the extinction cross section of a silver sphere with diameter $2R = 10$ nm, calculated within the GNOR (black line), LRA (blue line), and Kreibig (magenta line) approaches. As we see from Fig. 3.8 the Kreibig approach displays a size-dependent broadening as in the GNOR theory (in contrast to the LRA), but no size-dependent resonance shift (in agreement with the LRA). The SP linewidths are practically the same in the GNOR and Kreibig calculations due to the chosen value for D, see the caption of Fig. 2.2 for material parameters.

Since the value for A has been shown to be close to unity for different metals, it is therefore appropriate to ensure that the GNOR model agrees with this successful, but phenomenological approach, see Paper A. To this end, we calculate the extinction cross section of a metal sphere using the nonlocal polarizability [Eq. (3.12)] for the GNOR calculations, while the LRA polarizability [Eq. (3.7)] is modified to include the aforementioned additional damping [Eq. (3.16)]. We consider two values for A, namely $A = 0.5$ and $A = 1$, since different nanoparticle preparation methods may result in different surface properties. The diffusion constant D is varied until the full-width at half maximum of the LSPRs for both calculations coincide. This procedure is repeated for the range of sphere radii of $1 - 10$ nm, which are small enough so that retardation does not complicate the analysis (see Sec. 3.2.3). As the fitted diffusion constant D varies slightly with sphere radii, we use the average value for D. The diffusion constant D along with other relevant GNOR parameters for Na, Ag, Au, and Al are summarized in Table 3.1.

The variation in D with sphere radii, when fitted to the Kreibig approach, is due to the Kreibig approach only being valid up to second order in $1/R$. This is clear by inserting Eq. (3.16) into the LRA of Eq. (3.14b), i.e., with $D = 0$. In contrast, the GNOR model is valid up to all orders in $1/R$, as also discussed in Sec. 3.2.1 in the context of Fig. 3.7. Thus, a signature of the GNOR model could be to find the linewidth broadening of the SP resonance to exceed the $1/R$-dependency given by the Kreibig approach. Such measurements could also be used to determine the appropriate value for D.

3.2.3 Retardation effects

In the discussion in Sec. 3.2.1, we have assumed that the optical response of a small metal sphere ($2R < 20$ nm), when excited by a plane wave, is dominated by the dipole mode, and that retardation effects can be neglected. To justify that these assumptions are indeed appropriate, we compare calculations based on the nonlocal nonretarded dipole polarizability [Eq. (3.12)] and retarded nonlocal Mie theory, which takes into account all modes of the sphere (and not only the dipole mode). The nonlocal Mie theory has been presented by several authors and can be found in Refs. [80, 81, 102, 113]. In Fig. 3.9, we show the extinction cross section of a silver sphere with diameter $2R = 20$ nm calculated using the nonlocal Mie theory (black line) and dipolar polarizability (magenta line). The agreement between the two calculations is remarkable and confirms that only the dipole mode is present in the spectrum. Retardation is known to give rise to a redshift of the SP resonance with increasing particle size [157], and here we also note the presence of a very small redshift of the retarded calculation compared to the nonretarded. However, the shift is so small that we can justify to study nonlocal effects of a metal sphere with diameter below 20 nm using the simple nonlocal dipole polarizability.

	$\hbar\omega_{\text{P}}$ [eV]	$\hbar\gamma$ [eV]	v_{F} [10^6ms^{-1}]	D [10^{-4} m^{2}s^{-1}]	
				$A = 0.5$	$A = 1$
Na	6.04 [52]	0.16 [115]	1.07	1.08	2.67
Ag	8.99 [52]	0.025 [37]	1.39	3.61	9.62
Au	9.02 [52]	0.071 [37]	1.39	1.90	8.62
Al	15.8 [52]	0.6 [37]	2.03	1.86	4.59

Table 3.1: Plasma frequencies ω_{P}, Drude damping rates γ, Fermi velocities v_{F} and diffusion constants D for the metals Na, Ag, Au and Al. The method used for determining D is described in Sec. 3.2.2.

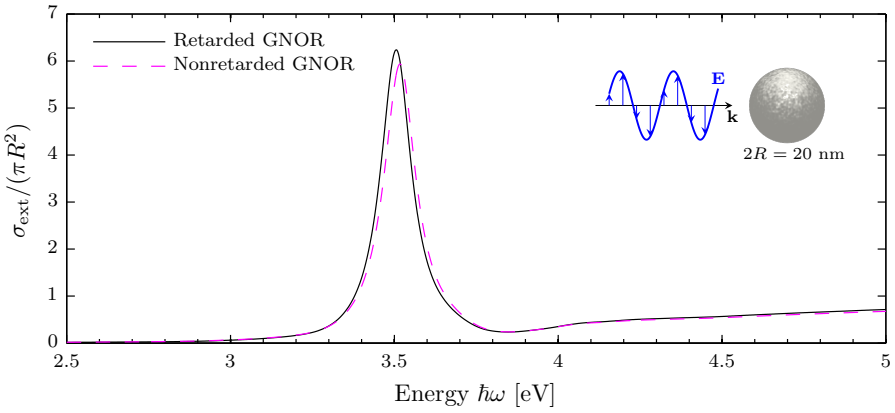

Figure 3.9: Extinction cross section, in units of geometric cross section πR^2, of Ag sphere with diameter $2R = 20$ nm as a function of energy $\hbar\omega$, calculated with retarded Mie theory (black solid line) and dipolar polarizability (magenta dashed line), given by Eq. (3.12). The GNOR approach has been used for both calculations.

3.2.4 Nonlocal multipolar response

We have in the previous sections focused on the dipole mode of a small sphere and shown that this mode dominates the extinction cross section spectrum for diameters below 20 nm. However, other excitation sources, such as an electron beam or a dipole emitter, produce significantly more inhomogeneous electric-field distribution than the plane-wave excitation used in determining the extinction cross section [113, 121]. When in the vicinity of a metal sphere, such sources can excite higher-order multipoles, even in spheres with diameters below 20 nm [113, 158]. Thus, it is relevant to consider the nonlocal resonance condition for all multipoles, given in Ref. [113] as

$$l\varepsilon_{\text{D}} + (l+1)\left(1 + \Delta_{\text{nl}}^{\text{sph}}\right)\varepsilon_{\text{B}} = 0, \qquad \Delta_{\text{nl}}^{\text{sph}} = l\frac{\varepsilon_{\text{D}} - \varepsilon_\infty}{\varepsilon_\infty}\frac{j_l(k_{\text{nl}}R)}{k_{\text{nl}}Rj_l'(k_{\text{nl}}R)}, \tag{3.17}$$

where l is the multipole order with $l = 1$ denoting the dipole mode, $l = 2$ the quadrupole mode, and so on. We see that for $l = 1$ Eq. (3.17) reduces to Eq. (3.13) from the previous section. Ref. [113] has also shown that the solution to Eq. (3.17) within the hydrodynamic model can be approximated as (to second order in $1/R$)

$$\omega \simeq \frac{\omega_{\text{p}}}{\sqrt{\varepsilon_\infty + \varepsilon_{\text{B}}(l+1)/l}} + \sqrt{\frac{l(l+1)\varepsilon_{\text{B}}}{\varepsilon_\infty}}\frac{\beta}{2R}, \tag{3.18}$$

which is also in accordance with findings in Ref. [95]. The first term in Eq. (3.18) is the size-independent LRA multipole resonance condition, while the second term is due to nonlocal response in the hydrodynamic model. Eq. (3.18) reveals, besides a $1/R$ dependence, that there is a delicate interplay in the blueshift between the material parameters of the metal, through $\varepsilon_\infty(\omega)$ and β, and the background medium ε_{B}. Furthermore, Eq. (3.18) shows that the blueshift increases with a large-permittivity background medium and higher multipole order l. Within the GNOR model, we can therefore anticipate, besides an l-dependent blueshift, an l-dependent linewidth broadening as well.

3.3 Dimer

The plasmonic dimer, which consists of two metallic nanoparticles in close proximity, constitutes another very interesting geometry. This is in particular due to the plasmon hybridization [2, 159] occurring between the two closely-spaced nanoparticles, which gives rise to strongly gap-dependent resonance energies and electric-field enhancements. Such features have been utilized in e.g. surface-enhanced Raman spectroscopy [160] and the plasmon ruler effect [161]. The dimer has been studied with a variety of theoretical and experimental techniques. The simplest theoretical approach is based on the classical LRA, which in the extreme case of a nanometer-sized dimer gap gives rise to unphysical results, such as diverging field enhancements in the gap of the dimer [162]. A complete breakdown of the LRA is seen in the touching configuration, where the number of hybridized bonding plasmon modes increases without limit to form a continuum of modes [91, 92], thus setting no bound to the resonance energies of the bonding plasmon modes and thereby the plasmon hybridization. Advanced descriptions based on DFT regularize the unphysical consequences of the LRA [163, 116, 114, 115, 32], where the physical mechanism for the regularization is attributed to quantum tunnelling, i.e., the charge transfer that may occur before reaching the touching configuration due to the spill-out of electrons. Results based on the hydrodynamic model, where only nonlocal response (and not electron spill-out) is taken into account, also display regularization of the LRA [91, 92, 70], albeit with field enhancements in the dimer gap that are still larger than shown by DFT simulations [115]. Measurements on dimers with vanishing gaps using both optical techniques [27, 30] and electron energy-loss spectroscopy [29, 164] are not in agreement with the LRA, and, in the touching case, also display limits on the resonance energies of the bonding plasmon modes, i.e., ultimate bounds to the plasmon hybridization. However, the physical mechanism for the discrepancy between LRA and the observed measurements is not conclusive with possible explanations being provided from both quantum tunneling [114, 115] and nonlocal response [34] perspectives.

In this section, we study a plasmonic dimer consisting of two identical Na cylinders by varying the gap from separated via touching to overlapping configurations, see Fig. 3.10 for a schematic illustration. The dimer is excited by a plane wave which is polarized along the dimer axis to strongly excite the hybridized modes. We numerically calculate the extinction cross section and the field enhancement in the gap of the dimer in the frameworks of the LRA, hydrodynamic model and GNOR model by using the freely available COMSOL implementation [165].

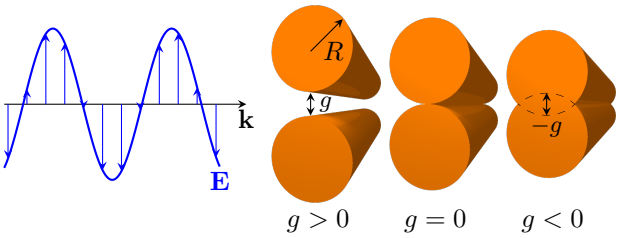

Figure 3.10: Sketch of the considered system, displaying the incident electric field, which is polarized along the dimer axis, impinging on a dimer consisting of two identical cylinders with radii R and separated by a gap g. The three cases of separated dimer ($g > 0$), touching dimer ($g = 0$) and overlapping dimer ($g < 0$) are shown.

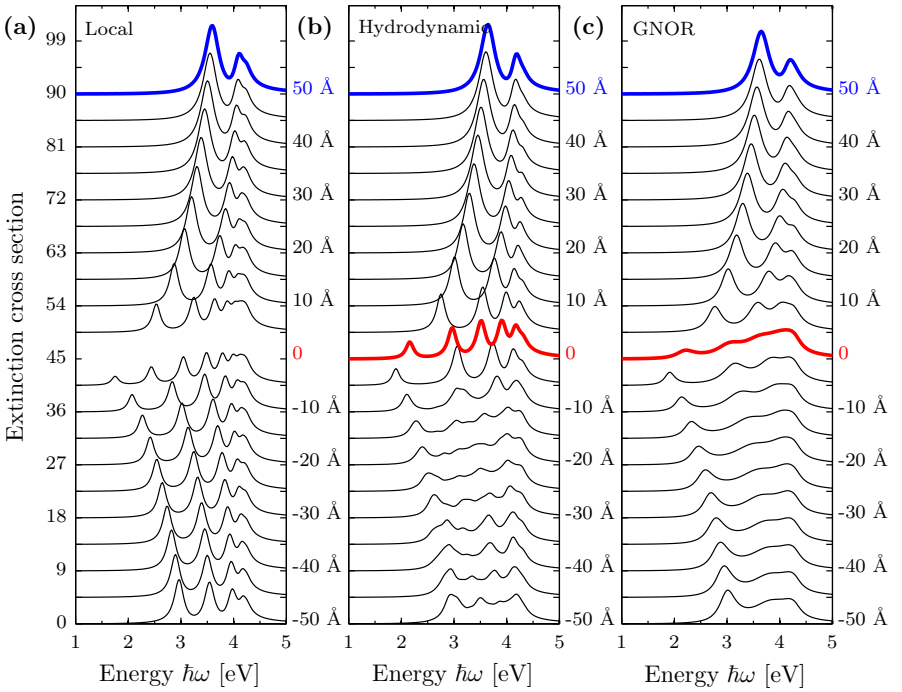

Figure 3.11: Extinction cross section, in units of cylinder diameter $2R$, as a function of energy for a Na dimer with $R = 10$ nm and gap size g varying from 50 Å to -50 Å in steps of 5 Å. Simulations are done using **(a)** LRA, **(b)** hydrodynamic model, and **(c)** GNOR model. The values next to the spectra denote the gap size g. Each spectrum is vertically displaced by 4.5 normalized units.

To properly understand the forthcoming optical spectra, we first discuss the plasmon hybridization occurring in the dimer system. When two cylinders are positioned in close proximity, they hybridize to form new plasmon modes, which can show up as resonances in the extinction cross section [159]. For large separation distances, the first modes to hybridize are the individual dipolar modes (angular momentum $l = 1$) of the cylinders to produce a lower-energy (with respect to the individual dipolar mode) bonding dipolar mode and a higher-energy antibonding dipolar mode. Since the net dipole moment of the antibonding mode is zero, this mode will be optically dark and not show up in the extinction cross section. Thus, we leave out further discussion of the antibonding modes. As the dimer separation decreases the plasmon hybridization increases and the resonance energy of the bonding dipolar mode decreases. Furthermore, with decreasing separation distance higher-order modes of the individual cylinders (i.e., $l > 1$) begin to hybridize as well. As an example the quadrupole mode of the individual cylinders hybridize to form bonding and antibonding quadrupole modes. Thus, in nanometer-proximity the dimer spectra can be quite complex and show multiple resonances due to the hybridization between many modes of the individual cylinder.

With this plasmon hybridization picture in mind, we consider now the extinction cross section of a Na dimer with radius $R = 10$ nm in the LRA, hydrodynamic model

and GNOR theory, see Figs. 3.11(a), (b), and (c), respectively. We vary the dimer gap from $g = 50$ Å (separated dimer) via touching configuration $g = 0$ to $g = -50$ Å (overlapping dimer). We begin our discussion by considering the LRA results for a dimer separated by a gap of 50 Å [blue curve in Fig. 3.11(a)]. The lowest-energy and strongest peak is due to the bonding dipole mode (BDP), while the next peak is actually due to two spectrally-close modes, the bonding quadrupole mode (BQP) and a higher-order mode (HOM). Of these two modes, the BQP has the largest amplitude and lowest energy. The electric field of the HOM is concentrated at the edges of the dimer (and not the gap, like the BDP and BQP), making it spectrally insensitive to the gap size (see Paper A for plots of the electric field distribution of the BDP, BQP, and HOM). As the gap decreases, the BDP and BQP redshift and additional bonding-mode resonances appear due to the increased plasmon hybridization. In fact as $g \to 0$ the bonding modes continue to redshift and the number of bonding modes increases without bound till a continuum of modes is found in the touching configuration $g = 0$ [91, 92]. The extinction cross section calculation for $g = 0$ does not converge in the LRA, which is why the spectrum is not present in Fig. 3.11(a). When the dimers overlap the nature of resonant modes changes and can no longer be considered as bonding modes. In particular, the induced charges pile up at the sharp edges of the junction of the overlapping dimer [162]. The interaction between the induced charges gives rise to the several resonances seen for e.g. $g = -5$ Å. As the overlap increases, the sharp edges at the junction smoothen and the interaction between the surface charges decreases, leading to a blueshift of the resonances. The spectrum of the overlapping dimer begins to increasingly resemble that of an elongated particle.

Turning our attention now to the results of the hydrodynamic model, see Fig. 3.10(b), we find that the separated dimers show less redshift with decreasing gap size compared to the results in the LRA. The size-dependent blueshift of the plasmon resonances observed in a spherical nanoparticle (see Sec. 3.2) translates into a *gap*-dependent blueshift for the bonding modes of the dimer. This gap-dependent blueshift counteracts the redshift due to plasmon hybridization, leading finally to a finite resonance energy and finite number of bonding modes in the touching limit $g = 0$ [red curve in Fig. 3.11(b)]. Furthermore, the increase in blueshift with angular momentum observed for the sphere (see Sec. 3.2.4) manifests itself in the dimer spectra as an increased blueshift for higher-order bonding modes. Thus, the BQP experiences a stronger blueshift than the BDP, leading to a weaker plasmon hybridization for the BQP than the BDP. This is also the reason for the lower number of resonances in the hydrodynamic spectra of close-proximity and short-overlap dimers compared to those of the LRA. For the overlapping dimers ($g < 0$) the strength of the resonant modes are weaker in the hydrodynamic calculations than in the LRA due to the nonlocal smearing of the surface charges at the otherwise sharp edges of the dimer junction.

Many of the considerations from the hydrodynamic results can be mapped over to the GNOR spectra, see Fig. 3.11(c). In particular, the gap-dependent blueshift observed in the hydrodynamic model is augmented with a gap-dependent broadening the GNOR model. This is clear for, e.g., the touching case $g = 0$ (red curve) where diffusion broadens the spectrum significantly in comparison to the sharp resonances of the hydrodynamic spectrum. Since the broadening is also angular-momentum dependent, many of the higher-order mode features in the spectra of the overlapping dimers become washed out due to diffusion.

3.3.1 Comparison with density-functional theory

To facilitate comparison with time-dependent DFT (TDDFT) calculations [114, 115] and other theoretical models based on quantum tunnelling, such as the quantum-

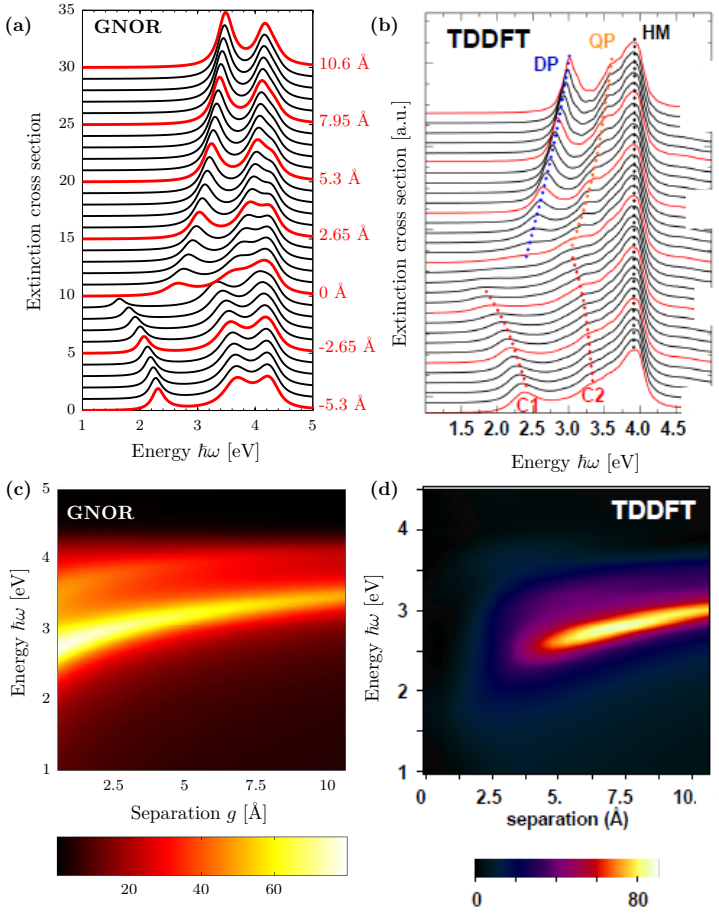

Figure 3.12: **(a-b)** Extinction cross section as a function of energy for a Na dimer with $R = 4.9$ nm and gap size g varying from -5.3 Å to 10.6 Å in steps of 0.53 Å using GNOR and time-dependent DFT, respectively. The values next to red-colored spectra denote the gap size g. **(c-d)** Electric-field enhancement at the center position of the gap of the same Na dimer as a function of energy and gap size using GNOR and time-dependent DFT, respectively. **(b)** and **(d)** are reproduced from Ref. [115].

corrected model (QCM) [166] and the quantum conductivity theory (QCT) [167], we display in Fig. 3.12 the evolution of the extinction cross section [Fig. 3.12(a-b)] and the electric-field enhancement [Fig. 3.12(c-d)] of a Na dimer with a smaller radius of $R = 4.9$ nm. Comparison of TDDFT with the LRA and the hydrodynamic model has already been shown in Refs. [114, 115], so we leave out these models in this section. Comparing first the extinction cross sections, we see that the GNOR theory captures quite accurately the gap-dependent broadening seen from TDDFT simulations, although the broadening is stronger in the TDDFT calculations. This slight discrepancy can be adjusted by increasing the value for the diffusion constant D in the GNOR simulations. The number of resonant modes in the separated and

overlapping dimer are also the same in both calculations. In the very narrow gap range of -2 Å $\lesssim g \lesssim 2$ Å, the TDDFT spectra are significantly more broadened than those of the GNOR model, which can be attributed to the overlap of the electron spill-out in TDDFT calculations. However, from the strong similarity of the spectra in the two calculations, it can be difficult to assign the broadening observed in measurements of dimers [29, 27] as a direct consequence of overlap of electron spill-out, as the GNOR theory does not include electron spill-out but still accounts for the gap-dependent broadening.

In Fig. 3.12(c) we see that the electric-field enhancement amplitude and trend with decreasing gap size are in very good agreement with TDDFT simulations [Fig. 3.12(d)]. The only discrepancy between the GNOR model and TDDFT simulations occurs at gap sizes below approximately 5 Å but before contact, where the overlap of electron spill-out in TDDFT calculations quenches the electric-field enhancement. The lack of agreement with TDDFT calculations for gaps below 5 Å is due to the hard-wall boundary conditions imposed in the GNOR model.

3.3.2 Ultimate plasmon hybridization

When the dimers are touching [red curve in Fig. 3.11(c)], the hybridization of the bonding plasmon modes is maximal and the resonance positions of these modes depend only on the dimer radius R. We have investigated the behavior of the resonance condition of the BDP and BQP modes as a function of R in Fig. 3.13. For the smallest dimer radii ($R \leq 10$ nm), the resonance positions of the BQP mode are not clearly distinguishable from the extinction spectra due to the weaker hybridization in smaller dimers. As the dimer radius increases the resonance energies of both the BDP and BQP modes decrease. This is due to the increased hybridization occurring for larger radii as the interacting metal surfaces between the two nanowires increase. Along with the numerical GNOR simulations (dots in Fig. 3.13), we also depict the results using a nonlocal transformation optics (TO) approach (dashed line) [91]. Although the nonlocal TO was originally used with the hydrodynamic model, we show in Fig. 3.13 that the nonlocal TO approach is still valid within the GNOR theory, as long as the substitution $\beta^2 \to \eta^2$ [recall Eq. (2.42)] is applied. As anticipated, we see in Fig. 3.13 that the nonlocal TO calculations agree quite well with the GNOR simulations for both the BDP and BQP modes. The small discrepancy between the nonlocal TO calculations and the GNOR simulations for large radii is due to lack of retardation effects in the TO calculation (notice the retardation-induced redshift of the GNOR simulations compared to the TO). The discrepancy for the smallest radii is due to the WKB approximation in the nonlocal TO calculations, which becomes inaccurate for increasing particle curvature (i.e., decreasing radii) and higher-order modes (note the larger discrepancy for the BQP mode than for the BDP mode for small radii).

We may deduce a simple relation for the resonance energies of the bonding plasmon modes by examining the position of the centroid of induced charges [115], given as the real part of the Feibelman parameter $d(\omega)$, see Sec. 3.1.1. In the GNOR theory, the centroid of the induced charges is positioned a short distance ($\sim 1-2$ Å) within the metal boundary as discussed in Sec. 3.1.1, see also insets of Fig. 3.13. However, within the LRA the induced charges reside on the geometrical surface. We can therefore mimic the position of the centroid of induced charges in the GNOR theory by considering separated dimers in the LRA with a gap of $g = 2\mathrm{Re}[d(\omega)]$. Within the LRA, the resonance condition of a separated dimer with gap size g has been determined using TO [168] and is given by the relation

$$\left(\sqrt{\frac{g}{4R}} + \sqrt{1+\frac{g}{4R}}\right)^{4n} = \mathrm{Re}\left[\frac{\varepsilon_{\mathrm{D}}(\omega)-1}{\varepsilon_{\mathrm{D}}(\omega)+1}\right], \tag{3.19}$$

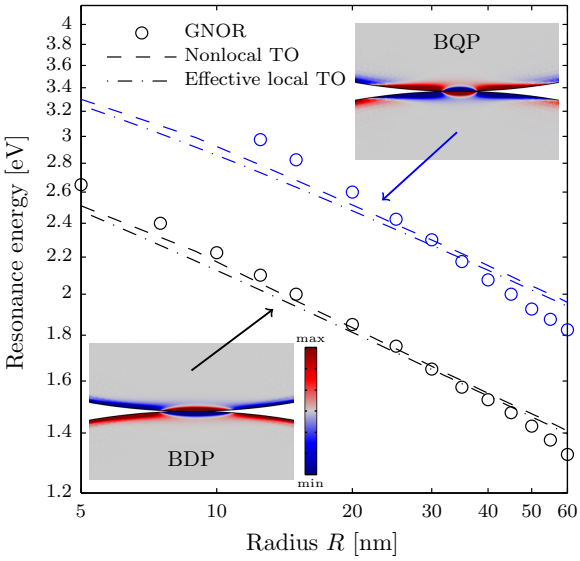

Figure 3.13: Resonance energies of the BDP (black) and BQP (blue) modes of touching Na nanowires ($g = 0$) as a function of dimer radius R. The dots display the simulations using the GNOR model, and the dashed lines show the results using the nonlocal TO approach. Finally, the dash-dotted lines show the results using the local-response TO approach, given by Eq. (3.19) with an effective gap $g = 2\mathrm{Re}[d(\omega)]$. The insets display the real part of the GNOR charge distributions of the BDP and BQP for a touching dimer with $R = 30$ nm.

where $n = 1$ corresponds to the BDP mode, $n = 2$ corresponds to the BQP mode, and so on. Assuming an undamped Drude model for the permittivity $\varepsilon_{\mathrm{D}}(\omega) = 1 - \omega_{\mathrm{p}}^2/\omega^2$ and expanding Eq. (3.19) to first-order in g/R, we find the simple relation for the LRA resonance condition for the modes of separated nanowires

$$\frac{\omega}{\omega_{\mathrm{p}}} \simeq \sqrt{n}\left[\frac{2\mathrm{Re}(\xi_{\mathrm{GNOR}})}{\sqrt{-\varepsilon_{\mathrm{D}}(\omega)}R}\right]^{\frac{1}{4}}, \tag{3.20}$$

where we have used that $g = 2\mathrm{Re}(\xi_{\mathrm{GNOR}})/\sqrt{-\varepsilon_{\mathrm{D}}(\omega)}$. Figure 3.13 displays the result of this effective LRA approach (dash-dotted lines), given by Eq. (3.19) with gap size $g = 2\mathrm{Re}[d(\omega)]$. We see that the GNOR resonance energies of touching nanowires can quite accurately be mimicked by the LRA result of separated nanowires, when the gap size is set to the distance between the centroid of induced charges. As anticipated from Eq. (3.20), we also see that the slope of the BDP and BQP resonance energies are very similar. The BQP energies simply occur at higher energies. Although diffusion plays a crucial role in the damping of the bonding plasmon modes for decreasing gap size (as seen in the extinction cross sections of Fig. 3.11) and in the electric-field enhancement amplitude [see Fig. 3.12(c)], Eq. (3.20) shows that the maximal hybridization resonance energies are mainly dependent on convection as described by the Fermi velocity, since the value for β contributes most to $\mathrm{Re}(\xi_{\mathrm{GNOR}})$ [recall Eq. (2.44)]. Only in the extreme limit where $D\omega$ becomes comparable to β^2 in magnitude will diffusion play a role in the position of the resonance energies.

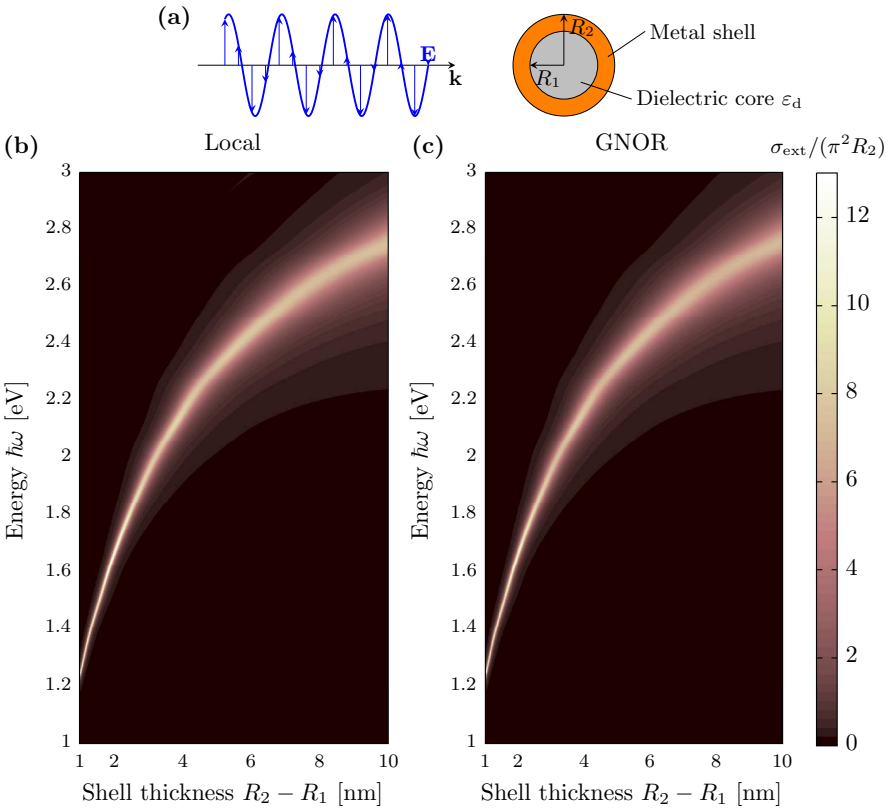

Figure 3.14: **(a)** Sketch of a plane wave with electric field polarized perpendicular to cylinder axis impinging on a coreshell nanowire with inner radius $R_1 = 15$ nm and varying outer radius R_2. The core is insulating with permittivity $\varepsilon_d = 1.5^2$ corresponding to silica, while the thin shell is Ag. **(b-c)** Extinction cross section, normalized to the area of the core-shell wire πR_2^2, as a function of energy $\hbar\omega$ and shell thickness $R_2 - R_1$ in the LRA and GNOR model, respectively. Both plots have the same color scale.

3.4 Core-shell nanowire

By modifying the structure of the metal nanoparticle to have a dielectric core with a metal shell, an increased tunability of the LSPRs is achieved due to the plasmon hybridization of the inner and outer surfaces of the metal [2]. Especially the spherical core-shell structure has received a considerable amount of attention in recent years [169, 170, 171, 172] due to its excellent and tunable sensing properties, which show great promise in biological studies such as cancer therapy [173]. The plasmon hybridization allows one to position the LSP resonance of the nanoshell as desired by simply varying the core size R_1 and/or outer radius R_2 appropriately [174].

The hybridization of the inner and outer surface plasmons increases when the metal shell becomes thinner [174], which gives rise to significantly altered LSP resonances compared to usual homogeneous metal nanoparticles, such as the sphere in Sec. 3.2. Studies of the hybridization between two spherical or cylindrical metal nanoparticles

in few-nm proximity reveal that effects of nonlocal response increase with increasing hybridization, see Sec. 3.3 and Refs. [70, 102, 121]. We would therefore anticipate a strong nonlocal response in the core-shell particle, since it features an ultra-thin metallic shell with resulting strong plasmon hybridization.

To study nonlocal effects in the core-shell geometry, we consider an infinite cylindrical nanowire with a dielectric core and a thin metal shell excited by a plane wave, see Fig. 3.14(a) for an illustration. By extending the nonlocal Mie theory for wires of Ref. [175] to core-shell structures, we can analytically determine the extinction cross section taking into account nonlocal response in the thin metal shell and retardation effects. The details of analytical expressions are presented in the appendix of Paper H.

We focus on a particular design, consisting of an insulating core with permittivity $\varepsilon_{\mathrm{d}} = 1.5^2$ corresponding to silica, inner radius of $R_1 = 15$ nm, and a thin Ag shell (see caption of Fig. 2.2 or Table 3.1 for material parameters). We are interested in studying the optical response of the core-shell nanowire when varying the shell thickness $R_2 - R_1$ by changing the outer radius R_2. Figure 3.14(b-c) shows the extinction cross section as a function of energy and shell thickness in the LRA and GNOR model, respectively. We leave out the hydrodynamic model in this study, since, as we will see, we do not gain more insight from this model. Considering first the LRA result, we see that the extinction cross section is dominated by a single resonance, which redshifts for decreasing shell thickness as a consequence of increased plasmon hybridization (in accordance to our study on dimers in Sec. 3.3). Thus, a great tunability of the surface plasmon resonance with shell thickness is present, allowing for tailoring of the optical response. When we consider the result from the GNOR theory [Fig. 3.14(c)], we find quite surprisingly the same optical response as in the LRA. In particular, we see no size-dependent resonance shift or linewidth broadening as encountered for the sphere (Sec. 3.2), even in the extreme case of a 1 nm thin shell. The lack of dependency on nonlocal response in this geometry was also found in Paper H in the study of refractive-index sensing and using the hydrodynamic model to describe the metal shell.

To find an answer to this surprising non-presence of nonlocal response, we consider in more detail the plasmon hybridization occurring in the core-shell geometry. In particular, we are interested in how the induced charges of the resonance seen in Fig. 3.14 are distributed. In Fig. 3.15(a) we illustrate how the core-shell modes can be understood as the hybridization between the cylinder modes and the cylindrical void modes. Figure 3.15(b) shows specifically the hybridization of the dipole modes of the cylinder and cylindrical void which leads to a lower-energy bonding mode and a higher-energy antibonding mode. The bonding plasmon is optically bright and is the mode we observe in Fig. 3.14 in both the LRA and GNOR calculations. From Fig. 3.15 we can see that the negative and positive induced charges are isolated to each side of the core-shell wire, thus separated by a distance of approximately the inner cylinder diameter, i.e., $2R_1 = 30$ nm for the design considered in Fig. 3.15. The smearing of induced charges over Ångstrom length scales will therefore not play a significant role on the optical response of the bonding plasmon mode, since the positive and negative induced charges are separated by much greater distances than the smearing length scale. In contrast, the strong effect of nonlocal response in spheres and dimers occur due to the induced positive and negative charges coming in close proximity when the particle diameter and dimer gap, respectively, are decreased. However, the antibonding mode, which has a net dipole moment of zero and is therefore (unfortunately) optically dark, has induced positive and negative charges on each side of the thin metal shell, which indicates that nonlocal effects could play a prominent role for this mode if the metal shell is sufficiently thin. As the electric field generated by a moving electron can excite plasmonic dark modes (see Chap. 4), a possible method to study nonlocal effects of the antibonding mode would be to use

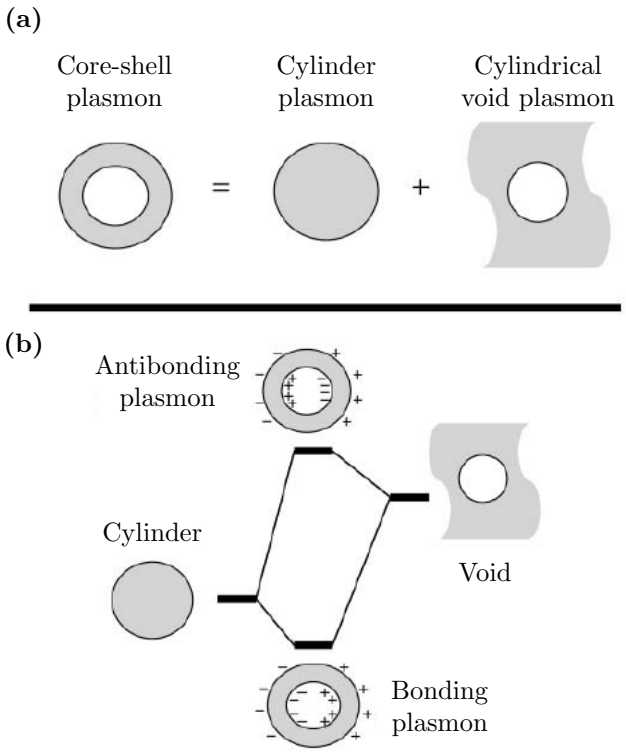

Figure 3.15: **(a)** The core-shell plasmon can be understood as the hybridization between the cylinder plasmon and the cylindrical void plasmon. **(b)** The dipole modes of the cylinder and cylindrical void hybridize to produce the lower-energy bonding mode (optically bright) and higher-order antibonding mode (optically dark). Modified from Ref. [176].

electron energy-loss spectroscopy.

3.5 Metal film

So far in the previous Secs. 3.1-3.4, we have only been concerned with the impact of nonlocal response on the optical spectrum for energies below the plasma energy $\hbar\omega_{\mathrm{p}}$. These studies have been motivated by the interest for surface plasmons, whose resonance energies mainly occur below the plasma frequency of the considered metal. However, nonlocal response also has a quite significant signature above the plasma frequency, where the curl-free (longitudinal) wave oscillates instead of being damped. This means that plane-wave excitation can actually couple to the curl-free wave at metal interfaces, producing a set of resonances above the plasma frequency for sufficiently small metal structures. These resonances are standing-wave patterns in the bulk of the metal structure and are a direct consequence of inclusion of the curl-free wave in nonlocal response.

Such optically-excited curl-free (longitudinal) waves have been seen experimentally in thin metal films (i.e., with thickness t below $\sim$ 10 nm). Lindau and Nils-

son [24, 177] were the first to show experimental evidence of a few dips above the plasma frequency in the transmittance spectra of thin silver films. They interpreted these dips as a consequence of the resonant excitation of confined bulk waves due to nonlocal response. Almost simultaneously, Anderegg et al. [25] provided photoelectric yield spectra (roughly proportional to absorption spectra) of thin potassium (K) films, showing a multitude of clear resonances above the plasma frequency. The experimental results by Anderegg et al. showed very good agreement with theoretical considerations based on the hydrodynamic model [25, 23]. Further experimental evidence of optically-excited curl-free waves in silver thin films was provided in Refs. [178, 179], however, no dips above the plasma frequency were observed. Instead, measurements revealed an increase in energy of the bulk plasmon resonance for decreasing film thickness, which could only be theoretically accounted for by inclusion of nonlocal response. More recently, measurements on thin magnesium (Mg) films also revealed excitations of confined curl-free waves [180] in agreement with hydrodynamic theory.

To theoretically examine the optically-excited curl-free waves, we calculate the absorbance spectrum of a metal film with thickness t in vacuum, which is excited by an incident plane wave at an angle. The plane wave is polarized parallel to the plane of incidence, see Fig. 3.16 for an illustration. The absorbance can be determined from the reflectance R and transmittance T as $A = 1 - R - T$. We favor the absorbance (over the transmittance or reflectance) since the excitations due to confined curl-free waves are more prominent in absorbance spectra [64, 25, 181]. A detailed derivation for the nonlocal reflectance and transmittance are provided by several authors and can be found in e.g. [64, 23, 107, 135, 181, 182]. Briefly, the incident, reflected and transmitted waves are written up as transverse waves (as shown in Fig. 3.16) described by a local dielectric function. Inside the thin metal film forward and backward propagating transverse waves are present along with forward and backward propagating longitudinal waves (not shown in Fig. 3.16). This gives a total of six amplitudes (the incident wave is known), which are determined using the Maxwell boundary conditions and the nonlocal ABC at the two interfaces of the metal film.

Figure 3.17 displays the absorbance as a function of energy for three different film thicknesses, i.e., 2, 3, and 4 nm, and two different metals, Na and Ag. Furthermore, each spectrum is calculated within the GNOR model, hydrodynamic model, and the LRA. Each spectrum also has labeled the position of either the free-electron plasma

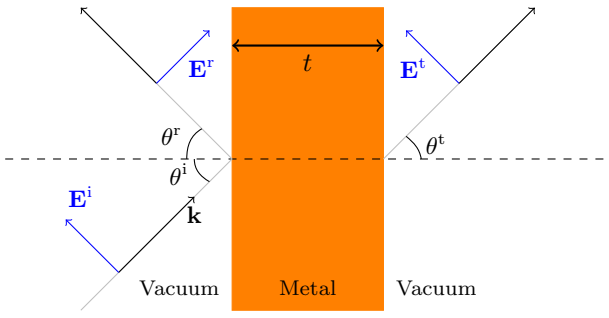

Figure 3.16: Sketch of the considered system, displaying the incident electric field, which is polarized parallel to the plane of incidence, impinging at an angle θ^{i} on a metal film of thickness t in vacuum. In the symmetric case discussed in Sec. 3.5, the angles θ^{r} of the reflected field and θ^{t} of the transmitted field are equal to the angle of the incident field.

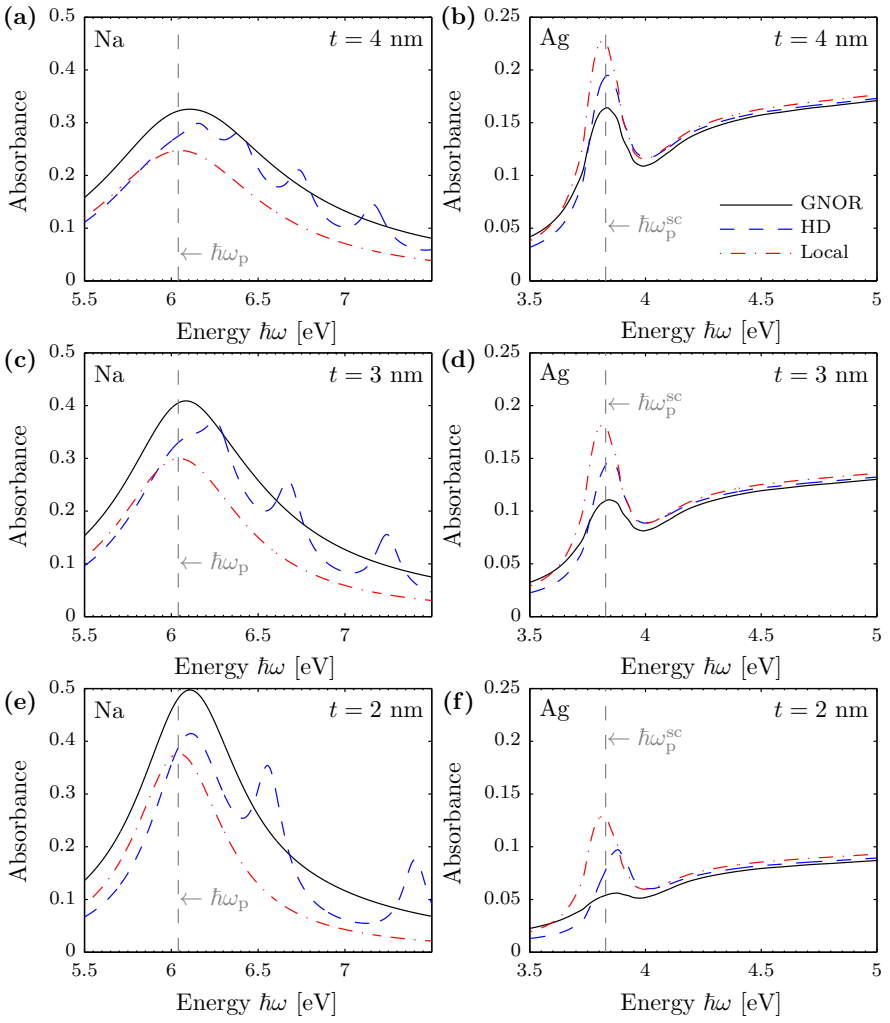

Figure 3.17: Absorbance spectra of as a function of energy $\hbar\omega$ in the GNOR model (black solid lines), hydrodynamic model (blue dashed lines) and LRA (red dash-dotted lines) for Na [left column, i.e. **(a)**, **(c)** and **(e)**] and Ag films [right column, i.e. **(b)**, **(d)** and **(f)**] in vacuum. The film thicknesses are **(a-b)** 4 nm, **(c-d)** 3 nm, and **(e-f)** 2 nm. The angle of the incident field is $\theta^{\rm i} = 70°$.

energy (relevant for Na) or the screened plasma energy (relevant for Ag). Considering first the LRA calculations on the Na film [red lines in Figs. 3.17(a), (c), and (e)], we see that the main feature is a peak at the plasma frequency $\omega_{\rm p}$. With decreasing film thickness the maximum absorbance increases, but the peak resonance energy does not change. For the hydrodynamic model and Na films [blue lines in Figs. 3.17(a), (c), and (e)], the spectra are significantly different above the plasma frequency from the LRA. A series of resonances are present in spectra due to confined curl-free waves

producing standing waves inside the thin film. We note that the spectral spacing and amplitude of the resonances increase with decreasing film thickness. In particular, it can be shown that the resonance condition for the confined curl-free waves is quite accurately described by the relation

$$\omega(\omega + i\gamma) = \frac{\omega_{\mathrm{p}}^2}{\varepsilon_\infty(\omega)} + \frac{n^2\pi^2}{t^2}\eta^2, \tag{3.21}$$

where n denotes the number of antinodes in the standing-wave pattern of the confined curl-free wave. With $\eta = \beta$ in the hydrodynamic model, Eq. (3.21) shows clearly an increasing spectral distance with decreasing thickness t. Considering finally the GNOR calculations of the Na film [black lines in Figs. 3.17(a), (c), and (e)], we find quite surprisingly no features due to the resonant excitations of the curl-free wave. The reason for this is that diffusion introduces an additional loss channel, which, depending on the value for D, may wash out the features due to the confined curl-free modes. Mathematically, we see that the imaginary part of the resonance condition in Eq. (3.21) becomes comparable to the real part when $\eta^2 = \beta^2 + D(\gamma - i\omega)$ as in the GNOR theory.

We now discuss the Ag films presented in Figs. 3.17(b), (d), and (f). Firstly, the LRA (red lines) shows again a peak as in the case of Na, but now at the screened plasma frequency $\omega_{\mathrm{p}}^{\mathrm{sc}}$ instead of the free-electron plasma frequency as a consequence of the interband effects in Ag. Furthermore, we see that the maximum absorbance decreases with film thickness, which is opposite to the trend in Na. Considering now the hydrodynamic model (blue lines), we find that the overall picture does not change significantly from the LRA. The difference is that the absorbance is decreased, and a subtle but important blueshift of the bulk plasma peak for decreasing film thickness is observed. The lack of resonances above the plasma frequency is due to the increased material losses in silver, i.e., larger $\mathrm{Im}(\varepsilon_\infty)$ in Eq. (3.21). The GNOR model (black lines) shows the same behavior as the hydrodynamic calculations, but with a decreased amplitude due to increased losses from diffusion.

To sum up, we find that for the simple metal Na strong resonant features above the plasma frequency occur in the hydrodynamic model but not in the GNOR model. Experimental measurements on other simple metals with equivalent optical response as Na (K in Ref. [25] and Mg in Ref. [180]) show resonant excitations due to confined curl-free waves, in agreement with the hydrodynamic calculations presented in Fig. 3.17 and in disagreement with the GNOR model. Thus, it seems that the additional dissipation channel in the GNOR model stemming from diffusion, which accurately captures size-dependent (Sec. 3.2) and gap-dependent (Sec. 3.3) surface plasmon damping, should not be present above the plasma frequency. This apparent issue can be circumvented by introducing a frequency-dependent diffusion constant, i.e., $D(\omega)$, with a very small contribution for frequencies above the plasma frequency. For the nonlocal calculations on Ag, we find no resonant excitations above the plasma frequency due to the significantly higher material losses in Ag than in Na. However, the nonlocal models do show a blueshift of the bulk plasma peak for decreasing film thickness, in agreement with the measurements of Refs. [178, 179]. The lack of resonances above the plasma frequency for Ag in both of the nonlocal calculations and in the measurements of Refs. [178, 179] adds confusion to the nature of the dips observed in the transmittance spectra of Lindau and Nilsson [24, 177], in particular whether these dips are really caused by nonlocal response, or rather an artefact of their experimental setup. Further perplexity is added, when the Ag film thicknesses of Lindau and Nilsson [24] and Abelès et al. [178] are compared. Lindau and Nilsson considered film thicknesses of $100-120$ Å, while Abelès et al. studied film thicknesses down to 6 Å. As shown in Fig. 3.17, the excitations due to confined curl-free wave

increase in amplitude with decreasing film thickness, which makes one wonder why Abelès et al. did not observe them, while Lindau and Nilsson did.

3.6 Concluding remarks

We have in the previous sections considered the implications of nonlocal response in many different geometries. It would be beneficial now to take a step back and see if a simple explanation can be deduced for when nonlocal response is important. As a first conclusion, we point out that the difference between nonlocal response (that is, with hard-wall ABC and homogeneous equilibrium electron density) and the LRA is how we model the *induced* charges, i.e., the charges occurring due to an exciting electric field. All of the effects (both nonlocal and in the LRA) we have seen for frequencies below the plasma frequency are a consequence of the induced charges at the surface. In a simplistic view, the *surface* plasmon is a surface-bound wave which must inherently have a strong dependence on the induced *surface* charges. In particular, the smearing of the charges beyond the geometrical surface of the considered geometry in nonlocal response introduces a dependence on the distance between negative and positive induced charges. For example, in the single sphere this dependence translates into a size-dependence (or radius dependence), while in the dimer we find a dependence on the gap size. This is further corroborated in the core-shell structure where, despite an ultrathin metal shell, nonlocal response did not show a significant impact on the optical response due to the large core separating the negative and positive induced charges.

The main shortcoming of the nonlocal models is the inaccurate treatment of the free electrons at the metal surface in the *absence* of an exciting electric field, i.e., the ground-state equilibrium electron density. In particular, the free electron density is modeled as being constant inside the metal and then abruptly dropping to zero outside the metal. From the pioneering work on density-functional theory by Lang and Kohn [183], we know that the equilibrium electron density should be smoothly-varying at the metal-vacuum interface, with Friedel oscillations inside the metal and electron spill-out outside the metal. The strength of current DFT treatments of metals is the inclusion of a self-consistent treatment of the equilibrium electron density. However, new results which have been published during the very end of this PhD suggest that it is possible to properly take into account a smoothly varying equilibrium electron density in a hydrodynamic treatment [184, 185], thus overcoming this limitation.

Chapter 4

Electron energy-loss spectroscopy

This chapter describes the experimental technique of electron energy-loss spectroscopy, which is performed in a transmission electron microscope (TEM). We begin in Sec. 4.1 by considering how EELS is performed in a TEM from an experimental point of view and, in this regard, we introduce relevant experimental parameters. Afterwards in Sec. 4.2, we study EELS in the theoretical framework of classical electromagnetism to provide a method for calculating and understanding the EEL signal. Finally, Secs. 4.3 and 4.4 are devoted to two separate EELS experiments and their theoretical interpretations. Section 4.3 concerns the study of localized plasmon resonances of chemically prepared silver nanoparticles dispersed on a TEM substrate, while Sec. 4.4 is devoted to the investigation of gap surface-plasmon waveguide modes in gold nanogrooves, fabricated using focused ion beam (FIB) milling.

The EELS experiments are performed using a FEI Titan scanning TEM (STEM), which is equipped with an extra bright field emission gun, an electron monochromator, and a spherical aberration corrector. The microscope is operated at acceleration voltages of 120 kV and 300 kV in the experiments of Secs. 4.3 and 4.4, respectively. The energy resolution, measured as the full-width at half-maximum of the zero-loss peak, achieved in the experiments is 0.15 ± 0.05 eV.

4.1 Experimental description

Electron energy-loss spectroscopy is the measurement of the energies lost by swift electrons due to inelastic scattering events in a thin specimen. EELS is performed in a transmission electron microscope, which means that the initial kinetic energies of the electrons is typically $80 - 300$ keV and the electrons can therefore penetrate samples with thicknesses up to approximately 1000 nm [186]. However, samples used for studying plasmonic excitations with EELS are usually significantly thinner, i.e., below approximately 150 nm depending on the material and microscope operating conditions, (see also e.g. Refs. [40, 41, 47, 187, 188] and Papers B and I for typical structure sizes) to avoid specific loss features such as plural plasmon scattering, but also to study small metallic volumes. In Fig. 4.1 we illustrate the possible excitation and scattering events due to an incident electron beam. The EEL spectrum is mainly composed of transmitted electrons that have not undergone any loss events in penetration of the sample, i.e., the elastically scattered electrons, and the inelastically scattered electrons that have lost energy due to a variety of excitations in the specimen. The relaxation of the excitations back to the unexcited state can be accommodated with the emission of electrons or photons. As an example, the relaxation of plasmonic events in metallic samples can occur with the emission of photons

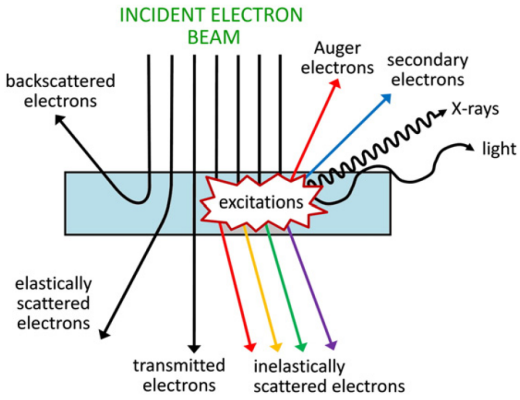

Figure 4.1: Schematic illustration displaying the possible excitation events due to impinging swift electrons. Reproduced from Ref. [191].

with energies in the visible range, which can be detected using cathodoluminescence spectroscopy [189]. The inelastic and elastic scattering events are due to the electrostatic interaction between the incident swift electron and the atomic electrons and nucleus, respectively. Since the nuclear mass is much larger than the electron rest mass, the elastically scattered electrons lose too little energy for detection in EELS. On the other hand, significant energy losses (from few eV to hundreds of eV) occur due to inelastic scattering, which comprises vast events such as plasmon excitations, exciton excitations, and single-electron excitations due to e.g. interband transitions and excitations of core electrons. In the EELS experiments discussed in Secs. 4.3 and 4.4, we consider only energy losses in the so-called low-loss region (i.e., below 50 eV), so we limit our current discussion to loss events occurring in this energy range, ruling out the high-energy losses due to core-loss events which can been used to map the chemical information of a specimen [190]. In particular, we focus on inelastic scattering due to plasmonic excitations.

A typical raw EEL spectrum acquired during the study of Ag nanoparticles, which will be detailed in Sec. 4.3, is shown in Fig. 4.2. The EEL spectrum is acquired in STEM mode (more info on this technique in Sec. 4.1.1) by positioning the focused electron beam to penetrate through the center of the nanoparticle, as shown in the insets of Fig. 4.2. In Fig. 4.2, the black line displays the EEL spectrum to scale, while the red line is the same spectrum but multiplied by a a factor of 500 to visualize the more subtle features. This also illustrates the magnitude of the main peak in the EEL spectra, the so-called zero-loss peak (ZLP). The ZLP is primarily a measure of all the incident electrons that have been elastically scattered and therefore sets the zero energy position in the spectrum. Additionally, the ZLP also contains contributions from inelastic scattering events with energy losses below the resolution of EELS, such as phonon losses. In the low-loss energy region and for thin samples, the ZLP is by far the strongest feature in the spectrum. Therefore, a number of different approaches have been devised to remove the ZLP by post-processing the EEL spectrum such that weak features in the spectrum can be accentuated, see Sec. 4.1.2. We also add that the energy resolution of EELS is usually given by the full-width at half-maximum (FWHM) of the ZLP peak, which with the aid of monochromators can be reduced to 0.1 eV or below [192]. In the energy range $3 - 4$ eV we see two peaks in the considered EEL spectrum that are due to inelastic scattering processes by plasmonic

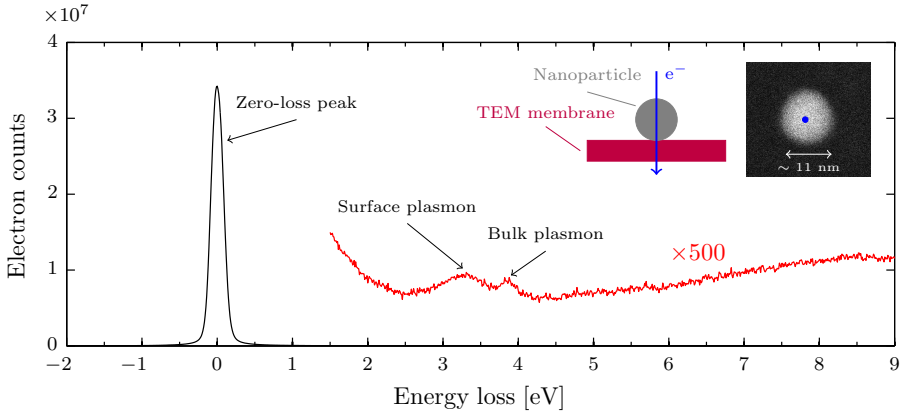

Figure 4.2: A typical raw low-loss EEL spectrum with different features labeled, acquired in the study of single Ag nanoparticles dispersed on a thin 10 nm silicon nitride TEM membrane. The spectrum is acquired by positioning a focused electron beam in the center of a silver nanoparticle with a diameter of approximately ~ 11 nm. The insets show a schematic side-view illustration and a STEM top-view image of the nanoparticle.

excitation. In particular, the lower-energy feature at approximately 3.2 eV is due to the excitation of the dipolar LSPR, which in the LRA is given by the resonance condition $\varepsilon_{\mathrm{D}}(\omega) = -2\varepsilon_{\mathrm{B}}$ as discussed in Sec. 3.2.1, while the higher-energy feature at approximately 3.8 eV, which corresponds to the screened plasma frequency of Ag, is due to the excitation of the bulk plasmon, given by the LRA condition $\mathrm{Re}[\varepsilon_{\mathrm{D}}(\omega)] = 0$ (see Sec. 3.1.1). The rest of the EEL spectrum is relatively featureless with a steady increase in EEL signal for increasing energy loss, which could be a sign of a broad valence plasmon peak from the silicon nitride TEM membrane with a bulk plasmon energy around 23 eV. Additionally, a weak feature around 8 eV from silver can be discerned.

4.1.1 Instrumentation

We distinguish between two approaches for performing EELS [191]. We denote the first as spectroscopy mode, where an incident highly-focused electron beam with a subnanometer-sized probe interacts with the sample. The EEL spectrum then contains information of the energy lost by the incident electrons from an area of the specimen on the size of the electron probe (Fig. 4.2 shows an example of such a spectrum). The second method is denoted energy filtering mode, where a parallel electron beam (as used in TEM mode) visualizes a larger area of the specimen and the image is then filtered according to the energy loss of the incident electrons. This method is abbreviated EFTEM (energy-filtered transmission electron microscopy) and is often used to study and image plasmonic excitations [45, 47, 193, 194, 195, 196, 197]. However, EFTEM has not been used in the experiments of Secs. 4.3 and 4.4, so we concentrate our discussion on the spectroscopy mode. This method is often abbreviated STEM-EELS, as it is EELS performed in STEM mode, where a focused electron probe is used instead of a parallel beam. Both methods, i.e., EFTEM and STEM-EELS, can provide the same information on the plasmonic response [198].

A schematic illustration of the working principle of STEM-EELS is shown in Fig. 4.3(a). The electron source, which may be a field emission gun (FEG) or a

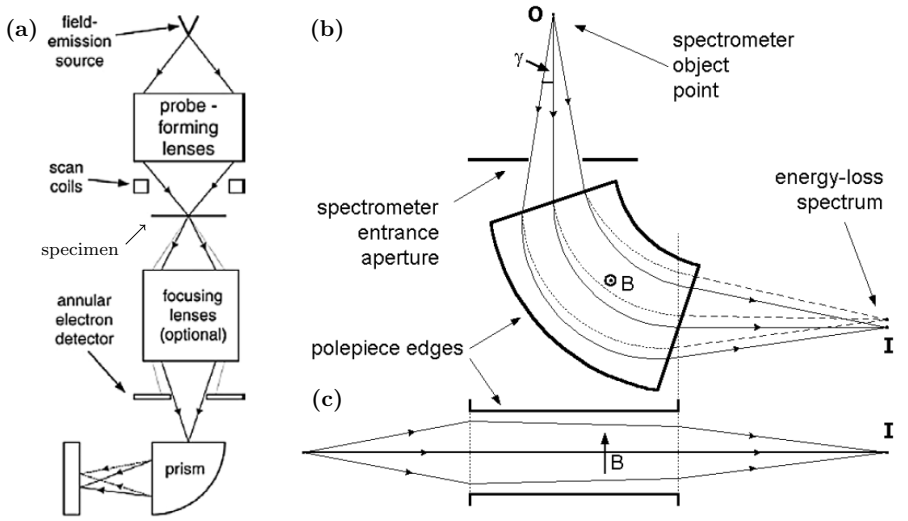

Figure 4.3: Schematic illustration of EELS instrumentation. **(a)** Procedure for EELS scanning TEM mode, i.e., STEM-EELS. **(b-c)** Magnetic prism in a plane perpendicular and parallel to the magnetic field, respectively. In **(b)** the solid lines (dashed lines) represent different trajectories of electrons with no energy loss (the same kinetic energy). Reproduced from Ref. [186].

thermionic source, emits electrons, which are accelerated to a desired energy, typically $80 - 300$ keV, and afterwards focused to a subnanometer-sized spot on the specimen by strong electromagnetic lenses. If the electromagnetic lenses are corrected for spherical abberations, the size of the probe can be below 1 Å [186]. The semi-angle of the cone of the electron probe is denoted the convergence semi-angle and is typically in the tens of mrad range. The scan coils raster-scan the focused electron probe across an area of the sample, which in concerto with the annular electron detector generate the image. The annular electron detector collects electrons that have been scattered through large angles by the specimen to generate a dark-field image of the sample, while those electrons that have been scattered with a smaller angle are directed through a magnetic prism to the EEL detector. The largest angle of the scattered electrons, which enter the magnetic prism, is called the collection semi-angle and is also typically tens of mrad (like the convergence semi-angle), depending on the position in the vertical direction of the entrance aperture, the acceleration voltage and the setup of the microscope. In the magnetic prism, a static magnetic field perpendicular to the direction of the electrons is present, see Figs. 4.3(b-c). Due to the Lorentz force, the electrons are dispersed according to their velocity (or kinetic energy). For example, compare the solid lines and dashed lines in Fig. 4.3(b) which show the trajectories of electrons that have not and have lost energy, respectively. Furthermore, the electromagnetic lenses in the magnetic prism are designed to also focus the electrons which astray from the straight path but have the same kinetic energy, see the solid lines in Fig. 4.3(b) which illustrate the different trajectories of electrons with the same kinetic energy that after the magnetic prism are focused to the same spot on the EEL detector.

Although there are contributions from the physical parameters of the TEM, such as the emission current (known as the Boersch effect [38]), acceleration voltage, and

the aberration of the lenses in the EEL spectrometer, the main source for the energy resolution of EELS in a well-aligned STEM is the electron source. The energy spread from a thermal tungsten filament is around 1 eV, while a cold FEG source has a lower spread of around $0.4 - 0.5$ eV. To improve the energy resolution of EELS beyond the energy spread of the electron source, an electron monochromator is usually utilized to filter the energy spread of the electron source. With an excited electron monochromator and a FEG electron source, an energy resolution of $0.1-0.2$ eV can be routinely achieved [199], as is also the case for the EELS experiments in Secs. 4.3 and 4.4. The electron monochromator installed in the FEI Titan microscope is a double focusing Wien filter [38], which is based on a Wien filter, named after its inventor Wilhelm Wien. In its original design, the Wien filter is comprised of a static magnetic flux density and static electric field with strengths B and E, respectively, where both fields are orthogonal to the direction of the electron beam and also mutually orthogonal. The deflecting forces of the electric field and magnetic flux density cancel for electrons with velocity $v_0 = E/B$ (i.e., vanishing Lorentz force), thus selecting only electrons with a specific kinetic energy. In particular, electrons with the velocity v_0 moving along the central axis of the filter will follow a straight-line path, while electrons entering the filter at an off-axis position will experience the deflecting forces of the static fields along the length of the filter, see Fig. 4.4 for a schematic illustration. Setting the correct length of the filter, or equivalently, the strength of the static fields, will allow to focus the off-axis electrons with velocity v_0 to the central axis. The focusing of the Wien filter only works in the dispersive plane (i.e., xz-plane in Fig. 4.4), thus creating a line focus. To also achieve focusing in the non-dispersive plane, such that a point focus is achieved, an additional (quadrupole) electric field is applied. This is known as the double focusing Wien filter.

4.1.2 Zero-loss peak removal

As mentioned in the discussion of Fig. 4.2 in Sec. 4.1, the ZLP is the strongest peak in the low-loss region when studying thin plasmonic systems. Thus, it can be beneficial to remove the ZLP during post-processing of the EEL spectra to best recover the plasmonic features. In this section, we therefore consider and compare different techniques to remove the ZLP. Due to the instrumental resolution, the recorded EEL spectrum $J(E)$, where E is the energy loss, is the convolution of the ideal spectrum

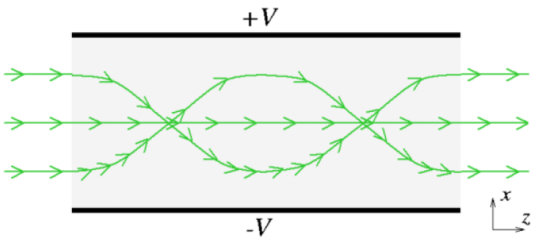

Figure 4.4: Schematic illustration of a Wien filter, where electrons with velocity $v_0 = E/B$ enter the filter both on and off the central axis. The deflection of the off-axis electrons is dominated in turns by the deflecting electric and magnetic fields, resulting in a cycloidal motion in the dispersive plane (xz-plane). Reproduced from the FEI monochromator manual.

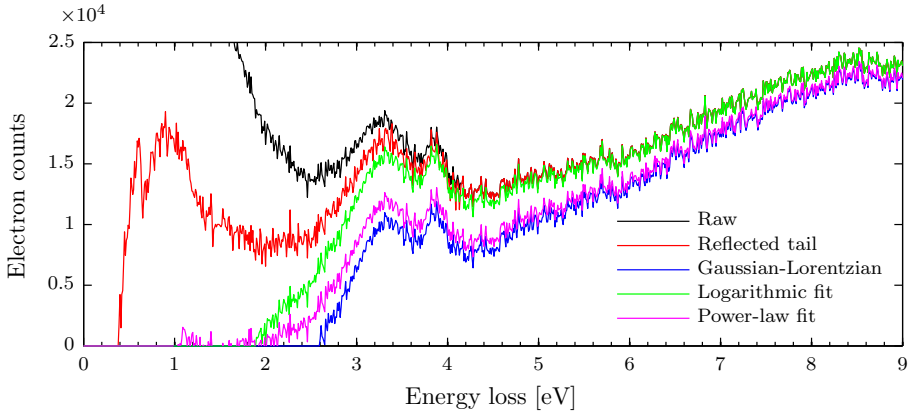

Figure 4.5: The raw EEL spectrum of Fig. 4.2 (black line) and the corresponding ZLP-removed spectra. The reflected-tail (red line), Gaussian-Lorentzian (blue line), logarithmic (green line), and power-law (magenta line) methods have been used to reconstruct the whole or part of the ZLP. The methods are described in Sec. 4.1.2.

$P(E)$ with the energy-spread function (ESF) of the microscope $R(E)$ [38]

$$J(E) = \int_{-\infty}^{\infty} \mathrm{d}E' R(E - E') P(E'). \tag{4.1}$$

Thus, to retrieve the ideal spectrum $P(E)$ a deconvolution scheme can be used. The ESF can be considered the instrumental broadening, and a EEL spectrum, recorded in the absence of the sample under investigation, can be used as input for $R(E)$. As an example, in the experiments on Ag nanoparticles (Sec. 4.3), an EEL spectrum recorded at a position far away from any particles (i.e., only signal from the substrate) could serve as an input for $R(E)$. To perform the deconvolution, the Fourier-ratio or Richardson–Lucy approaches can be used. The deconvolution methods can sharpen low-loss peaks by a factor $2 - 3$ and are therefore useful for very weak features [38]. However, the introduction of artifacts due to the deconvolution is not uncommon [192, 200], requiring care to be taken when using these methods.

On the other hand, if the considered peaks in the EEL spectrum are sufficiently visible (as in Fig. 4.2), it can often be adequate to fit a function to the ZLP of the spectrum and afterwards remove it. This is the procedure used for the post-processing of the EEL spectra in Secs. 4.3 and 4.4. In Fig. 4.5, we show four different functions fitted to the ZLP of the raw EEL spectra (black line) and subsequently removed from the spectra. For the reflected-tail method (red line), the negative energy part of the ZLP (i.e., energy losses below 0 eV) are mirrored around the 0 eV energy point to reconstruct the ZLP. In the Gaussian-Lorentzian method (blue line), a least-squares fitting of the sum of a Gaussian and Lorentzian function is used to model the ZLP. For the logarithmic (green line) and power-law (magenta line) fits, a logarithmic or power-law function, respectively, is used to fit the positive-energy tail of the ZLP (here, in the energy range $1 - 2$ eV), which is extrapolated to higher energies and subsequently subtracted from the raw EEL spectrum. The energy range used to fit the functions is optional and must be chosen such that the ZLP tail is most accurately modeled.

We can see that the raw EEL spectrum shows features due to resonant excitations at 3 to 4 eV, which are accentuated by all of the ZLP removal techniques. In

particular, we highlight that the resonance energy is not altered by any of the ZLP removal techniques, which is the main parameter extracted from the EEL spectra in the experiments of Secs. 4.3 and 4.4. The ZLP removal is useful in the subsequent processing of the resonance peaks, where it can be desirable to fit Gaussian or Lorentzian functions to have accurate estimates for the resonance energy (and in some cases linewidth). Specifically, we have used a nonlinear least-squares fit of a Gaussian function to determine the resonance energies of the plasmon modes in our experiments. The error in the resonance energy is then extracted as the 95% confidence interval for the estimate of the position of the center of the Gaussian function.

The low-energy peaks seen around 1 eV using the reflected-tail method (red line in Fig. 4.5) are not meaningful, as they are not present in the raw EEL spectrum, and therefore a consequence of the ZLP removal technique. However, for energy losses above 2 eV the reflected-tail method is in general accurate and reliable, as is also the case in Fig. 4.5. Additionally due to the little user-input needed, we have preferred to use the reflected-tail method to remove the ZLP from the EEL spectra in the experiments in Secs. 4.3 and 4.4.

4.2 Theoretical modeling

In the framework of classical electromagnetism, we describe the electron beam as a delta-function charge following a straight-line trajectory $\mathbf{r}_\mathrm{e}(t)$ given by the parametric function $\mathbf{r}_\mathrm{e}(t) = \mathbf{r}_0 + \mathbf{v}t$ [1, 37]. Here, $\mathbf{r}_0 = (x_0, y_0, z_0)$ denotes the impact parameter, i.e., the position of impact of the electron beam, $\mathbf{v}$ denotes the electron velocity, and t is time. Without loss of generality, we can set the electron trajectory to be along the z-axis, such that $\mathbf{v} = v\hat{\mathbf{z}}$. Hence, we can write the external charge density $\rho_\mathrm{ext}(\mathbf{r}, t)$ as

$$\rho_\mathrm{ext}(\mathbf{r}, t) = -e\delta\left[\mathbf{r} - \mathbf{r}_\mathrm{e}(t)\right] = -e\delta(x - x_0)\delta(y - y_0)\delta(z - z_0 - vt) \tag{4.2}$$

which after a temporal Fourier transform enters Maxwell's equations [Eq. (2.1)] as

$$\rho_\mathrm{ext}(\mathbf{r}, \omega) = \frac{-e}{v}\delta(x - x_0)\delta(y - y_0)e^{ik_\mathrm{e}(z - z_0)}, \tag{4.3}$$

where $k_\mathrm{e} = \omega/v$ is the electron wave vector. The corresponding external current density is then

$$\mathbf{J}_\mathrm{ext}(\mathbf{r}, \omega) = \rho_\mathrm{ext}(\mathbf{r}, \omega)\mathbf{v} = -e\delta(x - x_0)\delta(y - y_0)e^{ik_\mathrm{e}(z - z_0)}\hat{\mathbf{z}}. \tag{4.4}$$

By solving Maxwell's equations with the external charge density and current density, given by Eqs. (4.3) and (4.4), respectively, it can be shown that the electric field set up by a moving electron in vacuum $\mathbf{E}_\mathrm{e}^\mathrm{vac}$ is given as [37]

$$\mathbf{E}_\mathrm{e}^\mathrm{vac}(\mathbf{r}, \omega) = \frac{e\omega}{2\pi\varepsilon_0 v^2\gamma_\mathrm{e}}e^{ik_\mathrm{e}z}\left[\frac{i}{\gamma_\mathrm{e}}K_0\left(\frac{k_\mathrm{e}R}{\gamma_\mathrm{e}}\right)\hat{\mathbf{z}} - K_1\left(\frac{k_\mathrm{e}R}{\gamma_\mathrm{e}}\right)(\hat{\mathbf{x}} + \hat{\mathbf{y}})\right], \tag{4.5}$$

where $\gamma_\mathrm{e} = 1/\sqrt{1 - v^2/c^2}$ is the Lorentz contraction factor, K_0 and K_1 denote the modified Bessel functions of the second kind of zeroth and first orders, respectively, and $R^2 = x^2 + y^2$. To get a better understanding of the electric field generated by a moving electron, we can consider the modified Bessel functions for small arguments, i.e., for small values of R. We find

$$K_0(z) \simeq -\ln(z), \qquad K_1(z) \simeq z^{-1}, \tag{4.6}$$

which shows that both the transversal (xy-plane) and longitudinal (z-direction) electric components are very localized to the trajectory of the electron. Thus, to strongly

excite surface plasmons in metallic structures the electron beam has to be sufficiently close to the surface or penetrate the structure [201, 202].

When the moving electron is in the presence of a sample, the interaction between the electron and the sample will give rise to an induced electric field $\mathbf{E}_{\mathrm{e}}^{\mathrm{ind}}$, akin to the optically scattered field generated by a dielectric or metal geometry when excited by a plane wave [138]. The induced electric field acts back on the moving electron, which then suffers energy losses. In particular, the total energy loss ΔE suffered by an electron is given by the work done by the induced electric field on the electron. The total energy loss can be written up as [1, 121]

$$\Delta E = e\int_{-\infty}^{\infty} \mathrm{d}t\mathbf{v}\cdot\mathbf{E}_{\mathrm{e}}^{\mathrm{ind}}\left[\mathbf{r}_{\mathrm{e}}(t),t\right] = \int_{0}^{\infty}\mathrm{d}\omega\hbar\omega\Gamma_{\mathrm{EELS}}(\omega), \tag{4.7}$$

where, in the second equality, we have dispersed the total energy loss according to frequency and introduced the loss-probability function $\Gamma_{\mathrm{EELS}}(\omega)$, which corresponds to the signal detected in EEL spectra [1]. By performing a temporal Fourier transform of $\mathbf{E}_{\mathrm{e}}^{\mathrm{ind}}\left[\mathbf{r}_{\mathrm{e}}(t),t\right]$ and using the property $\mathbf{E}_{\mathrm{e}}^{\mathrm{ind}}(\mathbf{r},\omega) = [\mathbf{E}_{\mathrm{e}}^{\mathrm{ind}}(\mathbf{r},-\omega)]^{*}$, where * denotes complex conjugation, we can write the loss-probability as [201]

$$\Gamma_{\mathrm{EELS}}(\omega) = \frac{e}{\pi\hbar\omega}\int_{-\infty}^{\infty}\mathrm{d}t\mathbf{v}\cdot\mathrm{Re}\left\{\mathbf{E}_{\mathrm{e}}^{\mathrm{ind}}\left[\mathbf{r}_{\mathrm{e}}(t),\omega\right]e^{-i\omega t}\right\}. \tag{4.8}$$

Eq. (4.8) shows that determining the loss probability is reduced to calculating the induced electric field along the electron trajectory. The loss probability of several high-symmetry geometries, such as spheres [158], cylinders [203, 204], and thin films [1, 205] etc., have been calculated analytically within the LRA to which an excellent overview is found in Ref. [37]. Significantly less analytical progress has been seen in the context of nonlocal effects in EELS with some of the few considered geometries being cylinders [206], spheres [37], plane interfaces [207], and thin films [208]. However, the development of numerical methods based on the boundary-element method [209, 210, 211, 212], multiple scattering [213, 214], discrete-dipole approximation [215, 216], and finite-element solvers [46, 13, 112] allow for calculating arbitrarily shaped geometries, and in some cases even with the inclusion of nonlocal response [112, 121].

For systems that are translationally invariant along the direction of the electron (z-direction), Eq. (4.8) simplifies significantly. The loss probability pr. length $\Gamma_{\mathrm{EELS}}^{\mathrm{2D}}(\omega)$ is then (Paper B)

$$\Gamma_{\mathrm{EELS}}^{\mathrm{2D}}(\omega) = \frac{ev}{\pi\hbar\omega}\mathrm{Re}\left[\hat{\mathbf{z}}\cdot\mathbf{E}_{\mathrm{e}}^{\mathrm{ind}}\left(x_0,y_0;\omega\right)\right], \tag{4.9}$$

where (x_0, y_0) denotes the transverse position of the electron beam. As we see in Sec. 4.4, Eq. (4.9) quite accurately describes the EEL signal from gold nanogrooves with the electron beam parallel to the direction of invariance, even though the length of the samples studied are only $100-150$ nm. Another interesting feature is that for translationally invariant geometries, the loss probability is directly proportional to the photonic local density of states (LDOS) projected along the direction of the electron (z-direction) as [201]

$$\Gamma_{\mathrm{EELS}}^{\mathrm{2D}}(x_0,y_0;\omega) \propto \frac{1}{\hbar\omega}\tilde{\rho}_z(x_0,y_0;\omega), \tag{4.10}$$

where $\tilde{\rho}_z$ denotes the LDOS projected along the z-direction. Thus, by studying translationally invariant metallic structures, or realistically, structures which are invariant for a sufficient distance, the LDOS can be mapped with nanometer resolution, which is important for e.g. precise positioning of emitters in the proximity

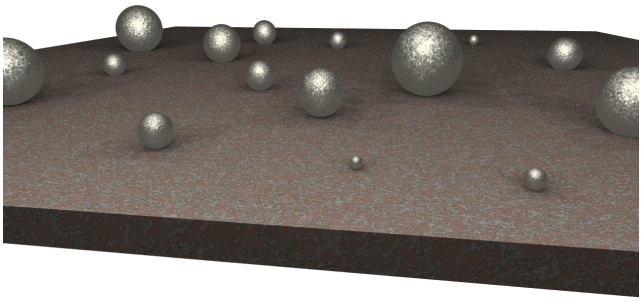

Figure 4.6: Schematic illustration of silver nanoparticles of different sizes dispersed on a 10 nm thick silicon nitride TEM membrane.

of metallic geometries to achieve controlled emitter-plasmon coupling [217]. While some 3D metal geometries also show correlation between optical measurements and EELS [201, 218, 219], a general relation between EELS and LDOS can not be expected [220], as EELS and optical measurements can be blind to plasmonic hot spots and dark modes, respectively.

4.3 Blueshift of surface plasmon resonance in silver nanoparticles

The work presented in this section is based on Papers E and I.

4.3.1 Motivation

Surface plasmons are usually well-described by the classical Drude model for nanoparticles with dimensions of tens of nanometer and larger [11]. In the quasistatic limit, i.e., when the wavelength of the exciting electromagnetic wave considerably exceeds the dimensions of the structure, the local-response Drude theory predicts that the resonance energy of localized SPs is independent of the size of the nanostructure, as discussed in Sec. 3.2. These predictions are however in conflict both with earlier [14, 150, 221, 222] and with more recent experimental results, which have shown a size dependency of the localized SP resonance in noble metal nanoparticles in the size range of 1-10 nm [19].

This dependence of the SP resonance on the size of noble metal nanostructures is believed to be a signature of quantum properties of the free-electron gas. With decreasing sizes of the nanoparticles, the quantum wave nature of the electrons is theoretically expected to manifest itself in the optical response due to the effects of quantum confinement [223, 224, 225, 226, 227] and nonlocal response [228, 121, 102, 206, 61, 70, 91], see also Chap. 2.

In Sec. 4.3 we report the experimental study of the SP resonance of chemically grown single Ag nanoparticles dispersed on 10 nm thick Si_3N_4 membranes with STEM EELS, see Fig. 4.6 for a schematic illustration. As discussed in Sec. 4.1, STEM EELS is perfectly suited to probe and access plasmonic nanostructures and SP resonances at length scales where quantum mechanics is anticipated to become important. Our measurements present a significant blueshift of the SP resonance energy from 3.2 to 3.7 eV for particle diameters ranging from 26 down to 3.5 nm. Our results also confirm very recent experiments made with Ag nanoparticles on different substrates using different STEM operating conditions [19], thereby strengthening the interpretation that the blueshift is predominantly associated with the intrinsic properties of the electron gas itself rather than having an extrinsic cause.

We initially compare our experimental data to three different models for a spherical particle: a purely classical local-response Drude model which assumes a constant electron density profile in the metal nanoparticle, a semiclassical local-response Drude model where the electron density varies inside the nanoparticle and is determined from the quantum mechanical problem of electrons moving in an infinite spherical potential well [226], and finally, a semiclassical model based on the hydrodynamic description of the motion of the electron gas (Sec. 2.3). As we are only concerned with the resonance shift, and not also the linewidth broadening, it is sufficient to use the hydrodynamic model instead of the more complete GNOR theory, see also Sec. 3.2 about nanospheres. In all three models, we model the presence of the substrate by an effective homogeneous background permittivity. We find good qualitative agreement between our experimental data and the two semiclassical models, thus supporting the anticipated nonlocal nature of SPs of Ag nanoparticles in the $1 - 10$ nm size regime. The experimentally observed blueshift is however significantly larger than the predictions by the two semiclassical models.

To better understand the quantitative discrepancy between our nonlocal model and the experimental observations, we gradually increase the complexity of our theoretical model. Assuming that the discrepancy is due to the imperfect modeling of the substrate, we consider first the dipole-dipole interaction of the spherical nanoparticle and the image charge created in a semi-infinite insulating substrate. As we find this model to also be inadequate at describing the larger experimental blueshift, we go one step further and solve the full electromagnetic plane-wave scattering problem of a spherical particle with nonlocal response situated on a finite-thickness substrate. Even here we still only find qualitative agreement between theory and experiments. Finally, we therefore discuss possible explanations to the discrepancy, such as the presence of an inhomogeneous equilibrium electron density in the metal nanoparticle and the effect of the electron probe.

4.3.2 Experimental setup

The nanoparticles are grown chemically following the method described in Ref. [229] and subsequently stabilized in an aqueous solution with borohydride ions. The mean size of the nanoparticles is 12 nm with a very broad size distribution ranging from 3 to 30 nm. The nanoparticle solution is dispersed on a 10 nm thick commercially available Si_3N_4 membrane (TEMwindows.com), which has a refractive index of approximately $n \approx 2.1$ [230]. To characterize our nanoparticles we have used an aberration-corrected STEM FEI Titan operated at 120 kV with a probe diameter of approximately 0.5 nm, and convergence and collection angles of 15 mrads and 17 mrads, respectively. We systematically performed EELS measurements at the surface and in the middle of each nanoparticle. The EELS spectra were taken with an exposure time of 90 ms to avoid beam damage as much as possible. To improve the signal-to-noise ratio we accumulated ten to fifteen spectra for each measurement point. We observed no evidence of damage after each measurement.

The EEL spectra were processed using the reflected-tail method, and the energies of the SP resonance peaks were subsequently determined by using a nonlinear least-squares fit of our data to Gaussian functions, as detailed in Sec. 4.1.2. Nanoparticle diameters were determined by calculating the area of the imaged particle and assigning to the area an effective diameter by assuming a perfect circular shape. The error bars in the size therefore correspond to the deviation from the assumption of a circular shape, which is estimated as the difference between the largest and smallest diameter of the particle.

4.3.3 Theory

In the following theoretical analysis our hypothesis is that the blueshift of the SP resonance energy is related to the properties of the electron density profile in the metal nanoparticle. Therefore, we use three different approaches to model the electron density of the Ag nanoparticle. In all three approaches, we calculate the optical response and thereby also the resonance energies of the nanoparticle through the quasistatic polarizability α of a sphere embedded in a homogeneous background dielectric with permittivity ε_{B}. With this approach, we make two implicit assumptions: the first is that we can neglect retardation effects and the second is that we can neglect the symmetry-breaking effect of the substrate. We have validated the quasistatic approach by comparing to fully retarded calculations, which shows excellent agreement in the particle size range we consider, see Sec. 3.2.3. The effect of the substrate will initially be taken into account indirectly by determining an effective homogeneous background permittivity ε_{B} using the average resonance frequency of the largest particles ($2R > 20$ nm) as the classical limit. In Secs. 4.3.6 and 4.3.7, we go beyond this approximation and consider properly the electromagnetic effect of the presence of the substrate.

The first, and simplest, approach is to assume a constant free-electron density n_0 in the metal particle, which drops abruptly to zero outside the particle. This assumption is the starting point of the classical local-response Drude model for the response of the Ag nanoparticle, where the polarizability is given by the Clausius–Mossotti relation [Eq. (3.7)], which is well-known to be size independent for subwavelength particles.

The second approach is to correct the standard approximation in local-response theory of a homogeneous electron density profile by using insight from the quantum wave nature of electrons to model the electron density profile and take into account the quantum confinement of the electrons. For nanometer-sized spheres, the classical polarizability given by the Clausius–Mossotti relation must be altered to take into account an inhomogeneous electron density. In Ref. [226], it is shown that in general the local-response polarizability for a sphere embedded in a homogeneous material is given as

$$\alpha_{\text{LQC}}(\omega) = 12\pi \int_0^R r^2 \mathrm{d}r \frac{\varepsilon_{\text{D}}(r,\omega) - \varepsilon_{\text{B}}}{\varepsilon_{\text{D}}(r,\omega) + 2\varepsilon_{\text{B}}}, \tag{4.11a}$$

now with a spatially varying Drude permittivity [227, 226]

$$\varepsilon_{\text{D}}(r,\omega) = \varepsilon_\infty(\omega) - \frac{\omega_{\text{p}}^2}{\omega(\omega + i\gamma)} \frac{n(r)}{n_0}. \tag{4.11b}$$

Here, $n(r)$ is the electron density in the metal nanoparticle. Clearly, if $n(r) = n_0$ we arrive at the classical Clausius–Mossotti relation Eq. (3.7) as expected. To determine the density profile in this local-response model, we follow the approach of Ref. [226] and assume that the free electrons move in an infinite spherical potential well. The approach just outlined of a local-response theory with an inhomogeneous electron density is very similar to the theoretical model used in Ref. [19] for explaining their

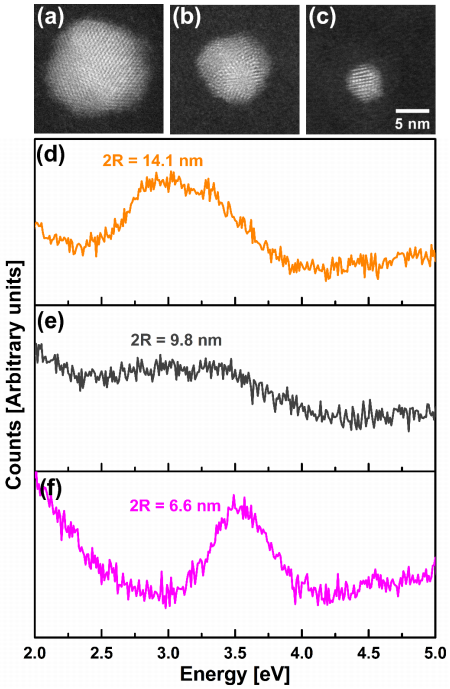

Figure 4.7: Aberration-corrected STEM images of Ag nanoparticles with diameters **(a)** 15.5 nm, **(b)** 10 nm, and **(c)** 5.5 nm, and normalized raw EELS spectra of similar-sized Ag nanoparticles **(d-f)**. The EELS measurements are acquired by directing the electron beam to the surface of the particle.

experimental results. It should be noted that any effects due to electron spill-out are neglected in all of the approaches that we consider.

The third and final approach is to compare our experimental data with the nonlocal hydrodynamic model in which the dynamics of the electron gas is governed by the semiclassical hydrodynamic equation of motion, which results in an inhomogeneous induced electron density profile (Sec. 2.3). The nonlocal hydrodynamic polarizability is given by Eq. (3.12) with $k_{\mathrm{nl}} = \sqrt{\varepsilon_{\mathrm{D}}(\omega)}/\xi_{\mathrm{H}}$.

4.3.4 Results

Figures 4.7(a-c) display STEM images of Ag nanoparticles with diameters of 15.5, 10.0, and 5.5 nm respectively. The images show that no chemical residue is left from the synthesis and that the particles are faceted. We find that approximately 70% of the studied nanoparticles have a relative size error (i.e., the ratio of the size error bar to the particle diameter) below 20% (determined from the 2D STEM images), verifying that the shape of the nanoparticles is to a first approximation overall spherical (further discussion in Sec. 4.3.5). On a subset of the particles, thickness measurements using image recordings at different tilt angles were performed, revealing information about the shape of the nanoparticle in the third dimension. Such 3D investigations confirmed that the shape is overall spherical, but however could not be completed for all particles due to stability issues: the positions of tiny nanoparticles fluctuate under

too long exposure of the electron beam, thus preventing accurate determination of the shape of the nanoparticle in the third dimension perpendicular to the substrate.

Figures 4.7(d-f) display raw normalized EELS data, acquired on Ag nanoparticles with diameters 14.1, 9.8, and 6.6 nm, respectively. The peaks correspond to the excitation of the SP. When the diameter of the nanoparticle decreases, the SP resonance clearly shifts progressively to higher energies. Figs. 4.7(d-f) also display that the amplitude and linewidth of the SP resonances can vary from particle to particle (with the same size) and at times show narrowing instead of the expected broadening of the resonance for decreasing nanoparticle sizes [223, 14, 224, 34]. This is for example seen in the linewidths in Figs. 4.7(d-f) which seem to decrease with size. However, as will be explained in more detail in the next paragraph, we did not find a systematic trend of the linewidths in our EELS measurements probably due to the shape variations in our ensemble of nanoparticles.

Figure 4.8 displays the resonance energy of the SP as a function of the diameter of the nanoparticles. A significant blueshift of the SP resonance of 0.5 eV is observed when the nanoparticle diameter decreases from 26 to 3.5 nm. This trend is in good agreement with the results shown in Ref. [19], despite the difference in the substrate and the STEM operating conditions, a strong indication that the blueshift of Ag nanoparticles is robust to extrinsic variations. Another prominent feature in Fig. 4.8 is the scatter of resonance energies at a fixed particle diameter. We mainly attribute the spread in resonance energies at a given particle size to shape variations in our ensemble of nanoparticles (see Sec. 4.3.5 for further discussion). Slight deviations from perfect circular shape in the STEM images will result in a delicate dependency on the location of the electron probe and give rise to splitting of SP resonance energies due to degeneracy lifting. In this regard, we also note that even a perfectly circular particle on a 2D STEM image may still possess some weak prolate or oblate deformation in the third dimension, resulting in a departure from spherical shape. Furthermore, shape deviations may also impact the linewidth of the SP resonance, since the electron probe can excite the closely-spaced non-degenerate resonance energies simultaneously, which

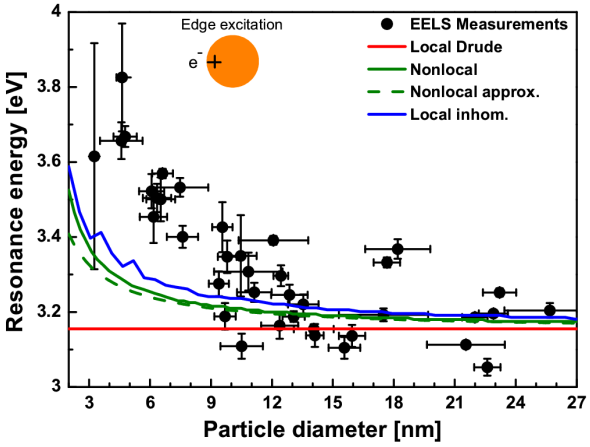

Figure 4.8: Nanoparticle SP resonance energy as a function of the particle diameter. The dots are EELS measurements taken at the surface of the particle and the lines are theoretical predictions. We use parameters from Ref. [53]: $\hbar\omega_{\rm p} = 8.282$ eV, $\hbar\gamma = 0.048$ eV, $n_0 = 5.9 \times 10^{28}$ m^{-3} and $v_{\rm F} = 1.39 \times 10^6$ m/s. From the average large-particle ($2R > 20$ nm) resonances we determine $\varepsilon_{\rm B} = 1.53$.

may appear as a single broadened peak. This broadening mechanism could explain the apparent linewidth narrowing for decreasing particle size seen in Figs. 4.7(d-f). However, we cannot rule out that other effects beyond shape deviations contribute to the spread of resonance energies and impact the SP resonance linewidth. These could for example be the facets or the particle-to-substrate interface [231].

Along with the EELS measurements in Fig. 4.8, we show Eq. (3.7) for the local-response Drude model (red line) and the semiclassical local-response model Eq. (4.11) (blue line). Furthermore, the nonlocal relation of Eq. (3.12) (green solid line) and the approximate nonlocal relation of Eq. (3.14a) (green dashed line) are also depicted, and we see that Eq. (3.14a) is accurate for particle sizes $2R \gtrsim 10$ nm.

Due to the narrow energy range in consideration ($\sim 3.0-3.9$ eV), we approximate $\varepsilon_\infty(\omega)$ as a second-order Taylor polynomial based on the frequency-dependent values given for Ag in Ref. [53], which are similar to those in Table 3.1. We find $\varepsilon_\infty(\omega) = (59.8 + i55.1)(\omega/\omega_\mathrm{p})^2 - (40.3 + i42.4)(\omega/\omega_\mathrm{p}) + (10.5 + i8.6)$. Since the refractive index of the Si_3N_4 substrate varies hardly ($n \approx 2.1$) in the narrow energy range we consider [230], we assume that the background permittivity ε_B is constant and determine it by approximating the average resonance energy of the largest particles ($2R > 20$ nm) as the classical limit.

It is clear that the local Drude theory is inadequate to describe the measurements of Fig. 4.8. The nonlocal quasistatic hydrodynamic model predicts a blueshift in agreement with the experimental EELS measurements. Interestingly, the measured blueshift is even larger than predicted. We also see that the local-response model with an inhomogeneous electron density profile shows a similar trend as the nonlocal hydrodynamic model, indicating that these two different models describe very similar physical effects. The oscillations in the resonance energy in the inhomogeneous local-response model seen for small particle diameter are due to small variations in the density profile with decreasing size (i.e., discrete changes in the number of electrons), as also stated in Ref. [19].

The inhomogeneous local-response model and the nonlocal hydrodynamic model, when applied to a sphere in a homogeneous background medium, agree qualitatively with the EELS measurements. However, they do not provide the full picture. One of the probable issues arising is that the substrate is taken into account indirectly through a homogeneous background medium, which however may not be adequate to describe the effects of the presence of a dielectric substrate. It has been shown that the dielectric substrate modifies the absorption spectrum of an isolated sphere [232] and also the waveguiding properties of nanowires [47, 233, 234]. In Secs. 4.3.6 and 4.3.7, we therefore explore if properly accounting for the substrate in the nonlocal hydrodynamic model can provide quantitative agreement with experimental measurements. However, first we consider the impact of shape variations of the nanoparticles on our measurements displayed in Fig. 4.8.

4.3.5 Shape analysis

The diameters of our nanoparticles are determined by using the free online image analysis tool ImageJ [235] which includes a particle analysis package. We use the images taken in STEM mode to measure the surface area A of the nanoparticle, whereafter we determine the mean nanoparticle diameter D using the relation $A = \pi(D/2)^2$. The particle analysis tool also evaluates the maximum D_max and minimum D_min diameters of the nanoparticle and the difference between these two diameters, i.e., $\Delta D = D_\mathrm{max} - D_\mathrm{min}$ provides us a measure for the error in the nanoparticle diameter (shown as the error bar in Fig. 4.8). The relative size error ($\Delta D/D$) then represents the deviation of the shape of the particles from a perfect circle.

Figure 4.9 displays a histogram with the number of particles as function of the relative size error (5% interval between each bar). The first observation is that the

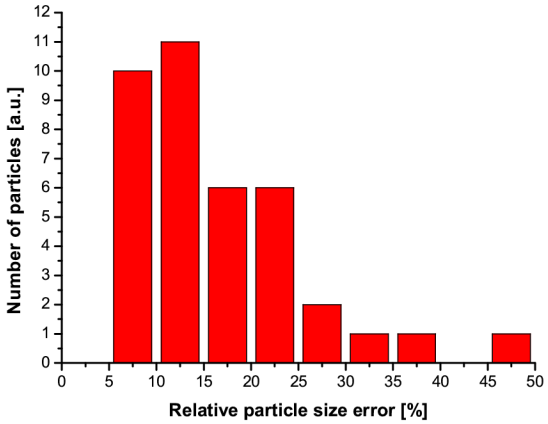

Figure 4.9: Histogram showing the distribution of relative size error $\Delta D/D$. The relative size error represents the shape deviation of the nanoparticle from a perfect circle in the 2D STEM image.

relative error in the diameter is spread from 5% to 50% with a maximum of counts centered on 15% deviation. We also see that more than 70% of the particles have an error smaller than 20%, thus giving us confidence that assuming the particles to be spherical is justified. We also emphasize that this analysis was made on STEM images which are the projections of the 3D shapes of the nanoparticles onto the plane parallel to the substrate. This lack of information in the third dimension leaves indeterminacy of the exact shape of the particle. However, since the nanoparticles are fabricated in a liquid phase suspension [229], i.e., growing identically in three dimensions, we can to a first approximation infer that we have the same relative size error distribution in the third dimension perpendicular to the substrate, thus assuming that particle orientation is independent of its shape deformation.

In order to understand the scattering of the SP resonance energies observed in Fig. 4.8, we model the deviation from the perfect spherical shape as an ellipsoidal particle with minor and major axes. We calculate the optical polarizability of two different types of ellipsoids: the prolate spheroid (one major and two equal minor axes) and the oblate spheroid (two equal major and one minor axes). The polarizability is calculated within the local Drude theory under two different polarizations of the incident electric field, parallel to the major axis or parallel the minor axis [11]. The perfect spherical sphere is deformed while keeping the volume constant. We use a relative deformation of the major (minor) axis of 20% for the prolate (oblate) particles which corresponds to the deviation of the majority of the nanoparticles studied.

The results are shown in Fig. 4.10. The red line represents the local Drude calculation for a perfect sphere (same as red line in Fig. 4.8). The grey patterned area corresponds to the span of resonance energies for the prolate particles, when a relative deviation of the major axis of 20% is allowed. The part of the area that is above the red line (i.e., blueshifted with respect to the perfect sphere) corresponds to a polarization along the minor axis, while the part below the red line (i.e., redshifted with respect to the perfect sphere) is due a polarization along the major axis. For the polarization along the minor axis, we see a blueshift of approximately 0.1 eV of the SP resonance while we obtain a redshift of approximately 0.2 eV for the polarization along the major axis. The increased redshift observed for the polarization along the

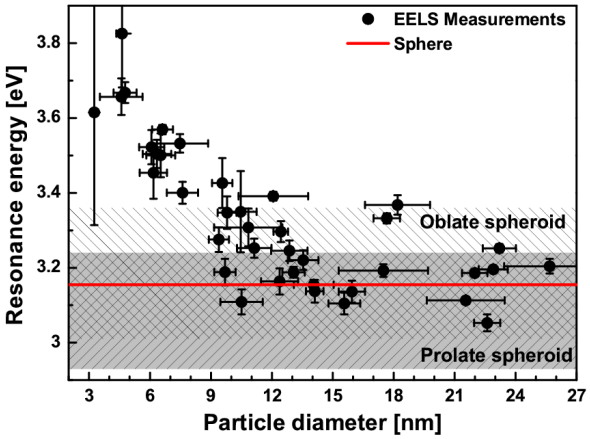

Figure 4.10: Local-response calculations of the SP resonance for perfectly spherical (red line), oblate (white patterned) and prolate (grey patterned) particles under excitation of different polarizations.

major axis is due to the fact that a size increase of 20% on the major axis will give only a size decrease of 9% on the minor axis (scales as $1/a_{\mathrm{major}}^2$, where a_{major} is the length of the major axis) for a constant volume. The same arguments are valid for the oblate case with the exception that here the blueshift is higher than the redshift (major and minor axes are inverted). However, the overall span of resonance energies considering both type of spheroids is approximately 0.4 eV. Interestingly, this interval is similar to the scattering of the resonance energy observed in Fig. 4.8 for particles above 10 nm, where the local theory is still valid. However, we emphasize that the measured resonance energies for the smallest particles (below 10 nm) exceeds this span of resonance energies, and thus the observed blueshift cannot be explained by a simple shape deviation argument.

In conclusion, we see that the deviation from the spherical shape into ellipsoid-like particles and the thereby prompted dependency on the location of the EELS probe when measuring the SP resonance gives a reasonable and probable explanation for the spread but not the magnitude of SP resonance energies observed in our measurements.

4.3.6 Substrate effects: dipole-dipole interaction

The optical polarizability α of a single sphere in a homogeneous background ε_{B} can be modified to take into account the presence of a semi-infinite substrate with permittivity ε_{S} using a simple image charge model. In this picture, the coupling between the sphere and the substrate is based on a dipole-dipole interaction between the dipole moment of the sphere and the weaker dipole moment of the image charges in the substrate. Taking only dipole moments into account is an approximation, which we go beyond in Sec. 4.3.7. Due to the symmetry-breaking presence of the substrate, there are two separate cases to be treated for the direction of the incident field: one when the incident electric field is parallel to the substrate, the other when the incident field is perpendicular to the substrate. It has been shown that the altered polarizability α_{sub} in the presence of the semi-infinite substrate is [161, 236, 12]

$$\alpha_{\mathrm{sub}} = \alpha \left[1 - \frac{\kappa\alpha}{4\pi\,(2R)^3} \frac{\varepsilon_{\mathrm{S}} - \varepsilon_{\mathrm{B}}}{\varepsilon_{\mathrm{S}} + \varepsilon_{\mathrm{B}}} \right]^{-1}, \tag{4.12}$$

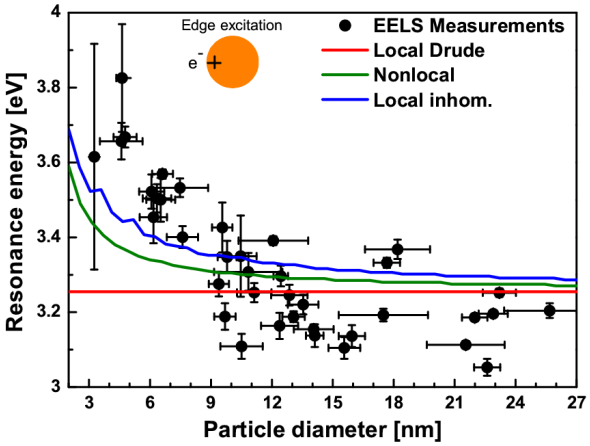

Figure 4.11: The same as Fig. 4.8, but calculated using Eq. (4.12) with $\kappa = 2$, $\varepsilon_{\mathrm{S}} = 2.08^2$ and $\varepsilon_{\mathrm{B}} = 1$.

where $\kappa = -1$ for a parallel incident electric field while $\kappa = 2$ for a perpendicular electric field. Since the electric field produced by a swift electron has electric field components both in the directions parallel and perpendicular to the plane of the substrate [see Eq. (4.5)], it is not immediately clear which value for κ is appropriate. Thus we take a pragmatic approach and use $\kappa = 2$ as this value best fits our experimental results.

Figure 4.11 shows calculations on the SP resonance energy performed using Eq. (4.12) with $\varepsilon_{\mathrm{S}} = 2.08^2$ and $\varepsilon_{\mathrm{B}} = 1$. Ellipsometry measurements of the complex refractive index $n = n' + in''$ on the Si_3N_4 substrate has been provided by the manufacturer of the TEM membranes (TEMwindows.com), showing an almost constant index of refraction of $n' \approx 2.08$ and a negligible extinction coefficient $n'' \approx 0$ in the energy range we consider ($3.0 - 3.9$ eV). The provided measurements are very similar to that of Ref. [230]. We emphasize that with the dipole-dipole model for the substrate no fitting of the background permittivity has been done.

Figure 4.11 shows that the dipole-dipole interaction predicts a slightly larger resonance energy in the classical limit (i.e., for the largest particles) compared to the fitted homogeneous background permittivity approach used for Fig. 4.8. However, the blueshift in the resonance energy for decreasing particle size in the two semiclassical models is very similar to the effective homogeneous background approach, and thus the dipole-dipole model for the substrate cannot fully account for the significantly larger experimental blueshift. We also see that many of the EELS measurements of the larger particles ($2R > 10$ nm) lie at lower resonance energies than predicted by any of the theoretical substrate models. These discrepancies suggest that the simple dipole-dipole model for the substrate is inadequate to describe our experimental observations, and that a complete understanding of the effect of the substrate requires the inclusion of higher-order multipoles and the finite thickness of the substrate, which will be discussed in the next section.

4.3.7 Substrate effects: multipolar interaction

We consider now the case of a metal sphere described by the hydrodynamic theory and situated on a substrate of thickness t, thus going beyond the semi-infinite substrate

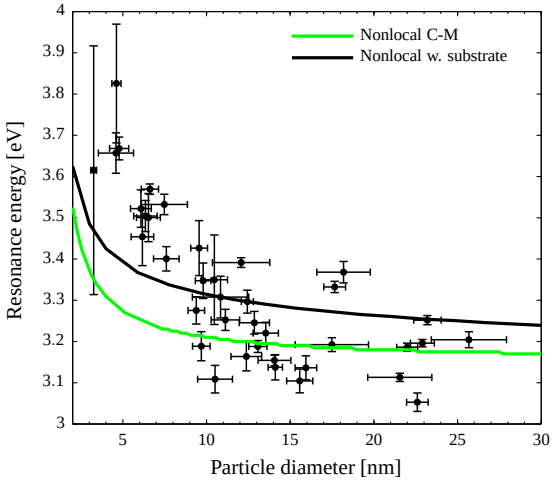

Figure 4.12: Experimental data as in Fig. 4.8. The green line represents calculations of a silver sphere with a hydrodynamic nonlocal response in a homogeneous environment using Eq. (3.12) with an effective background permittivity $\varepsilon_B = 1.53$. The black line represents calculations of a hydrodynamic nonlocal silver sphere in vacuum ($\varepsilon_B = 1$) situated on a 10 nm thick Si_3N_4 substrate with permittivity $\varepsilon_S = 2.08^2$.

presented in Sec. 4.3.6. We use an exact method based on scattering matrices and multipole expansions to calculate the fully retarded extinction cross section of the sphere-substrate system, when impinged by a plane wave, see Sec. 3.2 of Paper E for detailed derivation. With this method we take into account not only the dipole interaction but the multipolar interaction of the sphere and the associated image charges in the dielectric substrate.

The black line in Fig. 4.12 shows the resonance energy determined from extinction cross section calculations of a silver sphere with hydrodynamic nonlocal response in vacuum situated on a 10 nm thick Si_3N_4 substrate. Here no fitting of the background permittivity is performed and we use again $\varepsilon_S = 2.08^2$ as the permittivity of the substrate. The substrate-based calculation shows an overall higher resonance energy for all particle sizes, but is otherwise quite similar (in terms of trend with particle size) to the homogeneous effective background approach (green line in Fig. 4.12). Surprisingly higher order multipoles in the sphere, which are anticipated to be enhanced due to the presence of the substrate [237], show no significant contribution in the optical response. This is in fact due to the strongly dispersive background of the bound electrons in Ag at the resonance energies of the higher order multipoles, which heavily dampens the contribution from these modes. In summary, we have seen in detail in Fig. 4.12 that the substrate-based calculations do not show a larger shift in energy than the nonlocal polarizability, and does therefore not provide the explanation for the experimentally observed larger blueshift.

4.3.8 Influence of the electron probe

So far all of the theoretical models have been based on the exciting electric field being static (quasistatic polarizability) or a plane wave (extinction cross section), but the electric field of a swift electron differs significantly from both of these, see

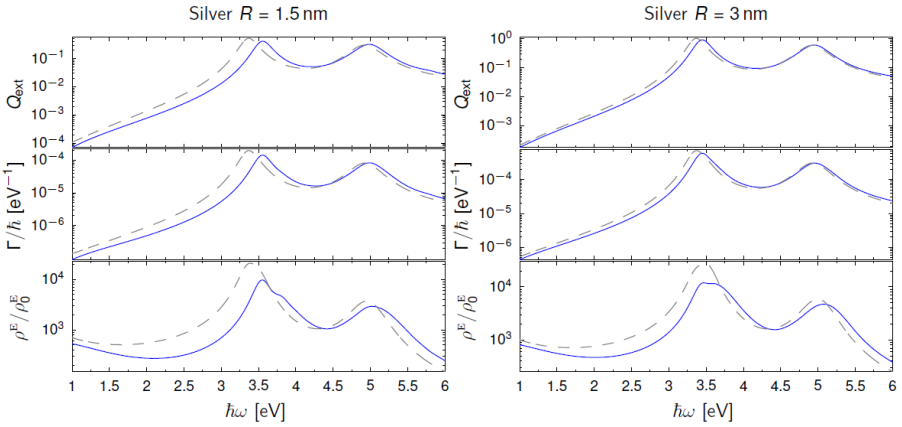

Figure 4.13: Extinction efficiency $Q_{\text{ext}} = \sigma_{\text{ext}}/(\pi R^2)$, EEL probability Γ, and normalized LDOS ρ^{E} as a function of energy $\hbar\omega$ of a silver sphere in vacuum with radii $R = 1.5$ nm (left column) and $R = 3$ nm (right column). Impact parameter is 1.5 nm from surface of the sphere for both radii. Hydrodynamic model and LRA is shown in solid blue and dashed gray lines, respectively. Reproduced from Supporting Information of Paper D (not included in thesis).

Eq. (4.5). Importantly, a swift electron in the vicinity of a nanoparticle is able to excite higher-order multipoles, such as the quadrupole mode, see e.g. Ref. [37] and Paper D (not included in this thesis). Furthermore, the extinction cross section is not always comparable to EEL signal, as discussed in Sec. 4.2. Thus, a discussion about the influence of the electron probe on the excited SP modes is needed.

Figure 4.13 is reproduced from the Supporting Information of Paper D and displays calculations of the extinction efficiency, EEL probability, and LDOS as a function of energy for a silver sphere in vacuum. The radii of the spheres are 1.5 nm (left column) and 3 nm (right column), and the impact parameter is 1.5 nm from the surface of the sphere for both radii. Calculations based on the hydrodynamic model and the LRA are shown in solid blue and dashed gray lines, respectively. For the current discussion, we are only interested in the second row, i.e., the calculations of the EEL probability. For the LRA we see that a resonance peak is present around an energy of 3.3 eV, corresponding to the dipole mode of the sphere. In particular, we note that the resonance energy is the same for both radii, since the sphere radii are in the quasistatic limit. The peak around 5 eV is not due to plasmonic excitations and is therefore ignored here. In the hydrodynamic model, we find as expected a blueshift of the dipole mode of the sphere, but no signature of any higher-order modes. We note also that the blueshift is not increased in the EEL probability compared to the extinction cross section (compare rows 1 and 2 in Fig. 4.13). As in the case of Sec. 4.3.7, the reason for the suppression of the higher-order modes is the losses of the bound electrons in Ag, i.e., $\text{Im}(\varepsilon_\infty)$, at the resonance energies of the higher-order modes. Thus, proper account of the exciting electric field of a swift electron does not seem to offer the explanation for the experimentally observed larger blueshift.

4.3.9 Further discussion

We discuss now possible issues with the theoretical models, which so far only account quantitatively for the experimental observations. An explanation in the context of

the inhomogeneity of the free-electron density could be the combined contribution of both the inhomogeneous static equilibrium electron density and nonlocality, i.e., including an inhomogeneous equilibrium density into the nonlocal model, as discussed briefly in Sec. 3.6. The Friedel oscillations are modeled in the local quantum-confined model given by Eq. (4.11) while nonlocality is neglected, and *vice versa* in the nonlocal hydrodynamic model given by Eq. (3.12). As seen in Fig. 4.8, the two effects separately give rise to similar-sized blueshifts, suggesting that the contribution of both effects simultaneously could add up to the significantly larger experimentally observed blueshift. Simply put, an extension of the nonlocal hydrodynamic model to include an inhomogeneous equilibrium free-electron density [184, 185] could produce a larger blueshift, which may be in accordance with the experimental observations. Furthermore, such a model could also take into account the electron spill-out effect, which in free-electron models has been argued to produce a redshift of the SP resonance [128, 60, 238, 126, 228], describing adequately simple metals. In contrast, it has also been shown that the spill-out effect in combination with the screening from the d electrons gives rise to the blueshift seen in Ag nanoparticles [131].

Additional size effects such as changes of the electronic band structure of the smallest nanoparticles, which are considerably more difficult to take into account, also impact the shift in SP resonance energy [14, 10, 239].

4.3.10 Concluding remarks

We have investigated the surface plasmon resonance of spherical silver nanoparticles ranging from 26 down to 3.5 nm in size with STEM EELS and observed a significant blueshift of 0.5 eV of the resonance energy. We have compared our experimental data with three different models based on the quasistatic optical polarizability of a sphere embedded in a homogeneous material. Two of the models, a nonlocal hydrodynamic model and a generalized local model, incorporate an inhomogeneity of the electron density induced by the quantum wave nature of the electrons. These two different models produce similar results in the SP resonance energy and describe qualitatively the blueshift observed in our measurements. Additional attempts to unveil the source of the discrepancy between theory and experiments included studying the electromagnetic effects of a sphere on a substrate and the exciting electric field of a moving electron. Unfortunately, none of the more complete theories provided better agreement with experimental observations.

The discrepancy between the different theoretical models and the larger observed blueshift suggest that a more detailed theoretical description of the system is needed to fully understand the influence of the confinement of free electrons on the SP resonance shift in silver nanoparticles. On the experimental side, further EELS studies of other metallic materials and on different substrates could unveil the mechanism behind the size dependency of the SP resonance of nanometer scale particles.

4.4 Extremely confined gap plasmons in gold nanogrooves

The work presented in this section is based on Paper B.

4.4.1 Introduction

While the majority of plasmonic EELS studies have been focused on localized SP resonances [221, 40, 41, 240, 19, 20, 39], EELS has also been used to study propagating SPs (i.e., waveguide modes) in e.g. metal thin films [241] and nanowires [242, 47, 188], where standing waves are formed by forward and backward-propagating waveguide modes. Gap SP (GSP) modes, i.e., propagating SP modes in a dielectric gap between

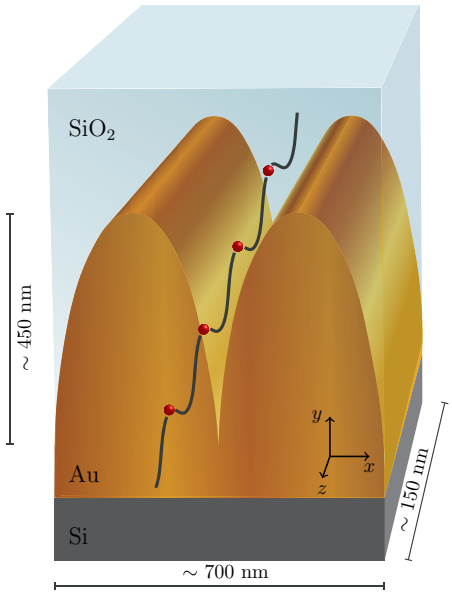

Figure 4.14: Artistic impression of a single gold nanogroove with the swift electron beam moving parallel to the groove axis. The groove is filled with silicon dioxide and the substrate is silicon. The period and height of the grooves are determined from the STEM images, while the thickness of the sample has been inspected in a SEM and also estimated from EELS data using both the log-ratio method and Kramers–Kronig analysis [38].

two metals [243], have been studied with cathodoluminescence [49] and photoluminescence [244]. However, GSP modes have to our knowledge never been experimentally examined with EELS. The GSP modes occur in a variety of geometries, from the simplest 1D MIM waveguide [245, 62] and metal nanowire-on-film geometries [244], to advanced structures such as the convex groove, V-groove, and trench and stripe waveguides [246, 247]. Furthermore, GSP modes offer enhanced properties compared to the usual propagating SP mode, such as extreme light confinement with improved propagation distances [248, 249], negative refraction [250, 251], highly efficient light absorption [246], and electrically driven circuitry [252].

In Sec. 4.4 we report on the experimental study of GSPs in ultra-sharp gold convex nanogrooves using EELS. The geometry of these nanogrooves is characterized by gradual, and relatively slow variations in the gap width when moving deeper inside a groove, see Fig. 4.14 for a schematic illustration. This means that the groove GSP modes can be considered as being formed by *local* MIM GSP modes (i.e., by GSP modes supported by constant-gap MIM configurations) that are weighted accordingly. In EELS experiments the strongly confined electric fields of moving electrons [recall Eq. (4.5)] excite thereby *local* MIM GSP modes, corresponding to the position of the electron beam inside the groove. Note, that a sample should necessarily be thin along the groove (Fig. 4.14) in order to be transparent for an electron beam, but not too thin with respect to the GSP wavelength. Overall, the considered groove geometry is ideal for studying MIM GSP modes, since the width of the insulating layer (gap size) decreases as the position of the electron probe is moved down the nanogroove, allowing us to map the evolution of MIM GSP modes for varying gap size in a single

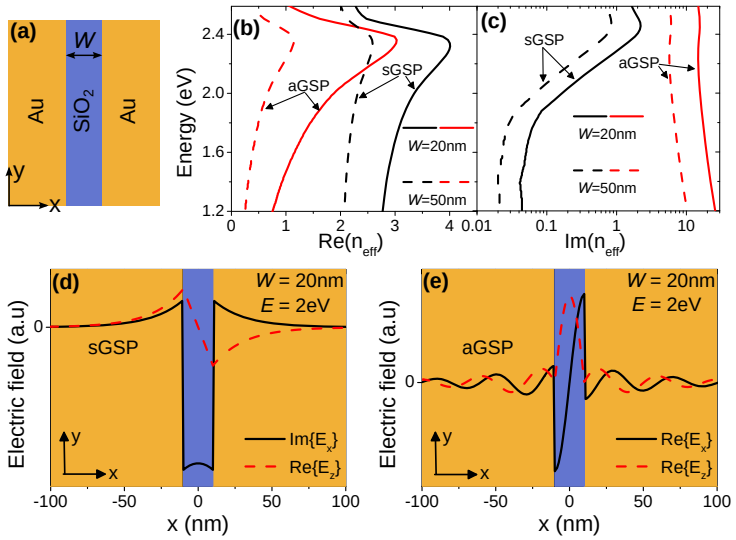

Figure 4.15: **(a)** Sketch of MIM waveguide, consisting of a SiO_2 spacer of width W sandwiched between two semi-infinite gold substrates. MIM GSP modes propagate along the z-direction. **(b-c)** Dispersion relation for MIM symmetric and antisymmetric GSP modes (MIM sGSP and aGSP, respectively) for $W = 20\,\text{nm}$ and $W = 50\,\text{nm}$. The permittivity of gold is taken from Ref. [54] and $\varepsilon_{SiO_2} = 2.1$. **(d-e)** Electric-field profiles calculated for MIM configuration with $W = 20\,\text{nm}$ and energy $E = 2\,\text{eV}$ for the MIM sGSP and aGSP, respectively.

groove. We will also explore how deep into the groove this local MIM picture remains accurate.

Using the nomenclature common to transverse-light excitation, the GSP modes can be classified according to the symmetry of their transversal electric component with respect to the mirror-symmetry plane of the groove (yz-plane in Fig. 4.14). The *symmetric* GSP (sGSP) modes have a net electric-dipole moment due to an antisymmetric induced-charge pattern with respect to the mirror-symmetry plane, whereas the *antisymmetric* GSP (aGSP) modes are optically dark due to a symmetric induced-charge distribution. This classification is hereafter applied to both MIM and groove GSP modes. In Sec. 4.4.2 we give a more detailed account on the field distributions and dispersion relations of GSP modes in MIM waveguides.

In this work, we intentionally propagate the electron beam along the axis of the groove within the mirror-symmetry plane (yz-plane, cf. Fig. 4.14) in order to allow for probing of modes near the groove bottom, and to study the optically dark modes. We verify experimentally the existence of the MIM aGSP mode in the crevice of the groove, with the mode showing an increase in energy as the gap size decreases. The presence of the MIM aGSP mode is confirmed at extremely narrow gaps of only 5 nm. Furthermore, we argue why the excitation of this mode, featuring very strong absorption, plays a crucial role in the experimental realization of non-resonant light absorption by ultra-sharp convex grooves with fabrication-induced asymmetry [246].

4.4.2 Nomenclature of metal-insulator-metal waveguide modes

Before we detail the experimental results and their theoretical interpretation, we briefly study the MIM waveguide to clarify the nomenclature we use throughout Sec. 4.4. MIM waveguides [see Fig. 4.15(a) for an illustration] support surface waves whose magnetic field component takes the form $H_y = A(x)e^{i\beta z}$, where β is the propagation constant. Due to the symmetry of the waveguide, the amplitude function $A(x)$ can either be symmetric or antisymmetric with respect to the center line, thus leading to two types of modes with dispersion relations given by [245, 243, 62]

$$\tanh\left(\frac{1}{2}\kappa_{\mathrm{d}}W\right) = -\begin{cases} \frac{\varepsilon_{\mathrm{d}}\kappa_{\mathrm{m}}}{\varepsilon_{\mathrm{m}}\kappa_{\mathrm{d}}}, & \text{(symmetric)} \\ \frac{\varepsilon_{\mathrm{m}}\kappa_{\mathrm{d}}}{\varepsilon_{\mathrm{d}}\kappa_{\mathrm{m}}}, & \text{(antisymmetric)} \end{cases}, \tag{4.13}$$

where W is the width of the dielectric spacer, ε_{d} is the relative permittivity of the dielectric, ε_{m} is the relative permittivity of the metal, $\kappa_{\mathrm{m}} = \sqrt{\beta^2 - k_0^2\varepsilon_{\mathrm{m}}}$, $\kappa_{\mathrm{d}} = \sqrt{\beta^2 - k_0^2\varepsilon_{\mathrm{d}}}$, and $k_0 = \omega/c$ is the free-space wave number. The two modes are also known as the MIM symmetric and antisymmetric gap surface plasmon modes (MIM sGSP and aGSP, respectively), where MIM sGSP is the most frequently studied mode as it is the only mode that would exist in subwavelength gaps of lossless MIM waveguides. That said, in real MIM waveguides with ohmic losses the MIM aGSP also subsists and is typically considerably more lossy than the MIM sGSP mode. It should be noted that the nomenclature of the two modes refers to the symmetry of the magnetic (H_y) or, equivalently, electric transversal (E_x) component. Accordingly, in *symmetric* waveguides the MIM sGSP and aGSP are only efficiently probed by light and electron beams, respectively. As we will see in Sec. 4.4.7, the slight asymmetry of the fabricated nanogrooves allows optical waves to couple more strongly to the aGSP mode of the groove, thus increasing the optical absorption beyond the case of a symmetric groove.

Figures 4.15(b-c) display solutions of Eq. (4.13) for a gold-SiO_2-gold waveguide with subwavelength gaps. The effective refractive index of the two modes, $n_{\mathrm{eff}} = \beta/k_0$, increases with decreasing gap width, showing a maximum in $\mathrm{Re}\{n_{\mathrm{eff}}\}$ at energy $E \simeq 2.35\,\mathrm{eV}$ which corresponds to the surface plasmon resonance. Additionally, we note that the propagation length $l = 1/[2k_0\mathrm{Im}(n_{\mathrm{eff}})]$ of the MIM aGSP mode at the SP resonance energy ($E \simeq 2.35\,\mathrm{eV}$) is around 50 nm for a MIM waveguide with a width of 50 nm, and decreases for decreasing gap size. Typical mode profiles of MIM sGSP and aGSP can be found in Figures 4.15(d) and 4.15(e), respectively, where the oscillatory behavior of the electric field into the gold for MIM aGSP is a consequence of $\mathrm{Re}\{n_{\mathrm{eff}}\} < \mathrm{Im}\{n_{\mathrm{eff}}\}$. The mode profiles clearly show the symmetric and antisymmetric nature of the transversal electric field component E_x for the sGSP and aGSP modes, respectively.

4.4.3 Fabrication

The fabrication of the gold nanogrooves is performed using a focused ion beam (FIB) setup. A gold film of 1.8 µm in thickness is deposited on a silicon substrate, after which areas of the gold are milled by the FIB to create the groove structure. With this technique ultra-sharp grooves with a 1D period of approximately 350 nm are fabricated (see Methods section of Paper B for details). Inside the FIB chamber, a layer of silicon dioxide is then deposited to separate the grooves from the top platinum layer used for protecting the sample during the preparation of the TEM lamella. The thickness of the silicon dioxide layer (approximately 500 nm) is sufficient to avoid the influence of the platinum layer when performing EELS measurements inside the groove. With a micromanipulator, the nanogroove sample is attached to a TEM

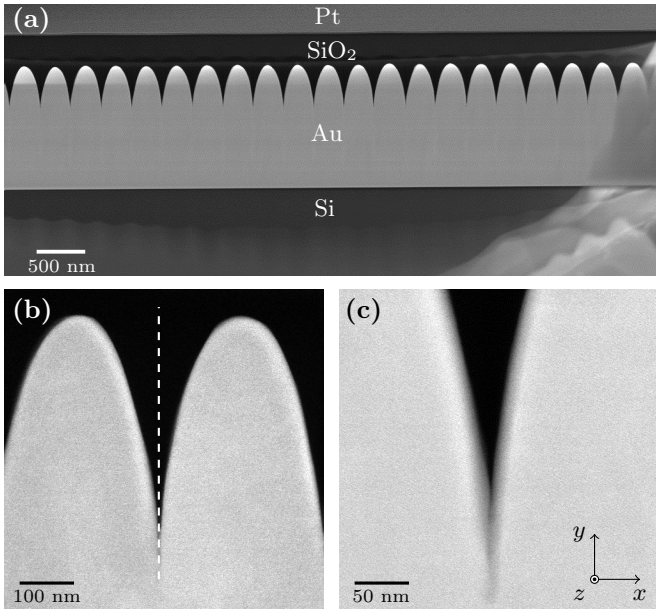

Figure 4.16: STEM images of **(a)** sample overview with material labels, **(b)** single groove zoom-in and **(c)** ultra-sharp groove crevice. The STEM images display the periodicity of the structure and the similarity in shape of each groove. Furthermore, the grooves are quite symmetric along the center line [dashed line in **(b)**] and extremely sharp, with around 5 nm gap sizes in the crevice.

lift-out grid such that the electron beam passes perpendicularly to the section of the sample and parallel to the axis of the groove, as illustrated in Fig. 4.14. In order to characterize the grooves in the TEM with EELS, we use the FIB to thin the nanogrooves along the z-direction to a thickness of approximately 150 nm. This ensures that the sample is sufficiently transparent for the electron beam. Note that as a consequence of the thinned sample, the structure can only be considered as a waveguide facilitating propagating modes when the electron beam probes MIM GSP modes at the base of the grooves, generally speaking when the groove width is considerably smaller than the sample thickness of ∼150 nm. In particular, for the study of propagating MIM aGSP modes the propagation length of the MIM aGSP mode at a given groove width should be comparable or less than the sample thickness.

Figure 4.16 shows typical STEM images of the gold nanogroove sample. In Fig. 4.16(a) an overview image of the sample is displayed with the gold nanogroove on top of a silicon substrate. The grooves are filled with silicon dioxide and the top platinum layer can also be seen. While slight fluctuations in shape and groove depths may be seen, overall the grooves are impressively similar (which is also reflected in our subsequent EELS measurements). Fig. 4.16(b) shows a zoom-in of a single groove, indicating the almost perfect symmetry with respect to the mirror-symmetry plane of the groove [see also the dashed white line in Fig. 4.16(b)]. However, as we will discuss later, the slight geometric asymmetry of the groove is crucial in understanding the plasmonic black gold effect studied in Ref. [246]. Finally, Fig. 4.16(c) is a close-up of a groove crevice, showing its extremely sharp nature. The side-to-side width of the

groove from the top to the bottom is calculated with an in-house image analysis code (written in MATLAB) and ranges from 320 nm down to widths smaller than 5 nm, thus confirming the ultra-sharp shape of the grooves. In the image analysis code, we connect the depth of the groove and the position of the electron probe with the width of the groove by considering each horizontal line of pixels of the image separately. The greyscale in the dark field STEM images is primarily determined by the atomic number of the material and the thickness of the sample crossed by the electron probe. The former explains the image intensity difference between the silicon dioxide and the gold layers, i.e., lower image intensity for silicon dioxide than gold. In order to determine the position of the interface between the gold and the silicon dioxide, we looked for the steepest change in intensity in each line of pixels. We numerically determined the derivative of the intensity profile for each line, which showed two peaks corresponding to the steepest changes on each interface of the groove. For a perfectly sharp intensity change, i.e., a step function, the derivative will give a Dirac function, while for a more gradual change of intensity the derivative will give a Gaussian-like function. Subsequently, we fitted these two peaks to Gaussian functions and the difference between the centers of these functions gave us the corresponding width of the groove. We quantified the error in the groove width as the sum of the FWHMs of the two Gaussian functions. The errors are plotted as horizontal bars in Figs. 4.17, 4.18, and 4.23(c). This conservative estimate for the error accounts for the convolution of the electron probe profile with the structure [on the order of the spatial resolution of the beam ($\sim$ 0.5 nm)], the surface roughness of the gold surface in the groove, misalignment of the axis of the electron probe compared to the axis of the groove and other sources of indeterminacy such as the possible residues left in the bottom of the groove by the FIB milling.

4.4.4 Experimental results

As mentioned in the introduction to this chapter, we characterize the grooves with a FEI Titan STEM operated at an acceleration voltage of 300 kV. The EELS data were recorded using both automated line-scan acquisition and single-spectrum acquisition, with optimized acquisition times ranging from 80 ms to 2.5 s, where the longer acquisition times were needed close to the groove crevice and also when acquiring spectra through the bulk gold. To further improve the signal-to-noise ratio we summed up to 20 spectra for each measurement point. As described in Sec. 4.1.2, we use the reflected-tail method to remove the ZLP from the spectra, and a nonlinear least-squares fit of a Gaussian function to determine the resonance energy. We performed a detailed analysis of six grooves on the same sample by systematically collecting EELS data from the top to the bottom of the groove. Since the results obtained for these six grooves are very similar [see Fig. 4.17], we focus our discussion on the results for two of the grooves only.

The EELS data along with their corresponding electron probe positions in the groove are displayed in Figs. 4.18(a-b). The EELS data are relatively featureless for a broad range of energies, but do show clear resonance peaks due to the excitation of SP mode(s). As the most prominent feature, we observe that the resonance peak blueshifts from 2.1 eV to approximately 2.6 eV when the position of the electron probe is moved from the top towards the bottom of the groove. This spectral sensitivity to the groove width, especially apparent for small groove widths, is a clear indication that the MIM aGSP mode (which is related to the local width of the groove) is probed in the crevice rather than (global) groove GSP modes, whose peak positions should not depend on the electron position in the groove. This interpretation is supported by simulations in Sec. 4.4.5.

In Fig. 4.18(c) we plot the energy of the resonance peak E as a function of the width W for two different grooves. The plot first shows a slow increase of the resonance

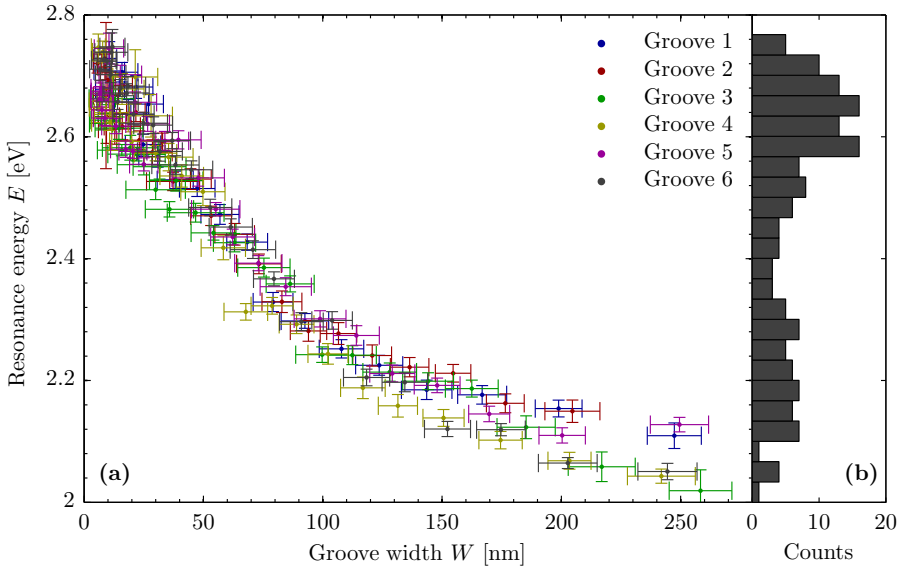

Figure 4.17: **(a)** Measured EELS peak as a function of groove width for six different grooves, confirming the consistency in measurements for other grooves in the same sample. **(b)** Histogram displaying the number of resonance energies within bin intervals of 0.03 eV [projection of data in **(a)** onto the E-axis], corresponding to the average energy error bar size. In Sec. 4.4.4 we focus on two grooves (named grooves 1 and 2).

energy from 2.1 eV to 2.3 eV as the groove width decreases from 250 nm down to 100 nm. This behavior is then followed by a stronger blueshift from 2.3 eV to 2.6 eV for widths decreasing from 100 nm to 5 nm. Numerically calculated EELS data of groove waveguides (to be discussed in Sec. 4.4.5) display the same trend, and we therefore interpret the dependence $E(W)$ as a result of two (spectrally-close) modes being excited simultaneously but with different strengths which depend on the position of the electron probe. For widths $W \gtrsim 100$ nm, the MIM aGSP mode is weakly excited due to the increased distance between the electron and the metal-insulator interfaces. This suggests the excitation of localized SPs supported by the top of the grooves.

Accordingly, the slow increase in resonance energy as the groove width decreases from 250 nm down to 100 nm represents the transition from localized SP excitations to propagating MIM aGSP modes. In the case of groove widths $W \lesssim 100$ nm, on the other hand, the MIM aGSP mode dominates the EELS data, which is signified by the strong dependence of the resonance peak on the groove width. We note that the MIM aGSP resonance energy in the crevice is very close to the measured bulk mode resonance energy of gold [2.7 eV, black solid line in Fig. 4.18(c)], which makes experimentally distinguishing the two modes difficult. For extremely narrow groove widths ($W < 10$ nm) the field delocalization of the electron beam [202] will eventually cause interactions with the bulk plasmons even for perfectly straight grooves. In the real experiment, additional effects of surface roughness of the walls, as well as from the convergence angle of the focused electron probe will be present. The convergence semi-angle is approximately 16 mrad, resulting in the displacement of the electron trajectory from the straight-line path by around 2.5 nm at the exit of the groove

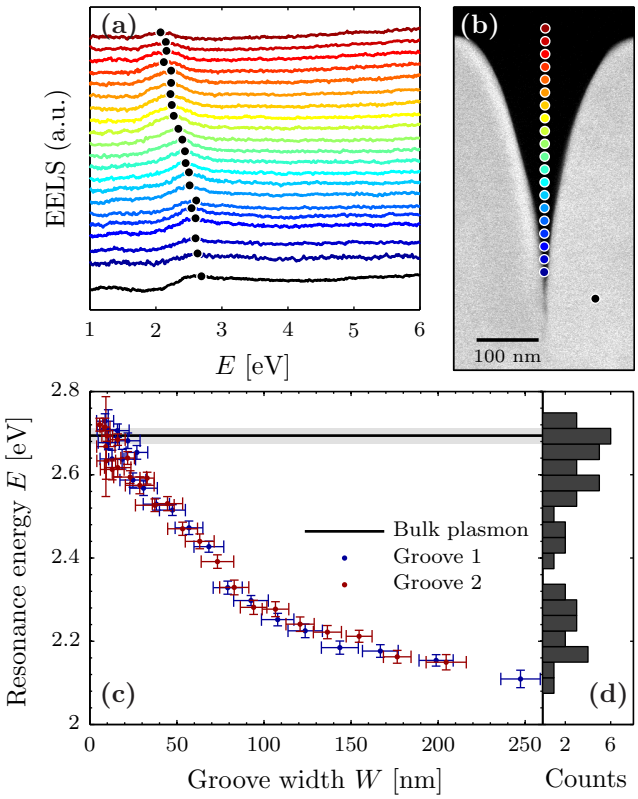

Figure 4.18: **(a)** Waterfall plot of experimental EELS measurements at the corresponding positions indicated on the groove image in **(b)**. The bottom black line displays the experimental EELS spectrum of bulk Au. **(c)** Peak resonance energy as a function of groove width for two different grooves, along with the measured bulk resonance energy of Au (solid black line with grey area displaying the error bar). **(d)** Histogram displaying the number of resonance energies within bin intervals of 0.04 eV [projection of data in **(c)** onto the E-axis]. The bin interval is chosen as the average energy error bar size.

(under the assumption that the focus point of the beam is at the front plane of the groove). Thus, at very narrow widths there is the possibility that both MIM aGSP and bulk plasmons are excited. Owing to the energy resolution of the microscope (0.15 ± 0.05 eV), it therefore becomes increasingly difficult to distinguish between the MIM aGSP resonance energy (at 2.6 eV) and the resonance energy of bulk gold (at 2.7 eV) in the EELS data. In fact, we cannot distinguish the two resonance peaks from a *single* spectrum, since their difference in energy is below the resolution of the microscope. However, depending on the exact position of the electron probe, we can excite one resonance more efficiently than the other, allowing us to determine the energy of one resonance in particular. This effect is visible in the spread of the resonance energies for narrow widths in Fig. 4.18(c), and is also confirmed in the histogram in Fig. 4.18(d). This histogram represents the statistics of all measured energy positions of resonance peaks (in both grooves 1 and 2), i.e. the data points in Fig. 4.18(c) projected onto the energy axis and binned into energy intervals of 0.04 eV.

The histogram shows a larger number of counts both at the resonance energy of the MIM aGSP mode (at 2.6 eV) and at the bulk resonance energy of gold (at 2.7 eV), with a dip in between these energies, thus supporting the interpretation that two different resonances close in energy are present.

The two different grooves in Fig. 4.18(c) show almost identical trends for the EELS peaks, indicating that the shape variation from groove to groove is small. More astonishing is that both grooves support MIM aGSPs in even extremely narrow gaps of only 5 nm. The two energy-shift regions, i.e., the slow increase for $W \gtrsim 100$ nm and the faster increase for $W \lesssim 100$ nm, and the presence of the MIM aGSP close to the bulk resonance energy in ultra-narrow gaps, are also observed for all other grooves studied during this work, see Fig. 4.17. Additionally, note that the interpretation of the EELS peak from the wide part of the grooves ($W \gtrsim 100$ nm) as a localized SP resonance is in agreement with control experiments, in which a thinning of a sample resulted in a blueshift of the EELS peak for the wide region in the top part of the groove (see Sec. 4.4.8), thus representing the expected blueshift of localized SPs for structures with either reduced sizes or decreasing aspect ratios in the direction parallel to the polarization of the applied electric field.

4.4.5 Numerical simulations

To support the interpretation of the experimental EELS data in Figures 4.17 and 4.18, we have performed fully retarded EEL calculations using the commercial software COMSOL Multiphysics. For the numerical analysis we consider the nanogroove structure to be infinite in the direction of the electron beam, i.e., z-direction, which allows us to simplify the problem to 2D. In the calculations, we only model a single unit cell of the one-dimensional groove array, applying periodic boundary conditions to the vertical sides of the cell. The parameters used for the single symmetric unit cell of the groove model in Fig. 4.19(b) are $\Lambda = 317$ nm, $H = 467$ nm, $a = 85$ nm, $r = 60$ nm, $\delta = 0.5$ nm, and $\alpha = 2^\circ$. The lower boundary of the simulation domain, representing the truncation of the optically thick gold substrate, behaves as a perfect electric conductor, while the silicon dioxide glass domain above the grooves is truncated using perfectly matched layers. The electron beam, moving in the z-direction (i.e., the direction of invariance), is modeled as an out-of-plane line current as described by Eq. (4.4). The loss probability pr. length $\Gamma^{\mathrm{2D}}_{\mathrm{EELS}}$, which is proportional to the measured EEL spectra, is then calculated using Eq. (4.9). Although the finite thickness of the sample is thus neglected, we can still expect the 2D approximation to be accurate for narrow groove widths (which is the region of interest) where the width-to-sample thickness ratio is low. Additionally, in the interpretation of the EELS spectra, the 2D approximation allows us to emphasize the importance of *propagating* MIM and groove GSP modes, which are typically properties of extended waveguide structures. Finally, we assume that the groove has perfect mirror symmetry, thereby neglecting any slight geometric asymmetries present in the sample.

The results of the theoretical analysis are summarized in Fig. 4.19. Fig. 4.19(a) shows calculated EELS data at the electron beam positions indicated in Fig. 4.19(b), displaying flat spectra with distinct resonances visible, in accordance with our experimental measurements. Furthermore, the same blueshift trend of the resonance peak is present in our simulations when the position of the electron probe is moved towards the bottom of the groove. The SP resonance shifts from approximately 2.3 eV to 2.5 eV. In Fig. 4.19(d) the black line displays the calculated resonance energy as a function of the groove width. We see that the initial slow blueshift for $W \gtrsim 100$ nm followed by a steep blueshift for $W \lesssim 100$ nm is accurately captured in our theoretical model. Furthermore, for $W \lesssim 50$ nm the calculations show a plateau at the resonance energy of 2.5 eV, which is close to the bulk resonance energy of gold (red dash-dotted

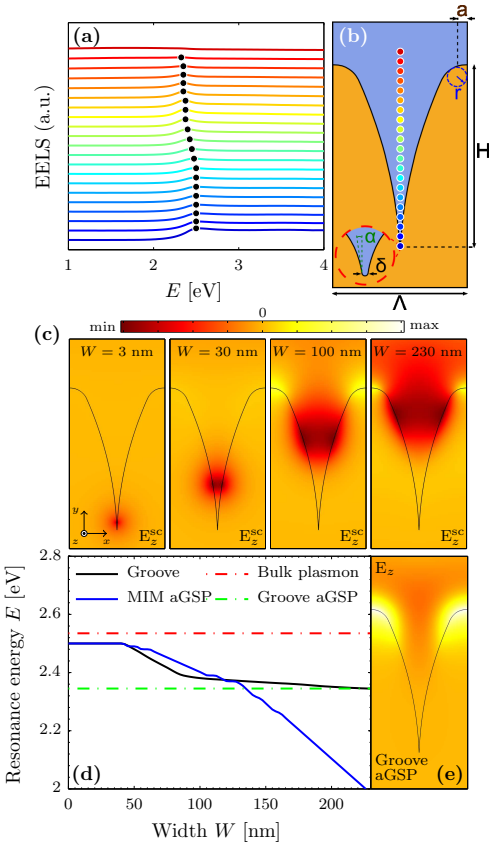

Figure 4.19: **(a)** Waterfall plot of theoretical EELS calculations at the corresponding position indicated on the groove model in **(b)**. **(c)** Longitudinal component of the scattered electric field (total **E**-field subtracted the **E**-field of the electron) for an electron beam probing at the resonance energy of four different groove widths W. **(d)** Peak resonance energy determined from EELS calculations as a function of width for the groove model in **(b)** (black line), MIM (Au-SiO_2-Au) waveguide (blue line), and bulk gold (red dash-dotted line). The green dash-dotted line represents the resonance energy of the groove aGSP mode. **(e)** Longitudinal component of the electric field of the groove aGSP mode at $E = 2.35\,\text{eV}$. Permittivity for gold is taken from Ref. [54]. We use $\varepsilon_{SiO_2} = 2.1$.

line). This is again in excellent agreement with our experimental observations, although the bulk resonance energy of gold from the data in Ref. [54] is slightly lower than the bulk resonance energy of our sample [at 2.7 eV, see Fig. 4.18(c)]. Fig. 4.19(c) displays the longitudinal component of the scattered **E**-field for an electron beam probe at the resonance energy of four different groove widths, demonstrating that the MIM aGSP mode is indeed excited for widths $W \lesssim 100$ nm, as confirmed by the local field distribution in the convex groove. Figure 4.20 complements Fig. 4.19(c) by displaying the induced-charge distributions in the grooves, confirming the symmetric induced-charge distribution and the local nature of the MIM aGSP excitations in the

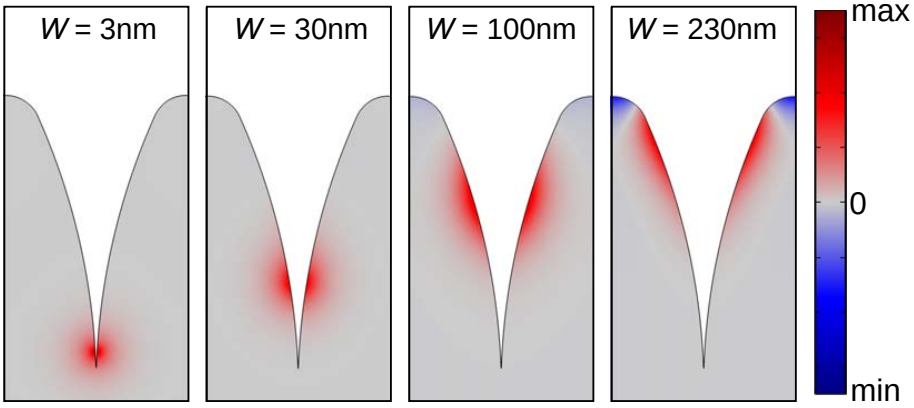

Figure 4.20: The panels show calculations of induced charge distributions in the convex gold groove for the electron beam positioned at four different widths W, but in each case at the corresponding resonance energy. The resonance energies for the four widths $W = 3$, 30, 100, and 230 nm are $E = 2.5$, 2.5, 2.38, and 2.35 eV, respectively. The induced charge distribution is calculated from the requirement of charge conservation, leading to $\rho = -i/\omega \nabla \cdot \mathbf{J}_{\mathrm{ind}}$, where $\mathbf{J}_{\mathrm{ind}} = -i\omega\varepsilon_0(\varepsilon_{\mathrm{m}} - \varepsilon_{\mathrm{d}})\mathbf{E}$ is the induced current, and $\mathbf{E}$ is the electric field in the metal. The induced-charge plots complement Fig. 4.19, confirming that only a local excitation (related to the existence of the MIM aGSP mode) occurs in the crevice of the groove.

crevice of the groove. In contrast, we see a noticeable field distribution at the top of the groove for $W \gtrsim 100$ nm, indicating the excitation of a *groove* aGSP mode and not a MIM aGSP mode. As revealed by mode analysis (see Supplementary Figure 2 of Paper B for details), the groove waveguide under study supports a single groove aGSP mode whose mode profile [Fig. 4.19(e)] agrees well with the field generated by the electrons in the top of the groove. This interpretation is further substantiated by the fact that the energy of the EELS resonance peak in Fig. 4.19(d) approaches the energy of the groove aGSP mode (green dash-dotted line) for large groove widths. In summary, the width dependence of the single peak observed in the *theoretical* EELS data originates from the strong excitation of MIM aGSP modes in the bottom of the groove, with decreasing strength as the electron probe moves up the groove, while at the same time the excitation efficiency of the groove aGSP mode increases. It should be emphasized that the explanations for leveling of the EELS peak dependence for larger groove widths are different for our experimental results [Fig. 4.18(c)] and 2D simulations [Fig. 4.19(d)], since, for the former (as argued in Sec. 4.4.4), this occurs due to the excitation of the localized SP resonance.

4.4.6 Metal-insulator-metal interpretation

To test the analogy between the MIM aGSP mode excited in convex grooves and the corresponding mode in MIM waveguides, we have also performed EELS calculations on the MIM (Au-SiO_2-Au) waveguide. As in the simulations of the groove, we position the electron probe in the center of the MIM waveguide and calculate the resonance energy of the MIM aGSP mode as a function of the width of the insulating layer. The almost identical EELS spectra for the two types of waveguides can be seen in Fig. 4.21 for two different MIM and groove widths (20 nm and 50 nm). We see that the amplitude and peak positions are very similar for the width $W = 50$ nm and become almost identical with decreasing width. Additionally, the induced-charge dis-

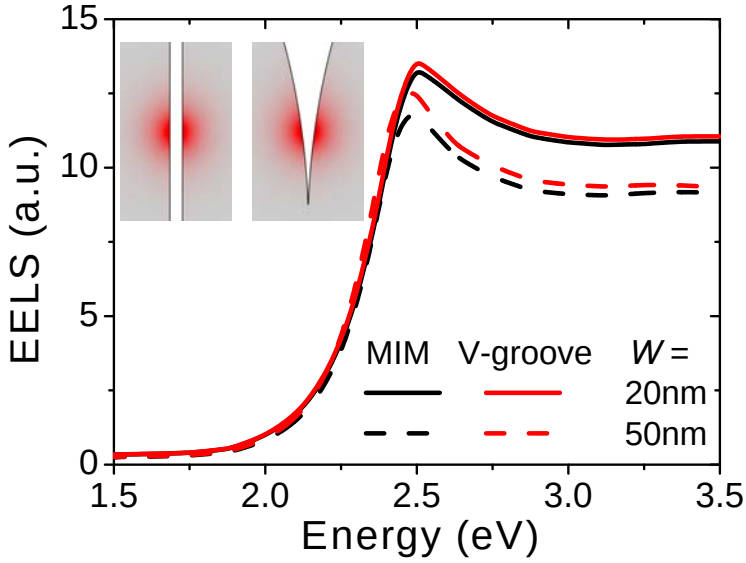

Figure 4.21: EELS calculations for two widths ($W = 20$ nm and 50 nm) of the MIM waveguide and EEL spectra for the electron beam positioned at the corresponding widths in the groove waveguide. EELS spectra are obtained with the electron beam positioned at the center line of the two types of waveguides. It is clear that the two types of waveguides produce almost identical EELS spectra, both with respect to amplitude and peak positioning (including a nearly identical blue shift of the peak positions for narrower gaps) and with very similar induced-charge distributions (see insets).

tributions (shown as insets in Fig. 4.21) are similar, strengthening the interpretation of the MIM aGSP mode being excited in the crevice of the groove. The blue line in Fig. 4.19(d) displays the main result, where we map the resonance energy of the MIM waveguide as a function of width. We see that the energy of the EELS peak is close, for $W \lesssim 125$ nm, to that pertaining to the MIM aGSP mode, becoming identical for $W \lesssim 50$ nm. As discussed in Sec. 4.4.2, we find that the propagation length of the MIM aGSP mode at the resonance energy is around 50 nm for a MIM waveguide with a width of 50 nm. Furthermore, the propagation length decreases with decreasing width, thus supporting the validity of the 2D approximation in our calculations when in the bottom of the groove.

When comparing the experimental EELS measurements with the theoretical groove simulations, we find that the experimentally measured resonance energy spans a broader range (2.1–2.6 eV) compared to the simulations (2.3–2.5 eV). As argued earlier, we attribute the discrepancy at narrow widths ($W \lesssim 50$ nm) to the difference in the permittivity of gold found in Ref. [54] used in our theoretical calculations and the permittivity of the gold in our sample. We substantiate this point of view by the fact that the procedure of thinning the sample using FIB leads to some gallium contamination and surface amorphization of the gold, which (depending on the FIB conditions used) can influence up to tens of nanometers for each of the groove surfaces [253, 254]. Note that despite the fact that this (probably) FIB-related damage affects the gold permittivity in the entire energy range considered, the discrepancy between measurements and 2D simulations at large groove widths ($W \gtrsim 100$ nm) is in any case expected as the EELS peaks are related to physically different phenomena

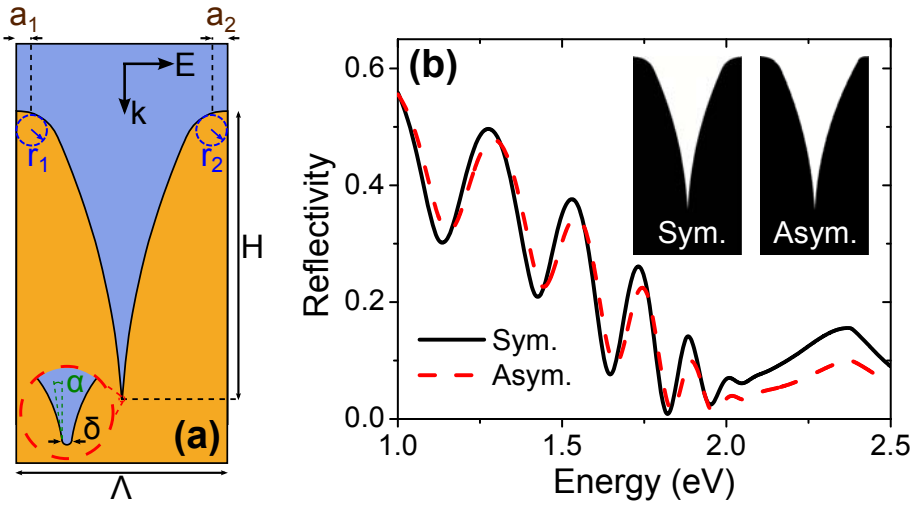

Figure 4.22: **(a)** Geometrical parameters defining the profile of the groove arrays. The small asymmetry in the groove profile is introduced by choosing $a_1 \neq a_2$ and $r_1 \neq r_2$. **(b)** Reflection spectra for normal incident light for a symmetric ($a_1 = a_2 = 85$ nm and $r_1 = r_2 = 60$ nm) and asymmetric ($a_1 = 85$ nm, $a_2 = 50$ nm, $r_1 = 60$ nm, and $r_2 = 20$ nm) groove array. The other parameters are as in Sec. 4.4.5. Inset shows geometric profiles of the considered grooves.

(3D localized SP and 2D groove aGSP mode, respectively).

4.4.7 Optical response from asymmetric groove arrays

The results obtained in the course of our EELS study allow us to add an important element to the interpretation of very efficient and broadband light absorption by ultra-sharp convex grooves in gold, presented in Ref. [246]. The incident light, which propagates downwards (i.e., in the xy-plane) for this purpose, couples through scattering off the groove wedges to the MIM sGSP mode (not probed by our EELS setup), which is adiabatically focused and, consequently, absorbed as it propagates into the depth of the groove. Quite surprisingly, the experimental measurements showed even better light absorption than the simulations in Ref. [246]. Those simulations were based on a completely symmetric groove geometry and (for the most part) normally incident light. However, the grooves are neither perfectly symmetric, as discussed in the context of Fig. 4.16, nor is the light in the experimental setup a perfect plane wave impinging normally to the surface. Thus, incoming light will, due to the inclined propagation and the slight asymmetry of the groove, in practice also couple to the significantly more lossy MIM aGSP mode, which we studied here with EELS. In fact, it was already shown in the supplementary information of Ref. [246] that a small inclined angle ($\sim 20^\circ$) of the incident light moderately improves the overall absorption, which we can now ascribe to excitation of the MIM aGSP mode. To test our hypothesis and to explain the unexpectedly high absorption of 'black gold', we have numerically calculated the light reflection from a symmetric and slightly asymmetric groove array for normal incident light. The introduction of a small asymmetry results in a weak excitation of the MIM aGSP mode, so that the absorption is still dominated by the MIM sGSP mode. Figure 4.22(a) shows a sketch of the groove structure

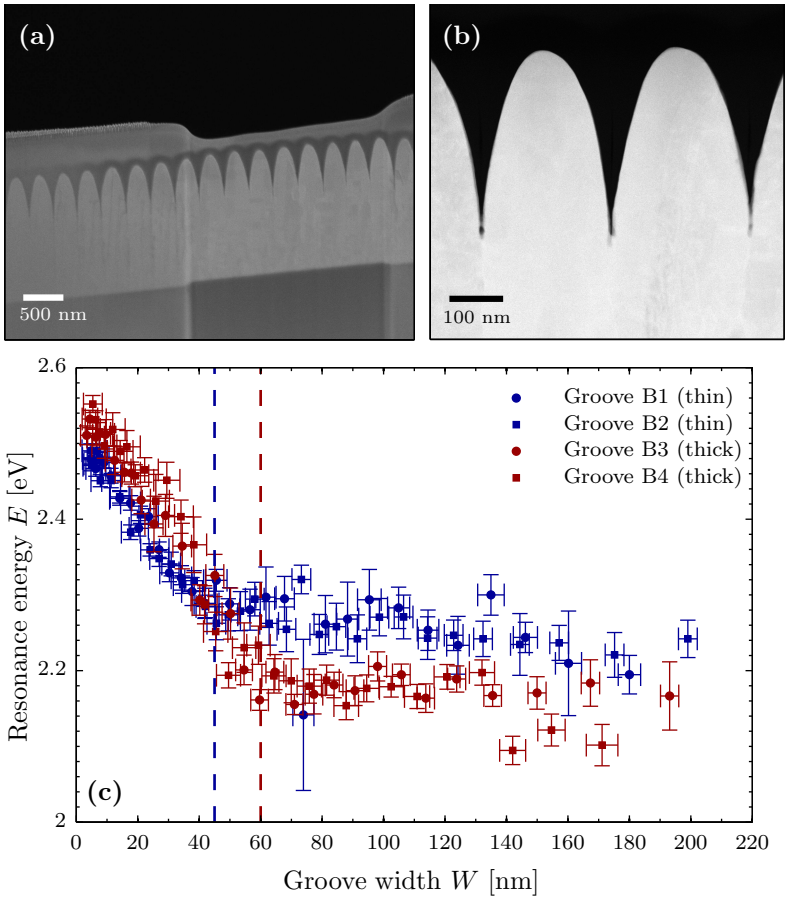

Figure 4.23: **(a)** SEM image of the control sample after thinning further down a 5 µm-wide section. A clear step in thickness separates the thin (right side of the image) and the thick (left side of the image) part of the sample. **(b)** Zoom-in on grooves located in the thin part of the sample. **(c)** Peak resonance energy as a function of groove width for two different grooves belonging to the thin part (grooves B1 and B2) and two other grooves belonging to the thick part (grooves B3 and B4).

and light polarization, while Figure 4.22(b) presents the calculated reflectivity. It is clear that the effect of slight asymmetry mostly affects the energy region $E > 1.7\,\mathrm{eV}$ with an overall lower reflectivity. The increased absorption is particularly noticeable for energies $E > 2\,\mathrm{eV}$, with increases as high as $\sim 40\%$ compared to the symmetric configuration, thus confirming the importance of the MIM aGSP mode to explain the black gold effect observed in Ref. [246].

4.4.8 Control experiment: influence of groove thickness

In this section, we detail additional experiments performed on a thinner sample (i.e., shorter distance parallel to the axis of the groove) to clearly show the nature of the two different types of modes observed in Sec. 4.4.4, i.e., the presence of localized SP modes on top of the groove and MIM aGSP propagating modes in the crevice. With a thinner sample, we study the influence of the thickness on the resonance energies of the groove. For this purpose, we prepared a second sample (denoted control sample in this section) using the same fabrication method as for the main nanogroove sample (described in Sec. 4.4.3). The groove has a similar shape, but with slightly different geometrical parameters. Figure 4.23(a) displays a SEM image of the control sample with a geometry similar to the main sample, but with a periodicity of $\Lambda = 250$ nm, and a height of $H = 340$ nm [Fig. 4.23(b)]. Using the FIB, we thinned down a 5 μm-wide section of the control sample, such that the influence of the sample thickness could be studied, see Fig. 4.23(a).

We performed EELS measurements on the control sample following the same protocol used for the main sample, see Sec. 4.4.4. Additionally we have taken EELS spectra with a larger energy dispersion (from 0 to 100 eV) and used them to estimate the thickness of the thin and the thick regions of the control sample, using both the log-ratio method and Kramers–Kronig analysis [38]. The results show a constant thickness profile inside the groove for both thin and thick regions of the sample with respective thicknesses of approximately 100 nm and 135 nm.

In Fig. 4.23(c) we plot the energy of the resonance peak as a function of the groove width for two different grooves belonging to the thin region (grooves B1 and B2) and for two other grooves belonging to the thick region (grooves B3 and B4). Despite the different geometrical parameters (i.e., periodicity and groove height), we observe the same overall behavior for the resonance energies between the main sample and the control sample, i.e., a weakly blueshifting mode for large widths and a more rapid blueshift for widths below approximately 70 nm. Interestingly, we also see a consistent energy difference between the thick and the thin regions of the control sample for widths above 70 nm. A more thorough analysis shows that the average energy of these modes for the thick region is 2.18 eV while the average energy is 2.24 eV for the thin region (an energy difference that is slightly larger than the average energy error bar: 0.05 eV). This observation is consistent with the blueshift observed in localized SP excitations for structures with either reduced sizes or decreasing aspect ratios in the direction parallel to the polarization of the applied electric field [12].

Moreover, the width at which the blueshift becomes stronger in both parts of the sample is different, as illustrated by the dashed vertical lines in Fig. 4.23(c). The onset of the stronger blueshift appears around 45 nm and 60 nm for the thin and the thick regions, respectively. As mentioned in Sec. 4.4.3, propagating plasmons are only expected for widths smaller than the thickness of the sample, in which case the sample can be considered as a two-dimensional system. Hence, reducing the thickness of the sample should lead to the onset of the propagating mode for smaller widths, as we observe experimentally in Fig. 4.23(c). The fact that the strong blueshift is similar for narrow widths, independent of the exact geometry and thickness of the samples (main sample and control sample), sustains our claim that the modes probed in this region correspond to the propagating MIM aGSP modes.

4.4.9 Concluding remarks

We have reported the application of EELS to the characterization of extremely confined GSP modes excited by electrons in nanometer-wide gaps. Using ultra-sharp convex grooves in gold, we have recorded the EELS data with high spatial (< 1 nm) and energy ($\sim$0.15 eV) resolution in the mirror-symmetry plane of the groove cross

section. Both experimental and theoretical EELS data have revealed resonance behavior associated with the excitation of the *antisymmetric* MIM GSP mode for extremely small gap widths, down to ∼5 nm. We believe that the excitation of this mode, featuring very strong absorption, can be related to the experimental results obtained in the recent study devoted to the phenomenon of plasmonic black gold, in which very efficient and broadband light absorption by ultra-sharp convex grooves has been observed [246]. Since realistically fabricated grooves are not perfectly symmetric, a part of the unexpectedly strong light absorption in the grooves can be ascribed to the MIM aGSP excitation due to fabrication induced asymmetry. The aGSP mode absorption thereby represents an additional (efficient) channel of energy dissipation that should be taken into account in the design of plasmonic nanophotonic circuits and devices.

Chapter 5

Conclusions and outlook

This thesis has been concerned with the theoretical aspects of nonlocal response and the experimental technique EELS. We have studied two models incorporating nonlocal response, the hydrodynamic model and the recently introduced GNOR model, which expands the hydrodynamic model by taking into account the diffusion of electrons. These models have been compared to the local-response approximation, which is commonly employed in the study of optical response of plasmonics systems. We have used EELS to study the localized surface plasmons supported by Ag nanoparticles with diameters ranging from 2 to 30 nm, and propagating gap surface plasmons in gold convex nanogrooves with extremely sharp crevices (down to 5 nm in width).

Specifically, we studied in Chapter 2 the general nonlocal equations governing the electromagnetic response of metals in arbitrary geometries. Without specifying the microscopic origin of the nonlocal response, we showed using a phenomenological approach that nonlocal response modifies the usual Maxwell wave equation by adding an additional Laplacian term, whose strength is proportional to the nonlocal length scale ξ. The presence of curl-free (longitudinal) waves in a nonlocal formalism required an additional boundary condition, which we derived to be the vanishing of the normal component of the induced current in the metal, under the assumption of a constant equilibrium electron density. We then considered two specific models for nonlocal response, the hydrodynamic model and the GNOR model. When comparing the nonlocal length scale ξ for the two models, we found that the two models had a similar frequency-dependent $\mathrm{Re}(\xi)$, but differed in the $\mathrm{Im}(\xi)$. The GNOR model had a considerably larger $\mathrm{Im}(\xi)$ than the hydrodynamic model due to the inclusion of diffusive currents quantified by the diffusion constant D.

In Chapter 3 we compared the two nonlocal models with the LRA in specific plasmonic systems. Firstly, we studied the SPP mode supported by the metal-insulator interface, which in the case of a lossless metal differed significantly from the LRA at the SP frequency. In particular, the nonlocal models showed no asymptote at the SP frequency as in the LRA. Instead a linear increase with $\mathrm{Re}(k)$ was observed in the nonlocal models with a slope proportional to $\mathrm{Re}(\eta)$. Additionally, the GNOR model also showed the same trend for $\mathrm{Im}(k)$ due to the additional loss channel of diffusion. In the realistic cases of metals with finite losses, signatures of nonlocal response were damped due to material losses and the nonlocal models did not differ from the LRA. Secondly, we studied the LSPR of a metal nanosphere. Here, we derived a nonlocal generalization to the Clausius–Mossotti factor and applied the result to calculate the extinction cross section of the sphere. In contrast to the LRA, we found a size-dependence on the LSPR (i.e., blueshift with decreasing size) in both of the nonlocal models and furthermore a size-dependent linewidth broadening (i.e., increase in broadening with decreasing size) in the GNOR model. Importantly, we

hereby showed that the well-known size-dependent broadening observed in nanoparticles several decades ago is in fact a sign of nonlocal response. Thirdly, we examined the optical spectra of a dimer consisting of two infinite nanowires in close proximity. Here, we found a gap-dependent resonance energy (for both nonlocal models) and a gap-dependent linewidth broadening (only for the GNOR model) of the bonding plasmon modes. Comparison of the GNOR spectra with DFT spectra showed very good agreement, thus providing an alternative explanation not based on quantum tunneling to the recent experimental observations on dimers. Additionally, we showed an ultimate limit to the plasmon hybridization due to nonlocal response, which could be described by a simple analytical relation using transformation optics. Fourthly, we studied the extinction cross section of the core-shell nanowire, which surprisingly showed no signature of nonlocal response even in the extreme case of a metal shell with thickness of only 1 nm. We deduced that the lack of dependence on nonlocal response was due to the induced charge distribution of the hybridized mode, which had the positive and negative induced charges separated by a distance given by approximately the diameter of the insulating core (which is much larger than the Ångstrom length scale of nonlocal response). Finally, we studied the absorbance of a thin metal film above the plasma frequency of the metal. We found resonant excitations above the plasma frequency in the hydrodynamic model for Na due to confined curl-free waves in the thin film. These excitations were damped in the GNOR model due to diffusion. In the study of a silver thin film, no resonant excitations were found due to the increased material losses compared to Na, but a slight blueshift of the bulk plasma peak in agreement with experiments was observed in both of the nonlocal models.

Chapter 4 was devoted to the experimental technique of EELS. In this first two sections we provided general experimental and theoretical descriptions of EELS. Afterwards, two EELS experiments and their theoretical interpretation were described. In the first EELS experiment, we studied the size dependence of the LSPR in silver spheres with diameters ranging from 30 nm down to 3.5 nm. Here, we found experimentally a blueshift of the LSPR of approximately 0.5 eV with decreasing particle diameter. The theoretical interpretation of the observations were based on two models, the hydrodynamic model using the derived Clausius–Mossotti factor and a LRA model with a spatially varying equilibrium electron density. Both models showed only qualitative agreement. In an attempt to find quantitative agreement between theory and measurements, we expanded the hydrodynamic model to properly take into account the substrate. Unfortunately the agreement did not improve significantly and we discussed possible reasons for the discrepancy, such as the influence of the electron probe and the inclusion of a spatially varying equilibrium electron density in the hydrodynamic model. In the second EELS experiment, we studied the propagating gap surface plasmon supported by gold convex nanogrooves. We mapped out the energy dependence of the antisymmetric GSP mode as function of groove width, which showed excellent agreement with the numerical simulations. Additionally, support for the theoretical interpretation of the aGSP mode of the groove at given a width being akin to the aGSP mode of the simpler MIM waveguide of the same width was also presented. Finally, it was shown that the optical excitation of the aGSP mode in slightly asymmetric grooves significantly increased the absorption of the structure, providing an additional explanation to the plasmonic black gold effect previously reported.

5.1 Outlook

From a theoretical point-of-view, the next step in modeling the optical response of nanoplasmonic systems could be to incorporate a spatially-varying equilibrium

electron density into the nonlocal response models. Excitingly, Refs. [184, 185] have already presented a path to do this in the hydrodynamic model. At a first glance, the addition of electron diffusion into the models of Refs. [184, 185] should not pose additional computational efforts. Such a model, i.e., GNOR with spatially-varying static electron density, should be able to account for all of the non-classical phenomena mentioned in the Introduction. Additionally, it might account for the large blueshift of the LSPR experimentally observed in Sec. 4.3.

On the experimental side, there is definitely need for more studies of small metal nanoparticles with EELS. Mapping of the LSPR with size for other metals, such as gold or aluminum, could provide insight into the size-dependency mechanism observed for silver. Another approach could be to experimentally rule out the effect of the substrate by studying silver (or other metal) nanoparticles encapsulated in a dielectric. Such a system is also theoretically simpler to describe, as it should be quite well approximated by a particle in a homogeneous embedding material.

While the majority of EELS experiments have been on the study of LSPs, there are significantly less studies of propagating surface plasmons, in particular for the case when the electron beam is parallel to direction of invariance. Thus, it seems that a vast category of geometries (i.e., extended structures with different cross sections) and their associated modes are left unexplored. The interesting part of studying translationally invariant structures is the direct connection between the EEL signal and the LDOS, as discussed in Sec. 4.2. Systematic mapping of the EEL signal of extended structures could thus be used as a fingerprint of the LDOS, which in the future perhaps could be utilized for the precise positioning of quantum emitters.

References

[1] R. H. Ritchie, 'Plasma losses by fast electrons in thin films', Phys. Rev. **106**, 874 (1957).

[2] E. Prodan, C. Radloff, N. Halas, and P. Nordlander, 'A hybridization model for the plasmon response of complex nanostructures', Science **302**, 419 (2003).

[3] D. K. Gramotnev and S. I. Bozhevolnyi, 'Plasmonics beyond the diffraction limit', Nature Photon. **4**, 83 (2010).

[4] D. K. Gramotnev and S. I. Bozhevolnyi, 'Nanofocusing of electromagnetic radiation', Nature Photon. **8**, 14 (2014).

[5] E. Hao and G. C. Schatz, 'Electromagnetic fields around silver nanoparticles and dimers', J. Chem. Phys. **120**, 357 (2004).

[6] O. Vazquez-Mena, T. Sannomiya, L. Villanueva, J. Voros, and J. Brugger, 'Metallic nanodot arrays by stencil lithography for plasmonic biosensing applications', ACS Nano **5**, 844 (2011).

[7] S. Lal, S. Clare, and J. Halas, 'Nanoshell-enabled photothermal cancer therapy: impending clinical impact', Acc. Chem. Res. **41**, 1842 (2008).

[8] S. I. Bozhevolnyi, V. S. Volkov, E. Devaux, J.-Y. Laluet, and T. W. Ebbesen, 'Channel plasmon subwavelength waveguide components including interferometers and ring resonators', Nature **440**, 508 (2006).

[9] R. Zia, J. A. Schuller, A. Chandran, and M. L. Brongersma, 'Plasmonics: the next chip-scale technology', Mater. Today **9**, 20 (2006).

[10] E. B. Guidez and C. M. Aikens, 'Quantum mechanical origin of the plasmon: from molecular systems to nanoparticles', Nanoscale **6**, 11512 (2014).

[11] S. A. Maier, *Plasmonics: Fundamentals and Applications* (Springer, New York, 2007).

[12] L. Novotny and B. Hecht, *Principles of nano-optics* (Cambridge University Press, Cambridge, 2012), 2 edition.

[13] H. Duan, A. I. Fernández-Domínguez, M. Bosman, S. A. Maier, and J. K. W. Yang, 'Nanoplasmonics: classical down to the nanometer scale', Nano Lett. **12**, 1683 (2012).

[14] U. Kreibig and L. Genzel, 'Optical absorption of small metallic particles', Surf. Sci. **156**, 678 (1985).

[15] U. Kreibig and M. Vollmer, *Optical Properties of Metal Clusters* (Springer-Verlag, Berlin, 1995).

[16] U. Kreibig and C. von Fragstein, 'The limitation of electron mean free path in small silver particles', Z. Phys. **224**, 307 (1969).

[17] J. Tiggesbäumker, L. Köller, K.-H. Meiwes-Broer, and A. Liebsch, 'Blue shift of the Mie plasma frequency in Ag clusters and particles', Phys. Rev. A **48**, R1749 (1993).

[18] K. P. Charlé, L. König, S. Nepijko, I. Rabin, and W. Schulze, 'The surface plasmon resonance of free and embedded Ag-clusters in the size range 1.5 nm $<$ D $<$ 30 nm', Cryst. Res. Technol. **33**, 1085 (1998).

[19] J. A. Scholl, A. L. Koh, and J. A. Dionne, 'Quantum plasmon resonances of individual metallic nanoparticles', Nature **483**, 421 (2012).

[20] S. Raza, N. Stenger, S. Kadkhodazadeh, S. V. Fischer, N. Kostesha, A.-P. Jauho, A. Burrows, M. Wubs, and N. A. Mortensen, 'Blueshift of the surface plasmon resonance in silver nanoparticles studied with EELS', Nanophotonics **2**, 131 (2013).

[21] K.-D. Tsuei, E. W. Plummer, A. Liebsch, K. Kempa, and P. Bakshi, 'Multipole plasmon modes at a metal surface', Phys. Rev. Lett. **64**, 44 (1990).

[22] A. Bennett, 'Influence of the electron charge distribution on surface-plasmon dispersion', Phys. Rev. B **1**, 203 (1970).

[23] A. Boardman, B. Paranjape, and R. Teshima, 'The effect of structure on surface plasmons', Surf. Sci. **49**, 275 (1975).

[24] I. Lindau and P. O. Nilsson, 'Experimental evidence for excitation of longitudinal plasmons by photons', Phys. Lett. A **31A**, 352 (1970).

[25] M. Anderegg, B. Feuerbacher, and B. Fitton, 'Optically excited longitudinal plasmons in potassium', Phys. Rev. Lett. **27**, 1565 (1971).

[26] C. Ciracì, R. T. Hill, J. J. Mock, Y. Urzhumov, A. I. Fernández-Domínguez, S. A. Maier, J. B. Pendry, A. Chilkoti, and D. R. Smith, 'Probing the ultimate limits of plasmonic enhancement', Science **337**, 1072 (2012).

[27] K. J. Savage, M. M. Hawkeye, R. Esteban, A. G. Borisov, J. Aizpurua, and J. J. Baumberg, 'Revealing the quantum regime in tunnelling plasmonics', Nature **491**, 574 (2012).

[28] J. Kern, S. Grossmann, N. V. Tarakina, T. Häckel, M. Emmerling, M. Kamp, J.-S. Huang, P. Biagioni, J. Prangsma, and B. Hecht, 'Atomic-scale confinement of resonant optical fields', Nano Lett. **12**, 5504 (2012).

[29] J. A. Scholl, A. Garcia-Etxarri, A. L. Koh, and J. A. Dionne, 'Observation of quantum tunneling between two plasmonic nanoparticles', Nano Lett. **13**, 564 (2013).

[30] H. Cha, J. H. Yoon, and S. Yoon, 'Probing quantum plasmon coupling using gold nanoparticle dimers with tunable interparticle distances down to the subnanometer range', ACS Nano **8**, 8554 (2014).

[31] S. F. Tan, L. Wu, J. K. Yang, P. Bai, M. Bosman, and C. A. Nijhuis, 'Quantum plasmon resonances controlled by molecular tunnel junctions', Science **343**, 1496 (2014).

[32] K. Andersen, K. L. Jensen, N. A. Mortensen, and K. S. Thygesen, 'Visualizing hybridized quantum plasmons in coupled nanowires: From classical to tunneling regime', Phys. Rev. B **87**, 235433 (2013).

[33] A. Boardman, *Electromagnetic surface modes. Hydrodynamic theory of plasmon-polaritons on plane surfaces.* (John Wiley and Sons, Chichester, 1982).

[34] N. A. Mortensen, S. Raza, M. Wubs, T. Søndergaard, and S. I. Bozhevolnyi, 'A generalized nonlocal optical response theory for plasmonic nanostructures', Nat. Commun. **5**, 3809 (2014).

[35] C. J. Powell and J. B. Swan, 'Origin of the characteristic electron energy losses in aluminum', Phys. Rev. **115**, 869 (1959).

[36] E. A. Stern and R. A. Ferrell, 'Surface plasma oscillations of a degenerate electron gas', Phys. Rev. **120**, 130 (1960).

[37] F. J. García de Abajo, 'Optical excitations in electron microscopy', Rev. Mod. Phys. **82**, 209 (2010).

[38] R. F. Egerton, *Electron Energy Loss Spectroscopy in the Electron Microscope* (New York: Springer, 2011), 3. edition.

[39] O. Nicoletti, F. de la Peña, R. K. Leary, D. J. Holland, C. Ducati, and P. A. Midgley, 'Three-dimensional imaging of localized surface plasmon resonances of metal nanoparticles', Nature **502**, 80 (2013).

[40] J. Nelayah, M. Kociak, O. Stephan, F. J. García de Abajo, M. Tence, L. Henrard, D. Taverna, I. Pastoriza-Santos, L. M. Liz-Marzan, and C. Colliex, 'Mapping surface plasmons on a single metallic nanoparticle', Nature Phys. **3**, 348 (2007).

[41] M. Bosman, V. J. Keast, M. Watanabe, A. I. Maaroof, and M. B. Cortie, 'Mapping surface plasmons at the nanometre scale with an electron beam', Nanotechnology **18**, 165505 (2007).

[42] J. Aizpurua, P. Hanarp, D. S. Sutherland, M. Käll, G. W. Bryant, and F. J. García de Abajo, 'Optical properties of gold nanorings', Phys. Rev. Lett. **90**, 057401 (2003).

[43] F. J. García de Abajo, 'Colloquium: Light scattering by particle and hole arrays', Rev. Mod. Phys. **79**, 1267 (2007).

[44] T. Ergin, N. Stenger, P. Brenner, J. B. Pendry, and M. Wegener, 'Three-dimensional invisibility cloak at optical wavelengths', Science **328**, 337 (2010).

[45] B. Schaffer, U. Hohenester, A. Trügler, and F. Hofer, 'High-resolution surface plasmon imaging of gold nanoparticles by energy-filtered transmission electron microscopy', Phys. Rev. B **79**, 041401 (2009).

[46] A. L. Koh, A. I. Fernández-Domínguez, D. W. McComb, S. A. Maier, and J. K. W. Yang, 'High-resolution mapping of electron-beam-excited plasmon modes in lithographically defined gold nanostructures', Nano Lett. **11**, 1323 (2011).

[47] O. Nicoletti, M. Wubs, N. A. Mortensen, W. Sigle, P. A. van Aken, and P. A. Midgley, 'Surface plasmon modes of a single silver nanorod: an electron energy loss study', Opt. Express **19**, 15371 (2011).

[48] C. E. Hofmann, E. J. R. Vesseur, L. A. Sweatlock, H. J. Lezec, F. J. García de Abajo, A. Polman, and H. A. Atwater, 'Plasmonic modes of annular nanoresonators imaged by spectrally resolved cathodoluminescence', Nano Lett. **7**, 3612 (2007).

[49] M. Kuttge, E. J. R. Vesseur, A. F. Koenderink, H. J. Lezec, H. A. Atwater, F. J. García de Abajo, and A. Polman, 'Local density of states, spectrum, and far-field interference of surface plasmon polaritons probed by cathodoluminescence', Phys. Rev. B **79**, 113405 (2009).

[50] M. Schnell, A. García-Etxarri, A. J. Huber, K. Crozier, J. Aizpurua, and R. Hillenbrand, 'Controlling the near-field oscillations of loaded plasmonic nanoantennas', Nature Photon. **3**, 287 (2009).

[51] J. Chen, M. Badioli, P. Alonso-Gonzalez, S. Thongrattanasiri, F. Huth, J. Osmond, M. Spasenovic, A. Centeno, A. Pesquera, P. Godignon, A. Zurutuza Elorza, N. Camara, F. J. García de Abajo, R. Hillenbrand, and F. H. L. Koppens, 'Optical nano-imaging of gate-tunable graphene plasmons', Nature **487**, 77 (2012).

[52] N. W. Ashcroft and N. D. Mermin, *Solid State Physics* (Saunders College Publishing, Fort Worth, 1976).

[53] A. D. Rakić, A. B. Djurišić, J. M. Elazar, and M. L. Majewski, 'Optical properties of metallic films for vertical-cavity optoelectronic devices', Appl. Opt. **37**, 5271 (1998).

[54] P. B. Johnson and R. W. Christy, 'Optical constants of the noble metals', Phys. Rev. B **6**, 4370 (1972).

[55] F. Hao and P. Nordlander, 'Efficient dielectric function for FDTD simulation of the optical properties of silver and gold nanoparticles', Chem. Phys. Lett. **446**, 115 (2007).

[56] N. A. Mortensen, 'Nonlocal formalism for nanoplasmonics: phenomenological and semi-classical considerations', Phot. Nanostr. **11**, 303 (2013).

[57] P. Ginzburg and A. Zayats, 'Localized surface plasmon resonances in spatially dispersive nano-objects: phenomenological treatise', ACS Nano **7**, 4334 (2013).

[58] J. B. Pendry, A. Aubry, D. R. Smith, and S. A. Maier, 'Transformation optics and subwavelength control of light', Science **337**, 549 (2012).

[59] A. D. Boardman, B. V. Paranjape, and Y. O. Nakamura, 'Surface plasmon-polaritons in a spatially dispersive inhomogeneous media', Phys. Stat. Sol. (b) **75**, 347 (1976).

[60] A. D. Boardman and B. V. Paranjape, 'The optical surface modes of metal spheres', J. Phys. F: Met. Phys. **7**, 1935 (1977).

[61] S. Raza, G. Toscano, A.-P. Jauho, M. Wubs, and N. A. Mortensen, 'Unusual resonances in nanoplasmonic structures due to nonlocal response', Phys. Rev. B **84**, 121412(R) (2011).

[62] S. Raza, T. Christensen, M. Wubs, S. I. Bozhevolnyi, and N. A. Mortensen, 'Nonlocal response in thin-film waveguides: Loss versus nonlocality and breaking of complementarity', Phys. Rev. B **88**, 115401 (2013).

[63] D. J. Griffiths, *Introduction to Electrodynamics* (Benjamin Cummings, 1998), 3 edition.

[64] A. R. Melnyk and M. J. Harrison, 'Theory of optical excitation of plasmons in metals', Phys. Rev. B **2**, 835 (1970).

[65] F. Sauter, 'Der Einfluß von Plasmawellen auf das Reflexionsvermögen von Metallen (I)', Z. Phys. **203**, 488 (1967).

[66] F. Forstmann and H. Stenschke, 'Electrodynamics at metal boundaries with inclusion of plasma waves', Phys. Rev. Lett. **38**, 1365 (1977).

[67] A. D. Boardman and R. Ruppin, 'The boundary conditions between spatially dispersive media', Surf. Sci. **112**, 153 (1981).

[68] P. Jewsbury, 'Electrodynamic boundary conditions at metal interfaces', J. Phys. F: Met. Phys. **11**, 195 (1981).

[69] J. M. McMahon, S. K. Gray, and G. C. Schatz, 'Nonlocal optical response of metal nanostructures with arbitrary shape', Phys. Rev. Lett. **103**, 097403 (2009).

[70] G. Toscano, S. Raza, A.-P. Jauho, N. A. Mortensen, and M. Wubs, 'Modified field enhancement and extinction in plasmonic nanowire dimers due to nonlocal response', Opt. Express **20**, 4176 (2012).

[71] K. R. Hiremath, L. Zschiedrich, and F. Schmidt, 'Numerical solution of nonlocal hydrodynamic Drude model for arbitrary shaped nano-plasmonic structures using Nédélec finite elements', J. Comp. Phys. **231**, 5890 (2012).

[72] X. Chen, H.-R. Park, M. Pelton, X. Piao, N. C. Lindquist, H. Im, Y. J. Kim, J. S. Ahn, K. J. Ahn, N. Park, D.-S. Kim, and S.-H. Oh, 'Atomic layer lithography of wafer-scale nanogap arrays for extreme confinement of electromagnetic waves', Nat. Commun. **4**, 2361 (2014).

[73] F. Bloch, 'Bremsvermögen von Atomen mit mehreren Elektronen', Z. Phys. A **81**, 363 (1933).

[74] G. Barton, 'Some surface effects in the hydrodynamic model of metals', Rep. Prog. Phys. **42**, 963 (1979).

[75] I. Tokatly and O. Pankratov, 'Hydrodynamic theory of an electron gas', Phys. Rev. B **60**, 15550 (1999).

[76] H. Jensen, 'Eigenschwingungen eines Fermi-Gases und Anwendung auf die Blochsche Bremsformel für schnelle Teilchen', Z. Phys. **106**, 620 (1937).

[77] S. C. Ying, 'Hydrodynamic response of inhomogeneous metallic systems', Il Nuovo Cimento **23**, 270 (1974).

[78] A. Eguiluz and J. Quinn, 'Hydrodynamic model for surface plasmons in metals and degenerate semiconductors', Phys. Rev. B **14**, 1347 (1976).

[79] A. Eguiluz, S. Ying, and J. Quinn, 'Influence of the electron density profile on surface plasmons in a hydrodynamic model', Phys. Rev. B **11**, 2118 (1975).

[80] R. Ruppin, 'Optical properties of a plasma sphere', Phys. Rev. Lett. **31**, 1434 (1973).

[81] R. Ruppin, 'Optical properties of small metal spheres', Phys. Rev. B **11**, 2871 (1975).

[82] G. Aers, B. Paranjape, and A. Boardman, 'The surface plasmon modes of spherical voids in irradiated metals', J. Phys. Chem. Solids **40**, 319 (1979).

[83] G. C. Aers, A. D. Boardman, and B. V. Paranjape, 'Non-radiative surface plasmon-polariton modes of inhomogeneous metal circular-cylinders', J. Phys. F: Met. Phys. **10**, 53 (1980).

[84] R. Ruppin, 'Optical properties of a spatially dispersive cylinder', J. Opt. Soc. Am. B **6**, 1559 (1989).

[85] F. Forstmann and H. Stenschke, 'Dispersion of plasmons at the surface of a metal and at the interface between two metals', Phys. Rev. B **17**, 1489 (1978).

[86] J. M. McMahon, S. K. Gray, and G. C. Schatz, 'Calculating nonlocal optical properties of structures with arbitrary shape', Phys. Rev. B **82**, 035423 (2010).

[87] J. M. McMahon, S. K. Gray, and G. C. Schatz, 'Optical properties of nanowire dimers with a spatially nonlocal dielectric function', Nano Lett. **10**, 3473 (2010).

[88] J. M. McMahon, S. K. Gray, and G. C. Schatz, 'Nonlocal dielectric effects in core-shell nanowires', J. Phys. Chem. C **114**, 15903 (2010).

[89] G. Toscano, S. Raza, S. Xiao, M. Wubs, A.-P. Jauho, S. I. Bozhevolnyi, and N. A. Mortensen, 'Surface-enhanced Raman spectroscopy: nonlocal limitations', Opt. Lett. **37**, 2538 (2012).

[90] G. Toscano, S. Raza, W. Yan, C. Jeppesen, S. Xiao, M. Wubs, A.-P. Jauho, S. I. Bozhevolnyi, and N. A. Mortensen, 'Nonlocal response in plasmonic waveguiding with extreme light confinement', Nanophotonics **2**, 161 (2013).

[91] A. I. Fernández-Domínguez, A. Wiener, F. J. García-Vidal, S. A. Maier, and J. B. Pendry, 'Transformation-optics description of nonlocal effects in plasmonic nanostructures', Phys. Rev. Lett. **108**, 106802 (2012).

[92] A. I. Fernández-Domínguez, P. Zhang, Y. Luo, S. A. Maier, F. J. García-Vidal, and J. B. Pendry, 'Transformation-optics insight into nonlocal effects in separated nanowires', Phys. Rev. B **86**, 241110 (2012).

[93] A. I. Fernández-Domínguez, Y. Luo, A. Wiener, J. B. Pendry, and S. A. Maier, 'Theory of three-dimensional nanocrescent light harvesters', Nano Lett. **12**, 5946 (2012).

[94] I. Villó-Pérez and N. R. Arista, 'Hydrodynamical model for bulk and surface plasmons in cylindrical wires', Surf. Sci. **603**, 1 (2009).

[95] W. Yan, N. A. Mortensen, and M. Wubs, 'Green's function surface-integral method for nonlocal response of plasmonic nanowires in arbitrary dielectric environments', Phys. Rev. B **88**, 155414 (2013).

[96] S. Raza, G. Toscano, A.-P. Jauho, N. A. Mortensen, and M. Wubs, 'Refractive-index sensing with ultrathin plasmonic nanotubes', Plasmonics **8**, 193 (2013).

[97] A. Moradi and E. Ebrahimi, 'Plasmon spectra of cylindrical nanostructures including nonlocal effects', Plasmonics **9**, 209 (2014).

[98] A. Wiener, A. I. Fernández-Domínguez, A. P. Horsfield, J. B. Pendry, and S. A. Maier, 'Nonlocal effects in the nanofocusing performance of plasmonic tips', Nano Lett. **12**, 3308 (2012).

[99] R. Ruppin, 'Effect of non-locality on nanofocusing of surface plasmon field intensity in a conical tip', Phys. Lett. A **340**, 299 (005).

[100] C. Ciracì, E. Poutrina, M. Scalora, and D. R. Smith, 'Origin of second-harmonic generation enhancement in optical split-ring resonators', Phys. Rev. B **85**, 201403 (2012).

[101] C. Ciracì, E. Poutrina, M. Scalora, and D. R. Smith, 'Second-harmonic generation in metallic nanoparticles: clarification of the role of the surface', Phys. Rev. B **86**, 115451 (2012).

[102] C. David and F. J. García de Abajo, 'Spatial nonlocality in the optical response of metal nanoparticles', J. Phys. Chem. C **115**, 19470 (2011).

[103] C. Ciracì, Y. Urzhumov, and D. R. Smith, 'Effects of classical nonlocality on the optical response of three-dimensional plasmonic nanodimers', J. Opt. Soc. Am. B **30**, 2731 (2013).

[104] A. Moreau, C. Ciracì, and D. R. Smith, 'Impact of nonlocal response on metallodielectric multilayers and optical patch antennas', Phys. Rev. B **87**, 045401 (2013).

[105] A. Wiener, A. I. Fernández-Domínguez, J. B. Pendry, A. P. Horsfield, and S. A. Maier, 'Nonlocal propagation and tunnelling of surface plasmons in metallic hourglass waveguides', Opt. Express **21**, 27509 (2013).

[106] D. de Ceglia, S. Campione, M. A. Vincenti, F. Capolino, and M. Scalora, 'Low-damping epsilon-near-zero slabs: nonlinear and nonlocal optical properties', Phys. Rev. B **87**, 155140 (2013).

[107] C. David, N. A. Mortensen, and J. Christensen, 'Perfect imaging, epsilon-near zero phenomena and waveguiding in the scope of nonlocal effects', Sci. Rep. **3**, 2526 (2013).

[108] J. Sun, Y. Huang, and L. Gao, 'Nonlocal composite media in calculations of the Casimir force', Phys. Rev. A **89**, 012508 (2014).

[109] W. Yan, M. Wubs, and N. A. Mortensen, 'Hyperbolic metamaterials: nonlocal response regularizes broadband supersingularity', Phys. Rev. B **86**, 205429 (2012).

[110] W. Yan, N. A. Mortensen, and M. Wubs, 'Hyperbolic metamaterial lens with hydrodynamic nonlocal response', Opt. Express **21**, 15026 (2013).

[111] A. Yanai, N. A. Mortensen, and U. Levy, 'Absorption and eigenmode calculation for one-dimensional periodic metallic structures using the hydrodynamic approximation', Phys. Rev. B **88**, 205120 (2013).

[112] A. Wiener, H. Duan, M. Bosman, A. P. Horsfield, J. B. Pendry, J. K. W. Yang, S. A. Maier, and A. I. Fernández-Domínguez, 'Electron-energy loss study of nonlocal effects in connected plasmonic nanoprisms', ACS Nano **7**, 6287 (2013).

[113] T. Christensen, W. Yan, S. Raza, A.-P. Jauho, N. A. Mortensen, and M. Wubs, 'Nonlocal response of metallic nanospheres probed by light, electrons, and atoms', ACS Nano **8**, 1745 (2014).

[114] T. V. Teperik, P. Nordlander, J. Aizpurua, and A. G. Borisov, 'Robust subnanometric plasmon ruler by rescaling of the nonlocal optical response', Phys. Rev. Lett. **110**, 263901 (2013).

[115] T. V. Teperik, P. Nordlander, J. Aizpurua, and A. G. Borisov, 'Quantum effects and nonlocality in strongly coupled plasmonic nanowire dimers', Opt. Express **21**, 27306 (2013).

[116] L. Stella, P. Zhang, F. J. García-Vidal, A. Rubio, and P. García-González, 'Performance of nonlocal optics when applied to plasmonic nanostructures', J. Phys. Chem. C **117**, 8941 (2013).

[117] J. M. Pitarke, V. M. Silkin, E. V. Chulkov, and P. M. Echenique, 'Theory of surface plasmons and surface plasmon polaritons', Rep. Prog. Phys. **70**, 1 (2007).

[118] S. C. Ying, J. R. Smith, and W. Kohn, 'Self-consistent screening of charges embedded in a metal surface', Journ. Vac. Sci. Tech. **9**, 575 (1972).

[119] C. Weizsäcker, 'Zur Theorie der Kernmassen', Z. Phys. **96**, 431 (1935).

[120] H. Bruus, *Theoretical Microfluidics*, volume 18 of *Oxford Master Series in Condensed Matter Physics* (Oxford University Press, Oxford, 2008).

[121] F. J. García de Abajo, 'Nonlocal effects in the plasmons of strongly interacting nanoparticles, dimers, and waveguides', J. Phys. Chem. C **112**, 17983 (2008).

[122] G. W. Hanson, 'Drift-diffusion: a model for teaching spatial-dispersion concepts and the importance of screening in nanoscale structures', IEEE Antennas Propag. Mag. **52**, 198 (2010).

[123] H. Raether, *Surface Plasmons on Smooth and Rough Surfaces and on Gratings* (Springer-Verlag, 1988).

[124] P. J. Feibelman, 'Surface electromagnetic fields', Prog. Surf. Sci. **12**, 287 (1982).

[125] P. Apell and Å. Ljungbert, 'Red shift of surface plasmons in small metal particles', Solid State Commun. **44**, 1367 (1982).

[126] P. Apell and Å. Ljungbert, 'A general non-local theory for the electromagnetic response of a small metal particle', Phys. Scripta **26**, 113 (1982).

[127] R. C. Monreal, T. J. Antosiewicz, and S. P. Apell, 'Competition between surface screening and size quantization for surface plasmons in nanoparticles', New J. Phys. **15**, 083044 (2013).

[128] P. Ascarelli and M. Cini, '"Red shift" of the surface plasmon resonance absorption by fine metal particles', Solid State Commun. **18**, 385 (1976).

[129] W. Ekardt, 'Dynamical polarizability of small metal particles: self-consistent spherical jellium background model', Phys. Rev. Lett. **52**, 1925 (1984).

[130] D. E. Beck, 'Self-consistent calculation of the collective excitations in neutral and charged jellium microspheres', Phys. Rev. B **43**, 7301 (1991).

[131] A. Liebsch, 'Surface-plasmon dispersion and size dependence of Mie resonance: silver versus simple metals', Phys. Rev. B **48**, 11317 (1993).

[132] J. G. Pedersen, S. Xiao, and N. A. Mortensen, 'Limits of slow light in photonic crystals', Phys. Rev. B **78**, 153101 (2008).

[133] A. B. Yakovlev and G. W. Hanson, 'Mode-transformation and mode-continuation regimes on waveguiding structures', IEEE Trans. Microwave Theory Tech. **48**, 67 (2000).

[134] K. Andersen, K. W. Jacobsen, and K. S. Thygesen, 'Spatially resolved quantum plasmon modes in metallic nano-films from first-principles', Phys. Rev. B **86**, 245129 (2012).

[135] R. Ruppin, 'Non-local optics of the near field lens', J. Phys. Condens. Matter **17**, 1803 (2005).

[136] G. Mie, 'Articles on the optical characteristics of turbid tubes, especially colloidal metal solutions', Ann. Phys. **25**, 377 (1908).

[137] H. C. van de Hulst, *Light scattering by small particles* (Dover Publications, Inc., New York, 1981).

[138] C. F. Bohren and D. R. Huffman, *Absorption and Scattering of Light by Small Particles* (John Wiley & Sons, Inc., New York, 1983).

[139] B. B. Dasgupta and R. Fuchs, 'Polarizability of a small sphere including nonlocal effects', Phys. Rev. B **24**, 554 (1981).

[140] R. Fuchs and F. Claro, 'Multipolar response of small metallic spheres: nonlocal theory', Phys. Rev. B **35**, 3722 (1987).

[141] J. Crowell and R. H. Ritchie, 'Radiative decay of Coulomb-stimulated plasmons in spheres', Phys. Rev. **172**, 436 (1968).

[142] W. Ekardt, 'Work function of small metal particles: self-consistent spherical jellium-background model', Phys. Rev. B **29**, 1558 (1984).

[143] W. Ekardt, 'Size-dependent photoabsorption and photoemission of small metal particles', Phys. Rev. B **31**, 6360 (1985).

[144] W. Ekardt, 'Collective multipole excitations in small metal particles: critical angular momentum l^{cr} for the existence of collective surface modes', Phys. Rev. B **32**, 1961 (1985).

[145] J. D. Jackson, *Classical electrodynamics* (Wiley, 1998), 3 edition.

[146] F. Wang and Y. R. Shen, 'General properties of local plasmons in metal nanostructures', Phys. Rev. Lett. **97**, 206806 (2006).

[147] P. Apell and D. R. Penn, 'Optical properties of small metal spheres: surface effects', Phys. Rev. Lett. **50**, 1316 (1983).

[148] Y. Luo, A. I. Fernández-Domínguez, A. Wiener, S. A. Maier, and J. B. Pendry, 'Surface plasmons and nonlocality: a simple model', Phys. Rev. Lett. **111**, 093901 (2013).

[149] K.-P. Charlé, F. Frank, and W. Schulze, 'The optical properties of silver microcrystallites in dependence on size and the influence of the matrix environment', Ber. Bunsenges. Phys. Chem. **88**, 350 (1984).

[150] K.-P. Charlé, W. Schulze, and B. Winter, 'The size dependent shift of the surface-plasmon absorption-band of small spherical metal particles', Z. Phys. D **12**, 471 (1989).

[151] K. P. Charlé, L. König, I. Rabin, and W. Schulze, 'The influence of CO on the surface plasmon absorption band of small silver clusters (D$\leq$20 Å)', Z. Phys. D **36**, 159 (1996).

[152] M. Gaudry, E. Cottancin, M. Pellarin, J. Lermé, L. Arnaud, J. R. Huntzinger, J. L. Vialle, M. Broyer, J. L. Rousset, M. Treilleux, and P. Mélinon, 'Size and composition dependence in the optical properties of mixed (transition metal/noble metal) embedded clusters', Phys. Rev. B **67**, 155409 (2003).

[153] L. Scaffardi and J. Tocho, 'Size dependence of refractive index of gold nanoparticles', Nanotechnology **17**, 1309 (2006).

[154] K. Kolwas and A. Derkachova, 'Damping rates of surface plasmons for particles of size from nano- to micrometers; reduction of the nonradiative decay', J. Quant. Spectrosc. Radiat. Transfer **114**, 45 (2013).

[155] Å. Ljungbert and P. Apell, 'The role of electron-hole pair excitations in the optical absorption of metals, particularly metal spheres', Solid State Commun. **46**, 47 (1983).

[156] P. Apell, R. Monreal, and F. Flores, 'Effective relaxation time in small spheres: diffuse surface scattering', Solid State Commun. **52**, 971 (1984).

[157] V. Myroshnychenko, J. Rodríguez-Fernández, I. Pastoriza-Santos, A. M. Funston, C. Novo, P. Mulvaney, L. M. Liz-Marzán, and F. J. García de Abajo, 'Modelling the optical response of gold nanoparticles', Chem. Soc. Rev. **37**, 1792 (2008).

[158] F. J. García de Abajo, 'Relativistic energy loss and induced photon emission in the interaction of a dielectric sphere with an external electron beam', Phys. Rev. B **59**, 3095 (1999).

[159] P. Nordlander, C. Oubre, E. Prodan, K. Li, and M. I. Stockman, 'Plasmon hybridization in nanoparticle dimers', Nano Lett. **4**, 899 (2004).

[160] K. Kneipp, Y. Wang, H. Kneipp, L. T. Perelman, I. Itzkan, R. R. Dasari, and M. S. Feld, 'Single molecule detection using surface-enhanced Raman scattering (SERS)', Phys. Rev. Lett. **78**, 1667 (1997).

[161] P. K. Jain, W. Huang, and M. A. El-Sayed, 'On the universal scaling behavior of the distance decay of plasmon coupling in metal nanoparticle pairs: a plasmon ruler equation', Nano Lett. **7**, 2080 (2007).

[162] I. Romero, J. Aizpurua, G. W. Bryant, and F. J. García de Abajo, 'Plasmons in nearly touching metallic nanoparticles: singular response in the limit of touching dimers', Opt. Express **14**, 9988 (2006).

[163] J. Zuloaga, E. Prodan, and P. Nordlander, 'Quantum description of the plasmon resonances of a nanoparticle dimer', Nano Lett. **9**, 887 (2009).

[164] S. Kadkhodazadeh, J. B. Wagner, H. Kneipp, and K. Kneipp, 'Coexistence of classical and quantum plasmonics in large plasmonic structures with subnanometer gaps', Appl. Phys. Lett. **103**, 083103 (2013).

[165] NanoPlasmonics Lab (2012). `http://www.nanopl.org`.

[166] R. Esteban, A. G. Borisov, P. Nordlander, and J. Aizpurua, 'Bridging quantum and classical plasmonics with a quantum-corrected model', Nat. Commun. **3**, 825 (2012).

[167] J. W. Haus, D. de Ceglia, M. A. Vincenti, and M. Scalora, 'Quantum conductivity for metal-insulator-metal nanostructures', J. Opt. Soc. Am. B **31**, 259 (2014).

[168] A. Aubry, D. Y. Lei, S. A. Maier, and J. B. Pendry, 'Interaction between plasmonic nanoparticles revisited with transformation optics', Phys. Rev. Lett. **105**, 233901 (2010).

[169] M. L. Brongersma, 'Nanoscale photonics: Nanoshells: gifts in a gold wrapper', Nature Mater. **2**, 296 (2003).

[170] G. Raschke, S. Brogl, A. S. Susha, A. L. Rogach, T. A. Klar, J. Feldmann, B. Fieres, N. Petkov, T. Bein, A. Nichtl, and K. Kürzinger, 'Gold nanoshells improve single nanoparticle molecular sensors', Nano Lett. **4**, 1853 (2004).

[171] C. L. Nehl, N. K. Grady, G. P. Goodrich, F. Tam, N. J. Halas, and J. H. Hafner, 'Scattering spectra of single gold nanoshells', Nano Lett. **4**, 2355 (2004).

[172] F. Tam, C. Moran, and N. J. Halas, 'Geometrical parameters controlling sensitivity of nanoshell plasmon resonances to changes in dielectric environment', J. Phys. Chem. B **108**, 17290 (2004).

[173] R. Bardhan, S. Lal, A. Joshi, and N. J. Halas, 'Theranostic nanoshells: from probe design to imaging and treatment of cancer', Acc. Chem. Res. **44**, 936 (2011).

[174] E. Prodan and P. Nordlander, 'Plasmon hybridization in spherical nanoparticles', J. Chem. Phys. **120**, 5444 (2004).

[175] R. Ruppin, 'Extinction properties of thin metallic nanowires', Opt. Commun. **190**, 205 (2001).

[176] N. J. Halas, 'Playing with plasmons: tuning the optical resonant properties of metallic nanoshells', MRS Bulletin **30**, 362 (2005).

[177] I. Lindau and P. O. Nilsson, 'Experimental verification of optically excited longitudinal plasmons', Phys. Scr. **3**, 87 (1971).

[178] F. Abelès, Y. Borensztein, M. De Crescenzi, and T. Lopez-Rios, 'Optical evidence for longitudinal waves in very thin Ag layers', Surf. Sci. **101**, 123 (1980).

[179] R. Kötz, D. Kolb, and F. Forstmann, 'Evidence for longitudinal waves in electroreflectance spectroscopy of silver', Surf. Sci. **91**, 489 (1980).

[180] M. M. Özer, E. J. Moon, A. G. Eguiluz, and H. H. Weitering, 'Plasmon response of a quantum-confined electron gas probed by core-level photoemission', Phys. Rev. Lett. **106**, 197601 (2011).

[181] A. R. Melnyk and M. J. Harrison, 'Resonant excitation of plasmons in thin films by elecromagnetic waves', Phys. Rev. Lett. **21**, 85 (1968).

[182] W. L. Mochán, M. del CastilloMussot, and R. G. Barrera, 'Effect of plasma waves on the optical properties of metal-insulator superlattices', Phys. Rev. B **35**, 1088 (1987).

[183] N. D. Lang and W. Kohn, 'Theory of metal surfaces: charge density and surface energy', Phys. Rev. B **1**, 4555 (1970).

[184] C. David and F. J. García de Abajo, 'Surface plasmon dependence on the electron density profile at metal surfaces', ACS Nano **8**, 9558 (2014).

[185] G. Toscano, C. Rockstuhl, F. Evers, H. Xu, N. A. Mortensen, and M. Wubs, 'Self-consistent hydrodynamic approach to nanoplasmonics: resonance shifts and spill-out effects', arXiv:1408.5862 (2014).

[186] R. F. Egerton, 'Electron energy-loss spectroscopy in the TEM', Rep. Prog. Phys. **72**, 016502 (2009).

[187] D. Rossouw and G. A. Botton, 'Resonant optical excitations in complementary plasmonic structures', Opt. Express **20**, 6968 (2012).

[188] D. Rossouw and G. A. Botton, 'Plasmonic response of bent silver nanowires for nanophotonic subwavelength waveguiding', Phys. Rev. Lett. **110**, 066801 (2013).

[189] E. J. R. Vesseur, R. de Waele, M. Kuttge, and A. Polman, 'Direct observation of plasmonic modes in Au nanowires using high-resolution cathodoluminescence spectroscopy', Nano Lett. **7**, 2843 (2007).

[190] M. Bosman, V. J. Keast, J. L. García-Muñoz, A. J. D'Alfonso, S. D. Findlay, and L. J. Allen, 'Two-dimensional mapping of chemical information at atomic resolution', Phys. Rev. Lett. **99**, 086102 (2007).

[191] V. Keast, 'Application of EELS in materials science', Mater. Charact. **73**, 1 (2012).

[192] V. Keast and M. Bosman, 'New developments in electron energy loss spectroscopy', Microsc. Res. Techniq. **70**, 211 (2007).

[193] J. Nelayah, L. Gu, W. Sigle, C. T. Koch, I. Pastoriza-Santos, L. M. Liz-Marzán, and P. A. van Aken, 'Direct imaging of surface plasmon resonances on single triangular silver nanoprisms at optical wavelength using low-loss EFTEM imaging', Opt. Lett. **34**, 1003 (2009).

[194] W. Sigle, J. Nelayah, C. T. Koch, and P. A. van Aken, 'Electron energy losses in Ag nanoholes—from localized surface plasmon resonances to rings of fire', Opt. Lett. **34**, 2150 (2009).

[195] W. Sigle, J. Nelayah, C. Koch, B. Ögüt, L. Gu, and P. van Aken, 'EFTEM study of surface plasmon resonances in silver nanoholes', Ultramicroscopy **110**, 1094 (2010).

[196] L. Gu, W. Sigle, C. T. Koch, B. Ögüt, P. A. van Aken, N. Talebi, R. Vogelgesang, J. Mu, X. Wen, and J. Mao, 'Resonant wedge-plasmon modes in single-crystalline gold nanoplatelets', Phys. Rev. B **83**, 195433 (2011).

[197] B. Ögüt, N. Talebi, R. Vogelgesang, W. Sigle, and P. A. van Aken, 'Toroidal plasmonic eigenmodes in oligomer nanocavities for the visible', Nano Lett. **12**, 5239 (2012).

[198] B. Schaffer, W. Grogger, G. Kothleitner, and F. Hofer, 'Comparison of EFTEM and STEM EELS plasmon imaging of gold nanoparticles in a monochromated TEM', Ultramicroscopy **110**, 1087 (2010).

[199] R. F. Egerton, 'New techniques in electron energy-loss spectroscopy and energy-filtered imaging', Micron **34**, 127 (2003).

[200] S. Lazar, G. A. Botton, and H. W. Zandbergen, 'Enhancement of resolution in core-loss and low-loss spectroscopy in a monochromated microscope', Ultramicroscopy **106**, 1091 (2006).

[201] F. J. García de Abajo and M. Kociak, 'Probing the photonic local density of states with electron energy loss spectroscopy', Phys. Rev. Lett. **100**, 106804 (2008).

[202] D. Muller and J. Silcox, 'Delocalization in inelastic scattering', Ultramicroscopy **59**, 195 (1995).

[203] N. Zabala, A. Rivacoba, and P. Echenique, 'Energy loss of electrons travelling through cylindrical holes', Surf. Sci. **209**, 465 (1989).

[204] A. Rivacoba, P. Apell, and N. Zabala, 'Energy loss probability of STEM electrons in cylindrical surfaces', Nucl. Instr. and Meth. in Phys. Res. B **96**, 465 (1995).

[205] E. Kröger, 'Berechnung der Energieverluste schneller Elektronen in dünnen Schichten mit Retardierung', Z. Physik **216**, 115 (1968).

[206] J. Aizpurua and A. Rivacoba, 'Nonlocal effects in the plasmons of nanowires and nanocavities excited by fast electron beams', Phys. Rev. B **78**, 035404 (2008).

[207] N. Zabala and P. Echenique, 'Energy loss of fast electrons moving near plane boundaries with dispersive media', Ultramicroscopy **32**, 327 (1990).

[208] E. Kröger, 'Transition radiation, Cerenkov radiation and energy losses of relativistic charged particles traversing thin foils at oblique incidence', Z. Physik **235**, 403 (1970).

[209] F. García de Abajo and J. Aizpurua, 'Numerical simulation of electron energy loss near inhomogeneous dielectrics', Phys. Rev. B **56**, 15873 (1997).

[210] F. García de Abajo and A. Howie, 'Relativistic electron energy loss and electron-induced photon emission in inhomogeneous dielectrics', Phys. Rev. Lett. **80**, 5180 (1998).

[211] F. J. García de Abajo and A. Howie, 'Retarded field calculation of electron energy loss in inhomogeneous dielectrics', Phys. Rev. B **65**, 115418 (2002).

[212] U. Hohenester and A. Trügler, 'MNPBEM–A Matlab toolbox for the simulation of plasmonic nanoparticles', Comp. Phys. Commun. **183**, 370 (2012).

[213] F. J. García de Abajo, 'Interaction of radiation and fast electrons with clusters of dielectrics: a multiple scattering approach', Phys. Rev. Lett. **82**, 2776 (1999).

[214] F. J. García de Abajo, 'Multiple scattering of radiation in clusters of dielectrics', Phys. Rev. B **60**, 6086 (1999).

[215] B. T. Draine and P. J. Flatau, 'Discrete-dipole approximation for scattering calculations', J. Opt. Soc. Am. A **11**, 1491 (1994).

[216] N. W. Bigelow, A. Vaschillo, V. Iberi, J. P. Camden, and D. J. Masiello, 'Characterization of the electron- and photon-driven plasmonic excitations of metal nanorods', ACS Nano **6**, 7497 (2012).

[217] A. Huck, S. Kumar, A. Shakoor, and U. L. Andersen, 'Controlled coupling of a single nitrogen-vacancy center to a silver nanowire', Phys. Rev. Lett. **106**, 096801 (2011).

[218] B. S. Guiton, V. Iberi, S. Li, D. N. Leonard, C. M. Parish, P. G. Kotula, M. Varela, G. C. Schatz, S. J. Pennycook, and J. P. Camden, 'Correlated optical measurements and plasmon mapping of silver nanorods', Nano Lett. **11**, 3482 (2011).

[219] M. Husnik, F. von Cube, S. Irsen, S. Linden, J. Niegemann, K. Busch, and M. Wegener, 'Comparison of electron energy-loss and quantitative optical spectroscopy on individual optical gold antennas', Nanophotonics **2**, 241 (2013).

[220] U. Hohenester, H. Ditlbacher, and J. R. Krenn, 'Electron-energy-loss spectra of plasmonic nanoparticles', Phys. Rev. Lett. **103**, 106801 (2009).

[221] F. Ouyang, P. Batson, and M. Isaacson, 'Quantum size effects in the surface-plasmon excitation of small metallic particles by electron-energy-loss spectroscopy', Phys. Rev. B **46**, 15421 (1992).

[222] S. Berciaud, L. Cognet, P. Tamarat, and B. Lounis, 'Observation of intrinsic size effects in the optical response of individual gold nanoparticles', Nano Lett. **5**, 515 (2005).

[223] L. Genzel, T. P. Martin, and U. Kreibig, 'Dielectric function and plasma resonance of small metal particles', Z. Phys. B **21**, 339 (1975).

[224] W. A. Kraus and G. C. Schatz, 'Plasmon resonance broadening in small metal particles', J. Chem. Phys. **79**, 6130 (1983).

[225] W. P. Halperin, 'Quantum size effects in metal particles', Rev. Mod. Phys. **58**, 533 (1986).

[226] O. Keller, M. Xiao, and S. Bozhevolnyi, 'Optical diamagnetic polarizability of a mesoscopic metallic sphere: transverse self-field approach', Opt. Comm. **102**, 238 (1993).

[227] Z. F. Öztürk, S. Xiao, M. Yan, M. Wubs, A.-P. Jauho, and N. A. Mortensen, 'Field enhancement at metallic interfaces due to quantum confinement', J. Nanophot. **5**, 051602 (2011).

[228] A. Ljungbert and S. Lundqvist, 'Non-local effects in the optical absorption of small metallic particles', Phys. Rev. Lett. **156**, 839 (1985).

[229] L. Mulfinger, S. D. Solomon, M. Bahadory, A. Jeyarajasingam, S. A. Rutkowsky, and C. Boritz, 'Synthesis and study of silver nanoparticles', J. Chem. Educ. **84**, 322 (2007).

[230] T. Bååk, 'Silicon oxynitride; a material for GRIN optics', Appl. Opt. **21**, 1069 (1982).

[231] C. Noguez, 'Surface plasmons on metal nanoparticles: the influence of shape and physical environment', J. Phys. Chem. C **111**, 3806 (2007).

[232] R. Ruppin, 'Optical absorption by a small sphere above a substrate with inclusion of nonlocal effects', Phys. Rev. B **45**, 11209 (1992).

[233] Z. Li, K. Bao, Y. Fang, Z. Guan, N. J. Halas, P. Nordlander, and H. Xu, 'Effect of a proximal substrate on plasmon propagation in silver nanowires', Phys. Rev. B **82**, 1 (2010).

[234] S. Zhang and H. Xu, 'Optimizing substrate-mediated plasmon coupling toward high-performance plasmonic nanowire waveguides', ACS Nano **6**, 8128 (2012).

[235] `http://imagej.nih.gov/ij/`.

[236] T. Yamaguchi, S. Yoshida, and A. Kinbara, 'Optical effect of the substrate on the anomalous absorption of aggregated silver films', Thin Solid Films **21**, 173 (1974).

[237] R. Ruppin, 'Surface modes and optical absorption of a small sphere above a substrate', Surf. Sci. **127**, 108 (1983).

[238] R. Ruppin, 'Plasmon frequencies of small metal spheres', J. Phys. Chem. Solids **39**, 233 (1978).

[239] H. Zhang, V. Kulkarni, E. Prodan, P. Nordlander, and A. O. Govorov, 'Theory of quantum plasmon resonances in doped semiconductor nanocrystals', J. Phys. Chem. C **118**, 16035 (2014).

[240] A. L. Koh, K. Bao, I. Khan, W. E. Smith, G. Kothleitner, P. Nordlander, S. A. Maier, and D. W. McComb, 'Electron energy-loss spectroscopy (EELS) of surface plasmons in single silver nanoparticles and dimers: influence of beam damage and mapping of dark modes', ACS Nano **3**, 3015 (2009).

[241] R. B. Pettit, J. Silcox, and R. Vincent, 'Measurement of surface-plasmon dispersion in oxidized aluminum films', Phys. Rev. B **11**, 3116 (1975).

[242] D. Rossouw, M. Couillard, J. Vickery, E. Kumacheva, and G. A. Botton, 'Multipolar plasmonic resonances in silver nanowire antennas imaged with a subnanometer electron probe', Nano Lett. **11**, 1499 (2011).

[243] B. Prade, J. Y. Vinet, and A. Mysyrowicz, 'Guided optical waves in planar heterostructures with negative dielectric constant', Phys. Rev. B **44**, 13556 (1991).

[244] H. Hu, Y. A. Akimov, H. Duan, X. Li, M. Liao, R. L. S. Tan, L. Wu, H. Chen, H. Fan, P. Bai, P. S. Lee, J. K. W. Yang, and Z. X. Shen, 'Photoluminescence via gap plasmons between single silver nanowires and a thin gold film', Nanoscale **5**, 12086 (2013).

[245] E. N. Economou, 'Surface plasmons in thin films', Phys. Rev. **182**, 539 (1969).

[246] T. Søndergaard, S. M. Novikov, T. Holmgaard, R. L. Eriksen, J. Beermann, Z. Han, K. Pedersen, and S. I. Bozhevolnyi, 'Plasmonic black gold by adiabatic nanofocusing and absorption of light in ultra-sharp convex grooves', Nat. Commun. **3**, 969 (2012).

[247] S. I. Bozhevolnyi and J. Jung, 'Scaling for gap plasmon based waveguides', Opt. Express **16**, 2676 (2008).

[248] H. T. Miyazaki and Y. Kurokawa, 'Squeezing visible light waves into a 3-nm-thick and 55-nm-long plasmon cavity', Phys. Rev. Lett. **96**, 097401 (2006).

[249] J. A. Dionne, H. J. Lezec, and H. A. Atwater, 'Highly confined photon transport in subwavelength metallic slot waveguides', Nano Lett. **6**, 1928 (2006).

[250] H. Shin and S. Fan, 'All-angle negative refraction for surface plasmon waves using a metal-dielectric-metal structure', Phys. Rev. Lett. **96**, 073907 (2006).

[251] H. J. Lezec, J. A. Dionne, and H. A. Atwater, 'Negative refraction at visible frequencies', Science **316**, 430 (2007).

[252] K. C. Y. Huang, M.-K. Seo, T. Sarmiento, Y. Huo, J. S. Harris, and M. L. Brongersma, 'Electrically driven subwavelength optical nanocircuits', Nature Photon. **8**, 244 (2014).

[253] J. McCaffrey, M. Phaneuf, and L. Madsen, 'Surface damage formation during ion-beam thinning of samples for transmission electron microscopy', Ultramicroscopy **87**, 97 (2001).

[254] N. I. Kato, 'Reducing focused ion beam damage to transmission electron microscopy samples', J. Electron Microsc. **53**, 451 (2004).

Paper A

S. Raza, M. Wubs, S. I. Bozhevolnyi, and N. A. Mortensen

Nonlocal study of ultimate plasmon hybridization

Opt. Lett. **40**, 839 (2015)

Author contributions
S. R. wrote the manuscript and created the figures. All authors were involved in discussing the obtained results and in correcting the manuscript.

March 1, 2015 / Vol. 40, No. 5 / OPTICS LETTERS 839

Nonlocal study of ultimate plasmon hybridization

Søren Raza,[1,2] Martijn Wubs,[1,2] Sergey I. Bozhevolnyi,[3] and N. Asger Mortensen[1,2,*]

[1]*Department of Photonics Engineering, Technical University of Denmark, DK-2800 Kgs. Lyngby, Denmark*

[2]*Center for Nanostructured Graphene (CNG), Technical University of Denmark, DK-2800 Kgs. Lyngby, Denmark*

[3]*Department of Technology and Innovation, University of Southern Denmark, DK-5230 Odense, Denmark*

**Corresponding author: asger@mailaps.org*

Received October 27, 2014; revised January 14, 2015; accepted January 15, 2015;
posted January 16, 2015 (Doc. ID 214449); published February 27, 2015

Within our recently proposed generalized nonlocal optical response (GNOR) model, where nonlocal response is included by taking into account both convective and diffusive currents of the conduction electrons, we revisit the fundamental problem of an optically excited plasmonic dimer. We consider the transition from separated dimers via touching dimers to finally overlapping dimers. In particular, we focus on the touching case, showing a fundamental limit on the hybridization of the bonding plasmon modes due to nonlocality. Using transformation optics, we determine a simple analytical equation for the resonance energies.

OCIS codes: (240.6680) Surface plasmons; (290.5850) Scattering, particles.
http://dx.doi.org/10.1364/OL.40.000839

One of the most fundamental and intriguing problems in plasmonics is the electromagnetic interaction of two metallic nanostructures, i.e., the dimer structure. The gap-dependent electric-field enhancement and bonding plasmon resonance energies have been utilized in e.g., surface-enhanced Raman spectroscopy and the plasmon ruler effect. The dimer has been studied with a variety of theoretical and experimental techniques. The simplest theoretical approach is based on the classical local-response approximation (LRA), which in the case of a nanometer-sized dimer gap gives rise to unphysical results, such as extreme field enhancements in the gap of the dimer [1]. A complete breakdown of the LRA is seen in the touching configuration, where the number of hybridized bonding plasmon modes increases without limit to form a continuum of modes [2], thus setting no ultimate bound to the resonance energies of the bonding plasmon modes and thereby the plasmon hybridization [3]. Advanced descriptions based on density-functional theory (DFT) regularize the unphysical consequences of the LRA [4–7], where the physical mechanism for the regularization is attributed to quantum tunneling, i.e., the charge transfer that may occur before reaching the touching configuration due to the spill-out of electrons. DFT simulations of optically excited dimers show a limit on the hybridization of bonding plasmon modes, yet no general relation for this limit has been extracted. Results based on the hydrodynamic model, where only nonlocal response (and not electron spill-out) is taken into account, also display regularizations of the LRA [2,8,9], albeit with field enhancements in the dimer gap that are still larger than shown by DFT simulations [7]. Measurements on dimers with vanishing gaps using both optical techniques [10,11] and electron energy-loss spectroscopy [12,13] are not in agreement with the LRA, and, in the touching case, also display limits on the resonance energies of the bonding plasmon modes, i.e., ultimate bounds to the plasmon hybridization. However, the physical mechanism for the discrepancy between LRA and the observed measurements is not conclusive with possible explanations being provided from both quantum tunneling [7] and nonlocal response [14] perspectives.

We revisit the problem of an optically excited plasmonic dimer (see Fig. 1) within the framework of our recently proposed GNOR model in which nonlocal response is caused both by convection and diffusion [14]. In contrast to DFT, the physically more transparent GNOR model allows for analytical results. We study the evolution of both the extinction cross-section and the electric-field enhancement in the dimer gap as the gap size varies from separated to overlapping dimers. In particular, we focus on the touching dimer and derive, using transformation optics (TO), a simple analytical relation for the resonance energies of the bonding plasmon modes. Furthermore, we show that previous nonlocal TO methods used for the hydrodynamic model [2] are accurate also for the GNOR model.

Given the nonlocal constitutive relation $\mathbf{D}(\mathbf{r},\omega) = \int \mathrm{d}\mathbf{r}'\varepsilon(\mathbf{r},\mathbf{r}')\mathbf{E}(\mathbf{r}',\omega)$, the wave equation is

$$\nabla\times\nabla\times\mathbf{E}(\mathbf{r},\omega) = \left(\frac{\omega}{c}\right)^2 \int \mathrm{d}\mathbf{r}'\varepsilon(\mathbf{r},\mathbf{r}')\mathbf{E}(\mathbf{r}',\omega). \quad (1)$$

Under the assumptions of a linear, isotropic, and short-ranged response function, Eq. (1) can be recast as [17]

$$\nabla\times\nabla\times\mathbf{E}(\mathbf{r},\omega) = \left(\frac{\omega}{c}\right)^2 [\varepsilon_{\mathrm{D}}(\omega) + \xi^2\nabla^2]\mathbf{E}(\mathbf{r},\omega), \quad (2)$$

where ξ describes the nonlocal correction to the local-response Drude permittivity $\varepsilon_{\mathrm{D}}(\omega) = \varepsilon_\infty(\omega) - \omega_{\mathrm{p}}^2/(\omega^2 + i\gamma\omega)$. Here, $\varepsilon_\infty(\omega)$ accounts for effects not due to the free

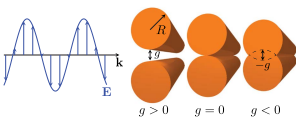

Fig. 1. Incident electric field, polarized along the dimer axis, impinges on a dimer consisting of two identical metal cylinders with radii R and separated by a gap g. The three studied cases of separated dimer ($g > 0$), touching dimer ($g = 0$), and overlapping dimer ($g < 0$) are shown.

0146-9592/15/050839-04$15.00/0

electrons, such as interband transitions. Within the hydrodynamic model, the nonlocality parameter is $\xi_H^2 = \varepsilon_\infty(\omega)\beta^2/(\omega^2 + i\omega\gamma)$ [17], where γ is the free-electron damping rate and $\beta^2 = 3/5v_F^2$ with v_F denoting the Fermi velocity of the conduction electrons. Nonlocal response in the hydrodynamic model arises from the inclusion of the Thomas–Fermi kinetic energy of the free electrons. The GNOR model expands the hydrodynamic model by taking into account the effects of electron diffusion [14]. Within the GNOR model, $\xi_{GNOR}^2 = \varepsilon_\infty(\omega)\eta^2/(\omega^2 + i\omega\gamma)$, where $\eta^2 = \beta^2 + D(\gamma - i\omega)$, and D is the diffusion constant. Although the mathematical formalism of the GNOR model is similar to the hydrodynamic model, with the simple substitution $\beta^2 \to \eta^2$, the physical differences are pronounced. In contrast to the hydrodynamic model, the GNOR model accurately captures the size-dependent damping of localized surface plasmons in individual particles [18] and reproduces DFT absorption spectra of dimers [7,14].

Before discussing the results of the nanowire dimer, we first outline the procedure to determine the diffusion constant D for different metals. The size-dependent damping of localized surface plasmons in nanoparticles has extensively been observed experimentally [18]. The phenomenological approach to account for this effect in the LRA, i.e., Eq. (2) with $\xi = 0$, has been to modify the Drude damping parameter as $\gamma \to \gamma + Av_F/R$ [18], which only applies for spherical particles of radius R. Here, A is a constant, which is related to the probability of the electron scattering off the surface of the particle. Both experimental data and more advanced theoretical calculations have been compared to this approach, resulting in a robust value for A close to unity for different metals [18]. It is therefore appropriate to ensure that the GNOR model agrees with this successful, but phenomenological approach. To this end, we calculate the extinction cross-section of a metal sphere using the nonlocal polarizability [19] for the GNOR calculations, while the LRA polarizability is modified to include the aforementioned additional damping with both $A = 0.5$ and $A = 1$. Two different values for A are considered, since different nanoparticle preparation methods may result in different surface properties. The diffusion constant D is varied until the full width at half-maximum of the localized surface plasmon resonances for both calculations coincide. This procedure is repeated for the range of sphere radii of 1–10 nm. As the fitted diffusion constant D varies slightly with sphere radii, we use the average value for D. The diffusion constant D along with other relevant GNOR parameters for Na, Ag, Au, and Al are summarized in Table 1. We also add that the nonfree-electron response $\varepsilon_\infty(\omega)$ can be determined from experimentally measured bulk dielectric functions [20].

Using the freely available COMSOL implementation of the GNOR theory [8], we calculate the extinction cross-section and electric-field enhancement of a large Na dimer with radius $R = 30$ nm when varying the gap distance. Figure 2(a) displays a waterfall plot of the extinction cross-section for two values of D (solid and dashed lines, respectively), when the gap is varied from +30 Å (separated) to −30 Å (overlapping) in steps of 3 Å. For separated nanowires, we see three distinct modes, the bonding dipole mode (BDP), bonding quadrupolar mode (BQP), and the higher order mode (HOM), also labeled in Fig. 2(a). The electric field norm of these three modes for a gap of 30 Å are displayed in Figs. 2(b)–2(d). As the gap decreases, the BDP and BQP redshift and dampen due to increased plasmon hybridization [8] and increased

Table 1. Plasma Frequencies ω_P, Damping Rates γ, Fermi Velocities v_F, and Diffusion Constants D for the Metals Na, Ag, Au, and Al[a]

				$D[10^{-4}\ \mathrm{m^2\,s^{-1}}]$	
	$\hbar\omega_P$ [eV]	$\hbar\gamma$ [eV]	v_F [10^6 ms^{-1}]	$A = 0.5$	$A = 1$
Na	6.04 [15]	0.16 [7]	1.07	1.08	2.67
Ag	8.99 [15]	0.025 [16]	1.39	3.61	9.62
Au	9.02 [15]	0.071 [16]	1.39	1.90	8.62
Al	15.8 [15]	0.6 [16]	2.03	1.86	4.59

[a]For determination of D, see the main text.

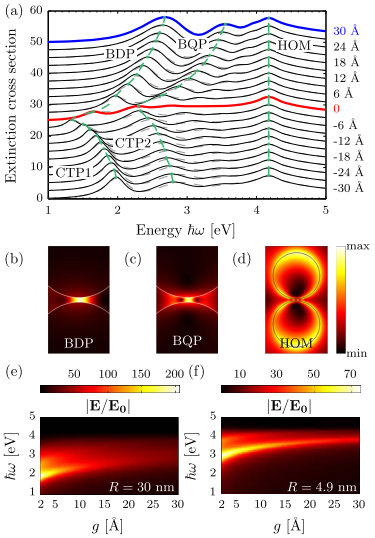

Fig. 2. (a) Extinction cross-section (in units of cylinder diameter $2R$) of a Na nanowire dimer of radius $R = 30$ nm with gap size g varying from 30 Å (separated) to −30 Å (overlapping) for two diffusion constant values: $D = 1.08 \times 10^{-4}\ \mathrm{m^2\,s^{-1}}$ (solid lines) and $D = 2.67 \times 10^{-4}\ \mathrm{m^2\,s^{-1}}$ (dashed lines). Each spectrum is vertically displaced with 2.5 normalized units. (b-d) Electric field amplitudes $|\mathbf{E}|$ of the BDP, BQP, and HOM, respectively, for a dimer with $g = 30$ Å [blue curve in (a)]. (e)–(f) Electric-field enhancement in the center of the dimer gap for dimers with $R = 30$ nm and $R = 4.9$ nm, respectively. Parameters for Na as in Table 1 with $\varepsilon_\infty = 1$.

absorption at the metal surfaces in the vicinity of the gap, respectively. However, the resonance energy of the HOM is unaffected by the gap size as the electric field of this mode is mainly distributed at the dimer edges, and not in the gap [see Fig. 2(d)]. When the gap vanishes [red line in Fig. 2(a)], the hybridization of the bonding modes is maximal, and no further resonance shifts or damping can occur. As the dimers begin to overlap ($g < 0$), the bonding modes disappear, and the charge transfer plasmons [labeled CTP1 and CTP2 in Fig. 2(a)] appear. The CTP1 and CTP2 blueshift with increasing dimer overlap as the dimer effectively becomes a single structure. Comparison of the two values for D [solid and dashed lines in Fig. 2(a)] reveal that the main features are robust with respect to D, and that an increased value for D primarily increases the widths of the bonding-mode resonances. In Fig. 2(e), we show the evolution of the electric-field enhancement, probed at the center point of the gap. As the gap size decreases, the electric-field enhancement increases due to increased interaction between the metal surfaces. Furthermore, as the bonding plasmon modes redshift, so does the maximal field enhancement. To facilitate comparison with DFT calculations [7], we also display in Fig. 2(f) the electric-field enhancement evolution of a Na dimer with a smaller radius of $R = 4.9$ nm. Here we see that the electric-field enhancement amplitude and trend with decreasing gap size are in very good agreement with DFT simulations of Ref. [7]. The only discrepancy between the GNOR model and DFT simulations occurs at gap sizes below approximately 5 Å but before contact, where the overlap of electron spill-out in DFT calculations quenches the electric-field enhancement. However, the GNOR model can still be seen providing a useful upper limit to the ultimate plasmon hybridization that might be tested experimentally.

When the dimers are touching, the hybridization of the bonding plasmon modes is maximal, and the resonance positions of these modes depend only on the dimer radius R. We have investigated the resonances of the BDP and BQP modes as a function of R in Fig. 3. For the smallest dimer radii ($R \leq 10$ nm), the resonance positions of the BQP mode are not clearly distinguishable from the extinction spectra due to the weaker hybridization in smaller dimers. As the dimer radius increases, the resonance energies of both the BDP and BQP modes decrease. This is due to the increased hybridization occurring for larger radii as the interacting metal surfaces between the two nanowires increase. Along with the GNOR simulations, we also depict the results using a nonlocal TO approach (dashed lines in Fig. 3) [2]. Although the nonlocal TO was originally used with the hydrodynamic model, we show in Fig. 3 that this approach is still valid within the GNOR theory, as long as the substitution $\beta^2 \to \eta^2$ is applied. As expected, we see that the nonlocal TO calculations agree quite well with the GNOR simulations for both the BDP and BQP modes.

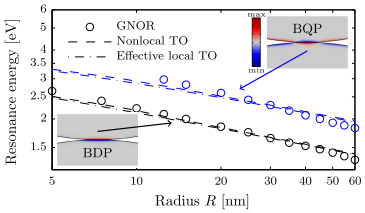

Fig. 3. Logarithmic plot of the resonance energies of the BDP (black) and BQP (blue) modes of touching Na nanowires as a function of dimer radius R. The dots display the GNOR simulations, and the dashed lines show the results using the nonlocal TO approach. The dashed–dotted lines show the results using the local-response TO approach, given by Eq. (3) with an effective gap $g = 2\,\mathrm{Re}[d(\omega)]$. The insets display the imaginary part of the GNOR charge distributions of the BDP and BQP for a touching dimer with $R = 30$ nm.

We may deduce a simple relation for the resonance energies of the bonding plasmon modes by examining the position of the centroid of induced charges [7], given as the real part of the Feibelman parameter $d(\omega)$ [21]. Using the definition of the Feibelman parameter [21], we find that $d(\omega) = i/k_{\mathrm{NL}}$ where $k_{\mathrm{NL}} = \sqrt{\varepsilon_{\mathrm{D}}(\omega)/\xi_{\mathrm{GNOR}}}$ is the nonlocal longitudinal wave vector. In the GNOR theory, the centroid of the induced charges is positioned a short distance $\{\mathrm{Re}[d(\omega)] \simeq v_{\mathrm{F}}/\omega_{\mathrm{P}} \approx 1$ Å$\}$ within the metal boundary, see insets of Fig. 3 (as a consequence of the additional boundary condition of vanishing free-electron current in the radial direction [14]). However, within the LRA, the induced surface charges reside on the geometrical surface. We can therefore mimic the position of the centroid of induced charges in the GNOR theory by considering separated dimers in the LRA with a gap of $g = 2\,\mathrm{Re}[d(\omega)]$. This approach is similar to the model of Ref. [9], however the effective gap size g of Ref. [9] is larger due to the application of a different additional boundary condition. Within the LRA, the resonance condition of a separated dimer with gap size g has been determined using TO [22] and is given by

$$\left(\sqrt{\frac{g}{4R}} + \sqrt{1 + \frac{g}{4R}}\right)^{4n} = \mathrm{Re}\left[\frac{\varepsilon_{\mathrm{D}}(\omega) - 1}{\varepsilon_{\mathrm{D}}(\omega) + 1}\right], \tag{3}$$

where $n = 1$ corresponds to the BDP mode, $n = 2$ corresponds to the BQP mode, and so on. Assuming an undamped Drude model for the permittivity $\varepsilon_{\mathrm{D}}(\omega) = 1 - \omega_{\mathrm{P}}^2/\omega^2$ and expanding Eq. (3) to first-order in g/R, we find the simple relation for the LRA resonance condition for the hybridized modes of separated nanowires

$$\frac{\omega}{\omega_{\mathrm{P}}} \simeq \sqrt{n}\left[\frac{2\,\mathrm{Re}(\xi_{\mathrm{GNOR}})}{\sqrt{-\varepsilon_{\mathrm{D}}(\omega)}R}\right]^{\frac{1}{4}}. \tag{4}$$

where we have used that $g = 2\,\mathrm{Re}(\xi_{\mathrm{GNOR}})/\sqrt{-\varepsilon_{\mathrm{D}}(\omega)}$. Figure 3 displays the result of this effective LRA approach (dashed–dotted lines), given by Eq. (3) with gap size $g = 2\,\mathrm{Re}[d(\omega)]$. We see that the GNOR resonance energies of touching nanowires can quite accurately be mimicked by the LRA result of separated nanowires, when the gap size is set to the distance between the centroid of induced charges. As anticipated from Eq. (4), we also see that the slopes of the BDP and BQP resonance energies are very similar. The BQP energies occur at

higher energies because of the $\sqrt{n}$ in Eq. (4). Although diffusion plays a crucial role in the damping of the bonding plasmon modes for decreasing gap size [as seen in the extinction cross sections of Fig. 2(a)] and in the electric-field enhancement amplitude [see Figs. 2(e)–2(f)], Eq. (4) shows that the maximal hybridization resonance energies are mainly dependent on convection as described by the Fermi velocity, since the value for β contributes most to $\mathrm{Re}(\xi_{\mathrm{GNOR}})$. Only in the extreme limit where $D\omega$ becomes comparable to β^2 in magnitude will diffusion play a role in the position of the resonance energies.

We have theoretically studied the extinction cross-section and electric-field enhancement of a plasmonic dimer consisting of two large Na cylinders using the GNOR model. As the gap size decreases, the extinction cross-section shows a damping of the bonding plasmon resonances, while the electric-field enhancement in the gap increases, but stays finite. Both trends are in good agreement with DFT calculations and experimental measurements on dimers. We have also examined the touching dimer and, using transformation optics, derived a simple analytical relation [Eq. (4)] for the resonance energies of the bonding plasmon modes that we propose to test experimentally. Finally, we have shown the first successful application of nonlocal TO to the GNOR model.

We thank Yu Luo for stimulating discussions. CNG is funded by the Danish National Research Foundation, Project DNRF58. N. A. M. and M. W. acknowledge financial support by Danish Council for Independent Research–Natural Sciences, Project 1323-00087. S. I. B. acknowledges financial support by European Research Council, Grant 341054 (PLAQNAP).

References

1. I. Romero, J. Aizpurua, G. W. Bryant, and F. J. García de Abajo, Opt. Express **14**, 9988 (2006).
2. A. I. Fernández-Domínguez, A. Wiener, F. J. García-Vidal, S. A. Maier, and J. B. Pendry, Phys. Rev. Lett. **108**, 106802 (2012).
3. E. Prodan, C. Radloff, N. Halas, and P. Nordlander, Science **302**, 419 (2003).
4. J. Zuloaga, E. Prodan, and P. Nordlander, Nano Lett. **9**, 887 (2009).
5. L. Stella, P. Zhang, F. J. García-Vidal, A. Rubio, and P. García-González, J. Phys. Chem. C **117**, 8941 (2013).
6. K. Andersen, K. L. Jensen, N. A. Mortensen, and K. S. Thygesen, Phys. Rev. B **87**, 235433 (2013).
7. T. V. Teperik, P. Nordlander, J. Aizpurua, and A. G. Borisov, Opt. Express **21**, 27306 (2013).
8. G. Toscano, S. Raza, A.-P. Jauho, N. A. Mortensen, and M. Wubs, Opt. Express **20**, 4176 (2012).
9. Y. Luo, A. I. Fernández-Domínguez, A. Wiener, S. A. Maier, and J. B. Pendry, Phys. Rev. Lett. **111**, 093901 (2013).
10. K. J. Savage, M. M. Hawkeye, R. Esteban, A. G. Borisov, J. Aizpurua, and J. J. Baumberg, Nature **491**, 574 (2012).
11. H. Cha, J. H. Yoon, and S. Yoon, ACS Nano **8**, 8554 (2014).
12. J. A. Scholl, A. Garcia-Etxarri, A. L. Koh, and J. A. Dionne, Nano Lett. **13**, 564 (2013).
13. S. Kadkhodazadeh, J. B. Wagner, H. Kneipp, and K. Kneipp, Appl. Phys. Lett. **103**, 083103 (2013).
14. N. A. Mortensen, S. Raza, M. Wubs, T. Søndergaard, and S. I. Bozhevolnyi, Nat. Commun. **5**, 3809 (2014).
15. N. W. Ashcroft and N. D. Mermin, *Solid State Physics* (Saunders College Publishing, 1976).
16. F. J. García de Abajo, Rev. Mod. Phys. **82**, 209 (2010).
17. G. Toscano, S. Raza, W. Yan, C. Jeppesen, S. Xiao, M. Wubs, A.-P. Jauho, S. I. Bozhevolnyi, and N. A. Mortensen, Nanophotonics **2**, 161 (2013).
18. U. Kreibig and M. Vollmer, *Optical Properties of Metal Clusters* (Springer-Verlag, 1995).
19. S. Raza, W. Yan, N. Stenger, M. Wubs, and N. A. Mortensen, Opt. Express **21**, 27344 (2013).
20. F. J. García de Abajo, J. Phys. Chem. C **112**, 17983 (2008).
21. P. J. Feibelman, Prog. Surf. Sci. **12**, 287 (1982).
22. A. Aubry, D. Y. Lei, S. A. Maier, and J. B. Pendry, Phys. Rev. Lett. **105**, 233901 (2010).

Paper B

S. Raza, N. Stenger, A. Pors, T. Holmgaard, S. Kadkhodazadeh, J. B. Wagner, K. Pedersen, M. Wubs, S. I. Bozhevolnyi, and N. A. Mortensen

Extremely confined gap surface-plasmon modes excited by electrons

Nat. Commun. **5**, 4125 (2014)

Author contributions

N. S., S. I. B. and N. A. M. conceived the experiment. S. K. aligned the microscope and imaged the sample. S. R., N. S. and S. K. performed the EELS measurements. S. R. and N. S. performed the EELS data analysis. S. R. and J. B. W. performed the sample thickness analysis. A. P. and S. R. performed the simulations. T. H. and K. P. fabricated the sample with groove arrays. S. R. created the figures of the main manuscript. S. R., N. S. and A. P. wrote the manuscript and supplemental information. All authors were involved in discussing the obtained results and in correcting the manuscript.

nature COMMUNICATIONS

ARTICLE

Received 9 Dec 2013 | Accepted 14 May 2014 | Published 18 Jun 2014

DOI: 10.1038/ncomms5125

Extremely confined gap surface-plasmon modes excited by electrons

Søren Raza[1,2,*], Nicolas Stenger[1,3,*], Anders Pors[4,*], Tobias Holmgaard[5], Shima Kadkhodazadeh[2], Jakob B. Wagner[2], Kjeld Pedersen[5], Martijn Wubs[1,3], Sergey I. Bozhevolnyi[4] & N. Asger Mortensen[1,3]

High-spatial and energy resolution electron energy-loss spectroscopy (EELS) can be used for detailed characterization of localized and propagating surface-plasmon excitations in metal nanostructures, giving insight into fundamental physical phenomena and various plasmonic effects. Here, applying EELS to ultra-sharp convex grooves in gold, we directly probe extremely confined gap surface-plasmon (GSP) modes excited by swift electrons in nanometre-wide gaps. We reveal the resonance behaviour associated with the excitation of the antisymmetric GSP mode for extremely small gap widths, down to ~ 5 nm. We argue that excitation of this mode, featuring very strong absorption, has a crucial role in experimental realizations of non-resonant light absorption by ultra-sharp convex grooves with fabrication-induced asymmetry. The occurrence of the antisymmetric GSP mode along with the fundamental GSP mode exploited in plasmonic waveguides with extreme light confinement is a very important factor that should be taken into account in the design of nanoplasmonic circuits and devices.

[1] Department of Photonics Engineering, Technical University of Denmark, DK-2800 Kongens Lyngby, Denmark. [2] Center for Electron Nanoscopy, Technical University of Denmark, DK-2800 Kongens Lyngby, Denmark. [3] Center for Nanostructured Graphene (CNG), Technical University of Denmark, DK-2800 Kongens Lyngby, Denmark. [4] Department of Technology and Innovation, University of Southern Denmark, DK-5230 Odense M, Denmark. [5] Department of Physics and Nanotechnology, Aalborg University, DK-9220 Aalborg Øst, Denmark. * These authors contributed equally to this work. Correspondence and requests for materials should be addressed to S.I.B. (email: seib@iti.sdu.dk) or N.A.M. (email: asger@mailaps.org).

Surface plasmons (SPs), that is, the collective excitation of the conduction electrons localized at the metal surface, allow for subwavelength localization and guiding of light[1,2], and electric field enhancements on the nanoscale[3]. These attractive properties of the SPs have found application in a wide variety of fields, that is from medical applications, such as bio-sensing[4] and cancer therapy[5], to plasmonic waveguiding[6]. However, the experimental mapping of SPs on the nanoscale using light remains an inherently difficult task owing to the diffraction limit. In contrast, the use of swift electrons to excite SPs offers a powerful spectroscopic technique known as electron energy-loss spectroscopy (EELS)[7]. Performing EELS in state-of-the-art transmission electron microscopes (TEMs) equipped with a monochromator and aberration corrector offers unmatched simultaneous spatial and spectral resolution[7,8]. Ritchie predicted the excitation of SPs using electrons[9], and, more recently, low-loss EELS has become an increasingly popular technique in plasmonics, especially in the study and mapping of localized SP resonances[8,10–15]. Although the majority of plasmonic EELS studies have been focused on localized SP resonances, EELS has also been used to study propagating SPs (that is, waveguide modes) in, for example, metal thin films[16] and nanowires[17–19], where standing waves are formed by forward- and backward-propagating waveguide modes. Gap SP (GSP) modes, that is, propagating SP modes in a dielectric gap between two metals[20], have been studied with cathodoluminescence[21] and photoluminescence[22]. However, GSP modes have, to our knowledge, never been experimentally examined with EELS. The GSP modes occur in a variety of geometries, from the simplest one-dimensional (1D) metal–insulator–metal (MIM) waveguide[23,24] and metal nanowire-on-film geometries[22] to advanced structures such as the convex groove, V-groove and trench and stripe waveguides[25,26]. Furthermore, GSP modes offer enhanced properties compared with the usual propagating SP mode, such as extreme light confinement with improved propagation distances[27,28], negative refraction[29,30], highly efficient light absorption[25] and electrically driven circuitry[31], to name a few important and distinct features of GSP modes in plasmonics.

Here, we report an experimental study of GSPs in ultra-sharp gold convex nanogrooves using EELS. The geometry of these nanogrooves is characterized by gradual and relatively slow variations in the gap width when moving deeper inside a groove. This means that the groove GSP modes can be considered as being formed by local MIM GSP modes (that is, by GSP modes supported by constant-gap MIM configurations) that are weighted accordingly, a representation which is widely used in integrated optics and plasmonics for effective-index approximation[26]. In EELS experiments (Fig. 1), the strongly confined electrical fields of moving electrons excite thereby local MIM GSP modes, corresponding to the position of the electron beam inside the groove. Note that a sample should necessarily be thin along the groove (Fig. 1) in order to be transparent for an electron beam, but not too thin with respect to the GSP wavelength. Overall, the considered groove geometry is ideal for studying MIM GSP modes, as the width of the insulating layer (gap size) decreases as the position of the electron probe is moved down the nanogroove, thus allowing us to map the evolution of MIM GSP modes for varying gap size in a single groove. We will also explore how deep into the groove this local MIM picture remains accurate.

Using the nomenclature common to transverse-light excitation, the GSP modes can be classified according to the symmetry of their transversal electric component with respect to the mirror-symmetry plane of the groove (*yz* plane in Fig. 1). The symmetric GSP (sGSP) modes have a net electric-dipole moment associated with an induced-charge pattern that is antisymmetric with respect to the mirror-symmetry plane, whereas the antisymmetric GSP (aGSP) modes are optically dark because of a symmetric induced-charge distribution. This classification is hereafter applied to both MIM and groove GSP modes. For a more detailed account on the field distributions and dispersion relations of GSP modes in convex groove and MIM waveguides, we refer to Supplementary Figs 1 and 2, as well as Supplementary Notes 1 and 2.

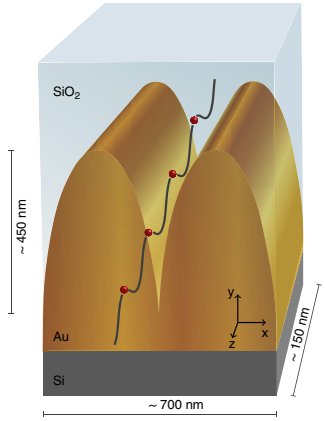

Figure 1 | Gold nanogroove. Artistic impression of a single gold nanogroove with the swift electron beam moving parallel to the groove axis. The groove is filled with SiO_2 and the substrate is Si. The period and height of the grooves are determined from the STEM images, while the thickness of the sample has been inspected in a scanning electron microscope and also estimated from EELS data using both the log-ratio method and Kramers–Kronig analysis[42].

In this work, we intentionally propagate the electron beam along the axis of the groove within the mirror-symmetry plane (*yz* plane, *cf.* Fig. 1) in order to allow for probing of modes near the groove bottom and to study the optically dark modes. We verify experimentally the existence of the MIM aGSP mode in the crevice of the groove, with the mode showing an increase in energy as the gap size decreases. The presence of the MIM aGSP mode is confirmed at extremely narrow gaps of only 5 nm. Furthermore, we argue why the excitation of this mode, featuring very strong absorption, has a crucial role in the experimental realization of non-resonant light absorption by ultra-sharp convex grooves with fabrication-induced asymmetry[25].

Results

Fabrication. The fabrication of the gold nanogrooves is performed using a focused ion beam (FIB) setup. A gold (Au) film of 1.8 μm in thickness is deposited on a silicon (Si) substrate, after which areas of the gold are milled by the FIB to create the groove structure. With this technique, ultra-sharp grooves with a 1D period of ~350 nm are fabricated (see Methods section for details). Inside the FIB chamber, a layer of silicon dioxide (SiO_2) is then deposited to separate the grooves from the top platinum layer used for protecting the sample during the preparation of the TEM lamella. The thickness of the SiO_2 layer (~500 nm) is sufficient to avoid the influence of the platinum layer when

performing EELS measurements inside the groove. With a micromanipulator, the nanogroove sample is attached to a TEM lift-out grid such that the electron beam passes perpendicularly to the section of the sample and parallel to the axis of the groove, as illustrated in Fig. 1. In order to characterize the grooves in the TEM with EELS, we use the FIB to thin the nanogrooves along the z direction to a thickness of $\sim$150 nm. This ensures that the sample is sufficiently transparent for the electron beam, while at the same time mechanically stable. Note that as a consequence of the thinned sample, the structure can only be considered as a waveguide facilitating propagating modes when the electron beam probes MIM GSP modes at the base of the grooves, that is, when the groove width is considerably smaller than the sample thickness of $\sim$150 nm.

Figure 2 shows typical scanning TEM (STEM) images of the gold nanogroove sample. In Fig. 2a, an overview image of the sample is displayed with the gold nanogroove on top of a Si substrate. The grooves are filled with SiO_2 and the top platinum layer can also be seen. Figure 2b shows a zoom-in of a single groove, indicating the almost perfect symmetry with respect to the mirror-symmetry plane of the groove (see also the dashed white line in Fig. 2b). However, as we will discuss later, the slight geometric asymmetry of the groove is crucial in understanding the plasmonic black gold effect studied in ref. 25. Finally, Fig. 2c is a close-up of a groove crevice, showing its extremely sharp nature. The side-to-side width of the groove from the top to the bottom is calculated with an in-house written image analysis code (see Methods section) and ranges from 320 nm down to widths smaller than 5 nm, thus confirming the ultra-sharp shape of the grooves. Although slight fluctuations in shape and groove depths may be seen, overall the grooves are impressively similar (which is also reflected in our subsequent EELS measurements).

Electron energy-loss spectroscopy. To characterize the grooves, we use an aberration-corrected FEI Titan STEM operated at an acceleration voltage of 300 kV (corresponding to an electron velocity of $v = 0.776c$) and with an electron probe size (that is, full width at half maximum (FWHM) of the probe profile) of $\sim$5 Å. The system is equipped with a monochromator, allowing us to perform EELS measurements with an energy resolution of 0.15 ± 0.05 eV. We performed a detailed analysis of six grooves on the same sample by systematically collecting EELS data from the top to the bottom of the groove (see Methods section). Since the results obtained for these six grooves are very similar (Supplementary Fig. 3), we present results for two of the grooves only.

The EELS data along with their corresponding electron probe positions in the groove are displayed in Fig. 3a,b. The only data treatment of the EELS data has been to subtract the zero-loss peak from the raw data using the reflected-tail method (see Methods section). The EELS data are relatively featureless for a broad range of energies, but do show clear resonance peaks owing to the excitation of SP mode(s). As the most prominent feature, we observe that the resonance peak blueshifts from 2.1 to $\sim$2.6 eV when the position of the electron probe is moved from the top towards the bottom of the groove. This spectral sensitivity to the

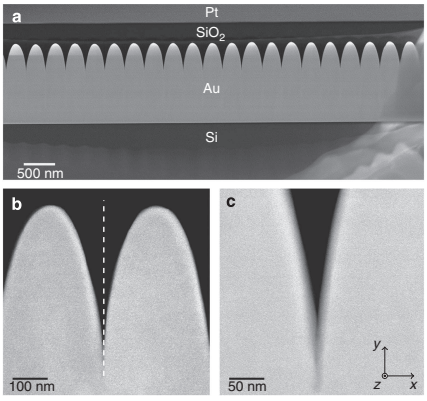

Figure 2 | STEM micrographs of a gold nanogroove. STEM images of (**a**) sample overview with material labels; (**b**) single groove zoom-in; and (**c**) ultra-sharp groove crevice. The STEM images display the periodicity of the structure and the similarity in shape of each groove. Furthermore, the grooves are quite symmetric along the center line (dashed line in **b**) and extremely sharp, with $\sim$5 nm gap sizes in the crevice.

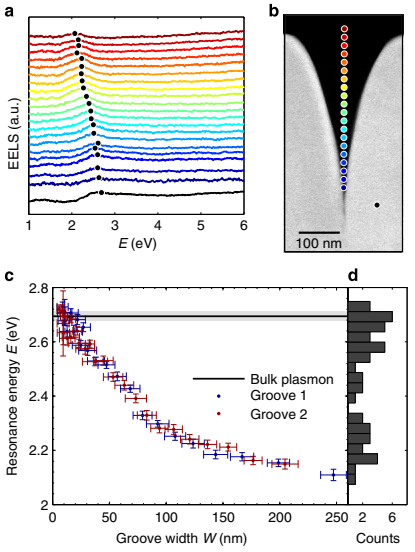

Figure 3 | Experimental EELS data. (**a**) Waterfall plot of experimental EELS measurements at the corresponding positions indicated on the groove image in **b**. The bottom black line displays the experimental EELS spectrum of bulk Au. (**c**) Peak resonance energy as a function of groove width for two different grooves, along with the measured bulk plasmon energy of Au (solid black line with grey area displaying the error bar). The vertical error bars correspond to the 95% confidence interval for the estimate of the position of the resonance energy in our experimental data, and the horizontal error bars represent the indeterminacy in measuring the width of the grooves based on the intensity contrast in our STEM images (see Methods section). (**d**) Histogram displaying the number of resonance energies within bin intervals of 0.04 eV (projection of data in **c** onto the E axis). The bin interval is chosen as the average energy error bar size.

groove width, especially apparent for small groove widths, is a clear indication that the MIM aGSP mode (which is related to the local width of the groove) is probed in the crevice rather than (global) groove GSP modes, whose peak positions should not depend on the electron position in the groove. This interpretation is supported by simulations (see text below and Fig. 4 along with Supplementary Figs 4 and 5).

In Fig. 3c, we plot the energy of the resonance peak E as a function of the width W for two different grooves. The plot first shows a slow increase of the resonance energy from 2.1 to 2.3 eV as the groove width decreases from 250 nm down to 100 nm. This behaviour is then followed by a stronger blueshift from 2.3 to 2.6 eV for widths decreasing from 100 to 5 nm. Numerically calculated EELS data of groove waveguides (to be discussed below) display the same trend, and we therefore interpret the dependence $E(W)$ as a result of two (spectrally close) modes being excited simultaneously but with different strengths that depend on the position of the electron probe. For widths $W \gtrsim 100$ nm, the MIM aGSP mode is weakly excited because of the increased distance between the electron and the metal–insulator interfaces. This suggests the excitation of localized SPs supported by the top of the grooves.

Accordingly, the slow increase in resonance energy as the groove width decreases from 250 nm down to 100 nm represents the transition from localized SP excitations to propagating MIM aGSP modes. In the case of groove widths $W \lesssim 100$ nm, on the other hand, the MIM aGSP mode dominates the EELS data, which is signified by the strong dependence of the resonance peak on the groove width. We note that the MIM aGSP resonance energy in the crevice is very close to the measured bulk mode resonance energy of gold (2.7 eV; black solid line in Fig. 3c), which makes it difficult to experimentally distinguish the two modes. For extremely narrow groove widths ($W < 10$ nm), the field delocalization of the electron beam[32] will eventually cause interactions with the bulk plasmons even for perfectly straight grooves. In the real experiment, additional effects of surface roughness of the walls, as well as from the convergence angle of the focused electron probe will be present. This convergence semi-angle is $\sim$16 mrad, resulting in the displacement of the electron trajectory from the straight-line path by $\sim$2.5 nm at the exit of the groove (under the assumption that the focus point of the beam is at the front plane of the groove). Thus, at very narrow widths, there is the possibility that both MIM aGSP and bulk plasmons are excited. Owing to the energy resolution of the microscope (0.15 ± 0.05 eV), it therefore becomes increasingly difficult to distinguish between the MIM aGSP resonance energy (at 2.6 eV) and the resonance energy of bulk gold (at 2.7 eV) in the EELS data. In fact, we cannot distinguish the two resonance peaks from a single spectrum, as their difference in energy is below the resolution of the microscope. However, depending on the exact position of the electron probe, we can excite one resonance more efficiently than the other, allowing us to determine the energy of one resonance in particular. This effect is visible in the spread of the resonance energies for narrow widths in Fig. 3c, and is also confirmed in the histogram in Fig. 3d. This histogram represents the statistics of all measured energy positions of resonance peaks (in both Grooves 1 and 2), that is, the data points in Fig. 3c projected onto the energy axis and binned into energy intervals of 0.04 eV. The histogram shows a larger number of counts both at the resonance energy of the MIM aGSP mode (at 2.6 eV) and at the bulk plasmon energy of gold (at 2.7 eV), with a dip in between these energies, thus supporting the interpretation that two different resonances close in energy are present.

The two different grooves in Fig. 3c show almost identical trends for the EELS peaks, indicating that the shape variation from groove to groove is small. More astonishing is that both grooves support MIM aGSPs in even extremely narrow gaps of only 5 nm. The two energy-shift regions, that is, the slow increase for $W \gtrsim 100$ nm and the faster increase for $W \lesssim 100$ nm, and the presence of the MIM aGSP close to the bulk plasmon energy in ultra-narrow gaps, are also observed for all other grooves studied during this work (Supplementary Fig. 3). In addition, note that the interpretation of the EELS peak from the wide part of the grooves ($W \gtrsim 100$ nm) as a localized SP resonance is in agreement with control experiments, in which a thinning of a sample resulted in a blueshift of the EELS peak for the wide region in the top part of the groove (Supplementary Fig. 6 and Supplementary Note 3), thus representing the expected blueshift of localized SPs

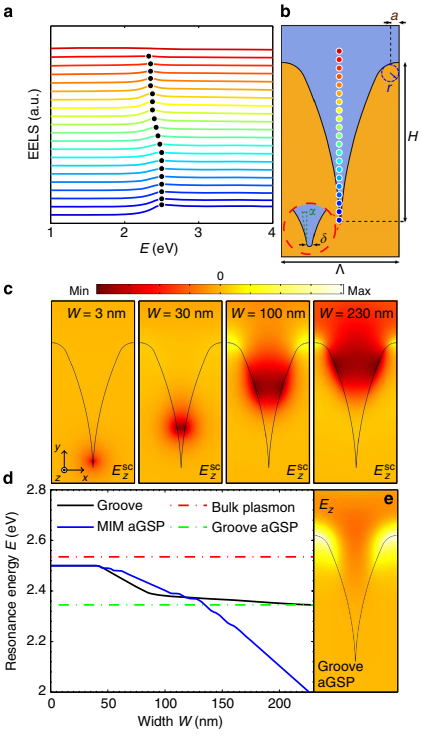

Figure 4 | Theoretical EELS data. (**a**) Waterfall plot of theoretical EELS calculations at the corresponding position indicated on the groove model in **b**. (**c**) Longitudinal component of the scattered electric field (total E-field subtracted the E-field of the electron) for an electron beam probing at the resonance energy of four different groove widths W. (**d**) Peak resonance energy determined from EELS calculations as a function of width for the groove model in **b** (black line), MIM (Au-SiO_2-Au) waveguide (blue line), and bulk gold (red dash-dotted line). The green dash-dotted line represents the resonance energy of the groove aGSP mode. (**e**) Longitudinal component of the electric field of the groove aGSP mode at $E = 2.35$ eV. Permittivity for gold is taken from ref. 33. We use $\varepsilon_{SiO_2} = 2.1$.

for structures with either reduced sizes or decreasing aspect ratios in the direction parallel to the polarization of the applied electric field (Supplementary Note 3).

Numerical simulations. To support the interpretation of the experimental EELS data in Fig. 3, we have performed fully retarded EELS calculations using the commercial software COMSOL Multiphysics (see Methods section). For the numerical analysis, we consider the nanogroove structure to be infinite in the direction of the electron beam, that is, z direction, which allows us to simplify the problem to two dimensional (2D). Although the finite thickness of the sample is thus neglected, we can still expect the 2D approximation to be accurate for narrow groove widths (which is the region of interest), in which the width-to-sample thickness ratio is low. In addition, in the interpretation of the EELS spectra, the 2D approximation allows us to emphasize the importance of propagating MIM and groove GSP modes, which are typically properties of extended waveguide structures. Finally, we assume that the groove has perfect mirror symmetry, thereby neglecting any slight geometric asymmetries present in the sample.

The results of the theoretical analysis are summarized in Fig. 4. Figure 4a shows calculated EELS data at the electron beam positions indicated in Fig. 4b, displaying flat spectra with distinct resonances visible, in accordance with our experimental measurements. Furthermore, the same blueshift trend of the resonance peak is present in our simulations when the position of the electron probe is moved towards the bottom of the groove. The SP resonance shifts from $\sim$2.3 to 2.5 eV. In Fig. 4d, the black line displays the calculated resonance energy as a function of the groove width. We see that the initial slow blueshift for $W \gtrsim 100$ nm followed by a steep blueshift for $W \lesssim 100$ nm is accurately captured in our theoretical model. Furthermore, for $W \lesssim 50$ nm, the calculations show a plateau at the resonance energy of 2.5 eV, which is close to the bulk plasmon energy of gold (red dash-dotted line). This is again in excellent agreement with our experimental observations, although the bulk plasmon energy of gold from the data in ref. 33 is slightly lower than the bulk plasmon energy of our sample (at 2.7 eV; Fig. 3c). Figure 4c displays the longitudinal component of the scattered E-field for an electron beam probe at the resonance energy of four different groove widths, demonstrating that the MIM aGSP mode is indeed excited for widths $W \lesssim 100$ nm, as confirmed by the local field distribution in the convex groove (for induced-charge distributions, see Supplementary Fig. 4). In contrast, we see a noticeable field distribution at the top of the groove for $W \gtrsim 100$ nm, indicating the excitation of a groove aGSP mode (that is, symmetric induced-charge distribution). As revealed by mode analysis (Supplementary Fig. 2), the groove waveguide under study supports a single groove aGSP mode whose mode profile (Fig. 4e) agrees well with the field generated by the electrons in the top of the groove. This interpretation is further substantiated by the fact that the energy of the EELS resonance peak in Fig. 4d approaches the energy of the groove aGSP mode (green dash-dotted line) for large groove widths. Finally, the peculiar dispersion of the single peak observed in the theoretical EELS data originates from the strong excitation of MIM aGSP modes in the bottom of the groove, with decreasing strength as the electron probe moves up the groove, while at the same time the excitation efficiency of the groove aGSP mode increases. It should be emphasized that the explanations for levelling of the EELS peak dependence for larger groove widths are different for our experimental results (Fig. 3c) and 2D simulations (Fig. 4d), as, for the former (as argued above), this occurs because of the excitation of the localized SP resonance.

MIM model. To test the analogy between the MIM aGSP mode excited in convex grooves and the corresponding mode in MIM waveguides, we have also performed EELS calculations on the MIM (Au–SiO_2–Au) waveguide. As in the simulations of the groove, we position the electron probe in the centre of the MIM waveguide and calculate the resonance energy of the MIM aGSP mode as a function of the width of the insulating layer. The blue line in Fig. 4d displays the main result, while the almost identical EELS spectra for the two types of waveguides can be seen in Supplementary Fig. 5. We see that the energy of the EELS peak is close, for $W \lesssim 125$ nm, to that pertaining to the MIM aGSP mode, becoming identical for $W \lesssim 50$ nm. From dispersion relation calculations of the MIM waveguide (Supplementary Fig. 1), we also find that the propagation length of the MIM aGSP mode at the resonance energy (2.5 eV) is below 10 nm for a MIM waveguide with a width of 50 nm. Furthermore, the propagation length decreases with decreasing width, thus supporting the validity of the 2D approximation in our calculations when in the bottom of the groove.

When comparing the experimental EELS measurements with the theoretical groove simulations, we find that the experimentally measured resonance energy spans a broader range (2.1–2.6 eV) compared with the simulations (2.3–2.5 eV). As argued earlier, we attribute the discrepancy at narrow widths ($W \lesssim 50$ nm) to the difference in the permittivity of gold found in ref. 33 used in our theoretical calculations and the permittivity of the gold in our sample. We substantiate this point of view by the fact that the procedure of thinning the sample using FIB leads to some gallium contamination and surface amorphization of the gold, which (depending on the FIB conditions used) can influence up to tens of nanometres for each of the groove surfaces[34,35]. Note that despite the fact that this (probably) FIB-related damage affects the gold permittivity in the entire energy range considered, the discrepancy between measurements and 2D simulations at large groove widths ($W \gtrsim 100$ nm) is in any case expected as the EELS peaks are related to physically different phenomena (three-dimensional (3D) localized SP and 2D groove aGSP mode, respectively).

The results obtained in the course of our EELS study allow us to add an important element to the interpretation of very efficient and broadband light absorption by ultra-sharp convex grooves in gold[25]. The incident light, which propagates downwards (that is, in the xy plane) for this purpose, couples through scattering off the groove wedges to the MIM sGSP mode (not probed by our EELS setup), which is adiabatically focused and, consequently, absorbed as it propagates into the depth of the groove. Quite surprisingly, the experimental measurements showed even better light absorption than the simulations. Those simulations were based on a completely symmetric groove geometry and (for the most part) normally incident light. However, the grooves are neither perfectly symmetric, as discussed in the context of Fig. 2, nor is the light in the experimental setup a perfect plane wave impinging normally to the surface. Thus, incoming light will, owing to the inclined propagation and the slight asymmetry of the groove, in practice also couple to the significantly more lossy MIM aGSP mode, which we studied here with EELS. In fact, it was already shown in the Supplementary Information of ref. 25 that a small inclined angle ($\sim$20°) of the incident light moderately improves the overall absorption, which we can now ascribe to excitation of the MIM aGSP mode. It should be stressed that the introduction of a small asymmetry results in a weak excitation of the MIM aGSP mode, so that the absorption is still dominated by the MIM sGSP mode. In addition, we have performed light-scattering simulations of slightly asymmetric grooves with normal incident light (Supplementary Fig. 7 and Supplementary Note 4), which confirm the increased (by $\sim$40%) absorption relative to the symmetric configuration.

Discussion

We have reported the application of EELS to the characterization of extremely confined GSP modes excited by electrons in nanometre-wide gaps. Using ultra-sharp convex grooves in gold, we have recorded the EELS data with high-spatial (<1 nm) and energy (~ 0.15 eV) resolution in the mirror-symmetry plane of the groove cross-section. Both experimental and theoretical EELS data have revealed resonance behaviour associated with the excitation of the antisymmetric MIM GSP mode for extremely small gap widths, down to ~ 5 nm. We believe that the excitation of this mode, featuring very strong absorption, can be related to the experimental results obtained in the recent study devoted to the phenomenon of plasmonic black gold, in which very efficient and broadband light absorption by ultra-sharp convex grooves has been observed[25]. Since, as opposed to simulations used to account for the observed effect, realistically fabricated grooves are not perfectly symmetric, a part of the unexpectedly strong light absorption in the grooves can be ascribed to the MIM aGSP excitation owing to fabrication-induced asymmetry (Supplementary Fig. 7 and Supplementary Note 4). We note that such a direct comparison between EELS measurements and optical response is in general possible but challenging, as electrons and photons excite different linear combinations of plasmonic eigenstates[36–38]. Furthermore, complications in carrying out EELS and optical spectroscopy under different environmental conditions can lead to slight energy shifts when confronting the two types of spectra (see ref. 39 and references therein).

Finally, it should be stressed that the MIM aGSP mode excitation should be expected to occur at any asymmetric junction/bend of GSP-based (gap or slot) plasmonic waveguides typically used in various plasmonic circuits[31,40,41]. The aGSP mode absorption thereby represents an additional (efficient) channel of energy dissipation that should be taken into account in the design of plasmonic nanophotonic circuits and devices.

Methods

Fabrication. The samples were prepared by first depositing 1.8-μm-thick gold films on a plasma-cleaned Si substrate by direct current sputtering at a deposition rate of 1 Å s^{-1}. Arrays of ultra-sharp grooves in gold were fabricated using a cross-beam system (FIB and scanning electron microscope), where a beam with a constant current (50 pA) of Ga^+ ions is focused onto the gold surface at normal incidence, with the position of the beam controlled by a lithography system. To fabricate deep and narrow grooves, several consecutive runs (using single-line writing) of each groove were performed. Using this method, a 350-nm-period 1D array of ultra-sharp convex grooves featuring practically parallel walls at the bottom were fabricated.

The array of grooves was then filled and covered with a ~ 500 nm SiO_2 layer by *in situ* deposition utilizing a gas injection system and e-beam deposition with the electron column. A layer of platinum was then deposited in order to protect the array of grooves. The TEM lamella was cut free on three sides and at the bottom (in the Si substrate) before welding the lamella to an etched tungsten tip using *in situ* platinum deposition. The lamella was detached from the sample using the FIB and welded on a TEM grid using the gas injection system. Finally, the lamella was carefully thinned to ~ 150 nm with the FIB to allow investigation in the TEM.

EELS measurements. The EELS measurements were performed with a FEI Titan TEM equipped with a monochromator and a probe aberration corrector. The microscope was operated in STEM mode at an acceleration voltage of 300 kV, providing a probe diameter of 0.5 nm and a zero-loss peak width of 0.15 ± 0.05 eV. The EELS data were recorded using both automated line-scan acquisition and single-spectrum acquisition, with optimized acquisition times ranging from 80 ms to 2.5 s, where the longer acquisition times were needed close to the groove crevice and also when acquiring spectra through the bulk gold. To further improve the signal-to-noise ratio, we summed up to 20 spectra for each measurement point.

The EELS data were analysed by first removing the zero-loss peak using the reflected-tail method[42]. Afterwards, the resonances were fitted to Gaussian functions using a nonlinear least-squares fit, from which the resonance energies were extracted. The error in the resonance energy is given by the 95% confidence interval for the estimate of the position of the centre of the Gaussian function. Our conclusions remain unchanged when performing data analysis beyond the reflected-tail method, that is, with a power-law removal of the zero-loss peak combined with the elimination of the above-plasmon resonance background because of substrate effects[43].

Image analysis. The analysis of the STEM images were done in MATLAB. To connect the depth of the groove and the position of the electron probe with the width of the groove, we considered each horizontal line of pixels of the image separately. The greyscale in the dark-field STEM images is primarily determined by the atomic number of the material and the thickness of the sample crossed by the electron probe. The former explains the image intensity difference between the SiO_2 and the gold layers, that is, lower image intensity for SiO_2 than gold. In order to determine the position of the interface between the gold and the SiO_2, we looked for the steepest change in intensity in each line of pixels. We numerically determined the derivative of the intensity profile for each line that showed two peaks corresponding to the steepest changes on each interface of the groove. For a perfectly sharp intensity change, that is, a Heaviside step function, the derivative will give a Dirac function, whereas for a more gradual change of intensity the derivative will give a Gaussian-like function, which is akin to the derivative of the error function in statistics. Subsequently, we fitted these two peaks to Gaussian functions, and the difference between the centres of these functions gave us the corresponding width of the groove. We quantified the error in the groove width as the sum of the FWHMs of the two Gaussian functions. The errors are plotted as horizontal bars in Fig. 3 and in Supplementary Figs 3 and 6c. This conservative estimate for the error accounts for the convolution of the electron probe profile with the structure (on the order of the spatial resolution of the beam (~ 0.5 nm)), the surface roughness of the gold surface in the groove, misalignment of the axis of the electron probe compared with the axis of the groove and other sources of indeterminacy, such as the possible residues left in the bottom of the groove by the FIB milling.

Simulations. All modelling results are performed using the commercially available finite-element software (COMSOL Multiphysics, version 4.3b). In the calculations, we only model a single unit cell of the 1D groove array, applying periodic boundary conditions to the vertical sides of the cell. The parameters used for the single symmetric unit cell of the groove model in Fig. 4b are $\Lambda = 317$ nm, $H = 467$ nm, $a = 85$ nm, $r = 60$ nm, $\delta = 0.5$ nm and $\alpha = 2°$. The lower boundary of the simulation domain, representing the truncation of the optically thick gold substrate, behaves as a perfect electric conductor, while the SiO_2 glass domain above the grooves is truncated using perfectly matched layers. The electron beam, moving in the z direction (that is, the direction of invariance), is modelled as an out-of-plane line current $j_z(\mathbf{R},\omega) = ev\delta(\mathbf{R}-\mathbf{R}_0)e^{-ik_z z}$, where δ is the Dirac delta function and $\mathbf{R} = (x,y)$ with $\mathbf{R}_0 = (x_0,y_0)$ being the transverse location of the electron beam. Here, e is the charge of the electron, $v = 0.776c$ is the electron speed corresponding to an acceleration voltage of 300 keV, c is the speed of light in vacuum, and $k_z = \omega/v$. The loss probability Γ_{EELS}, which is proportional to the measured EELS spectra, can be calculated as $\Gamma_{\mathrm{EELS}}(\omega) = ev/(\pi\hbar\omega)\mathrm{Re}\{E_z^{\mathrm{ind}}(\mathbf{R}_0,\omega)\}$, where $\hbar$ is the reduced Planck constant and E_z^{ind} is the z component of the induced electric field at the position of the electron[7]. The permittivity of gold is described by interpolated experimental values[33], whereas the permittivity of SiO_2 assumes the constant value $\varepsilon_{SiO_2} = 2.1$ in the considered energy range. Note that a related COMSOL approach was recently used in an independent study of bow-tie antennas[44], but alternative modelling packages exist[45,46].

References

1. Gramotnev, D. K. & Bozhevolnyi, S. I. Plasmonics beyond the diffraction limit. *Nat. Photonics* **4,** 83–91 (2010).
2. Gramotnev, D. K. & Bozhevolnyi, S. I. Nanofocusing of electromagnetic radiation. *Nat. Photonics* **8,** 14–23 (2014).
3. Hao, E. & Schatz, G. C. Electromagnetic fields around silver nanoparticles and dimers. *J. Chem. Phys.* **120,** 357–366 (2004).
4. Vazquez-Mena, O., Sannomiya, T., Villanueva, L., Voros, J. & Brugger, J. Metallic nanodot arrays by stencil lithography for plasmonic biosensing applications. *ACS Nano* **5,** 844–853 (2011).
5. Lal, S., Clare, S. & Halas, J. Nanoshell-enabled photothermal cancer therapy: impending clinical impact. *Acc. Chem. Res.* **41,** 1842–1851 (2008).
6. Bozhevolnyi, S. I., Volkov, V. S., Devaux, E., Laluet, J.-Y. & Ebbesen, T. W. Channel plasmon subwavelength waveguide components including interferometers and ring resonators. *Nature* **440,** 508–511 (2006).
7. García de Abajo, F. J. Optical excitations in electron microscopy. *Rev. Mod. Phys.* **82,** 209–275 (2010).
8. Nicoletti, O. *et al.* Three-dimensional imaging of localized surface plasmon resonances of metal nanoparticles. *Nature* **502,** 80–84 (2013).
9. Ritchie, R. H. Plasma losses by fast electrons in thin films. *Phys. Rev.* **106,** 874–881 (1957).
10. Ouyang, F., Batson, P. & Isaacson, M. Quantum size effects in the surface-plasmon excitation of small metallic particles by electron-energy-loss spectroscopy. *Phys. Rev. B* **46,** 15421–15425 (1992).
11. Nelayah, J. *et al.* Mapping surface plasmons on a single metallic nanoparticle. *Nat. Phys.* **3,** 348–353 (2007).

12. Bosman, M., Keast, V. J., Watanabe, M., Maaroof, A. I. & Cortie, M. B. Mapping surface plasmons at the nanometre scale with an electron beam. *Nanotechnology* **18,** 165505 (2007).
13. Koh, A. L. *et al.* Electron energy-loss spectroscopy (EELS) of surface plasmons in single silver nanoparticles and dimers: Influence of beam damage and mapping of dark modes. *ACS Nano* **3,** 3015–3022 (2009).
14. Scholl, J. A., Koh, A. L. & Dionne, J. A. Quantum plasmon resonances of individual metallic nanoparticles. *Nature* **483,** 421–427 (2012).
15. Raza, S. *et al.* Blueshift of the surface plasmon resonance in silver nanoparticles studied with EELS. *Nanophotonics* **2,** 131–138 (2013).
16. Pettit, R. B., Silcox, J. & Vincent, R. Measurement of surface-plasmon dispersion in oxidized aluminum films. *Phys. Rev. B* **11,** 3116–3123 (1975).
17. Rossouw, D., Couillard, M., Vickery, J., Kumacheva, E. & Botton, G. A. Multipolar plasmonic resonances in silver nanowire antennas imaged with a subnanometer electron probe. *Nano Lett.* **11,** 1499–1504 (2011).
18. Nicoletti, O. *et al.* Surface plasmon modes of a single silver nanorod: an electron energy loss study. *Opt. Express* **19,** 15371–15379 (2011).
19. Rossouw, D. & Botton, G. A. Plasmonic response of bent silver nanowires for nanophotonic subwavelength waveguiding. *Phys. Rev. Lett.* **110,** 066801 (2013).
20. Prade, B., Vinet, J. Y. & Mysyrowicz, A. Guided optical waves in planar heterostructures with negative dielectric constant. *Phys. Rev. B* **44,** 13556–13572 (1991).
21. Kuttge, M., Cai, W., García de Abajo, F. J. & Polman, A. Dispersion of metal-insulator-metal plasmon polaritons probed by cathodoluminescence imaging spectroscopy. *Phys. Rev. B* **80,** 033409 (2009).
22. Hu, H. *et al.* Photoluminescence via gap plasmons between single silver nanowires and a thin gold film. *Nanoscale* **5,** 12086–12091 (2013).
23. Economou, E. N. Surface plasmons in thin films. *Phys. Rev.* **182,** 539–554 (1969).
24. Raza, S., Christensen, T., Wubs, M., Bozhevolnyi, S. I. & Mortensen, N. A. Nonlocal response in thin-film waveguides: loss versus nonlocality and breaking of complementarity. *Phys. Rev. B* **88,** 115401 (2013).
25. Søndergaard, T. *et al.* Plasmonic black gold by adiabatic nanofocusing and absorption of light in ultra-sharp convex grooves. *Nat. Commun.* **3,** 969 (2012).
26. Bozhevolnyi, S. I. & Jung, J. Scaling for gap plasmon based waveguides. *Opt. Express* **16,** 2676–2684 (2008).
27. Miyazaki, H. T. & Kurokawa, Y. Squeezing visible light waves into a 3-nm-thick and 55-nm-long plasmon cavity. *Phys. Rev. Lett.* **96,** 097401 (2006).
28. Dionne, J. A., Lezec, H. J. & Atwater, H. A. Highly confined photon transport in subwavelength metallic slot waveguides. *Nano Lett.* **6,** 1928–1932 (2006).
29. Shin, H. & Fan, S. All-angle negative refraction for surface plasmon waves using a metal-dielectric-metal structure. *Phys. Rev. Lett.* **96,** 073907 (2006).
30. Lezec, H. J., Dionne, J. A. & Atwater, H. A. Negative refraction at visible frequencies. *Science* **316,** 430–432 (2007).
31. Huang, K. C. Y. *et al.* Electrically driven subwavelength optical nanocircuits. *Nat. Photonics* **8,** 244–249 (2014).
32. Muller, D. & Silcox, J. Delocalization in inelastic scattering. *Ultramicroscopy* **59,** 195–213 (1995).
33. Johnson, P. B. & Christy, R. W. Optical constants of the noble metals. *Phys. Rev. B* **6,** 4370–4379 (1972).
34. McCaffrey, J., Phaneuf, M. & Madsen, L. Surface damage formation during ion-beam thinning of samples for transmission electron microscopy. *Ultramicroscopy* **87,** 97–104 (2001).
35. Kato, N. I. Reducing focused ion beam damage to transmission electron microscopy samples. *J. Electron Microsc.* **53,** 451–458 (2004).
36. García de Abajo, F. J. & Kociak, M. Probing the photonic local density of states with electron energy loss spectroscopy. *Phys. Rev. Lett.* **100,** 106804 (2008).
37. Hohenester, U., Ditlbacher, H. & Krenn, J. R. Electron-energy-loss spectra of plasmonic nanoparticles. *Phys. Rev. Lett.* **103,** 106801 (2009).
38. Christensen, T. *et al.* Nonlocal response of metallic nanospheres probed by light, electrons, and atoms. *ACS Nano* **8,** 1745–1758 (2014).
39. Husnik, M. *et al.* Comparison of electron energy-loss and quantitative optical spectroscopy on individual optical gold antennas. *Nanophotonics* **2,** 241–245 (2013).
40. Cai, W., Shin, W., Fan, S. & Brongersma, M. L. Elements for plasmonic nanocircuits with three-dimensional slot waveguides. *Adv. Mater.* **22,** 5120–5124 (2010).
41. Kriesch, A. *et al.* Functional plasmonic nanocircuits with low insertion and propagation losses. *Nano Lett.* **13,** 4539–4545 (2013).
42. Egerton, R. F. *Electron Energy-Loss Spectroscopy in the Electron Microscope* 3rd edn (Springer, 2011).
43. Kadkhodazadeh, S. *et al.* Scaling of the surface plasmon resonance in gold and silver dimers probed by EELS. *J. Phys. Chem. C* **118,** 5478–5485 (2014).
44. Wiener, A. *et al.* Electron-energy loss study of nonlocal effects in connected plasmonic nanoprisms. *ACS Nano* **7,** 6287–6296 (2013).
45. Bigelow, N. W., Vaschillo, A., Iberi, V., Camden, J. P. & Masiello, D. J. Characterization of the electron- and photon-driven plasmonic excitations of metal nanorods. *ACS Nano* **6,** 7497–7504 (2012).
46. Hörl, A., Trügler, A. & Hohenester, U. Tomography of particle plasmon fields from electron energy loss spectroscopy. *Phys. Rev. Lett.* **111,** 076801 (2013).

Acknowledgements

The Center for Nanostructured Graphene is sponsored by the Danish National Research Foundation, Project DNRF58. The A. P. Møller and Chastine Mc-Kinney Møller Foundation is gratefully acknowledged for the contribution towards the establishment of the Center for Electron Nanoscopy. N.S. acknowledges financial support by a Lundbeck Foundation grant no. R95-A10663; A.P., T.H., K.P. and S.I.B. acknowledge financial support from the Danish Council for Independent Research (FTP contract no. 09-072949 ANAP).

Author contributions

N.S., S.I.B. and N.A.M. conceived the experiment; S.K. aligned the microscope and imaged the sample; S.R., N.S. and S.K. performed the EELS measurements; S.R. and N.S. performed the EELS data analysis; S.R. and J.B.W. performed the sample thickness analysis; A.P. and S.R. performed the simulations; T.H. and K.P. fabricated the sample with groove arrays. All authors were involved in discussing the results obtained and in writing the manuscript.

Additional information

Supplementary Information accompanies this paper at http://www.nature.com/naturecommunications

Competing financial interests: The authors declare no competing financial interests.

Reprints and permission information is available online at http://npg.nature.com/reprintsandpermissions/

How to cite this article: Raza, S. *et al.* Extremely confined gap surface-plasmon modes excited by electrons. *Nat. Commun.* 5:4125 doi: 10.1038/ncomms5125 (2014).

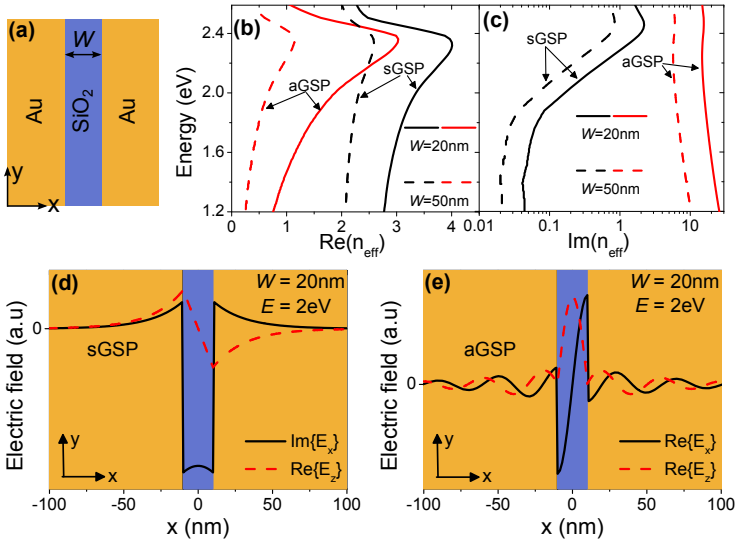

Supplementary Figure 1: Gap surface plasmon modes in MIM waveguides. (a) Sketch of MIM waveguide, consisting of a SiO_2 spacer of width W sandwiched between two semi-infinite gold substrates. MIM GSP modes propagate along the z-direction. **(b,c)** Dispersion relation for MIM symmetric and antisymmetric GSP modes (MIM sGSP and aGSP, respectively) for $W = 20\,\text{nm}$ and $W = 50\,\text{nm}$. The permittivity of gold is taken from experimental data[1] and $\varepsilon_{SiO_2} = 2.1$. **(d,e)** Electric-field profiles calculated for MIM configuration with $W = 20\,\text{nm}$ and energy $E = 2\,\text{eV}$ for the MIM sGSP and aGSP, respectively.

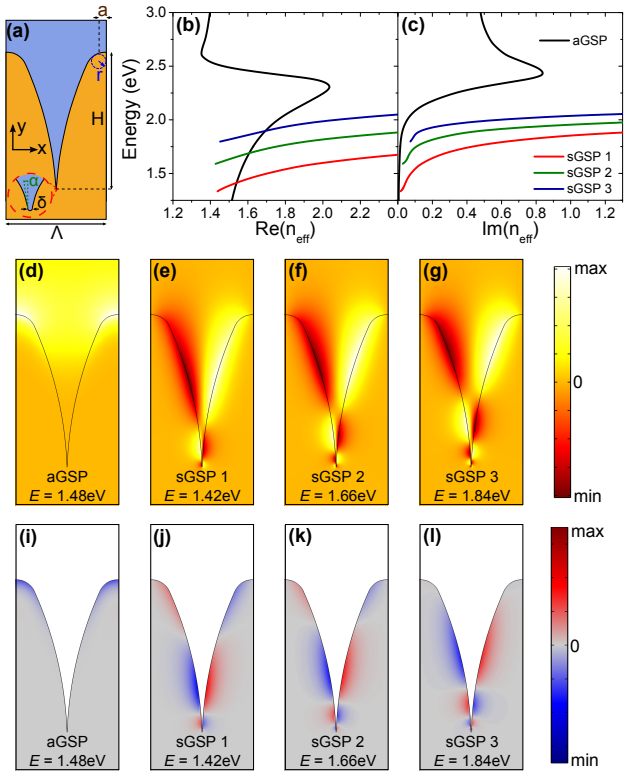

Supplementary Figure 2: Groove GSP modes in convex grooves. **(a)** Sketch of convex gold groove surrounded by SiO_2. **(b,c)** Dispersion relation of four different groove GSP modes in the energy interval 1.25-3 eV: one antisymmetric and three symmetric modes are displayed. **(d-g)** Longitudinal electric field component (E_z) and **(i-l)** charge distribution at energies corresponding to $\mathrm{Re}\{n_{\mathrm{eff}}\} = 1.55$ for the four different modes.

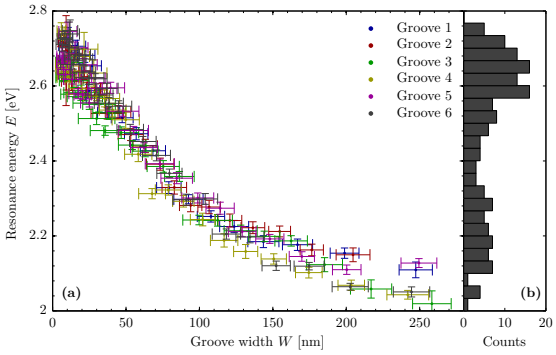

Supplementary Figure 3: Peak resonance energy as a function of groove width. (a) Measured EELS peak as a function of groove width for six different grooves. The vertical error bars correspond to the 95% confidence interval for the estimate of the position of the resonance energy in our experimental data and the horizontal error bars represent the indeterminacy in measuring the width of the grooves based on the intensity contrast in our STEM images (see Methods). **(b)** Histogram displaying the number of resonance energies within bin intervals of 0.03 eV [projection of data in **(a)** onto the E-axis], corresponding to the average energy error bar size. In the main text we address two grooves (named grooves 1 and 2) both belonging to the main sample. Here, (a) confirms the consistency in measurements for other grooves in the same sample. Moreover, we see a weak blueshift for widths $W \gtrsim 100$ nm followed by a stronger blueshift for $W \lesssim 100$ nm, while (b), showing two maxima for $E \gtrsim 2.6$ eV with a noticeable reduction of bin counts in between, indicates the presence of two resonance energies in the bottom of the groove: the excitation of the MIM aGSP mode at ~ 2.6 eV and the bulk plasmon of gold at ~ 2.7 eV.

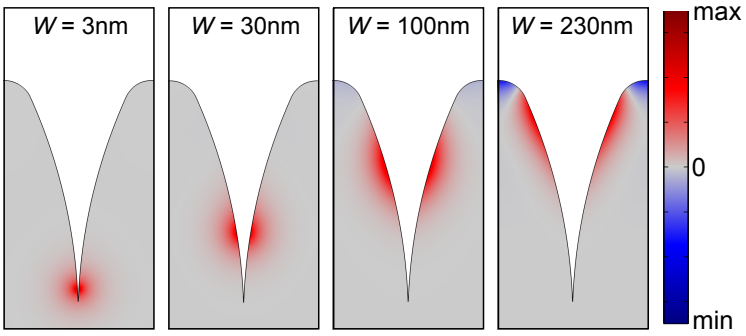

Supplementary Figure 4: EELS induced-charge plots at the resonance energy of four different groove widths. The panels show calculations of induced charge distributions in the convex groove studied in the main text for the electron beam positioned at four different widths W, but in each case at the corresponding resonance energy. The resonance energies for the four widths W =3, 30, 100, and 230 nm are E =2.5, 2.5, 2.38, and 2.35 eV, respectively. The induced charge distribution is calculated from the requirement of charge conservation, leading to $\rho = -i/\omega \nabla \cdot \mathbf{J}_{\text{ind}}$ (time convention: $e^{-i\omega t}$) where ω is the angular frequency, $\mathbf{J}_{\text{ind}} = -i\omega\varepsilon_0(\varepsilon_{\text{m}} - \varepsilon_{\text{d}})\mathbf{E}$ is the induced current, ε_0 is the vacuum permittivity, ε_{d} is the relative permittivity of the dielectric, ε_{m} is the relative permittivity of the metal, and $\mathbf{E}$ is the electric field in the metal. The induced-charge plots complement Fig. 4(c) in the main text, confirming that only a local excitation (related to the existence of the MIM aGSP mode) occurs in the crevice of the groove.

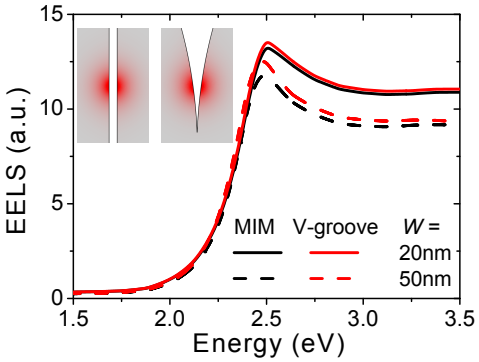

Supplementary Figure 5: EELS spectra for MIM and convex groove waveguides. In the main text we demonstrated perfect agreement between the spectral position of the EELS peak of MIM and groove waveguides for electron beams probing the groove structure below $W \sim 50\,\mathrm{nm}$ (see Fig. 4(d) in the main text). To further substantiate the point that the EELS response in the crevice of convex grooves is determined by the groove width (corresponding to the electron beam position) in the same fashion as that of MIM waveguides, we show EELS calculations for two widths ($W = 20\,\mathrm{nm}$ and $50\,\mathrm{nm}$) of the MIM waveguide and EELS spectra for the electron beam positioned at the corresponding widths in the groove waveguide. EELS spectra are obtained using Comsol Multiphysics with the electron beam positioned at the center line of the two types of waveguides and having the velocity $v = 0.776c$. Metal and insulator are assumed to be gold and SiO_2, respectively. It is clear that the two types of waveguides produce almost identical EELS spectra, both with respect to amplitude and peak positioning (including a nearly identical blue shift of the peak positions for narrower gaps) and with very similar induced-charge distributions.

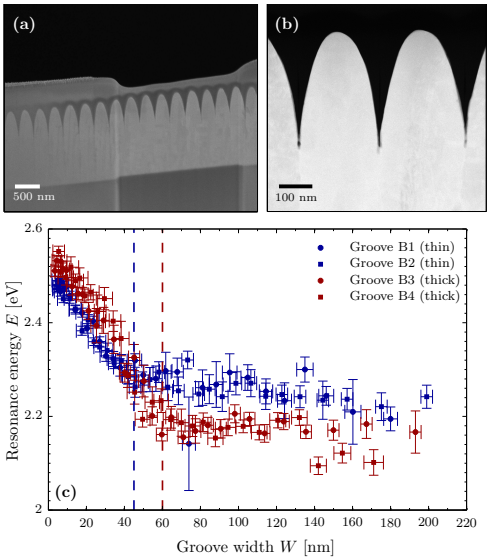

Supplementary Figure 6: Control experiment. **(a)** SEM image of the control sample after thinning further down a 5 μm-wide section. A clear step in thickness separates the thin (right side of the image) and the thick (left side of the image) part of the sample. **(b)** Zoom-in on grooves located in the thin part of the sample. **(c)** Peak resonance energy as a function of groove width for two different grooves belonging to the thin part (grooves B1 and B2) and two other grooves belonging to the thick part (grooves B3 and B4). The vertical error bars correspond to the 95% confidence interval for the estimate of the position of the resonance energy in our experimental data and the horizontal error bars represent the indeterminacy in measuring the width of the grooves based on the intensity contrast in our STEM images (see Methods).

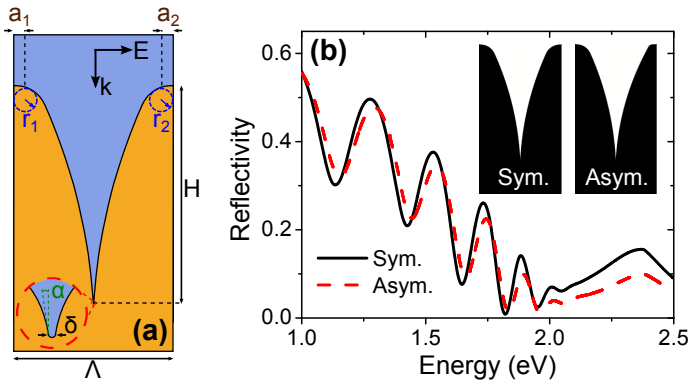

Supplementary Figure 7: Reflection from groove arrays. (a) Geometrical parameters defining the profile of the groove arrays. The small asymmetry in the groove profile is introduced by choosing $a_1 \neq a_2$ and $r_1 \neq r_2$. **(b)** Reflection spectra for normal incident light for a symmetric ($a_1 = a_2 = 85$ nm and $r_1 = r_2 = 60$ nm) and asymmetric ($a_1 = 85$ nm, $a_2 = 50$ nm, $r_1 = 60$ nm, and $r_2 = 20$ nm) groove array. The other parameters are as in the main text: $\Lambda = 317$ nm, $H = 467$ nm, $\delta = 0.5$ nm, and $\alpha = 2°$. The metal is assumed to be gold with permittivity taken from the supplementary material of Ref. 1, whereas the dielectric medium is SiO_2 with permittivity $\varepsilon_{SiO_2} = 2.1$. Inset shows profiles of the considered grooves.

Supplementary Note 1: Metal-insulator-metal waveguides

Metal-insulator-metal (MIM) waveguides support surface TM waves whose magnetic field component, cf. Supplementary Fig. 1(a), takes the form $H_y = A(x)e^{i\beta z}$, where β is the propagation constant. Due to the symmetry of the waveguide, the amplitude function $A(x)$ can either be symmetric or antisymmetric with respect to the center line, thus leading to two types of modes with dispersion relations given by[2–4]

$$\tanh\left(\frac{1}{2}\kappa_{\mathrm{d}}W\right) = -\begin{cases} \frac{\varepsilon_{\mathrm{d}}\kappa_{\mathrm{m}}}{\varepsilon_{\mathrm{m}}\kappa_{\mathrm{d}}}, & \text{(symmetric)} \\ \frac{\varepsilon_{\mathrm{m}}\kappa_{\mathrm{d}}}{\varepsilon_{\mathrm{d}}\kappa_{\mathrm{m}}}, & \text{(antisymmetric)} \end{cases}, \tag{1}$$

where W is the width of the dielectric spacer, ε_{d} is the relative permittivity of the dielectric, ε_{m} is the relative permittivity of the metal, $\kappa_{\mathrm{m}} = \sqrt{\beta^2 - k_0^2\varepsilon_{\mathrm{m}}}$, $\kappa_{\mathrm{d}} = \sqrt{\beta^2 - k_0^2\varepsilon_{\mathrm{d}}}$, and k_0 is the free-space wave number. The two modes are also known as the MIM symmetric and antisymmetric gap surface plasmon modes (MIM sGSP and aGSP, respectively), where MIM sGSP is the most frequently studied mode as it is the only mode that would exist in subwavelength gaps of lossless MIM waveguides. That said, in real MIM waveguides with Ohmic losses the MIM aGSP also subsists and is typically considerably more lossy than the MIM sGSP mode[5]. It should be noted that the nomenclature of the two modes refers to the symmetry of the magnetic (H_y) or, equivalently, electric transversal (E_x) component. Accordingly, in symmetric waveguides [Fig. 1(a)] the MIM sGSP and aGSP are only efficiently probed by light and electron beams, respectively.

Supplementary Fig. 1(b,c) displays solutions of Eq. (1) for a gold-SiO_2-gold waveguide with subwavelength gaps. As expected, the effective refractive index of the two modes, $n_{\mathrm{eff}} = \beta/k_0$, in-

creases with decreasing gap width, showing a maximum in $\mathrm{Re}\{n_{\mathrm{eff}}\}$ at energy $E \simeq 2.35\,\mathrm{eV}$ which corresponds to the surface plasmon resonance. Typical mode profiles of MIM sGSP and aGSP can be found in Supplementary Figs. 1(d) and 1(e), respectively, where the oscillatory behavior of the electric field into the gold for MIM aGSP is a consequence of $\mathrm{Re}\{n_{\mathrm{eff}}\} < \mathrm{Im}\{n_{\mathrm{eff}}\}$.

Supplementary Note 2: Convex groove waveguides

The convex groove waveguide consists of a periodic array of grooves, one of which is sketched in Supplementary Fig. 2(a). The geometrical parameters are the same as those used in the main text: $\Lambda = 317\,\mathrm{nm}$, $H = 467\,\mathrm{nm}$, $\delta = 0.5\,\mathrm{nm}$, $\alpha = 2^{\circ}$, $a = 85\,\mathrm{nm}$, and $r = 60\,\mathrm{nm}$. The corresponding groove GSP modes are then found by assuming a solution of the form $\mathbf{E}(x, y)e^{i\beta z}$ for the electric field, which converts the electric wave equation into an eigenvalue problem for $[\beta, \mathbf{E}]$ that is solved using Comsol Multiphysics. Supplementary Fig. 2(b,c) shows the dispersion relations for groove GSP modes in the interval $1.25 - 3\,\mathrm{eV}$, with longitudinal electric field component and induced charge distribution for the four modes displayed in Supplementary Fig. 2(d-l). Using the same nomenclature as for MIM GSP modes, calculations show three symmetric and one antisymmetric groove GSP mode, where the groove sGSP modes clearly increase in mode order for increasing energy (see the number of nodes in the electric-field profiles along the groove wall). It should be stressed that for an electron beam positioned along the center line of the groove only the groove aGSP mode of Supplementary Fig. 2(d) can be excited, and that this mode, due to its field concentration at the top of the groove, is not probed in the crevice. For this reason, the lower part of the groove is expected to behave similarly to a MIM waveguide with respect to the EELS response for

symmetric excitation.

Supplementary Note 3: Control experiment: The influence of groove thickness

In order to clarify the nature of the two different types of modes, i.e., the presence of localized SP modes on top of the groove and MIM aGSP propagating modes in the crevice, we studied the influence of the thickness (parallel to the axis of the groove) on the resonance energies of the groove. For this purpose, we prepared a second sample (control sample) using the method described in the Methods section. The groove has a similar shape, but with slightly different geometrical parameters. Supplementary Fig. 6(a) displays a SEM image of the control sample with a geometry similar to the main sample (see main text), but with a periodicity of $\Lambda = 250$ nm, and a height of $H = 340$ nm [Fig. 6(b)]. Using the FIB, we thinned down a 5 μm-wide section of the control sample, such that the influence of the sample thickness could be studied, see Fig. 6(a).

We performed EELS measurements on the control sample following the same protocol used for the main sample. For the grooves in the thin and thick parts of the control sample, we acquired a series of EELS spectra from the top to the bottom of the groove, along the mirror-symmetry plane of the groove inside the dielectric section. Additionally, we have taken EELS spectra with a larger energy dispersion (from 0 to 100 eV) and used them to estimate the thickness of the thin and the thick regions of the sample. The results show a constant thickness profile inside the groove for both thin and thick regions of the sample with respective thicknesses of approximately 100 nm and 135 nm.

In Supplementary Fig. 6(c) we plot the energy of the resonance peak as a function of the groove

width for two different grooves belonging to the thin region (grooves B1 and B2) and for two other grooves belonging to the thick region (grooves B3 and B4). Despite the different geometrical parameters (i.e., periodicity and groove height), we observe the same overall behavior for the resonance energies between the main sample and the control sample, i.e., a weakly blueshifting mode for large widths and a more rapid blueshift for widths below approximately 70 nm. Interestingly, we also see a consistent energy difference between the thick and the thin region of the control sample for widths above 70 nm. A more thorough analysis shows that the average energy of these modes for the thick region is 2.18 eV while the average energy is 2.24 eV for the thin region (an energy difference that is slightly larger than the average energy error bar: 0.05 eV). This observation is consistent with the blueshift observed in localized SP excitations for structures with either reduced sizes or decreasing aspect ratios in the direction parallel to the polarization of the applied electric field (See Chapter 12 in supplementary material of Ref. 6).

Moreover, the width at which the blueshift becomes stronger in both parts of the sample is different, as illustrated by the dashed vertical lines in Supplementary Fig. 6(c). The onset of the stronger blueshift appears around 45 nm and 60 nm for the thin and the thick regions, respectively. As mentioned in the main text, propagating plasmons are only expected for widths smaller than the thickness of the sample, in which case the sample can be considered as a two-dimensional system. Hence, reducing the thickness of the sample should lead to the onset of the propagating mode for smaller widths, as we observe experimentally. The fact that the strong blueshift is similar for narrow widths, independent of the exact geometry and thickness of the samples (main sample and control sample), sustains our claim that the modes probed in this region correspond to the

propagating MIM aGSP modes.

Indeed, for a width of 50 nm the calculated propagation constant for the MIM aGSP mode is less than 10 nm, one order of magnitude smaller than the thicknesses measured in both the main sample and the control sample, excluding the possibility that standing or localized modes deep in the groove were probed.

Supplementary Note 4: Reflection from asymmetric groove arrays

With the experimental verification of the presence of the lossy MIM aGSP mode in the crevice of convex groove arrays, it is evident that the mode may play an important role in the strong broadband light absorption that was experimentally observed in similar groove arrays[7]. So far, the strong absorption has been explained by excitation of the MIM sGSP mode at the top of the groove, which is then adiabatically focused and absorbed as it propagates down into the groove[7]. The fabricated structures, however, possess a small degree of asymmetry which, together with inclined incident light, allow for excitation of the MIM aGSP mode that may contribute noticeably to the overall absorption. To test our hypothesis and to explain the unexpectedly high absorption of 'black gold', we have numerically calculated the light reflection from a symmetric and slightly asymmetric groove array for normal incident light. Supplementary Fig. 7(a) shows a sketch of the groove structure and light polarization, while Supplementary Fig. 7(b) presents the calculated reflectivity. It is clear that the effect of slight asymmetry, which we ascribe to the excitation of the MIM aGSP mode, mostly affects the energy region $E > 1.7\,\mathrm{eV}$ with an overall lower reflectivity.

The increased absorption is particularly noticeable for energies $E > 2\,\mathrm{eV}$, with increases as high as $\sim 40\%$ compared to the symmetric configuration.

Supplementary References

1. Johnson, P. B. & Christy, R. W. Optical constants of the noble metals. *Phys. Rev. B* **6**, 4370–4379 (1972).

2. Economou, E. N. Surface plasmons in thin films. *Phys. Rev.* **182**, 539 (1969).

3. Prade, B., Vinet, J. Y. & Mysyrowicz, A. Guided optical waves in planar heterostructures with negative dielectric constant. *Phys. Rev. B* **44**, 13556–13572 (1991).

4. Raza, S., Christensen, T., Wubs, M., Bozhevolnyi, S. I. & Mortensen, N. A. Nonlocal response in thin-film waveguides: Loss versus nonlocality and breaking of complementarity. *Phys. Rev. B* **88**, 115401 (2013).

5. Davoyan, A., Bozhevolnyi, S. I., Kivshar, Y. S. & Shadrivov, I. V. Backward and forward modes guided by metal-dielectric-metal plasmonic waveguides. *J. Nanophoton.* **4**, 043509 (2010).

6. Novotny, L. & Hecht, B. *Principles of Nano-Optics* (Cambridge University Press, Cambridge, 2012), 2nd edn.

7. Søndergaard, T. *et al.* Plasmonic black gold by adiabatic nanofocusing and absorption of light in ultra-sharp convex grooves. *Nat. Commun.* **3**, 969 (2012).

Paper C

N. A. Mortensen, S. Raza, M. Wubs, T. Søndergaard and S. I. Bozhevolnyi

A generalized non-local optical response theory for plasmonic nanostructures

Nat. Commun. **5**, 3809 (2014)

Author contributions
N. A. M, S. I. B, T. S. and M. W. conceived the basic idea. N. A. M. derived the complex response model. S. R. performed all numerical simulations and the analytical analysis of spherical particles. Figures were prepared by N. A. M. and S. R. All authors interpreted and discussed the results and the writing of the manuscript was done in a joint effort.

nature COMMUNICATIONS

ARTICLE

Received 2 Jan 2014 | Accepted 3 Apr 2014 | Published 2 May 2014

DOI: 10.1038/ncomms4809

A generalized non-local optical response theory for plasmonic nanostructures

N.A. Mortensen[1,2], S. Raza[1,3], M. Wubs[1,2], T. Søndergaard[4] & S.I. Bozhevolnyi[5]

Metallic nanostructures exhibit a multitude of optical resonances associated with localized surface plasmon excitations. Recent observations of plasmonic phenomena at the sub-nanometre to atomic scale have stimulated the development of various sophisticated theoretical approaches for their description. Here instead we present a comparatively simple semiclassical generalized non-local optical response theory that unifies quantum pressure convection effects and induced charge diffusion kinetics, with a concomitant complex-valued generalized non-local optical response parameter. Our theory explains surprisingly well both the frequency shifts and size-dependent damping in individual metallic nanoparticles as well as the observed broadening of the crossover regime from bonding-dipole plasmons to charge-transfer plasmons in metal nanoparticle dimers, thus unravelling a classical broadening mechanism that even dominates the widely anticipated short circuiting by quantum tunnelling. We anticipate that our theory can be successfully applied in plasmonics to a wide class of conducting media, including doped semiconductors and low-dimensional materials such as graphene.

[1] Department of Photonics Engineering, Technical University of Denmark, DK-2800 Kongens Lyngby, Denmark. [2] Center for Nanostructured Graphene (CNG), Technical University of Denmark, DK-2800 Kongens Lyngby, Denmark. [3] Center for Electron Nanoscopy, Technical University of Denmark, DK-2800 Kongens Lyngby, Denmark. [4] Department of Physics and Nanotechnology, Aalborg University, DK-9220 Aalborg, Denmark. [5] Department of Technology and Innovation, University of Southern Denmark, DK-5230 Odense, Denmark. Correspondence and requests for materials should be addressed to N.A.M. (email: asger@mailaps.org).

Studies of transport and wave dynamics in complex and confined geometries[1] are now bridging several fields ranging from nanoplasmonics[2–4] and metamaterials[5] to molecular electronics[6] and mesocopic quantum transport[7,8], with, for example, charge carriers responding to externally perturbing fields as well as exhibiting stochastic kinetics and entropic effects such as diffusion[9]. When considering ultrafast responses of optically driven collective plasma oscillations in nanoscale geometries, it is expected that the optical response should exhibit both quantum properties of the electron gas as well as classical diffusion dynamics of the optically induced charge. The coexistence and interplay of quantum and classical effects have profound implications for our understanding of light–matter interactions at the nanoscale, with direct relevance to the emerging field of quantum plasmonics[10].

The behaviour of plasmon resonances of individual silver metallic nanoparticles (MNPs)[11,12] and gold MNP dimers[13] seems to be possible to understand only by invoking quantum-mechanical effects, that is, quantum electron transitions and quantum tunnelling, respectively. At the same time, one might question the necessity of considering numerous quantum-level transitions in nm-sized NPs (that is, consisting of thousands of atoms and with a size much exceeding the Fermi wavelength) in the case of monomers and the very possible existence of ultrafast tunnelling phenomena (that is, tunnelling currents oscillating at optical frequencies) in the case of dimers. While classical electrodynamics in a Drude local response approximation (LRA) unambiguously fails to explain the observed phenomena, we show that the possibility for semiclassical accounts has not been exhausted.

Linear response theory is inherent to our understanding of situations where matter is subject to externally perturbing fields. Common strategies assume a temporally instantaneous and spatially local response, while nature is rich in examples where underlying degrees of freedom are responsible for a much more complex response. Materials exhibiting frequency dispersion are well known for having complex-valued response functions due to Kramers–Kronig relations that originate from the ubiquitous principle of causality. By contrast, spatial dispersion can usually be neglected and most materials are well treated within LRA. Insulators represent a prime example since the polarization of one particular atom in the crystal is only weakly affected by coupling to neighbouring atoms. Conducting media constitute a clear exception to this picture[14,15] and despite the widespread use of LRA approaches, the free carriers may mediate a response over finite distances that cannot necessarily be neglected in a nanoplasmonic context.

In terms of the Maxwell equations, the electrical field in a medium with non-local response is formally governed by

$$\nabla\times\nabla\times\mathbf{E}(\mathbf{r}) = \left(\frac{\omega}{c}\right)^2 \int d\mathbf{r}'\varepsilon(\mathbf{r},\mathbf{r}')\mathbf{E}(\mathbf{r}') \qquad (1)$$

where $\varepsilon(\mathbf{r}, \mathbf{r}')$ is the non-local response function. This general concept of non-local response of conducting media originates from the competing mechanisms of pressure-driven convective flow of charge as well as disorder- or entropy-driven diffusion of charge[14]. Quite surprisingly, while the literature is rich on discussions of the former effect within hydrodynamic models, the importance of the latter in nanoplasmonic systems remains unexplored, and, according to our knowledge, there is no unifying real-space description applicable to realistic plasmonic nanostructures. Pioneering works focused on pressure-driven convective flow of charge in ideal geometries[16–19], while the exploration of non-local response in arbitrarily shaped metal nanostructures has only recently been initiated[20], emphasizing real-space rigorous formulations of semiclassical hydrodynamic equations[21] and different solution strategies[22–26]. Thus, large blueshifts in nanoscale noble metal plasmonic structures[11,27,28] have been interpreted in the context of the quantum pressure-related non-local response[27,28], while quantum confinement[11] and surface-screening[29] explanations have also been proposed.

Here we develop a semiclassical generalized non-local optical response (GNOR) theory that incorporates both quantum pressure effects and induced charge diffusion kinetics. We show that the GNOR approach can account for the main features observed in recent optical experiments with plasmonic nanostructures[11,13,28,30] without accounts for quantized-energy transitions and without invoking quantum tunnelling that should not, as we argue later on, be important at optical frequencies.

Results

Isotropic and short-range non-local response. We take equation (1) as our starting point, while assuming a generic short-range isotropic response. Irrespective of the detailed microscopic mechanism behind the non-local response, the wave equation in the metal can then be reframed as[31]

$$\nabla\times\nabla\times\mathbf{E}(\mathbf{r}) = \left(\frac{\omega}{c}\right)^2\left[\varepsilon_{\mathrm{D}} + \xi^2\nabla^2\right]\mathbf{E}(\mathbf{r}), \qquad (2)$$

where ε_{D} is the Drude dielectric function usually associated with Ohmic local response of the electron gas (possibly generalized to also include interband effects), while the GNOR parameter ξ represents a phenomenological length scale associated with the short-range non-local correction to the local response Drude part. Importantly, the GNOR parameter accounts for mechanisms of very different origins that may compete or play in concert, while causing the same Laplacian-type correction to the LRA. For example, both convection and diffusion can lead to spatial dispersion in conducting media[14]. Within LRA, the induced charge density Δn is a delta function at the surface of the metal and diffusion will naturally smear this charge density with the short-time dynamics characteristic for pure diffusion (Fig. 1c). Also, convection tends to spread the charge density and within the common hydrodynamic Drude model, convection maps directly to the form of equation (2), that is, with a Laplacian correction to the local response Drude part[24]. In the following, we treat both dynamical effects on an equal footing by considering both propagating longitudinal pressure waves (in a hydrodynamic model) and diffusion (in convection-diffusion model). The main result of our analysis is the following expression for the GNOR parameter:

$$\xi^2 \simeq \frac{\beta^2}{\omega^2} - i\frac{D}{\omega} \qquad (3)$$

where $\beta \propto v_{\mathrm{F}}$ is a characteristic velocity associated with pressure waves in the electron gas (v_{F} being the Fermi velocity) while D is the diffusion constant for the charge-carrier diffusion. The former is already known to cause frequency shifts (blueshifts)[17,21,22], while the latter turns out to cause line broadening, that is the GNOR parameter ξ is in general a complex-valued quantity. As also anticipated from more general discussions[14], our rigorous semiclassical treatment shows that non-local effects may manifest themselves over distances greatly exceeding atomic dimensions and become comparable to characteristic structure dimensions, such as the radius R of a nanoparticle (Fig. 1a) or the gap distance g in a dimer (Fig. 1b). As a main result, we show that the GNOR even dominates more pure quantum-mechanical effects in the electromagnetic response at optical frequencies, such as the anticipated effect of quantum-mechanical tunnelling currents in dimers with sub-nanometre gaps (Fig. 1b).

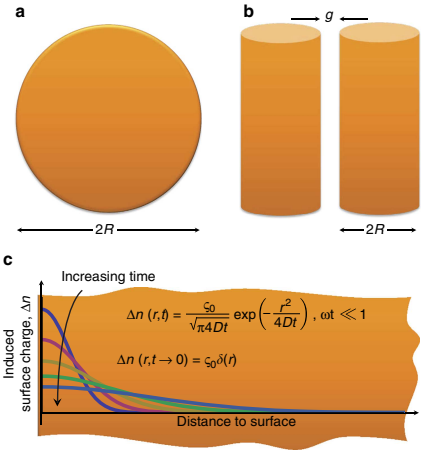

Figure 1 | Nanoplasmonic monomer and dimer structures. (**a**) Spherical particle of radius R, known to experimentally exhibit size-dependent damping[37,38] and resonant shifts[11,12,28]. (**b**) Nanowires of radius R arranged parallel to each other with a dimer gap g. Dimers are known experimentally to exhibit gap size-dependent broadening and shifts of hybridized plasmonic resonances[13,30]. (**c**) Diffusive temporal spreading of an initially pure surface charge ς_0 into the metal volume (orange-shaded area) of a plasmonic nanoparticle. By accounting for diffusion of charge, the GNOR theory can explain size-dependent broadening and shifts of nanoparticle resonances, as well as gap size-dependent broadening and shifts for dimer resonances. Unlike other theories (including the QCM[52]), our GNOR theory does not invoke quantum tunnelling to explain gap size-dependent spectral broadening.

Semiclassical response models. We consider the standard equation-of-motion for an electron in an external electrical field subject to the continuity equation. The common LRA simply neglects effects of quantum pressure as well as the diffusion contributions to the induced currents. We address these two aspects in turn and finally discuss how they play in concert to result in a complex-valued GNOR parameter.

Within the hydrodynamic model (including quantum pressure, but neglecting diffusion), the response is governed by a generalized constitutive equation[21,22]

$$\frac{\beta^2}{\omega(\omega+i\gamma)}\boldsymbol{\nabla}(\boldsymbol{\nabla}\cdot\mathbf{J}_{\rm conv})+\mathbf{J}_{\rm conv}=\sigma_{\rm D}\mathbf{E} \qquad (4)$$

where $\sigma_{\rm D}$ is the usual Drude conductivity. Within Thomas–Fermi theory, $\beta^2=(3/5)v_{\rm F}^2$ and $\gamma=1/\tau$ is the damping rate also present in the Drude theory.

Taking the opposite standpoint (including diffusion, while neglecting quantum pressure), linearization of the problem gives (Supplementary Note 1)

$$\frac{D}{i\omega}\boldsymbol{\nabla}(\boldsymbol{\nabla}\cdot\mathbf{J}_{\rm dif})+\mathbf{J}_{\rm dif}=\sigma_{\rm D}\mathbf{E} \qquad (5)$$

as also derived recently in the context of metamaterial wire media[32]. Our key observation is that this result is mathematically similar to equation (4), while the different physical origins cause different prefactors for the non-local correction to Ohm's law.

Turning to the Maxwell wave equation, the above non-local $\boldsymbol{\nabla}(\boldsymbol{\nabla}\cdot\mathbf{J})$ corrections to Ohm's law can be rewritten as a Laplacian correction to the Drude dielectric function[24,31], as anticipated in equation (2). The convection and diffusion components of the current are of the same mathematical form and subject to the same boundary conditions. Thus, in the linear response the considered non-local contributions add up (as in semiconductor drift-diffusion theory), as confirmed by linearizing the full hydrodynamic diffusion-convection problem (Supplementary Note 1), revealing how both quantum and classical kinetic effects can play in concert contributing to the non-local response. Therefore, we arrive at equation (2) with

$$\xi^2=\frac{\beta^2}{\omega(\omega+i\gamma)}-i\frac{D}{\omega}=\frac{\beta^2+D(\gamma-i\omega)}{\omega(\omega+i\gamma)}, \qquad (6)$$

which becomes equation (3) when neglecting damping. Note that for higher ω, diffusion becomes relatively more important compared with convection. Another important practical observation is that diffusion effectively causes the following modification of the non-local β-parameter appearing in prior hydrodynamic work: $\beta^2\rightarrow\beta^2+D(\gamma-i\omega)$. We explicitly neglect electron spill-out and the possible existence of associated quantum-tunnelling phenomena (see also Supplementary Note 2). Consequently, boundary conditions remain unchanged in the presence of diffusion ($\mathbf{n}\cdot\mathbf{J}=0$ on the metal surfaces so that no electrons escape the metal volumes). Thus, existing numerical schemes and methods[22–26] can readily be exploited to implement the GNOR approach for various plasmonic configurations.

The diffusion constant is generally interlinked with other transport parameters such as the scattering time, that is, $D\propto\tau=\gamma^{-1}$. For $\omega\gg\gamma$, we thus recover equation (3) for the GNOR parameter that now explicitly exposes the two competing length scales that were previously discussed only qualitatively[14], that is, the convection length β/ω on the one hand and the diffusion length $\sqrt{D/\omega}$ on the other hand. The damping associated with the latter is an important new finding that turns out to be crucial when approaching the nanoscale. Diffusion degrades plasmonic excitations, providing an additional broadening mechanism that, mathematically, is enacted by an imaginary contribution to ξ^2.

Validity domain. For classical gases (such as dilute plasmas, electrolytes and weakly doped semiconductors), the velocity distribution is governed by Maxwell–Boltzmann statistics and D is proportional to the temperature, as given by the Einstein relation. For metals on the other hand, Fermi–Dirac statistics implies a narrow transport velocity distribution[14] with a characteristic velocity $v_{\rm F}$. As a result, the diffusion constant is simply $D\simeq v_{\rm F}^2\tau$, corresponding to a mean-free path of $\ell=v_{\rm F}\tau$. We point out that our diffusive model is valid for structural dimensions exceeding the mean-free path that in pure single crystals[33] can be of the order of 100 nm for Ag and Au, down to ~3 nm for Na (see Supplementary Table 1). Moreover, in realistic plasmonic nanostructures, ℓ depends on actual material-processing conditions, becoming shorter than in single-crystalline bulk metals. This enlarges the validity domain of a diffusion description to include structures with dimensions of only a few nanometres. For even smaller dimensions, electrons will move ballistically between the surfaces of the structure, and surface scattering might become important. For metals, equation (6) simplifies to $\xi^2=\frac{v_{\rm F}^2}{\omega^2}(\frac{3}{5}-\frac{i\omega}{\gamma})+\mathcal{O}(\gamma/\omega)$. This result leads to an important insight into the interplay of different broadening mechanisms: the lower the Ohmic loss and absorption, the more important is the non-local response due to long-range diffusion of the induced charge. Re-introducing the diffusion constant

and the β-parameter we arrive at equation (3) that holds if the mean-free path significantly exceeds the convective length, that is, $\ell \gg v_F/\omega$. The existence of spatial dispersion in homogenous media, as for example, appearing within the common hydrodynamic Drude model, can be derived from higher-level descriptions such as the Boltzmann equation or the random-phase approximation (RPA). Beyond hydrodynamics, confined structures with broken translational invariance constitute a largely unexplored territory, with few attempts dealing with RPA aspects of localized plasmon resonances[34]. In support of our prediction of diffusive broadening, recent RPA studies reveal an increased plasmon linewidth associated with Landau damping[35], that is, electron-hole pair excitation near the surface of nanostructures as also observed in studies based on time-dependent density functional theory (TD-DFT)[36].

We provide in the following two key examples of the GNOR approach, demonstrating that the interplay of quantum pressure and diffusion has a remarkable impact on the optical response of plasmonics nanostructures and solving long-standing open problems.

Size-dependent damping. In general, the hydrodynamic corrections give a blueshift of resonances as the characteristic dimensions are reduced[17,22,27,28], which is in qualitative accordance with recent optical spectroscopy on gold-particle gap structures[27] and electron-energy loss spectroscopy (EELS) studies of silver nanoparticles[11,28]. With the complex-valued GNOR parameter ξ at hand, we now anticipate the blueshift to occur along with broadening of the resonant response when decreasing characteristic structure dimensions. In the case of a spherical particle, the blueshift has a β/R dependence[28], leading us to foresee that the line-broadening scales as $1/R$ as well. In the quasi-static limit ($\lambda \gg R$), one can straightforwardly work out the complex-valued resonance frequency $\omega = \omega' + i\omega''$ by considering the polarizability pole (Supplementary Note 3). As usual, the real part ω' gives the surface plasmon resonance frequency, while the imaginary part ω'' is related to the resonance linewidth. For simplicity, we consider the case of a particle in vacuum with no interband effects and find (to second order in $1/R$)

$$\omega' \simeq \frac{\omega_p}{\sqrt{3}} + \frac{\sqrt{2}\beta}{2R}, \qquad (7)$$

$$\omega'' \simeq -\frac{\gamma}{2} - \frac{\sqrt{6}}{24}\frac{D\omega_p}{\beta R}. \qquad (8)$$

It transpires clearly that the $1/R$ size-dependent non-local effects are present in both the resonance frequency and linewidth. It should be emphasized that, until now, line shifts have been explained by non-local response (and competing theories), whereas the line broadening was 'put in by hand'. Here by using the GNOR theory we have arrived at a unified explanation of both experimentally observed phenomena by non-local effects. Line broadening has been seen experimentally in the extinction of small particles[37–41] and EELS measurements on plasmons in thin nanowires and bow-tie antennas have also revealed plasmon losses exceeding the expectations based on bulk-damping parameters[42,43]. In the literature such line broadening has often been phenomenologically accounted for by a size-dependent damping rate[37–41], but without placing it in the context of non-local semiclassical equations of motion.

The phenomenology introduced by Kreibig[37,38] describes the linewidth broadening by introducing a size-dependent correction to the damping rate: $\gamma \to \gamma + Av_F/R$. Equipped with the GNOR theory, one does not need to assume the $1/R$ dependence: it comes immediately out as a consequence of the GNOR correction to the dipolar sphere polarizability. By comparison with the Kreibig model, we formally find that $A = \sqrt{\frac{1}{24}\frac{D\omega_p}{\beta v_F}}$. For metals this implies that $A \sim \omega_p\tau/4$. Use of bulk values for noble metals (see Supplementary Table 1) would estimate a too high A parameter compared with experiments where for spheres A is found to be of the order unity[37,38].

So far, we have assumed that the transport time is given by the bulk relaxation time τ_0. However, in the experiments dealing with plasmonic nanostructures, it has been found that one has to increase the collision frequency[44,45] or the imaginary part of permittivity[46] by several times as compared with the bulk metal (gold) parameters for the simulations to better correspond to the experimental observations. This size-independent correction factor was ascribed to the influence of the surface scattering and grain boundary effects in nanostructures[44–46]. In our case, we can simply introduce the characteristic relaxation time τ_s associated with these effects, which can be estimated from the condition that $A \sim 1$ as $\tau_s \sim 4/\omega_p$.

With the above refinement at hand we can demonstrate using numerical simulations (Fig. 2) that, in agreement with equations (7) and (8), the hydrodynamic response causes a blueshift (Fig. 2a), whereas the diffusion causes an additional broadening (Fig. 2b). In the latter figure, it is also shown that a similar resonance broadening (but not the blueshift) is predicted by the LRA with additional Kreibig damping.

Our real-space non-local wave equation (equation (2)) along with the GNOR parameter (equation (3)), which unravels the fundamental link between diffusive broadening and the Kreibig-like surface scattering thereby enables one to solve a long-

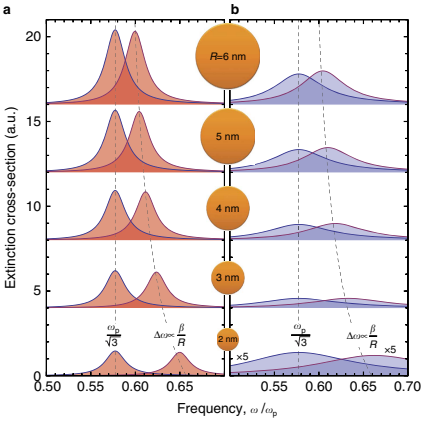

Figure 2 | Extinction cross-section for the dipole resonance in a metal sphere. The sphere radius R is varied from 2 to 6 nm. (**a**) LRA ($\beta = D = 0$) versus hydrodynamic non-local response ($\beta \neq 0$, $D = 0$), showing a blueshift $\Delta\omega$ (indicated by blueshifting-dashed lines) with respect to the common local response resonance at $\omega_p/\sqrt{3}$ (indicated by vertical-dashed lines). (**b**) LRA (including $1/R$ Kreibig damping[38] with the experimentally relevant value of $A = 1$) versus the GNOR model ($\beta \neq 0$, $D \neq 0$), with the latter capturing both the line shift and broadening. The metal parameters for sodium are used[49,38]: $\omega_p = 5.89$ eV, $\gamma = 0.16$ eV, $v_F = 1.05 \times 10^6$ m s^{-1}, $\beta = 0.81 \times 10^6$ m s^{-1}, $D = 2.04 \times 10^{-4}$ m^2 s^{-1}, and $A = 1$.

standing open problem: surface-related scattering can now be computationally accounted for also in complex-shaped geometries beyond that of spherical symmetry and low radius of curvature.

Nanowire dimers. Plasmonic dimers (Fig. 1b) are rich on hybridization phenomena as the gap distance g is reduced[47] and non-local hydrodynamic effects on both hybridization and field enhancement have been anticipated[22]. To elucidate the diffusion contribution to non-local effects, we may consider dimers of nanowires where the nanowire radius R itself is too large to cause either non-local hydrodynamic effects or increased damping of the Kreibig kind. Nevertheless, we expect that the dimer would exhibit non-local effects once the dimer gap distance g turns comparable in magnitude to ξ, resulting in additional broadening in the vicinity of the gap as v_F/g increases. With our present formalism, this can now be quantified without any need to invoke *ad hoc* assumptions specifically for dimers.

Although diffusion is of a classical origin, the discussion of its effect in dimers ties up with very recent experiments on dimers in the quantum-tunnelling regime[13]. *Ab initio* approaches show a crossing from the classical hybridization of localized surface plasmon resonances to tunnelling-mediated charge-transfer plasmons (CTPs)[36,48–50]. Being able to push experiments into this intriguing regime[13,30,51], commonly associated with expectations of quantum physics, leaves an open question: Can this regime be adequately described with semiclassical models? While non-local response within the hydrodynamic semiclassical model has been found unsuccessful in explaining features from TD-DFT[48–50], there have been phenomenological attempts of classically modelling the crossover regime. The 'quantum-corrected model' (QCM)[52] adds an artificial conducting and lossy material in the gap to mimic short-circuiting currents associated with quantum tunnelling. While apparently successful in qualitatively fitting results of *ab initio* simulations[49,50,52], the model raises concerns regarding its physical foundation. The well-established understanding of mesoscopic quantum electron transport[7] is that the tunnelling through the classically forbidden gap region is elastic (ballistic transport) while energy relaxation takes place inside the metallic contact regions. Opposite to that, the artificial gap material introduced in the QCM causes dissipation within the gap, while there is no associated relaxation occurring on the metal sides of the junction.

While *ab initio* works emphasize tunnelling[52,49,50], recent experiments on dimers[13,30] do not offer explicit evidence that the broadening is associated with quantum tunnelling. The formation of a sub-nanometre gap is evident from the observed DC voltage-driven tunnelling current[13], while there is no explicit confirmation of AC tunneling currents caused by the optical driving. Optical rectification phenomena are possible by photon-assisted inelastic tunnelling currents[53], while earlier time-resolved elastic-tunnelling experiments have reported tunnelling RC times (i.e. the characteristic time scale of the equivalent resistor-capacitor circuit) in the picosecond range[54], thus suggesting a suppression of optical frequency tunneling currents that would take place in femtoseconds. This apparently makes quantum-tunnelling dynamics too slow and a less likely mechanism to explain the broadening of dimer modes at optical frequencies. Applying the GNOR framework, we demonstrate in the following that the diffusion offers a strong competing damping mechanism. In fact, for fast driving of the junction[55], diffusion may completely dominate the dissipation of the dimer junction as we illustrate by a circuit analysis (see Supplementary Note 2).

The diffusion-driven damping occurs right inside the surface of the metals (not in the gap), becoming progressively more pronounced for smaller gaps and vanishing for large gaps. To exemplify this in detail, we revisit recent non-local (hydrodynamic) simulations[49], while making sure to account for the diffusive broadening as well by use of the complex-valued GNOR parameter (Fig. 3). For relatively large gaps, one observes the bonding-dipole plasmon (BDP) along with higher-order modes known to appear below the plasma frequency within the LRA[56] (for a larger radius this becomes particularly clear, see Supplementary Fig. 1). As the gap is reduced to the non-local regime $g \lesssim v_F/\omega$, as considered in Fig. 3 for $R = 4.9$ nm, resonances are slightly blueshifted with respect to the LRA result[22]. When the gap shrinks further, progressively stronger hybridization[47] and accordingly larger BDP redshifts are clearly seen. At the same time, the BDP is gradually suppressed owing to the increasing role of diffusion as the contact point, $g = 0$, is approached. This is in strong contrast to predictions from both the LRA[56] (with even diverging field enhancement) and from previous non-local theories that treated the β-parameter real-valued[22,49,50,57] (see Supplementary Fig. 1). As we enter the contact regime, the BDP fades away, vanishing completely for $g < 0$. For touching wires, the CTP appears, whose resonance blueshifts and grows in strength for larger wire overlaps. We note that, for $g \sim 0$, the diffusive broadening is so strong that only

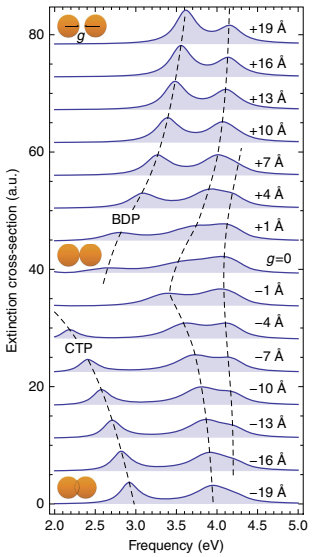

Figure 3 | Extinction cross-section for a nanowire dimer with a sub-nanometre gap within the GNOR model. The radius of the sodium wires is $R = 4.9$ nm with the gap g varying from -19 to $+19$ Å. Progressively stronger hybridization occurs as the gap narrows, with both a clear redshift and broadening of the BDP. As the gap closes, the CTP develops and blueshifts as the wires start to overlap. Higher-order modes (also indicated by dashed lines) exhibit hybridization and broadening too. The diffusion with constant $D = 1.36 \times 10^{-4}\,m^2\,s^{-1}$ causes GNOR spectra in accordance with TD-DFT calculations[49] and in overall agreement with the broadening observed experimentally[13,30].

higher-order modes persist (as the induced surface charge is located away from the contact point), while both BDP and the CTP are strongly suppressed. This makes a discussion on their possible coexistence problematic[51]. Finally, we note that in the anticipated tunnelling regime the extinction spectra are strongly broadened by the complex non-local response. In fact, our semiclassical approach is in remarkable agreement with the TD-DFT results[48–50], with the diffusion contribution being responsible for 'repairing' the apparent incompatibility of TD-DFT calculations and earlier hydrodynamic predictions[49,50]. Our semiclassical GNOR theory thereby pinpoints induced charge diffusion as the dominant broadening mechanism in recent EELS and optical experiments on plasmonic dimers[13,30], thus challenging tunnelling-current interpretations for which the phenomenological QCM was constructed.

Discussion

In this article we have presented a semiclassical (GNOR) approach that is offering a long-sought unification of non-local response mechanisms having both quantum-mechanical and classical origins. The GNOR theory places established observations of size-dependent damping into the context of non-local response and offers an accurate classical explanation of spectral broadening in MNP monomers and dimers without invoking quantum-mechanical tunnelling, whose efficiency at optical frequencies is questionable. We have so far considered degenerate electron systems such as metals, where screening is strong and non-local effects manifest themselves in the nanometre to sub-nanometre regime. In the search for a new mesoscopic regime, where plasmons potentially exhibit both semiclassical dynamics and quantum effects, low-density-doped semiconductors and tunable low-dimensional materials (including the graphene family of two-dimensional materials) appear attractive[58]. Quantum light–matter interactions[59] and non-local response[60] were already considered for graphene plasmonics, and, for such non-degenerate systems, our theory anticipates temperature-dependent non-local response that might lead to novel non-local effects accessible via experimental observations.

Methods

The optical response of dimers was obtained by solving the non-local wave equation with the aid of a commercially available finite-element method. The numerical code is an extension to the COMSOL 4.2a RF Module, which incorporates non-local hydrodynamic effects in the optical response of arbitrarily shaped nanoplasmonic structures, possessing one dimension with translational symmetry. The code is freely available from http://www.nanopl.org and the implementation, testing and performance are reported elsewhere[22,24]. Prior results on dimers[49] were obtained with the same code, while only utilizing a real-valued β-parameter. All numerical results can alternatively be calculated with the aid of a non-local boundary-element method[26]. Similarly, the complex-valued GNOR parameter can be substituted in non-local transformation optics approaches originally developed with a real-valued β-parameter in mind[57].

References

1. Van Rossum, M. & Nieuwenhuizen, T. Multiple scattering of classical waves: microscopy, mesoscopy, and diffusion. *Rev. Mod. Phys.* **71,** 313–371 (1999).
2. Schuller, J. A. *et al.* Plasmonics for extreme light concentration and manipulation. *Nat. Mater.* **9,** 193–204 (2010).
3. Gramotnev, D. K. & Bozhevolnyi, S. I. Plasmonics beyond the diffraction limit. *Nat. Photon.* **4,** 83–91 (2010).
4. Gramotnev, D. K. & Bozhevolnyi, S. I. Nanofocusing of electromagnetic radiation. *Nat. Photon.* **8,** 14–23 (2014).
5. Engheta, N. Circuits with light at nanoscales: optical nanocircuits inspired by metamaterials. *Science* **317,** 1698–1702 (2007).
6. Nitzan, A. & Ratner, M. Electron transport in molecular wire junctions. *Science* **300,** 1384–1389 (2003).
7. Datta, S. *Electronic Transport in Mesoscopic Systems* (Cambridge University Press, 1995).
8. Beenakker, C. W. J. Random-matrix theory of quantum transport. *Rev. Mod. Phys.* **69,** 731–808 (1997).
9. Burada, P. S., Hänggi, P., Marchesoni, F., Schmid, G. & Talkner, P. Diffusion in confined geometries. *Chemphyschem* **10,** 45–54 (2009).
10. Tame, M. S. *et al.* Quantum plasmonics. *Nat. Phys.* **9,** 329–340 (2013).
11. Scholl, J. A., Koh, A. L. & Dionne, J. A. Quantum plasmon resonances of individual metallic nanoparticles. *Nature* **483,** 421–427 (2012).
12. Ouyang, F., Batson, P. & Isaacson, M. Quantum size effects in the surface-plasmon excitation of small metallic particles by electron-energy-loss spectroscopy. *Phys. Rev. B* **46,** 15421–15425 (1992).
13. Savage, K. J. *et al.* Revealing the quantum regime in tunnelling plasmonics. *Nature* **491,** 574–577 (2012).
14. Landau, L. D., Lifshitz, E. M. & Pitaevskii, L. P. *Course on Theoretical Physics* 2nd edn, Vol. 8 (Butterworth Heinemann, 1984).
15. Boardman, A. *Electromagnetic Surface Modes* (John Wiley and Sons, 1982).
16. Fuchs, R. & Kliewer, K. L. Optical properties of an electron gas: further studies of a nonlocal description. *Phys. Rev.* **185,** 905–913 (1969).
17. Ruppin, R. Optical properties of a plasma sphere. *Phys. Rev. Lett.* **31,** 1434–1437 (1973).
18. Dasgupta, B. B. & Fuchs, R. Polarizability of a small sphere including nonlocal effects. *Phys. Rev. B* **24,** 554–561 (1981).
19. Garcia de Abajo, F. J. Nonlocal effects in the plasmons of strongly interacting nanoparticles, dimers, and waveguides. *J. Phys. Chem. C* **112,** 17983–17987 (2008).
20. McMahon, J. M., Gray, S. K. & Schatz, G. C. Nonlocal optical response of metal nanostructures with arbitrary shape. *Phys. Rev. Lett.* **103,** 097403 (2009).
21. Raza, S., Toscano, G., Jauho, A.-P., Wubs, M. & Mortensen, N. A. Unusual resonances in nanoplasmonic structures due to nonlocal response. *Phys. Rev. B* **84,** 121412(R) (2011).
22. Toscano, G., Raza, S., Jauho, A.-P., Mortensen, N. A. & Wubs, M. Modified field enhancement and extinction in plasmonic nanowire dimers due to nonlocal response. *Opt. Express* **20,** 4176–4188 (2012).
23. Hiremath, K. R., Zschiedrich, L. & Schmidt, F. Numerical solution of nonlocal hydrodynamic Drude model for arbitrary shaped nano-plasmonic structures using Nédélec finite elements. *J. Comp. Phys.* **231,** 5890–5896 (2012).
24. Toscano, G. *et al.* Nonlocal response in plasmonic waveguiding with extreme light confinement. *Nanophotonics* **2,** 161–166 (2013).
25. Luo, Y., Fernández-Domínguez, A. I., Wiener, A., Maier, S. A. & Pendry, J. B. Surface plasmons and nonlocality: a simple model. *Phys. Rev. Lett.* **111,** 093901 (2013).
26. Yan, W., Mortensen, N. A. & Wubs, M. Green's function surface-integral method for nonlocal response of plasmonic nanowires in arbitrary dielectric environments. *Phys. Rev. B* **88,** 155414 (2013).
27. Ciracì, C. *et al.* Probing the ultimate limits of plasmonic enhancement. *Science* **337,** 1072–1074 (2012).
28. Raza, S. *et al.* Blueshift of the surface plasmon resonance in silver nanoparticles studied with EELS. *Nanophotonics* **2,** 131–138 (2013).
29. Monreal, R. C., Antosiewicz, T. J. & Apell, S. P. Competition between surface screening and size quantization for surface plasmons in nanoparticles. *New J. Phys.* **15,** 083044 (2013).
30. Scholl, J. A., Garcia-Etxarri, A., Koh, A. L. & Dionne, J. A. Observation of quantum tunneling between two plasmonic nanoparticles. *Nano Lett.* **13,** 564–569 (2013).
31. Mortensen, N. A. Nonlocal formalism for nanoplasmonics: phenomenological and semi-classical considerations. *Phot. Nanostr.* **11,** 303–309 (2013).
32. Hanson, G. W. Drift-diffusion: a model for teaching spatial-dispersion concepts and the importance of screening in nanoscale structures. *IEEE Antennas Propag. Mag.* **52,** 198–207 (2010).
33. Sondheimer, E. H. The mean free path of electrons in metals. *Adv. Phys.* **1,** 1–42 (1952).
34. Ichikawa, M. Theory of localized plasmons for metal nanostructures in random-phase approximation. *J. Phys. Soc. Jpn* **80,** 044606 (2011).
35. Li, X., Xiao, D. & Zhang, Z. Landau damping of quantum plasmons in metal nanostructures. *New J. Phys.* **15,** 023011 (2013).
36. Andersen, K., Jensen, K. L., Mortensen, N. A. & Thygesen, K. S. Visualizing hybridized quantum plasmons in coupled nanowires: From classical to tunneling regime. *Phys. Rev. B* **87,** 235433 (2013).
37. Kreibig, U. & Fragstein, C. The limitation of electron mean free path in small silver particles. *Z. Physik.* **224,** 307–323 (1969).
38. Kreibig, U. & Vollmer, M. *Optical Properties of Metal Clusters* (Springer-Verlag, 1995).
39. Gaudry, M. *et al.* Size and composition dependence in the optical properties of mixed (transition metal/noble metal) embedded clusters. *Phys. Rev. B* **67,** 155409 (2003).
40. Scaffardi, L. & Tocho, J. Size dependence of refractive index of gold nanoparticles. *Nanotechnology* **17,** 1309–1315 (2006).
41. Kolwas, K. & Derkachova, A. Damping rates of surface plasmons for particles of size from nano- to micrometers; reduction of the nonradiative decay. *J. Quant. Spectrosc. Radiat. Transfer* **114,** 45–55 (2013).

42. Nicoletti, O. *et al.* Surface plasmon modes of a single silver nanorod: an electron energy loss study. *Opt. Express* **19,** 15371–15379 (2011).
43. Wiener, A. *et al.* Electron-energy loss study of nonlocal effects in connected plasmonic nanoprisms. *ACS Nano* **7,** 6287–6296 (2013).
44. Zhang, S. *et al.* Experimental demonstration of near-infrared negative-index metamaterials. *Phys. Rev. Lett.* **95,** 137404 (2005).
45. Liu, N., Mesch, M., Weiss, T., Hentschel, M. & Giessen, H. Infrared perfect absorber and its application as plasmonic sensor. *Nano Lett.* **10,** 2342–2348 (2010).
46. Pors, A., Nielsen, M. G. & Bozhevolnyi, S. I. Broadband plasmonic half-wave plates in reflection. *Opt. Lett.* **38,** 513–515 (2013).
47. Prodan, E., Radloff, C., Halas, N. & Nordlander, P. A hybridization model for the plasmon response of complex nanostructures. *Science* **302,** 419–422 (2003).
48. Stella, L., Zhang, P., García-Vidal, F. J., Rubio, A. & García-González, P. Performance of nonlocal optics when applied to plasmonic nanostructures. *J. Phys. Chem. C* **117,** 8941–8949 (2013).
49. Teperik, T. V., Nordlander, P., Aizpurua, J. & Borisov, A. G. Robust subnanometric plasmon ruler by rescaling of the nonlocal optical response. *Phys. Rev. Lett.* **110,** 263901 (2013).
50. Teperik, T. V., Nordlander, P., Aizpurua, J. & Borisov, A. G. Quantum effects and nonlocality in strongly coupled plasmonic nanowire dimers. *Opt. Express* **21,** 27306–27325 (2013).
51. Kadkhodazadeh, S., Wagner, J. B., Kneipp, H. & Kneipp, K. Coexistence of classical and quantum plasmonics in large plasmonic structures with subnanometer gaps. *Appl. Phys. Lett.* **103,** 083103 (2013).
52. Esteban, R., Borisov, A. G., Nordlander, P. & Aizpurua, J. Bridging quantum and classical plasmonics with a quantum-corrected model. *Nat. Commun.* **3,** 825 (2012).
53. Ward, D. R., Hüser, F., Pauly, F., Carlos Cuevas, J. & Natelson, D. Optical rectification and field enhancement in a plasmonic nanogap. *Nat. Nanotechnol.* **5,** 732–736 (2010).
54. Weiss, S., Botkin, D., Ogletree, D. F., Salmeron, M. & Chemla, D. S. The ultrafast response of a scanning tunneling microscope. *Phys. Status Solidi B* **188,** 343–359 (1995).
55. Grifoni, M. & Hänggi, P. Driven quantum tunneling. *Phys. Rep.* **304,** 229–354 (1998).
56. Romero, I., Aizpurua, J., Bryant, G. W. & García de Abajo, F. J. Plasmons in nearly touching metallic nanoparticles: singular response in the limit of touching dimers. *Opt. Express* **14,** 9988–9999 (2006).
57. Fernández-Domínguez, A. I., Wiener, A., García-Vidal, F. J., Maier, S. A. & Pendry, J. B. Transformation-optics description of nonlocal effects in plasmonic nanostructures. *Phys. Rev. Lett.* **108,** 106802 (2012).
58. Britnell, L. *et al.* Strong light-matter interactions in heterostructures of atomically thin films. *Science* **340,** 1311–1314 (2013).
59. Koppens, F. H. L., Chang, D. E. & García de Abajo, F. J. Graphene plasmonics: A platform for strong light-matter interactions. *Nano Lett.* **11,** 3370–3377 (2011).
60. Wang, W. & Kinaret, J. M. Plasmons in graphene nanoribbons: interband transitions and nonlocal effects. *Phys. Rev. B* **87,** 195424 (2013).

Acknowledgements

We acknowledge Giuseppe Toscano for use of his finite-element code and we thank Jørn Hvam, Antti-Pekka Jauho and Wei Yan for stimulating discussions. The Center for Nanostructured Graphene (CNG) is funded by the Danish National Research Foundation, Project DNRF58. The A P Møller and Chastine Mc-Kinney Møller Foundation is gratefully acknowledged for the contribution towards the establishment of the Center for Electron Nanoscopy. N.A.M. and M.W. acknowledge financial support by Danish Council for Independent Research—Natural Sciences, Project 1323-00087.

Author contributions

N.A.M, S.I.B, T.S. and M.W. conceived the basic idea. N.A.M. derived the complex response model. S.R. performed all numerical simulations and the analytical analysis of spherical particles. Figures were prepared by N.A.M. and S.R. All authors interpreted and discussed the results and the writing of the manuscript was done in a joint effort.

Additional information

Supplementary Information accompanies this paper at http://www.nature.com/naturecommunications

Competing financial interests: The authors declare no competing financial interests.

Reprints and permission information is available online at http://npg.nature.com/reprintsandpermissions/

How to cite this article: Mortensen, N. A. *et al.* A generalized non-local optical response theory for plasmonic nanostructures. *Nat. Commun.* 5:3809 doi: 10.1038/ncomms4809 (2014).

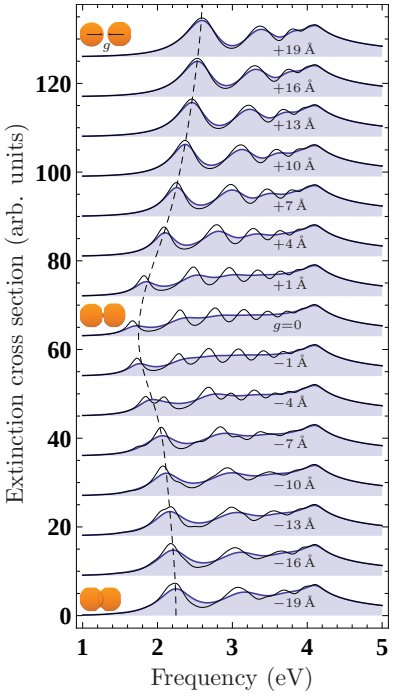

Supplementary Figure 1: Extinction cross section for a nanowire dimer with a sub-nanometer gap taking the nonlocal hydrodynamic-diffusion response into account. The radius of the sodium wires is $R = 25\,\text{nm}$ with the gap g varying from $-19\,\text{Å}$ to $+19\,\text{Å}$. Calculations are for the same parameters as in Figure 3 in the main text. For comparison, the solid black lines show the nonlocal response in the absence of diffusion ($\beta \neq 0$ and $D = 0$).

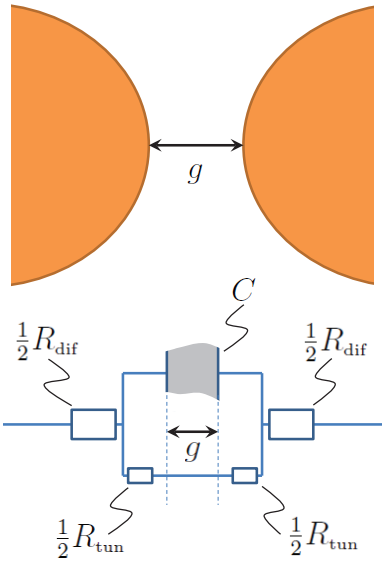

Supplementary Figure 2: Circuit model for diffusion-tunneling dynamics in the dimer gap region.

	Fermi wavelength λ_{F}	Mean-free path $\ell = v_{\mathrm{F}}\tau$	Convection length $v_{\mathrm{F}}/\omega_{\mathrm{p}}$	Diffusion length $\sqrt{D/\omega_{\mathrm{p}}}$	Scattering time $\omega_{\mathrm{p}}\tau$
Ag/Au	0.52 nm	103 nm	0.10 nm	1.9 nm	10^3 [1]
Ag	0.52 nm	40 nm	0.10 nm	1.1 nm	421 [2]
Au	0.52 nm	50 nm	0.11 nm	1.3 nm	465 [2]
Na	0.68 nm	2.6 nm	0.12 nm	0.32 nm	21 [2]
Na	0.68 nm	4.4 nm	0.12 nm	0.42 nm	37 [3]
Na	0.68 nm	2.3 nm	0.12 nm	0.31 nm	20 [4]

Supplementary Table 1: Table of central length scales and parameters for Au, Ag, and Na. The entries for different metals are based on Fermi wavelengths (λ_{F}), Fermi velocities (v_{F}), and plasma frequencies (ω_{p}) taken from Ref. 1, while the values for τ originate from various references as indicated in the right-most column of the table.

Supplementary Note 1

In this section we offer the detailed derivation of the hydrodynamic-diffusion problem of an electron responding to an external electric field. We start from the linearized hydrodynamic equation-of-motion for an electron in an electric field[5,6]

$$\partial_t \boldsymbol{v} = -\gamma \boldsymbol{v} + \frac{(-e)}{m}\boldsymbol{E} - \frac{\beta^2}{n_0}\boldsymbol{\nabla} n_1. \tag{1}$$

Here, $\boldsymbol{v}$ is the velocity correction to the static sea of electrons and for the density $n(\boldsymbol{r},t) = n_0 + n_1(\boldsymbol{r},t)$ the latter term is likewise the small $(n_1/n_0 \ll 1)$ induced density variation associated with the driving $\boldsymbol{E}$ field. Now, rather than the usual simple form for the continuity equation we instead have the linearized convection-diffusion equation

$$\partial_t(-e)n_1 = D\nabla^2(-e)n_1 - \boldsymbol{\nabla}\cdot\{(-e)n_0\boldsymbol{v}\} = -\boldsymbol{\nabla}\cdot\boldsymbol{J} \tag{2}$$

where the current density is then given by Fick's law

$$\boldsymbol{J} = (-e)n_0\boldsymbol{v} - D\boldsymbol{\nabla}(-e)n_1. \tag{3}$$

Multiplying the equation-of-motion, Supplementary Equation (1), by the equilibrium density n_0, taking the time-derivative ∂_t and re-arranging we get

$$(\partial_t + \gamma)\partial_t\{(-e)n_0\boldsymbol{v}\} = \frac{n_0e^2}{m}\partial_t\boldsymbol{E} - \beta^2\boldsymbol{\nabla}\{\partial_t(-e)n_1\}. \tag{4}$$

Using Fick's law, Supplementary Equation (3), we then find

$$(\partial_t + \gamma)\left[\partial_t\boldsymbol{J} + D\boldsymbol{\nabla}(\partial_t(-e)n_1)\right] = \frac{n_0e^2}{m}\partial_t\boldsymbol{E} - \beta^2\boldsymbol{\nabla}\{\partial_t(-e)n_1\}. \tag{5}$$

From the diffusion-convection equation, Supplementary Equation (2), we consequently get

$$(\partial_t + \gamma)\left[\partial_t \boldsymbol{J} - D\boldsymbol{\nabla}(\boldsymbol{\nabla}\cdot\boldsymbol{J})\right] = \frac{n_0 e^2}{m}\partial_t \boldsymbol{E} + \beta^2 \boldsymbol{\nabla}(\boldsymbol{\nabla}\cdot\boldsymbol{J}). \tag{6}$$

Finally, Fourier transforming with respect to time and re-arranging the terms we get

$$\underbrace{\left[\frac{\beta^2}{\omega(\omega+i\gamma)} + \frac{D}{i\omega}\right]}_{\xi^2}\boldsymbol{\nabla}(\boldsymbol{\nabla}\cdot\boldsymbol{J}) + \boldsymbol{J} = \underbrace{\frac{\frac{e^2 n_0}{m}}{-i\omega+\gamma}}_{\sigma_{\mathrm{D}}}\boldsymbol{E}. \tag{7}$$

This is the generalized constitutive equation with a complex nonlocal correction to the local-response Ohm's law. According to our previous work[7], the Maxwell's equation can then be re-written in the form of the equations in the main text, i.e. Equation (2) with ξ^2 given by Equation (6).

In our use of Supplementary Equation (7) we neglect electron spill-out and the associated boundary conditions used in prior nonlocal hydrodynamics[6–9] remain unchanged in the presence of diffusion. This means that $\boldsymbol{n}\cdot\boldsymbol{J} = 0$ on the metal surfaces, implying that no electrons escape the metal volumes. This is an appropriate description of noble metals commonly employed in plasmonics while spill-out effects are important in less common metals like sodium[3,10,11].

The local-response approximation (LRA) neglects the Laplacian term in Supplementary Equation (7) and in problems using such a constitutive equation the induced charge Δn becomes a delta function at the surface of the metal. The nonlocal correction will smear this density profile due to both convection and diffusion. Related phenomena and formalisms are known from semiconductor drift-diffusion theory[12] as well as from fluid mechanics and chemical engineer-

ing, where convection-diffusion systems may exhibit an increased effective diffusivity of chemical species known as Taylor dispersion[13,14].

In Supplementary Table 1 we summarize characteristic length scales and parameters for noble metals commonly considered in experimental realizations as well as in recent theoretical works.

Supplementary Note 2

For the dimer we here address the relative importance of diffusive damping (characterized by a resistance $R_{\rm dif}$ in a circuited model) and the damping associated with the relaxation of a possible quantum tunneling current (characterized by $R_{\rm tun}$) short-circuiting the classically forbidden capacitive gap (characterized by a capacitance C). In a simple picture, C and $R_{\rm tun}$ constitute a parallel circuit[15] connected in series with $R_{\rm dif}$, see Supplementary Figure 2. The circuit impedance is then

$$Z = R_{\rm dif} + \frac{R_{\rm tun}}{1+i\omega\tau_{\rm tun}} = R_{\rm dif} - \frac{i}{\omega C} + \mathcal{O}[1/(\omega\tau_{\rm tun})^2] \tag{8}$$

where $\tau_{\rm tun} = R_{\rm tun}C$ is the tunneling RC time[15]. The tunneling dynamics simplifies in the slow adiabatic-following regime and the limit of fast external driving[16]. This analysis suggests that the high-frequency dimer dynamics can become entirely dominated by the diffusive broadening and the junction capacitance. Tunneling dynamics has been explored in the context of the mesoscopic capacitance[17] and ultra-fast tunneling experiments have reported tunneling RC times in the picosecond range[15,18]. Thus, at optical frequencies the plasmon response is expected to be fast on the scale of the characteristic RC time and from the experiments it seems reasonable to assume that $\omega\tau_{\rm tun} \gg 1$. Consequently, the relaxation is dominated by diffusive broadening rather than the

short-circuiting tunneling current.

We note that the above circuit analysis is completely independent on whether tunneling relaxation occurs within the gap (as it is the case in the quantum-corrected model[19]) or if it takes place inside the metal surfaces (in agreement with the common understanding of relaxation within mesoscopic quantum electron transport).

In Supplementary Figure 1 we show the extinction for dimers of $R = 25\,\text{nm}$ wires and with a gap g varying from $-19\,\text{Å}$ to $+19\,\text{Å}$. While the wires themselves have a too large radius ($R \gg |\xi|$) to support nonlocal effects, the small gap ($g \sim |\xi|$) causes a strong broadening associated with the complex-valued nonlocal response.

Supplementary Note 3

We consider a metal sphere of radius R embedded in a homogeneous background dielectric environment with permittivity ε_b. In the quasi-static limit, the optical response of the sphere is described by the dipole polarizability α that features a nonlocal generalization of the Clausius–Mossotti factor, and is given as[20,21]

$$\alpha = 4\pi R^3 \frac{\varepsilon_\text{D} - \varepsilon_\text{b}\,(1+\delta_\text{nl})}{\varepsilon_\text{D} + 2\varepsilon_\text{b}\,(1+\delta_\text{nl})}, \quad \delta_\text{nl} = \frac{\varepsilon_\text{D} - \varepsilon_\infty}{\varepsilon_\infty} \frac{j_1(k_\text{nl}R)}{k_\text{nl}R j_1'(k_\text{nl}R)}, \tag{9}$$

where $\varepsilon_\text{D} = \varepsilon_\infty - \omega_\text{p}^2/(\omega^2 + i\gamma\omega)$ is the Drude dielectric function, $k_\text{nl}^2 = (\omega^2 + i\omega\gamma - \omega_\text{p}^2)/(\beta^2 + D\gamma - iD\omega)$ is the wave vector of the longitudinal wave, and j_1 is the spherical Bessel function of first order.

Supplementary References

1. Ashcroft, N. W. & Mermin, N. D. *Solid State Physics* (Saunders College Publishing, Fort Worth, 1976).

2. Blaber, M. G., Arnold, M. D. & Ford, M. J. Search for the ideal plasmonic nanoshell: The effects of surface scattering and alternatives to gold and silver. *J. Phys. Chem. C* **113**, 3041–3045 (2009).

3. Teperik, T. V., Nordlander, P., Aizpurua, J. & Borisov, A. G. Robust subnanometric plasmon ruler by rescaling of the nonlocal optical response. *Phys. Rev. Lett.* **110**, 263901 (2013).

4. Stella, L., Zhang, P., García-Vidal, F. J., Rubio, A. & García-González, P. Performance of nonlocal optics when applied to plasmonic nanostructures. *J. Phys. Chem. C* **117**, 8941–8949 (2013).

5. Boardman, A. *Electromagnetic Surface Modes. Hydrodynamic theory of plasmon-polaritons on plane surfaces.* (John Wiley and Sons, Chichester, 1982).

6. Raza, S., Toscano, G., Jauho, A.-P., Wubs, M. & Mortensen, N. A. Unusual resonances in nanoplasmonic structures due to nonlocal response. *Phys. Rev. B* **84**, 121412(R) (2011).

7. Toscano, G. *et al.* Nonlocal response in plasmonic waveguiding with extreme light confinement. *Nanophotonics* **2**, 161–166 (2013).

8. Jewsbury, P. Electrodynamic boundary-conditions at metal interfaces. *J. Phys. F* **11**, 195–206 (1981).

9. Yan, W., Wubs, M. & Mortensen, N. A. Hyperbolic metamaterials: Nonlocal response regularizes broadband supersingularity. *Phys. Rev. B* **86**, 205429 (2012).

10. Liebsch, A. Surface-plasmon dispersion and size dependence of mie resonance: Silver versus simple metals. *Phys. Rev. B* **48**, 11317–11328 (1993).

11. Monreal, R. C., Antosiewicz, T. J. & Apell, S. P. Competition between surface screening and size quantization for surface plasmons in nanoparticles. *New J. Phys.* **15**, 083044 (2013).

12. Seeger, K. *Semiconductor Physics*, vol. 40 of *Springer Series in Solid-State Sciences* (Springer Verlag, New York, 1991), 5 edn.

13. Taylor, G. Dispersion of soluble matter in solvent flowing slowly throught a tube. *Proc. Roy. Soc. A* **219**, 186–203 (1953).

14. Bruus, H. *Theoretical Microfluidics*, vol. 18 of *Oxford Master Series in Condensed Matter Physics* (Oxford University Press, Oxford, 2008).

15. Weiss, S., Botkin, D., Ogletree, D. F., Salmeron, M. & Chemla, D. S. The ultrafast response of a scanning tunneling microscope. *Phys. Stat. Sol. (b)* **188**, 343–359 (1995).

16. Grifoni, M. & Hänggi, P. Driven quantum tunneling. *Phys. Rep.* **304**, 229–354 (1998).

17. Büttiker, M., Thomas, H. & Prêtre, A. Mesoscopic capacitors. *Phys. Lett. A* **180**, 364 – 369 (1993).

18. Keil, U. D., Ha, T., Jensen, J. R. & Hvam, J. M. Femtosecond tunneling response of surface plasmon polaritons. *Appl. Phys. Lett.* **72**, 3074–3076 (1998).

19. Esteban, R., Borisov, A. G., Nordlander, P. & Aizpurua, J. Bridging quantum and classical plasmonics with a quantum-corrected model. *Nat. Commun.* **3**, 825 (2012).

20. Raza, S. *et al.* Blueshift of the surface plasmon resonance in silver nanoparticles studied with EELS. *Nanophotonics* **2**, 131–138 (2013).

21. Raza, S., Yan, W., Stenger, N., Wubs, M. & Mortensen, N. A. Blueshift of the surface plasmon resonance in silver nanoparticles: substrate effects. *Opt. Express* **21**, 27344–27355 (2013).

Paper E

S. Raza, W. Yan, N. Stenger, M. Wubs, and N. A. Mortensen

Blueshift of the surface plasmon resonance in silver nanoparticles: substrate effects

Opt. Express **21**, 27344 (2013)

Author contributions
S. R. derived the equations, except for those in Sec. 3.2, and was the main author of the manuscript. S. R. created the figures. W. Y. derived the equations and wrote Sec. 3.2. The electron energy-loss measurements and transmission electron microscope images were done by S. R. and N. S. All authors were involved in discussing the obtained results and in correcting the manuscript.

Blueshift of the surface plasmon resonance in silver nanoparticles: substrate effects

Søren Raza,[1,2] **Wei Yan,**[1,3] **Nicolas Stenger,**[1,3] **Martijn Wubs,**[1,3] **and N. Asger Mortensen**[1,3,*]

[1]*Department of Photonics Engineering, Technical University of Denmark, DK-2800 Kgs. Lyngby, Denmark*
[2]*Center for Electron Nanoscopy, Technical University of Denmark, DK-2800 Kgs. Lyngby, Denmark*
[3]*Center for Nanostructured Graphene (CNG), Technical University of Denmark, DK-2800 Kgs. Lyngby, Denmark*
[*]*asger@mailaps.org*

Abstract: We study the blueshift of the surface plasmon (SP) resonance energy of isolated Ag nanoparticles with decreasing particle diameter, which we recently measured using electron energy loss spectroscopy (EELS) [1]. As the particle diameter decreases from 26 down to 3.5 nm, a large blueshift of 0.5 eV of the SP resonance energy is observed. In this paper, we base our theoretical interpretation of our experimental findings on the nonlocal hydrodynamic model, and compare the effect of the substrate on the SP resonance energy to the approach of an effective homogeneous background permittivity. We derive the nonlocal polarizability of a small metal sphere embedded in a homogeneous dielectric environment, leading to the nonlocal generalization of the classical Clausius–Mossotti factor. We also present an exact formalism based on multipole expansions and scattering matrices to determine the optical response of a metal sphere on a dielectric substrate of finite thickness, taking into account retardation and nonlocal effects. We find that the substrate-based calculations show a similar-sized blueshift as calculations based on a sphere in a homogeneous environment, and that they both agree qualitatively with the EELS measurements.

OCIS codes: (240.6680) Surface plasmons; (250.5403) Plasmonics; (160.4236) Nanomaterials; (000.1600) Classical and quantum physics; (260.3910) Metal optics.

References and links

1. S. Raza, N. Stenger, S. Kadkhodazadeh, S. V. Fischer, N. Kostesha, A.-P. Jauho, A. Burrows, M. Wubs, and N. A. Mortensen, "Blueshift of the surface plasmon resonance in silver nanoparticles studied with EELS," Nanophotonics **2**, 131–138 (2013).
2. G. Mie, "Beiträge zur Optik trüber Medien, speziell kolloidaler Metallösungen," Ann. Phys. **330**, 377–445 (1908).
3. S. A. Maier, *Plasmonics: Fundamentals and Applications* (Springer, New York, 2007).
4. N. D. Lang and W. Kohn, "Theory of metal surfaces: Charge density and surface energy," Phys. Rev. B **1**, 4555–4568 (1970).
5. A. Boardman, B. Paranjape, and R. Teshima, "The effect of structure on surface plasmons," Surf. Sci. **49**, 275–292 (1975).
6. A. J. Bennett, "Influence of the electron charge distribution on surface-plasmon dispersion," Phys. Rev. B **1**, 203–207 (1970).

#194714 - $15.00 USD Received 26 Jul 2013; revised 20 Sep 2013; accepted 20 Sep 2013; published 4 Nov 2013

7. P. Apell, "A simple derivation of the surface contribution to the reflectivity of a metal, and its use in the Van der Waals interaction," Phys. Scr. **24**, 795–806 (1981).
8. P. J. Feibelman, "Surface electromagnetic fields," Prog. Surf. Sci. **12**, 287–407 (1982).
9. R. Ruppin, "Optical properties of a plasma sphere," Phys. Rev. Lett. **31**, 1434–1437 (1973).
10. A. D. Boardman and B. V. Paranjape, "The optical surface modes of metal spheres," J. Phys. F: Met. Phys. **7**, 1935–1945 (1977).
11. P. Apell and Å. Ljungbert, "A general non-local theory for the electromagnetic response of a small metal particle," Phys. Scr. **26**, 113–118 (1982).
12. C. Schwartz and W. L. Schaich, "Hydrodynamic models of surface plasmons," Phys. Rev. B **26**, 7008–7011 (1982).
13. A. I. Fernández-Domínguez, A. Wiener, F. J. García-Vidal, S. A. Maier, and J. B. Pendry, "Transformation-optics description of nonlocal effects in plasmonic nanostructures," Phys. Rev. Lett. **108**, 106802 (2012).
14. C. David and F. J. García de Abajo, "Spatial nonlocality in the optical response of metal nanoparticles," J. Phys. Chem. C **115**, 19470–19475 (2012).
15. G. Toscano, S. Raza, A.-P. Jauho, N. A. Mortensen, and M. Wubs, "Modified field enhancement and extinction in plasmonic nanowire dimers due to nonlocal response," Opt. Express **20**, 4176–4188 (2012).
16. C. Ciracì, R. T. Hill, J. J. Mock, Y. Urzhumov, A. I. Fernández-Domínguez, S. A. Maier, J. B. Pendry, A. Chilkoti, and D. R. Smith, "Probing the ultimate limits of plasmonic enhancement," Science **337**, 1072–1074 (2012).
17. U. Kreibig and C. Fragstein, "The limitation of electron mean free path in small silver particles," Z. Physik **224**, 307–323 (1969).
18. L. Genzel, T. P. Martin, and U. Kreibig, "Dielectric function and plasma resonance of small metal particles," Z. Phys. B **21**, 339–346 (1975).
19. P. Apell and D. R. Penn, "Optical properties of small metal spheres: Surface effects," Phys. Rev. Lett. **50**, 1316–1319 (1983).
20. O. Keller, M. Xiao, and S. Bozhevolnyi, "Optical diamagnetic polarizability of a mesoscopic metallic sphere: transverse self-field approach," Opt. Comm. **102**, 238–244 (1993).
21. U. Kreibig and L. Genzel, "Optical absorption of small metallic particles," Surf. Sci. **156**, 678–700 (1985).
22. K.-P. Charlé, W. Schulze, and B. Winter, "The size dependent shift of the surface-plasmon absorption-band of small spherical metal particles," Z. Phys. D **12**, 471–475 (1989).
23. H. Hövel, S. Fritz, A. Hilger, U. Kreibig, and M. Vollmer, "Width of cluster plasmon resonances: Bulk dielectric functions and chemical interface damping," Phys. Rev. B **48**, 18178–18188 (1993).
24. J. Tiggesbäumker, L. Köller, K.-H. Meiwes-Broer, and A. Liebsch, "Blue shift of the Mie plasma frequency in Ag clusters and particles," Phys. Rev. A **48**, R1749–R1752 (1993).
25. S. Berciaud, L. Cognet, P. Tamarat, and B. Lounis, "Observation of intrinsic size effects in the optical response of individual gold nanoparticles," Nano Lett. **5**, 515–518 (2005).
26. F. Ouyang, P. Batson, and M. Isaacson, "Quantum size effects in the surface-plasmon excitation of small metallic particles by electron-energy-loss spectroscopy," Phys. Rev. B **46**, 15421–15425 (1992).
27. J. A. Scholl, A. L. Koh, and J. A. Dionne, "Quantum plasmon resonances of individual metallic nanoparticles," Nature **483**, 421–427 (2012).
28. A. Boardman, *Electromagnetic Surface Modes. Hydrodynamic theory of plasmon-polaritons on plane surfaces.* (John Wiley and Sons, Chichester, 1982).
29. P. Apell, "The electromagnetic field near a metal surface in the semi-classical infinite barrier model," Phys. Scr. **17**, 535–542 (1978).
30. L. Mulfinger, S. D. Solomon, M. Bahadory, A. Jeyarajasingam, S. A. Rutkowsky, and C. Boritz, "Synthesis and study of silver nanoparticles," J. Chem. Educ. **84**, 322–325 (2007).
31. F. J. García de Abajo, "Optical excitations in electron microscopy," Rev. Mod. Phys. **82**, 209–275 (2010).
32. J. Aizpurua, A. Rivacoba, and S. P. Apell, "Electron-energy losses in hemispherical targets," Phys. Rev. B **54**, 2901–2909 (1996).
33. A. Boardman and R. Ruppin, "The boundary conditions between spatially dispersive media," Surf. Sci. **112**, 153–167 (1981).
34. D. J. Griffiths, *Introduction to Electrodynamics* (Benjamin Cummings), 3rd ed.
35. F. Bloch, "Bremsvermögen von Atomen mit mehreren Elektronen," Z. Phys. A **81**, 363–376 (1933).
36. S. Raza, G. Toscano, A.-P. Jauho, M. Wubs, and N. A. Mortensen, "Unusual resonances in nanoplasmonic structures due to nonlocal response," Phys. Rev. B **84**, 121412(R) (2011).
37. G. Toscano, S. Raza, W. Yan, C. Jeppesen, S. Xiao, M. Wubs, A.-P. Jauho, S. I. Bozhevolnyi, and N. A. Mortensen, "Nonlocal response in plasmonic waveguiding with extreme light confinement," Nanophotonics **2**, 161–166 (2013).
38. F. Sauter, "Der Einfluß von Plasmawellen auf das Reflexionsvermögen von Metallen (I)," Z. Physik **203**, 488–494 (1967).
39. F. Forstmann and H. Stenschke, "Electrodynamics at metal boundaries with inclusion of plasma waves," Phys. Rev. Lett. **38**, 1365–1368 (1977).
40. G. Barton, "Some surface effects in the hydrodynamic model of metals," Rep. Prog. Phys. **42**, 963–1016 (1979).

#194714 - $15.00 USD Received 26 Jul 2013; revised 20 Sep 2013; accepted 20 Sep 2013; published 4 Nov 2013

41. J. D. Jackson, *Classical electrodynamics*, 3rd ed. (Wiley, 1998).
42. I. Villo-Perez, Z. Mišković, and N. Arista, "Plasmon spectra of nano-structures: A hydrodynamic model," in "Trends in Nanophysics," V. Bârsan and A. Aldea, eds. (Springer Berlin Heidelberg, 2010), Engineering Materials, pp. 217–254.
43. Y. Luo, A. I. Fernández-Domínguez, A. Wiener, S. A. Maier, and J. B. Pendry, "Surface plasmons and nonlocality: A simple model," Phys. Rev. Lett. **111**, 093901 (2013).
44. I. Lindau and P. O. Nilsson, "Experimental evidence for excitation of longitudinal plasmons by photons," Phys. Lett. A **31**, 352–353 (1970).
45. K.-P. Charlé, L. König, S. Nepijko, I. Rabin, and W. Schulze, "The surface plasmon resonance of free and embedded Ag-clusters in the size range 1,5 nm $<$ D $<$ 30 nm," Cryst. Res. Technol. **33**, 1085–1096 (1998).
46. W. Yan et al., in preparation (2013).
47. C. Bohren and D. Huffman, *Absorption and Scattering of Light by Small Particles* (John Wiley & Sons, 1983).
48. C. David, N. A. Mortensen, and J. Christensen, "Perfect imaging, epsilon-near zero phenomena and waveguiding in the scope of nonlocal effects," Sci. Rep. **3**, 2526 (2013).
49. T. Bååk, "Silicon oxynitride; a material for GRIN optics," Appl. Opt. **21**, 1069–1072 (1982).
50. A. D. Rakić, A. B. Djurišić, J. M. Elazar, and M. L. Majewski, "Optical properties of metallic films for vertical-cavity optoelectronic devices." Appl. Opt. **37**, 5271–5283 (1998).
51. R. Ruppin, "Surface modes and optical absorption of a small sphere above a substrate," Surf. Sci. **127**, 108–118 (1983).
52. A. Liebsch, "Surface-plasmon dispersion and size dependence of Mie resonance: silver versus simple metals," Phys. Rev. B **48**, 11317–11328 (1993).
53. R. Carmina Monreal, T. J. Antosiewicz, and S. P. Apell, "Competition between surface screening and size quantization for surface plasmons in nanoparticles," New J. Phys. **15**, 083044 (2013).

1. Introduction

The use of metal nanoparticles to create astonishing colors in stained glass dates back to ancient Roman times. However, the mechanism behind the color generation was not fully understood until Mie in 1908 rigorously and exactly solved Maxwell's electrodynamical equations for the problem of plane wave scattering off a sphere [2]. From Mie's solution it follows that resonant modes of the metal sphere, which we now refer to as localized SPs [3], give rise to large absorption cross sections at specific wavelengths, resulting in the colorful stained glass. In Mie's treatment of the problem it is assumed that the material properties of the sphere can be described by a single frequency-dependent function, the local-response dielectric function $\varepsilon(\omega)$. While in most cases a classical treatment based on the dielectric function is justified, important effects due to surface structure [4–8], nonlocal response [9–16] and quantum size effects [17–20] manifest themselves in the response of metal nanoparticles, when the particle sizes are below ~ 10 nm. Many experiments on tiny nanoparticles using both optical measurements [21–25] and electron energy-loss studies [1, 26, 27] have shown that the classical approach is insufficient to describe the experimental observations. The interpretation of these results has been based on semi-classical models, such as the nonlocal hydrodynamic [28] and semi-classical infinite barrier (SCIB) [29] approaches, or more complicated quantum calculations using density functional theory [4].

Recently, we performed EELS on chemically synthesized Ag nanoparticles with diameters ranging from 3.5 to 26 nm [1]. We observed a large blueshift of the localized SP resonance energy from 3.2 eV to 3.7 eV, when the particle size decreased. We interpreted these non-classical observations using two different semi-classical models, the hydrodynamic model and the model presented by Keller et al. [20], which both only qualitatively could explain the observations. In this paper, we focus on the hydrodynamic model and derive the nonlocal polarizability of a hydrodynamic sphere in a homogeneous environment, which leads to the nonlocal generalization of the Clausius–Mossotti factor. We also study the effect of the substrate on the resonance energy of the nanoparticle. Specifically, we develop an exact formalism to calculate the optical response of a metal sphere on a dielectric substrate of finite thickness, taking into account both retardation and nonlocal response. The theoretical calculations are compared to the EELS

#194714 - $15.00 USD Received 26 Jul 2013; revised 20 Sep 2013; accepted 20 Sep 2013; published 4 Nov 2013

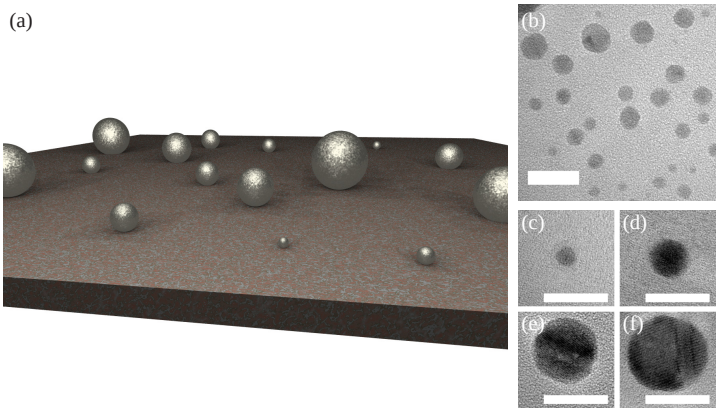

Fig. 1. (a) Schematic image of the Ag nanoparticles deposited on 10 nm thick Si_3N_4 substrate. (b) Bright-field TEM image of sample. (c-f) Bright-field TEM images of single nanoparticles with diameters 3, 6, 10 and 13 nm, respectively. All scale bars are 10 nm long.

measurements.

2. Experiment: electron energy loss spectroscopy

The silver nanoparticles are chemically synthesized [30] and afterwards stabilized in an aqueous solution with borohydride ions to prevent aggregation. Subsequently, the solution with nanoparticles is deposited on a plasma-cleaned 10 nm thick Si_3N_4 TEM membrane purchased from TEMwindows.com. The mean particle diameter is 12 nm with a broad size distribution from 2 nm up to 30 nm, see Fig. 1, which gives us the advantage of being able to perform all of the measurements on the same sample.

The EELS measurements are performed with a FEI Titan transmission electron microscope (TEM) equipped with a monochromator and a probe aberration corrector. The microscope is operated in scanning TEM (STEM) mode at an acceleration voltage of 120 kV, providing a probe diameter of 0.5 nm and a zero-loss peak width of 0.15 ± 0.05 eV. In a spherical particle only the amplitude of the SP, and not the resonance energy, is dependent on the position of the electron beam [31]. We therefore acquire the EELS spectra by directing the electron probe close to the surface of the silver nanoparticle (aloof trajectory), thereby enhancing the excitation of the SP. Details on the data analysis and further experimental information can be found in Ref. [1].

3. Theory: hydrodynamic model

In the following theoretical approaches we will assume that the shape of the nanoparticles can be approximated to be spherical. Details and discussion about this approximation can be found in Ref. [1]. Here, we note from the TEM images in Figs. 1(b)-(f) that the overall shape of the nanoparticles is spherical, especially for particle sizes below 10 nm in diameter, which justifies our approximation. Furthermore, large shape deviations from a sphere, such as hemispherical or disk-shaped particles, would also manifest themselves in the EELS spectra in terms of new resonances or electron beam position-dependent resonances [32], which we do not observe.

#194714 - $15.00 USD Received 26 Jul 2013; revised 20 Sep 2013; accepted 20 Sep 2013; published 4 Nov 2013

We base the interpretation of our experimental results on the hydrodynamic model. We first derive the exact nonlocal polarizability of a metal sphere embedded in a homogeneous material, thereby generalizing the well-known Clausius–Mossotti factor to nonlocal response. The free electrons of the sphere are described by the semiclassical hydrodynamic model, which takes into account nonlocal response but neglects the spill-out of the electrons outside the spheres due to the finiteness of their confining potential. Secondly, the effect of the substrate is taken into account. Here, we present an exact formalism to calculate the retarded optical response of a sphere with hydrodynamic nonlocal response, on a dielectric substrate of finite thickness.

The starting point of the hydrodynamic model is Maxwell's equations in terms of the free-electron density n and free-electron current $\mathbf{J}$ [28, 33, 34]

$$\nabla \cdot \mathbf{D} = -en, \tag{1a}$$

$$\nabla \cdot \mathbf{H} = 0, \tag{1b}$$

$$\nabla \times \mathbf{E} = i\omega\mu_0 \mathbf{H}, \tag{1c}$$

$$\nabla \times \mathbf{H} = -i\omega \mathbf{D} + \mathbf{J}, \tag{1d}$$

where the constitutive relation $\mathbf{B} = \mu_0 \mathbf{H}$ for non-magnetic materials has been utilized. Here, we introduce the polarization effects due to the bound charges through the constitutive relation for the displacement field $\mathbf{D} = \varepsilon_0 \varepsilon_\infty \mathbf{E}$, where ε_∞ in general is frequency-dependent and takes into account those polarization effects that are not due to the free electrons, such as interband transitions. The continuity equation, which connects the free-electron density and the free-electron current, follows directly from Eqs. (1a) and (1d),

$$\nabla \cdot \mathbf{J} = -i\omega en. \tag{2}$$

To complete the description of the electromagnetic response of the metal, a relation which connects the free-electron current to the electric field is needed. To this end, we consider the linearized nonlocal hydrodynamic equation [28, 35], which in its real-space formulation becomes [15, 36, 37]

$$\frac{\beta^2}{\omega(\omega + i\gamma)} \nabla (\nabla \cdot \mathbf{J}) + \mathbf{J} = \varepsilon_0 \sigma \mathbf{E}, \tag{3}$$

where $\sigma = i\omega_p^2/(\omega + i\gamma)$ is the classical Drude conductivity, and $\beta^2 = 3/5 v_F^2$ with v_F being the Fermi velocity. Within a hydrodynamic description the pressure of the electron gas is included, which gives rise to the presence of compression (longitudinal) waves and leads to spatial dispersion that is observable in truly nanoplasmonic systems. Equations (1)-(3) constitute the basic set of equations within the retarded hydrodynamic approach. At an interface between two materials, these equations are supplemented by boundary conditions (BCs). In this study we consider only metal-dielectric interfaces, where Maxwell's BCs must be augmented by a single additional boundary condition (ABC) which states that the normal component of the free-electron current density must vanish [33, 36, 38–40]. The ABC can be derived as a consequence of neglecting the spill-out of electrons.

3.1. Hydrodynamic sphere in homogeneous environment: nonlocal Clausius–Mossotti factor

We consider a small isotropic metal sphere of radius R embedded in a homogeneous dielectric environment with permittivity ε_B. The polarizability α of this sphere is a well-known result in classical optics [3, 41] and is given by

$$\alpha = 4\pi R^3 \frac{\varepsilon_D - \varepsilon_B}{\varepsilon_D + 2\varepsilon_B}, \tag{4}$$

#194714 - $15.00 USD Received 26 Jul 2013; revised 20 Sep 2013; accepted 20 Sep 2013; published 4 Nov 2013

where $\varepsilon_D = \varepsilon_\infty - \omega_p^2/(\omega^2 + i\gamma\omega)$ is the classical Drude permittivity. The factor $(\varepsilon_D - \varepsilon_B)/(\varepsilon_D + 2\varepsilon_B)$ is called the Clausius–Mossotti factor and notice that it is independent of the sphere radius. The polarizability is derived in the quasistatic approximation under the assumption of a static surrounding electric field, thus neglecting spatial variations in the exciting electric field. Our goal is now to derive a generalization to this formula, taking hydrodynamic nonlocal response of the sphere into account. We begin by introducing the electric and current scalar potentials ϕ and ψ, respectively, defined as

$$\mathbf{E} = -\nabla\phi, \qquad \mathbf{J} = -\nabla\psi. \tag{5}$$

By inserting Eq. (5) into the hydrodynamic Eqs. (1)-(3), it can straightforwardly be shown that the scalar potentials inside the metal sphere are governed by the equations [42]

$$\left(\nabla^2 + k_{NL}^2\right) n = 0, \tag{6a}$$

$$\nabla^2\phi = \tfrac{e}{\varepsilon_0\varepsilon_\infty} n, \tag{6b}$$

$$\psi = \tfrac{1}{i\omega-\gamma}\left(\varepsilon_0\omega_p^2\phi - e\beta^2 n\right), \tag{6c}$$

where the nonlocal longitudinal wave vector is given as $k_{NL}^2 = (\omega^2 + i\omega\gamma - \omega_p^2/\varepsilon_\infty)/\beta^2$. In the surrounding dielectric, the current density $\mathbf{J}$ and electron density n vanish, and the electric scalar potential must instead satisfy the usual Laplace equation $\nabla^2\phi = 0$. Finally, Maxwell's BCs and the hydrodynamic ABC for the scalar potentials translate into

$$\phi^{in} = \phi^{out}, \qquad \varepsilon_\infty \frac{\partial\phi^{in}}{\partial r} = \varepsilon_B \frac{\partial\phi^{out}}{\partial r}, \qquad \frac{\partial\psi^{in}}{\partial r} = 0, \tag{7}$$

where *in* and *out* refers to inside and outside the metal, respectively. The general solutions to the electric scalar potential and free-electron density inside and outside the sphere are

$$n^{in} = \sum_{l,m} A_l j_l(k_{NL} r) Y_{lm}(\theta,\phi), \qquad n^{out} = 0, \tag{8a}$$

$$\phi^{in} = \sum_{l,m} \left[D_l r^l - A_l \tfrac{e}{\varepsilon_0\varepsilon_\infty k_{NL}^2} j_l(k_{NL} r)\right] Y_{lm}(\theta,\phi), \tag{8b}$$

$$\phi^{out} = \sum_{l,m} \left[B_l r^l + C_l r^{-(l+1)}\right] Y_{lm}(\theta,\phi). \tag{8c}$$

Here, j_l and Y_{lm} are the spherical Bessel function of the first kind and the spherical harmonics, respectively. The current scalar potential ψ can be determined from Eq. (6c). We neglect variations in the exciting electric field and assume a constant electric field surrounding the sphere, here directed in the $\hat{\mathbf{z}}$ direction i.e. $\mathbf{E}^{out} = E_0\hat{\mathbf{z}}$. Thus, this poses the requirement that $\lim_{r\to\infty}\phi^{out} = -E_0 z = -E_0 r\cos(\theta)$, which excludes all orders of (l,m) in the sums in Eq. (8) except $(l,m) = (1,0)$. Applying the BCs from Eq. (7) and following the usual approach to introducing the polarizability [3], we determine the nonlocal polarizability α_{NL} to be

$$\alpha_{NL} = 4\pi R^3 \frac{\varepsilon_D - \varepsilon_B(1+\delta_{NL})}{\varepsilon_D + 2\varepsilon_B(1+\delta_{NL})}, \qquad \delta_{NL} = \frac{\varepsilon_D - \varepsilon_\infty}{\varepsilon_\infty} \frac{j_1(k_{NL}R)}{k_{NL}R j_1'(k_{NL}R)}, \tag{9}$$

where the prime denotes differentiation with respect to the argument. We see that nonlocal effects enter the Clausius–Mossotti factor as an elegant and simple rescaling of either the metal permittivity from ε_D to $\tilde{\varepsilon}_D = \varepsilon_D(1+\delta_{NL})^{-1}$ or of the background permittivity from ε_B to $\tilde{\varepsilon}_B = \varepsilon_B(1+\delta_{NL})$. Both approaches are equally valid, but we choose to examine the rescaled

#194714 - $15.00 USD Received 26 Jul 2013; revised 20 Sep 2013; accepted 20 Sep 2013; published 4 Nov 2013

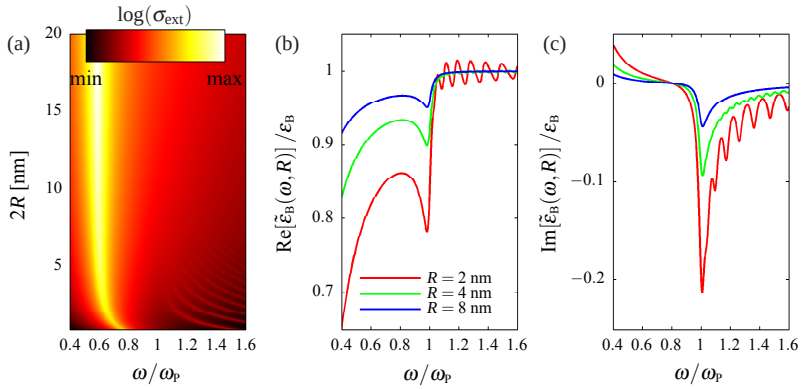

Fig. 2. (a) Extinction cross section based on the nonlocal Clausius–Mossotti factor, Eq. (9), as a function of diameter $2R$ and normalized frequency ω/ω_P. The real and imaginary parts of the normalized rescaled background permittivity $\tilde{\varepsilon}_B/\varepsilon_B$ as a function of normalized frequency are shown in (b) and (c), respectively, for three different sphere radii: 2 nm (red), 4 nm (green) and 8 nm (blue). Free-electron gas parameters used for the calculations: $\gamma/\omega_P = 0.05$, $\beta/c = 5\times10^{-3}$, $\varepsilon_\infty = 1$ and $\varepsilon_B = 1$.

background permittivity since the nonlocal blueshift of the SP resonance, which is discussed in the following, can be more easily understood in terms of a change in the background permittivity, and this approach also follows the line of reasoning in the recent work of Ref. [43]. We point out that the rescaled background permittivity $\tilde{\varepsilon}_B$ is now both frequency- and size-dependent. Finally, we note that when $\beta \to 0$ then $\delta_{NL} \to 0$ in Eq. (9) and the classical size-independent Clausius–Mossotti factor is retrieved.

With the nonlocal polarizability we can determine the extinction cross section σ_{ext} of a metal sphere using the relation [3]

$$\sigma_{ext} = \frac{1}{\pi R^2}\left[\frac{(\omega/c)^4}{6\pi}|\alpha_{NL}|^2 + (\omega/c)\mathrm{Im}(\alpha_{NL})\right]. \tag{10}$$

In Fig. 2(a) we show the extinction cross section as a function of diameter and frequency for a model sphere in vacuum and with only a free-electron response. The blueshift of the SP resonance energy for decreasing particle diameter, which is known to be present from generalized nonlocal Mie theory [9], is captured accurately by the simple nonlocal Clausius–Mossotti factor in Eq. (9). Furthermore, we see that as the particle diameter increases the resonance energy approaches the well-known classical limit $\omega/\omega_P = 1/\sqrt{3} \approx 0.577$. For the smallest diameters ($2R < 5$ nm) a series of strongly size-dependent resonances above the plasma frequency can be distinguished. These are resonant pressure-type (longitudinal) waves that arise due to the confinement of the free electron gas. Comparison with the generalized Mie theory [9] (not displayed) shows that the spectral location and spectral width of the pressure resonances predicted by the nonlocal Clausius–Mossotti factor are exact.

Using the nonlocal Clausius–Mossotti factor we can deduce a simple approximate, but accurate relation which determines the resonance frequencies of the pressure modes. The poles of the nonlocal correction δ_{NL} in Eq. (9) determine the spectral position of the pressure modes, which provides us with the condition $j_1'(k_{NL}R) = 0$. We rewrite this condition in terms of the

#194714 - $15.00 USD Received 26 Jul 2013; revised 20 Sep 2013; accepted 20 Sep 2013; published 4 Nov 2013

standard Bessel functions and use the large-argument asymptotic form of the Bessel function $J_l(x) \simeq \sqrt{2/(\pi z)}\cos(z - l\pi/2 - \pi/4)$, since the product $k_{\rm NL}R \geq 1$ due to the high frequencies ($\omega > \omega_{\rm P}$) at which these resonances occur. After some straightforward algebraic manipulations we find (for negligible damping) the relation

$$\omega^2 \simeq \frac{\omega_{\rm P}^2}{\varepsilon_\infty} + \frac{\beta^2\pi^2}{R^2}n^2, \tag{11}$$

where formally $n = 1, 2, 3, ...$ However, upon comparison with extinction cross section calculations we find that the mode $n = 1$ is optically dark and therefore does not show up in the extinction spectrum [44].

Figures 2(b) and 2(c) display the frequency dependency of the real and imaginary parts of the rescaled background permittivity $\tilde{\varepsilon}_{\rm B}(\omega, R)$, respectively, for three different radii. In Fig. 2(b) we see that below the plasma frequency $\mathrm{Re}(\tilde{\varepsilon}_{\rm B})/\varepsilon_{\rm B}$ decreases from unity with decreasing radii, leading to the size-dependent blueshift observed in the extinction cross section. In the same frequency interval, we see from Fig. 2(c) that $\mathrm{Im}(\tilde{\varepsilon}_{\rm B})/\varepsilon_{\rm B}$ does not vary significantly and is close to zero. Above the plasma frequency both $\mathrm{Re}(\tilde{\varepsilon}_{\rm B})/\varepsilon_{\rm B}$ and $\mathrm{Im}(\tilde{\varepsilon}_{\rm B})/\varepsilon_{\rm B}$ display periodic variations, which give rise to the pressure resonances in the extinction cross section. Finally, as the radius increases the frequency dependence of both $\mathrm{Re}(\tilde{\varepsilon}_{\rm B})/\varepsilon_{\rm B}$ and $\mathrm{Im}(\tilde{\varepsilon}_{\rm B})/\varepsilon_{\rm B}$ weakens, and the classical limits $\mathrm{Re}(\tilde{\varepsilon}_{\rm B})/\varepsilon_{\rm B} \to 1$ and $\mathrm{Im}(\tilde{\varepsilon}_{\rm B})/\varepsilon_{\rm B} \to 0$ are approached.

The above derivation of the nonlocal polarizability $\alpha_{\rm NL}$ of a metal sphere in a homogeneous dielectric environment is expected to describe many experimental situations of spheres in glass or gels [22, 23, 45]. It can also be used, although its accuracy remains to be tested, in case an inhomogeneous environment is described with an effective homogeneous background dielectric function, see Sec. 4.

3.2. Hydrodynamic sphere on substrate of finite thickness

We consider next the case of a metal sphere situated on a substrate, as in the experiment, so we drop the assumption that the background is homogeneous. We present here an exact method based on scattering matrices and multipole expansions to calculate the extinction cross section of the sphere-substrate system, when impinged by a plane wave [46]. The dielectric constant and the thickness of the substrate are denoted $\varepsilon_{\rm S}$ and t, respectively.

The system in study consists of a metal sphere in contact with a dielectric substrate, where the origin of the coordinate system is located at the contact point and the z-axis is taken normal to the substrate. The incident plane wave and scattered wave are expanded in spherical waves [47] with $\mathbf{a}_{lm}^{\sigma}$ and $\mathbf{b}_{lm}^{\sigma}$ denoting the expansion coefficients of the incident and scattered waves, respectively. Here, $\sigma = 1, 2$ represent TE and TM polarizations, respectively.

In the absence of the substrate, the incident and scattered spherical wave amplitudes are related through Mie's scattering matrix for the metal sphere as $\mathbf{b}_{l'm'}^{\sigma'} = \mathbf{T}_{l'm'\sigma'}^{lm\sigma}\mathbf{a}_{lm}^{\sigma}$, where

$$\mathbf{T}_{l'm'\sigma'}^{lm\sigma} = t_l^{(\sigma)}\delta_{ll'}\delta_{mm'}\delta_{\sigma\sigma'}, \tag{12}$$

is Mie's scattering matrix, which takes retardation effects into account, and $\delta_{ii'}$ is the Kronecker delta.

Here, the coefficients $t_l^{(\sigma)}$ are the nonlocal Mie scattering coefficients given as [9, 14]

$$t_l^{(1)} = -\frac{j_l(x_{\rm D})\,j_l'(x_{\rm B}) - j_l(x_{\rm B})\,j_l'(x_{\rm D})}{j_l(x_{\rm D})h_l^{(1)\prime}(x_{\rm B}) - h_l^{(1)}(x_{\rm B})\,j_l'(x_{\rm D})}, \tag{13a}$$

$$t_l^{(2)} = -\frac{\left[c_l + j_l'(x_{\rm D})\right]\varepsilon_{\rm B}\,j_l(x_{\rm B}) - \varepsilon_{\rm D}\,j_l(x_{\rm D})\,j_l'(x_{\rm B})}{\left[c_l + j_l'(x_{\rm D})\right]\varepsilon_{\rm B}h_l^{(1)}(x_{\rm B}) - \varepsilon_{\rm D}\,j_l(x_{\rm D})h_l^{(1)\prime}(x_{\rm B})}, \tag{13b}$$

#194714 - $15.00 USD Received 26 Jul 2013; revised 20 Sep 2013; accepted 20 Sep 2013; published 4 Nov 2013

where $x_{\rm B} = \omega\sqrt{\varepsilon_{\rm B}}R/c$, $x_{\rm D} = \omega\sqrt{\varepsilon_{\rm D}}R/c$ and $h_l^{(1)}$ denotes the spherical Hankel function of the first kind. The nonlocal correction c_l to the Mie coefficients is given as

$$c_l = l(l+1)\frac{j_l(x_{\rm NL})\,j_l(x_{\rm D})}{x_{\rm NL}\,j_l'(x_{\rm NL})}\frac{\varepsilon_{\rm D}-\varepsilon_\infty}{\varepsilon_\infty}, \tag{13c}$$

with $x_{\rm NL} = k_{\rm NL}R$. We note that for $l = 1$ the nonlocal correction in Eq. (13c) has the same structural form as $\delta_{\rm NL}$ in the nonlocal Clausius–Mossotti factor, Eq. (9). In fact they are related as $c_1 = 2j_1(x_{\rm D})\delta_{\rm NL}$.

In the presence of the substrate, reflections from the substrate must be taken into account, which changes Mie's scattering matrix $\mathbf{T}$ to the total scattering matrix $\mathbf{M}$ given as

$$\mathbf{M} = (\mathbf{I} - \mathbf{TS})^{-1}\mathbf{T}. \tag{14}$$

The total scattering matrix $\mathbf{M}$ takes into account the interactions between the substrate and the sphere through the substrate scattering matrix $\mathbf{S}$. To derive $\mathbf{M}$, we use the transformation relations between plane waves and spherical waves, and characterize the interactions between the scattered spherical waves $\mathbf{b}$ and the substrate by the plane wave reflections. In particular, $\mathbf{S}$ is given as

$$\mathbf{S}^{lm1}_{l'm'1} = s^{mm'}_{ll'}\iint {\rm d}k_x{\rm d}k_y\frac{f_1 y^{(1)}_{lm}y^{(1)}_{l'-m'} + f_2 y^{(2)}_{lm}y^{(2)}_{l'-m'}}{k_{\rm Bz}}, \tag{15a}$$

$$\mathbf{S}^{lm2}_{l'm'2} = s^{mm'}_{ll'}\iint {\rm d}k_x{\rm d}k_y\frac{f_2 y^{(1)}_{lm}y^{(1)}_{l'-m'} + f_1 y^{(2)}_{lm}y^{(2)}_{l'-m'}}{k_{\rm Bz}}, \tag{15b}$$

$$\mathbf{S}^{lm2}_{l'm'1} = -s^{mm'}_{ll'}\iint {\rm d}k_x{\rm d}k_y\frac{f_2 y^{(1)}_{lm}y^{(2)}_{l'-m'} + f_1 y^{(2)}_{lm}y^{(1)}_{l'-m'}}{k_{\rm Bz}}, \tag{15c}$$

$$\mathbf{S}^{lm1}_{l'm'2} = -s^{mm'}_{ll'}\iint {\rm d}k_x{\rm d}k_y\frac{f_1 y^{(1)}_{lm}y^{(2)}_{l'-m'} + f_2 y^{(2)}_{lm}y^{(1)}_{l'-m'}}{k_{\rm Bz}}, \tag{15d}$$

with

$$s^{mm'}_{ll'} = \frac{2i^{l'-l}(-1)^{l+m+m'+1}}{k_{\rm B}\sqrt{l'(l'+1)}\sqrt{l(l+1)}}, \quad y^{(1)}_{lm} = \frac{\partial Y_{lm}(\Omega_{\mathbf{k}_{\rm B}})}{\partial\theta_{\mathbf{k}_{\rm B}}}, \quad y^{(2)}_{lm} = \frac{mY_{lm}(\Omega_{\mathbf{k}_{\rm B}})}{\sin\theta_{\mathbf{k}_{\rm B}}}, \tag{16}$$

where $\mathbf{k}_{\rm B}$ represents the wavevector of the plane wave in the background with $|\mathbf{k}_{\rm B}| = k_{\rm B} = \sqrt{\varepsilon_{\rm B}}\omega/c$, $k_{\rm Bz}$ is the z component of $\mathbf{k}_{\rm B}$ with the imaginary part being positive, $\sin\theta_{\mathbf{k}_{\rm B}}$ is defined as $\sin\theta_{\mathbf{k}_{\rm B}} = \sqrt{k_x^2+k_y^2}/k_{\rm B}$, and the integration ranges of k_x and k_y are both from $-\infty$ to ∞. The coefficients f_σ in Eq. (15) represent the reflection coefficients of the substrate for TE and TM polarized plane waves, respectively, in which the substrate plays its role. The coefficients f_σ are expressed as

$$f_\sigma = \frac{r_\sigma\left[1-\exp(ik_{\rm Sz}2t)\right]}{1-r_\sigma^2\exp(ik_{\rm Sz}2t)}\exp(ik_{\rm Bz}2R), \tag{17a}$$

where $k_{\rm Sz}$ represents the z component of the wavevector in the substrate. Furthermore, r_σ is the reflection coefficient between the background and the semi-infinite substrate given as

$$r_1 = \frac{k_{\rm Bz}-k_{\rm Sz}}{k_{\rm Bz}+k_{\rm Sz}}, \quad r_2 = \frac{\varepsilon_{\rm S}k_{\rm Bz}-\varepsilon_{\rm B}k_{\rm Sz}}{\varepsilon_{\rm S}k_{\rm Bz}+\varepsilon_{\rm B}k_{\rm Sz}}. \tag{17b}$$

#194714 - $15.00 USD Received 26 Jul 2013; revised 20 Sep 2013; accepted 20 Sep 2013; published 4 Nov 2013

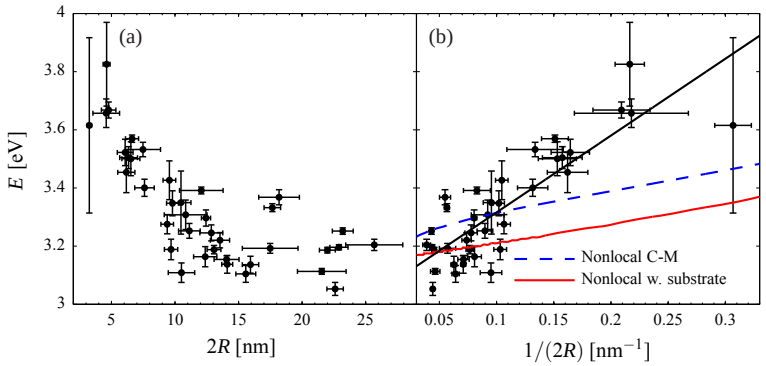

Fig. 3. EELS measurements of the SP resonance energy E plotted as a function of (a) diameter $2R$ and (b) inverse diameter $1/(2R)$. In (b), the black solid line is a linear fit to the experimental data and serves as a guide to the eye, while the blue dashed line represents calculations of a nonlocal sphere in a homogeneous environment [nonlocal Clausius–Mossotti factor, Eq. (9)]. From the average large-particle ($2R > 20$ nm) resonances we fit $\varepsilon_B = 1.53$. The red solid line represents calculations of a nonlocal sphere in vacuum situated on a 10 nm thick Si_3N_4 substrate with permittivity $\varepsilon_S = 4.4$ [49]. Material parameters for Ag are taken from Ref. [50] and the Fermi velocity is $v_F = 1.39 \times 10^6$ m/s.

At this stage, we add that the reflection coefficients in Eq. (17b) can be exchanged with their nonlocal expressions, see e.g. [48], to describe the interactions between a metal sphere and metal film, while taking nonlocal response into account in both metal structures. Such a system was recently studied experimentally in Ref. [16].

With the total scattering matrix $\mathbf{M}$, we can numerically compute the extinction cross section of the metal sphere on a substrate of finite thickness, using the relation

$$\sigma_{\text{ext}} = -\frac{1}{k_B^2 |E_0|^2} \text{Re}(\mathbf{a}^T \mathbf{M} \mathbf{a}^*), \tag{18}$$

where $|E_0|$ is the amplitude of the incident field, and superscripts T and * denote the transpose and complex conjugate, respectively. From the extinction cross section we determine the SP resonance energy.

4. Results

In Fig. 3(a), we show the EELS measurements of the SP resonance energy E as a function of the particle diameter $2R$. Two distinct features are present. The first is the spread of the resonance energy at a fixed particle diameter. In [1], we argue in detail that the spread is due to shape variations of the nanoparticle. Briefly, from the 2D STEM images we determine the area of the particle A and assign it a diameter, assuming a spherical shape $\left(\text{i.e. } A = \pi R^2\right)$. Different particles with slight deviations from spherical shape can lead to the same area and ultimately the same diameter. However, their SP resonance changes and this is what we observe experimentally. The important second feature we observe is a significant blueshift of the resonance energy of 0.5 eV as the particle diameter decreases. The blueshift is in good agreement with earlier results [24, 26, 27]. A classical local-response theory based on a size-independent dielectric

#194714 - $15.00 USD Received 26 Jul 2013; revised 20 Sep 2013; accepted 20 Sep 2013; published 4 Nov 2013

function of the material does not predict any frequency shift at all.

Figure 3(b) displays again the SP resonance energy E, now as a function of the inverse particle diameter $1/(2R)$. The experimental measurements suggest a linear relationship between the energy and inverse particle diameter. The nearly linear trend is also seen in the theoretical calculations based on the hydrodynamic model, shown with dashed and solid lines in Fig. 3(b), albeit with a smaller slope. We point out that the apparent $1/(2R)$ dependent blueshift is only a first-order approximation in the hydrodynamic theory [1]. The dashed line in Fig. 3(b) corresponds to calculations of a hydrodynamic sphere embedded in a homogeneous environment, i.e. the nonlocal Clausius–Mossotti factor described in Sec. 3.1. The permittivity of the background dielectric is fitted to the average resonance of the largest particles ($2R > 20$ nm) to ensure the correct classical SP resonance. We find $\varepsilon_B = 1.53$. The solid line shows the resonance energy determined from extinction cross section calculations of a hydrodynamic sphere in vacuum situated on a 10 nm thick Si_3N_4 substrate, as described in Sec. 3.2. Here no fitting of the background permittivity is performed and we use $\varepsilon_S = 4.4$ as the permittivity of the substrate, suitable for Si_3N_4 [49]. The same material parameters for the Ag sphere are used in both calculations [50]. While the substrate-based calculation shows an overall lower resonance energy for all particle sizes, both approaches show a linear tendency with a nearly identical slope. Compared to a free-space environment the presence of the dielectric substrate should induce a larger blueshift in the hydrodynamic model [1], and indeed it does (comparison not shown in Fig. 3). The fitted effective background permittivity in the calculations based on the nonlocal Clausius-Mossotti relation is larger than that of free space, and this makes that the two theoretical curves in Fig. 3(b) become almost parallel. Especially for the smallest particles $\left[1/(2R) > 0.1\ \text{nm}^{-1}\right]$ the trend is striking similar, which indicates that (i) only the dipole mode of the sphere is important and (ii) the dipole mode is not significantly altered by the presence of the substrate. However, for larger particle diameters $\left[1/(2R) < 0.1\ \text{nm}^{-1}\right]$ the substrate alters the dipole mode, which is visible in the slight convex curvature of the solid line in Fig. 3(b), in contrast to the concave curvature of the dashed line. Surprisingly higher order multipoles in the sphere, which are anticipated to be enhanced due to the presence of the substrate [51], show no significant contribution in the optical response. This is in fact due to the large interband absorption present in Ag at the resonance energies of the higher order multipoles, which heavily dampens the contribution from these modes.

From Fig. 3(b) we see that the experimentally observed blueshift exceeds the theoretical blueshift predicted by the nonlocal Clausius–Mossotti factor. In [1], we conjectured that the presence of the substrate could induce the experimentally observed larger blueshift, but from Fig. 3(b) we see in more detail that the substrate-based calculations do not show a larger shift in energy than the nonlocal Clausius–Mossotti factor.

5. Conclusions

We have studied the experimentally observed blueshift of the SP resonance energy of Ag nanoparticles, when the particle diameters decrease from 26 nm to 3.5 nm. To interpret the measurements we considered two different systems within the theory of the nonlocal hydrodynamic model: a metal sphere embedded in a homogeneous environment and a metal sphere situated on a dielectric substrate of finite thickness. Surprisingly, we find that both systems give rise to similar-sized blueshifts with decreasing particle size, despite the presence of the symmetry-breaking substrate. Both theoretical calculations are in qualitative agreement with the measurements, but the theoretically calculated blueshift is smaller than the blueshift observed in the EELS measurements. Thus, we conclude that the inclusion of the substrate in the theoretical calculations can not quantitatively explain the measurements. This leads us to believe that the deviation between theory and experiment are to be sought for in the intrinsic

#194714 - $15.00 USD Received 26 Jul 2013; revised 20 Sep 2013; accepted 20 Sep 2013; published 4 Nov 2013

properties of silver, such as the spill-out of electrons in combination with the screening from the *d* electrons [52,53] and size-dependent changes in the electronic band structure [23], which are not taken into account in a hydrodynamic description.

Acknowledgments

We thank Prof. U. Kreibig and Prof. A.-P. Jauho for stimulating discussions. We also acknowledge the help and collaboration from our co-authors in Ref. [1]. The Center for Nanostructured Graphene is sponsored by the Danish National Research Foundation, Project DNRF58. The A. P. Møller and Chastine Mc-Kinney Møller Foundation is gratefully acknowledged for the contribution toward the establishment of the Center for Electron Nanoscopy.

#194714 - $15.00 USD Received 26 Jul 2013; revised 20 Sep 2013; accepted 20 Sep 2013; published 4 Nov 2013

Paper F

S. Raza, T. Christensen, M. Wubs, S. I. Bozhevolnyi, and N. A. Mortensen

Nonlocal response in thin-film waveguides: loss versus nonlocality and breaking of complementarity

Phys. Rev. B **88**, 115401 (2013)

Author contributions
S. R. derived the equations, was the main author of the manuscript and created figures 1, 2, 4, and 5. T. C. created figure 3 and co-wrote the manuscript. All authors were involved in discussing the obtained results and in correcting the manuscript.

PHYSICAL REVIEW B 88, 115401 (2013)

Nonlocal response in thin-film waveguides: Loss versus nonlocality and breaking of complementarity

Søren Raza,[1,2] Thomas Christensen,[1,3] Martijn Wubs,[1,3] Sergey I. Bozhevolnyi,[4] and N. Asger Mortensen[1,3,*]

[1]*Department of Photonics Engineering, Technical University of Denmark, DK-2800 Kgs. Lyngby, Denmark*

[2]*Center for Electron Nanoscopy, Technical University of Denmark, DK-2800 Kgs. Lyngby, Denmark*

[3]*Center for Nanostructured Graphene, Technical University of Denmark, DK-2800 Kgs. Lyngby, Denmark*

[4]*Institute of Sensors, Signal and Electrotechnics, University of Southern Denmark, DK-5230 Odense, Denmark*

(Received 6 May 2013; revised manuscript received 29 July 2013; published 3 September 2013)

We investigate the effects of nonlocal response on the surface-plasmon polariton guiding properties of the metal-insulator (MI), metal-insulator-metal (MIM), and insulator-metal-insulator (IMI) waveguides. The nonlocal effects are described by a linearized hydrodynamic model, which includes the Thomas-Fermi internal kinetic energy of the free electrons in the metal. We derive the nonlocal dispersion relations of the three waveguide structures taking into account also retardation and interband effects, and examine the delicate interplay between nonlocal response and absorption losses in the metal. We also show that nonlocality breaks the complementarity of the MIM and IMI waveguides found in the nonretarded limit.

DOI: 10.1103/PhysRevB.88.115401 PACS number(s): 73.20.Mf, 78.20.−e, 71.10.Ca, 78.68.+m

I. INTRODUCTION

Guiding of light at metal-dielectric interfaces has attracted a lot of attention in recent years due to the subwavelength light confinement achievable by excitation of propagating surface-plasmon polariton (SPP) modes.[1,2] SPP guiding in a number of configurations is not limited by the diffraction limit, allowing for the manipulation and concentration of light on the nanoscale.[3] At the same time, stronger SPP mode confinement is typically associated with stronger mode absorption in the metal, resulting in a trade-off between light confinement and propagation distances.[4] This trade-off can be tailored by considering various waveguide structures, where especially waveguides based on thin metal films or narrow dielectric gaps between two metal surfaces have shown to provide a considerably better trade-off.[5,6] Symmetric metal-insulator-metal (MIM) and insulator-metal-insulator (IMI) waveguides, see Fig. 1, are the most fundamental of this class of waveguide structures and provide a solid foundation for the understanding of more complex plasmonic waveguides. The key property of the IMI waveguide is its ability to support the so-called long-range SPP mode, which exhibits considerably low propagation loss. Furthermore, the MIM configuration forms the basis for the effective-index modeling (EIM) technique of more complex waveguiding structures, such as V-groove, slot, and trench waveguides.[5,7]

The MIM and IMI waveguides have been extensively studied experimentally[8–12] and theoretically.[6,13–16] A key feature of any theoretical description of SPPs involves a suitable choice for the modeling of the response of free electrons of the metal. By far, the most common approach in the literature has been to apply the local-response approximation (LRA). The LRA solutions for the MIM and IMI structures were determined very early by Economou[17] and comprise two SPP modes being of even and odd symmetry with respect to the electric and magnetic fields, respectively. The properties of these modes are determined by their respective dispersion relations, i.e., by the relations between the frequency ω and the SPP propagation constant k, which are given by transcendental equations. In the nonretarded limit of the LRA, the surface modes of the MIM and IMI structures become identical,[18] which is an interesting property that stems from Babinet's principle of complementary structures.[19–21]

However, issues with the approach of the LRA arise when either considering large values of k, where an unphysical limit is found for the frequency, or considering narrow insulator or metal widths ($w < 10$ nm), where singularities occur.[4,22] In particular when investigating extremely narrow V-grooves, as recently realized experimentally,[23] with techniques such as EIM, the inadequacy of the LRA manifests itself. Nonlocal response (or spatial dispersion) has been shown to remove this flawed behavior of the SPP modes in waveguiding structures such as single metal-dielectric interfaces,[24] infinite cylinders,[25] and more recently, hyperbolic metamaterials,[26] conical tips,[27,28] hybrid plasmonic waveguides,[29] wedges, and V-grooves.[30]

Extensive theoretical work has been done on the fundamental MIM and IMI waveguides, yet only a few studies[24,31–33] have focused on nonlocal effects in these structures. In this paper, we fill this gap by determining the dispersion relations of SPP modes of the IMI and MIM waveguides taking into account nonlocal response, retardation effects as well as interband transitions in the metals. We also revisit the simple metal-insulator (MI) waveguide structure. The nonlocal response is described by a linearized semiclassical hydrodynamic model,[34,35] which includes the quantum kinetics of the free-electron gas described by Thomas-Fermi theory.

The derivations and corresponding results for the nonlocal retarded dispersion relations of the IMI, MIM, and MI waveguides are presented in Sec. II. With the dispersion relations for the three waveguides at hand, we examine in detail the interplay between losses and nonlocality in the metal by gradually increasing the absorption losses. The fundamental influence of losses versus nonlocality on the SPP dispersion has, to our knowledge, not yet been investigated. Furthermore, we compare modes of the IMI and MIM waveguides with and without retardation and nonlocality and show that only in the nonretarded LRA do the modes of these two complementary

waveguides become identical. Retardation and nonlocality are shown to break their complementarity. These topics are discussed in Sec. III. Finally, Sec. IV concludes the paper.

II. THEORY

A. Nonlocal theory for thin-film systems

To determine the modes of thin-film systems, we first outline the main equations for the electric and magnetic fields that must be solved. We then consider the class of guided solutions with transverse magnetic (TM) polarization. The boundary conditions for the metal-dielectric interfaces are also discussed.

The free-electron gas of the metals comprising the thin-film waveguides is described by a nonlocal hydrodynamic equation of motion.[35,36] An intuitive way of describing the effect of nonlocal response is that it serves to smear out the charges at the surface of the metal on the scale of the Thomas-Fermi screening length.[37–39] One of the key impacts of this charge smearing is the removal of field divergences that are known to occur in the LRA.[40–44] The hydrodynamic equation relating the current density $\mathbf{J}(\mathbf{r},\omega)$ to the electric field $\mathbf{E}(\mathbf{r},\omega)$ is given by[36,40]

$$\frac{\beta_{\mathrm{F}}^2}{\omega(\omega+i\gamma)}\boldsymbol{\nabla}\left[\boldsymbol{\nabla}\cdot\mathbf{J}(\mathbf{r},\omega)\right]+\mathbf{J}(\mathbf{r},\omega)=\sigma(\omega)\mathbf{E}(\mathbf{r},\omega), \quad (1)$$

where $\sigma(\omega)=i\varepsilon_0\omega_{\mathrm{p}}^2/(\omega+i\gamma)$ is the Drude conductivity and $\beta_{\mathrm{F}}^2=(3/5)v_{\mathrm{F}}^2$ is the nonlocal parameter obtained from Thomas-Fermi theory, where v_{F} is the Fermi velocity of the metal. By combining Eq. (1) with Maxwell's equations, the general equations describing the electric field $\mathbf{E}(\mathbf{r},\omega)$ in a metal with hydrodynamic nonlocal response can be compactly written as[24,36,45]

$$\left(\nabla^2+k_{\mathrm{m}}^2\right)\boldsymbol{\nabla}\times\mathbf{E}(\mathbf{r},\omega)=0, \quad (2a)$$

$$\left(\nabla^2+k_{\mathrm{nl}}^2\right)\boldsymbol{\nabla}\cdot\mathbf{E}(\mathbf{r},\omega)=0, \quad (2b)$$

where $k_{\mathrm{m}}\equiv k_0\sqrt{\varepsilon_{\mathrm{m}}}$ is the usual wave vector in the metal while $k_{\mathrm{nl}}\equiv\sqrt{\omega^2+i\gamma\omega-\omega_{\mathrm{p}}^2/\varepsilon_\infty}/\beta_{\mathrm{F}}$ is the additional longitudinal wave vector present in a nonlocal description of the metal. Here, $k_0\equiv\omega/c$ is the vacuum wave vector, $\varepsilon_{\mathrm{m}}\equiv\varepsilon_\infty(\omega)-\omega_{\mathrm{p}}^2/(\omega^2+i\gamma\omega)$ is the local-response Drude permittivity including additional frequency-dependent polarization effects through $\varepsilon_\infty(\omega)$ not due to the free-electron plasma response.

At this stage, we point out that for a homogeneous material, we may advantageously Fourier transform Eq. (1) and Maxwell's equations to $\mathbf{k}$ space. Using the Helmholtz decomposition, we can uniquely decompose the electric field and current density into transverse ($\mathbf{F}_{\mathrm{T}}\cdot\mathbf{k}=0$) and longitudinal ($\mathbf{F}_{\mathrm{L}}\times\mathbf{k}=0$) components. The transverse ε_{T} and longitudinal ε_{L} components of the permittivity tensor of the homogeneous material are then determined as[35]

$$\varepsilon_{\mathrm{T}}(\omega)=\varepsilon_{\mathrm{m}}(\omega)=\varepsilon_\infty(\omega)-\frac{\omega_{\mathrm{p}}^2}{\omega(\omega+i\gamma)}, \quad (3a)$$

$$\varepsilon_{\mathrm{L}}(k,\omega)=\varepsilon_\infty(\omega)-\frac{\omega_{\mathrm{p}}^2}{\omega(\omega+i\gamma)-\beta^2k^2}, \quad (3b)$$

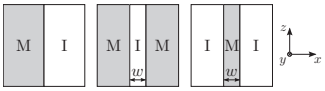

FIG. 1. The three waveguide systems: metal-insulator (MI), metal-insulator-metal (MIM), and insulator-metal-insulator (IMI) along with the chosen coordinate system.

where the k dependence (which in the real-space representation corresponds to nonlocal response) is only present in the longitudinal component of the permittivity tensor. Just as the influence of the electric field also at preceding times results in the frequency dispersion of the material response, so does the influence of the electric field also at neighboring locations result in momentum dispersion. For the inhomogeneous structures that we consider in this paper, i.e., MI, MIM, and IMI, the full $\mathbf{k}$-space approach is not particularly practical, due to the breaking of symmetry along the out-of-plane direction, and we instead opt to consider all equations in real space initially.

The electric field in the insulator regions with permittivity ε_{d} is described by the Helmholtz equation

$$\left(\nabla^2+k_{\mathrm{d}}^2\right)\mathbf{E}(\mathbf{r},\omega)=0, \quad (4)$$

where $k_{\mathrm{d}}\equiv k_0\sqrt{\varepsilon_{\mathrm{d}}}$ is the wave vector in the insulator.

Once the electric field has been determined, the magnetic field $\mathbf{H}(\mathbf{r},\omega)$ can be found from Faraday's law

$$\mathbf{H}(\mathbf{r},\omega)=\frac{1}{i\omega\mu_0}\boldsymbol{\nabla}\times\mathbf{E}(\mathbf{r},\omega), \quad (5)$$

and then the free-electron current density $\mathbf{J}(\mathbf{r},\omega)$ in the metal can be found as

$$\mathbf{J}(\mathbf{r},\omega)=\boldsymbol{\nabla}\times\mathbf{H}(\mathbf{r},\omega)+i\omega\varepsilon_0\varepsilon_\infty(\omega)\mathbf{E}(\mathbf{r},\omega). \quad (6)$$

Without loss of generality, we set the propagation direction along the z axis and define the x axis as perpendicular to the propagation plane, as in Fig. 1. Then the electric and magnetic fields for TM polarization can be simplified to

$$\mathbf{E}(\mathbf{r},\omega)=\left[E_x(x)\hat{\boldsymbol{e}}_{\boldsymbol{x}}+E_z(x)\hat{\boldsymbol{e}}_{\boldsymbol{z}}\right]e^{ikz}, \quad (7a)$$

$$\mathbf{H}(\mathbf{r},\omega)=H_y(x)e^{ikz}\hat{\boldsymbol{e}}_{\boldsymbol{y}}, \quad (7b)$$

where k is the SPP propagation constant. With the definitions in Eqs. (7), we can simplify the general expressions of Eqs. (2) and (4)–(6) to the following component form:

$$\left(\frac{\partial^2}{\partial x^2}-\kappa_{\mathrm{nl}}^2\right)\left[kE_z(x)-i\frac{\partial E_x(x)}{\partial x}\right]=0, \quad (8a)$$

$$\left(\frac{\partial^2}{\partial x^2}-\kappa_{\mathrm{m}}^2\right)\left[kE_x(x)+i\frac{\partial E_z(x)}{\partial x}\right]=0, \quad (8b)$$

$$H_y(x)=\frac{1}{\omega\mu_0}\left[kE_x(x)+i\frac{\partial E_z(x)}{\partial x}\right], \quad (8c)$$

$$J_x(x)=-ikH_y(x)+i\omega\varepsilon_0\varepsilon_\infty E_x(x), \quad (8d)$$

which are to be solved in the metal regions, while in the insulator regions the governing equations are

$$\left(\frac{\partial^2}{\partial x^2} - \kappa_{\rm d}^2\right) E_x(x) = 0, \tag{9a}$$

$$E_z(x) = \frac{i}{k}\frac{\partial E_x(x)}{\partial x}. \tag{9b}$$

The magnetic fields in the insulator regions are also determined using Eq. (8c). For convenience, we have defined a propagation constant normal to the interfaces in the respective regions given as

$$\kappa_j^2 \equiv k^2 - k_j^2 \quad \text{for} \quad j \in \{\text{m,d,nl}\}. \tag{10}$$

With Eqs. (8) and (9), solutions for the electric field, magnetic field, and current density can be determined in the metal and insulator regions. At the metal-dielectric interfaces, we must connect the solutions using boundary conditions (BCs). Maxwell's BCs provide two of the three needed, namely the continuity of the tangential components of the electric and magnetic fields (E_z and H_y, respectively). In our treatment, we neglect effects due to electron spill-out and quantum tunneling, which unambiguously determines the third and additional BC to be the vanishing of the normal component of the free-electron current density (J_x).[26,35,36,46] With this assumption, we reduce our range of consideration to widths larger than 1 nm for the MIM waveguide.[47,48]

B. Single metal-insulator (MI) interface

Before considering thin-film waveguides, it is instructive to revisit the fundamental problem of SPPs propagating at a single MI interface. The MI problem with hydrodynamic nonlocal response in the metal has been solved by Boardman *et al.*,[24] in the simplest of cases where interband contributions and intraband damping were neglected. These results were recently generalized to include such contributions,[33] however, without considering the delicate interplay between the absorption losses and nonlocality in the metal, which we examine in Sec. III.

The retarded nonlocal dispersion relation for a single MI interface is exactly given as

$$1 = -\frac{\varepsilon_{\rm m}\kappa_{\rm d}}{\varepsilon_{\rm d}\kappa_{\rm m}} - \delta_{\rm nl}, \tag{11}$$

where $\delta_{\rm nl}$ is an important nonlocal correction that will also appear below for the more complex thin-film waveguides and is given as

$$\delta_{\rm nl} = \frac{k^2}{\kappa_{\rm nl}\kappa_{\rm m}}\frac{\varepsilon_{\rm m} - \varepsilon_\infty}{\varepsilon_\infty}. \tag{12}$$

We emphasize that when $\beta_{\rm F} \to 0$, the local-response dispersion relation in Ref. 17 is retrieved since $\delta_{\rm nl} \to 0$. We also note that the k solutions of the radical equation in Eq. (11) can be obtained analytically by the standard method for solving radical equations through squaring, and can be represented in terms of the solutions of a third-order polynomial.

For completeness, we also note that in the nonretarded limit $c \to \infty$, the nonlocal correction $\delta_{\rm nl}$ simplifies to

$$\delta_{\rm nl}^{\rm nr} \equiv \lim_{c\to\infty} \delta_{\rm nl} = \frac{k}{\kappa_{\rm nl}}\frac{\varepsilon_{\rm m} - \varepsilon_\infty}{\varepsilon_\infty}, \tag{13}$$

and the dispersion relation for a single MI interface Eq. (11) simplifies to

$$1 = -\frac{\varepsilon_{\rm m}}{\varepsilon_{\rm d}} - \delta_{\rm nl}^{\rm nr}. \tag{14}$$

The nonretarded local-response dispersion relation is retrieved by letting $\delta_{\rm nl}^{\rm nr} \to 0$ in Eq. (14).

C. Metal-insulator-metal (MIM)

The problem of determining the SPP modes of the MIM waveguide can, as in the LRA, be simplified by considering the even and odd modes separately. The symmetry considerations apply to the electric field. The exact retarded nonlocal dispersion relation for the fundamental, even mode is

$$\tanh\left(\frac{\kappa_{\rm d} w}{2}\right) = -\frac{\varepsilon_{\rm d}\kappa_{\rm m}}{\varepsilon_{\rm m}\kappa_{\rm d}}(1 + \delta_{\rm nl}), \tag{15a}$$

while for the odd mode, we find

$$\coth\left(\frac{\kappa_{\rm d} w}{2}\right) = -\frac{\varepsilon_{\rm d}\kappa_{\rm m}}{\varepsilon_{\rm m}\kappa_{\rm d}}(1 + \delta_{\rm nl}), \tag{15b}$$

where w is the width of insulator slab. These equations are in agreement with recent results.[33] In the nonretarded limit, Eqs. (15) simplifies to

$$\tanh\left(\frac{kw}{2}\right) = -\frac{\varepsilon_{\rm d}}{\varepsilon_{\rm m}}\left(1 + \delta_{\rm nl}^{\rm nr}\right), \tag{16a}$$

$$\coth\left(\frac{kw}{2}\right) = -\frac{\varepsilon_{\rm d}}{\varepsilon_{\rm m}}\left(1 + \delta_{\rm nl}^{\rm nr}\right). \tag{16b}$$

As previously mentioned, inclusion of nonlocal response regularizes the unphysical divergences encountered in the LRA. This property is also preserved for the MIM waveguide, and we may see how it comes about by examining the limit $w \to 0$ for the fundamental mode (which in the LRA produces a singularity). In this regard, we may neglect retardation effects and additionally simplify Eq. (16a) by using the small-x expansion $\tanh(x) \simeq x$. This yields

$$k = -\frac{2\varepsilon_{\rm d}}{\varepsilon_{\rm m}}[w - \Delta_{\rm MIM}]^{-1}, \quad \Delta_{\rm MIM} = \frac{i\varepsilon_{\rm d}(\varepsilon_{\rm m} - \varepsilon_\infty)}{2k_{\rm nl}\varepsilon_{\rm m}\varepsilon_\infty}, \tag{17}$$

where $\Delta_{\rm MIM}$ is the nonlocal correction, which vanishes in the local-response limit $\beta_{\rm F} \to 0$. We emphasize that k stays finite even in the case of $w = 0$ in contrast to the diverging local-response relation[22] given by Eq. (17) with $\Delta_{\rm MIM} = 0$.

D. Insulator-metal-insulator (IMI)

The two SPP modes of the IMI waveguide can be classified into even and odd modes, as in the case of the MIM waveguide. However, while the symmetry characterization applied to the electric field for the MIM waveguide, here it is with respect to the magnetic field.[26] The nonlocal modes for the IMI waveguide have previously been studied in the case of a lossless metal without interband contributions.[31] Here, we generalize these results to include such contributions, which are important in realistic waveguides. The retarded nonlocal

dispersion relation for the odd and even modes are

$$\coth\left(\frac{\kappa_m w}{2}\right) = -\frac{\varepsilon_m \kappa_d}{\varepsilon_d \kappa_m} - \delta_{nl} \coth\left(\frac{\kappa_{nl} w}{2}\right), \quad (18a)$$

$$\tanh\left(\frac{\kappa_m w}{2}\right) = -\frac{\varepsilon_m \kappa_d}{\varepsilon_d \kappa_m} - \delta_{nl} \tanh\left(\frac{\kappa_{nl} w}{2}\right). \quad (18b)$$

We note that, in contrary to the MIM waveguide, the odd mode Eq. (18a) is in fact the fundamental mode.

In the nonretarded limit, Eqs. (18a) and (18b) simplify to

$$\coth\left(\frac{kw}{2}\right) = -\frac{\varepsilon_m}{\varepsilon_d} - \delta_{nl}^{nr} \coth\left(\frac{\kappa_{nl} w}{2}\right), \quad (19a)$$

$$\tanh\left(\frac{kw}{2}\right) = -\frac{\varepsilon_m}{\varepsilon_d} - \delta_{nl}^{nr} \tanh\left(\frac{\kappa_{nl} w}{2}\right). \quad (19b)$$

As in the case for the MIM waveguide, we can again examine the limit of $w \to 0$ for the fundamental mode. Neglecting retardation effects and using the small-x expansion $\coth(x) \simeq 1/x$, we find

$$k = -\frac{2\varepsilon_d}{w\varepsilon_m}\left[1 - \left(\frac{\Delta_{IMI}}{w}\right)^2\right], \quad (20a)$$

$$\Delta_{IMI} = \frac{2\varepsilon_d}{k_{nl}\varepsilon_m}\sqrt{\frac{\varepsilon_m - \varepsilon_\infty}{\varepsilon_m \varepsilon_\infty}}. \quad (20b)$$

Here, Δ_{IMI} is the nonlocal correction for the IMI waveguide that vanishes for vanishing β_F. Unlike the MIM waveguide, the nonlocal correction does not regularize the diverging k when $w = 0$. Due to the confinement of the electron plasma in the IMI waveguide, as opposed to the MIM waveguide, the regularization of the dispersion likely requires inclusion of electron spill-out, which is not treated here, see Sec. II A. Further elaboration on the comparison of Eqs. (20) with Eq. (17), in the context of complementarity, is done in Sec. III B.

III. RESULTS

The dispersion relations introduced in Sec. II are complex-valued transcendental equations of the implicit form $F(\omega,k) = 0$, with the propagation constant in general being a complex number $k = k' + ik''$. Thus to determine the waveguide modes, solutions to the dispersion relations must be found in the complex k plane for each frequency, which in general is a nontrivial task. Fortunately, a robust and reliable numerical scheme suitable for determining the zeros in the complex plane, based on the Cauchy integral formula, has been previously developed[49,50] and is employed in this work.

In the following, we focus on the free-electron properties (i.e., $\varepsilon_\infty = 1$) of the modes of the three different waveguides. This allows us to rescale the dispersion relations with normalized quantities, here introduced as $\Omega = \omega/\omega_p$, $K = kc/\omega_p$, $\Gamma = \gamma/\omega_p$, $\eta = \beta_F/c$, and for the IMI and MIM waveguides, $W = w\omega_p/c$. The normalized parameters Γ and η characterize the losses and the strength of nonlocality in the metals, respectively.

This section is divided into two parts: Sec. III A concerns the interplay between metal losses and nonlocality. Here, we first study this interplay in the simple MI waveguide that does not contain any geometric length scales, whereafter we examine how nonlocal effects are enhanced in confined waveguides such as the MIM and IMI waveguides. Section III B deals with the breaking of complementarity in the MIM and IMI waveguides due to nonlocal response.

A. Losses and nonlocality

1. MI waveguide

Due to the absence of length scales associated with the geometry, the MI waveguide is an ideal system to study, when considering the interplay between losses and nonlocality of the SPP mode. An additional benefit of studying the MI structure is that it is not obscured by the effects of multiple interface reflections that is present in the MIM and IMI structures, such that only the intrinsic properties of free electrons affect the waveguiding properties. In this section, we therefore focus on how the presence of absorption losses in the metal, i.e., a finite-valued Γ, affects the nonlocal and local retarded modes of the MI waveguide, as described by Eq. (11) with and without δ_{nl}, respectively.

The interplay between losses and nonlocality in the MI waveguide is seen in Fig. 2, where we display the effect of increasing the metal losses on the local and nonlocal dispersion relations of the SPP mode, given by Eq. (11) with $\eta = 5 \times 10^{-3}$. In the lossless case ($\Gamma = 0$), the local dispersion relation converges towards the well-known $\Omega_{SP} = 1/\sqrt{2\varepsilon_d}$ limit for large K values, while the nonlocal dispersion relation increases in frequency without bound, in agreement with earlier results.[24] However, in the presence of very weak losses ($\Gamma = 10^{-3}$) the infinite K values at the frequency Ω_{SP} in the LRA are removed and the SPP mode bends back. This back-bending effect is a well-known textbook result,[4] which occurs for any positive value for Γ in the LRA. The extreme sensitivity to even minute losses in the LRA is due to the vanishing group velocity $v_g = \partial\omega/\partial k$ at Ω_{SP}.[51] In striking contrast, the nonlocal SPP mode [i.e., Re(K)] is robust due to the finite group velocity $v_g \geqslant \beta_F$. Consequently, no pronounced slow-light enhancement of weak losses takes place and the nonlocal SPP mode does not bend back until the losses of the system start to dominate. Although nonzero Im(K) is generated for the nonlocal SPP mode for $\Gamma \neq 0$, the real part of the propagation constant Re(K) remains largely unaffected. It is also interesting to note that the behavior of Im(K), which is related to the SPP propagation length l_{SPP} through $l_{SPP} = 1/[2\mathrm{Im}(K)]$, changes drastically from $\Gamma = 10^{-3}$ to 10^{-2}. For $\Gamma = 10^{-3}$, the nonlocal SPP mode propagates longer than the local one in the frequency region $\Omega > \Omega_{SP}$, while the opposite result is seen for $\Gamma = 10^{-2}$. At the same time, Re(K) for the nonlocal mode is unchanged and substantially larger than in the LRA, resulting in shorter wavelengths and thereby stronger confinement of the SPP mode at the MI surface. Not until $\Gamma = 10^{-1}$, which is significantly larger than the nonlocal parameter η, do the losses in the metal dominate over nonlocality and force the nonlocal SPP mode to bend back. At such losses, the local and nonlocal models result in almost identical solutions. Intuitively, we may understand this result by recalling that the influence of nonlocal effects is related to the free movement of the electron gas, which can be significantly impaired in the case of large losses, i.e., high collision frequencies.

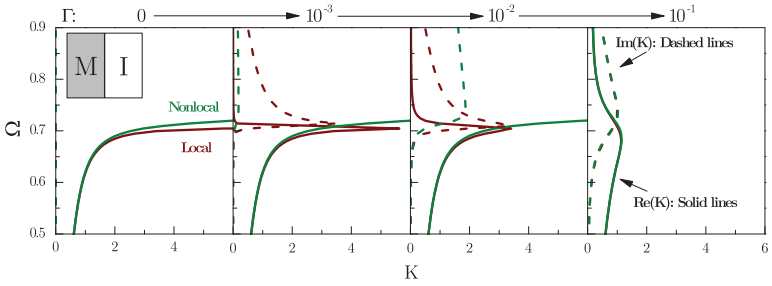

FIG. 2. (Color online) Local and nonlocal complex dispersion relations of the SPP mode of the MI waveguide, given by Eq. (11), with $\varepsilon_d = 1$ and metal losses increasing from $\Gamma = 0$ to 10^{-1}. Local results are shown in red, while nonlocal are shown in green. Solid lines display the real part of the propagation constant, Re(K), while the dashed lines display the imaginary part of the propagation constant, Im(K). The value $\eta = 5 \times 10^{-3}$ suitable for noble metals has been used.

The transition of the nonlocal mode from being dominated primarily by nonlocality to being dominated by losses (i.e., $\Gamma = 10^{-2} \rightarrow 10^{-1}$ in Fig. 2) is investigated in more detail in Fig. 3. To explain the transition, we must also consider the presence of the high-energy branch known as the Brewster mode[52] (for clarity not shown in Fig. 2) and not only the SPP mode. The Brewster mode, which is also a solution emerging from Eq. (11), does not correspond to a true surface wave, since, in the lossless case, the wave is unbound and radiative. In fact, the Brewster mode corresponds to a zero-valued reflection coefficient, which for a lossless Drude metal can be satisfied in the transparency window $\Omega > 1$. In Fig. 3, we see the merging of two separated modes, plotted as red and blue lines. For the lowest loss of $\log(\Gamma) = -1.7$, the red line corresponds to the continuation of the Brewster mode to frequencies lower than $\Omega = 1$ (see inset of Fig. 3), which in the lossless case would be a forbidden region (i.e., only purely lossy solutions exist).[52] The blue line represents the standard, low-loss, nonlocal SPP mode. As the losses increase [$\log(\Gamma) = -1.6 \rightarrow -1.575$], the real parts of the dispersion of the Brewster mode and SPP mode begin to merge.[53] At approximately $\log(\Gamma) = -1.55$, the mode-appearance has qualitatively changed, with the appearance of the usual well-known loss-dominated SPP mode (in blue), which is also present in LRA, as well as the emergence of a relatively flat-band, nonlocal surface plasmon mode (in red) near the surface plasmon resonance Ω_{SP}.[35] We notice that the nonlocal flat-band mode is significantly damped in comparison with the usual SPP mode, and that the damping increases drastically with increased material loss. In contrast, the usual SPP mode is not nearly so sensitive to the small change in material loss from $\log(\Gamma) = -1.55$ to -1.5. A similarly abrupt qualitative merging of two modes was previously studied in Ref. 53 in the context of mode-interaction in spatially separated waveguiding structures in a local description, by consideration of complex-frequency poles of the dispersion

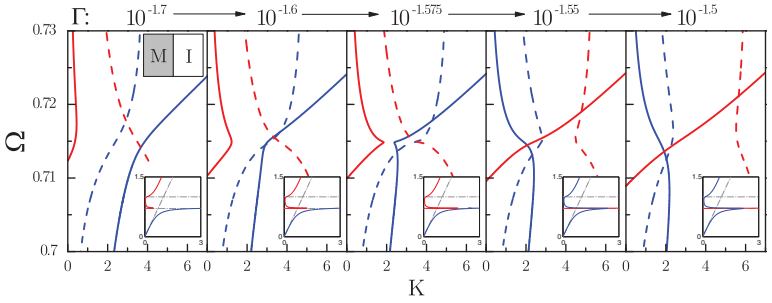

FIG. 3. (Color online) Nonlocal complex dispersion relations of the SPP and Brewster modes of the MI waveguide, both attained from solution of Eq. (11), with $\varepsilon_d = 1$ and metal losses increasing from $\Gamma = 10^{-1.7}$ to $10^{-1.5}$. Solid lines display the real part of the propagation constant, Re(K), while the dashed lines display the imaginary part of the propagation constant, Im(K). The insets show zoom-outs of the real dispersion relation and illustrate more clearly the Brewster mode. The transition and mode evolution from nonlocality to loss-dominated behavior is explored. The value $\eta = 5 \times 10^{-3}$ suitable for noble metals has been used.

equation, migrating across the real-frequency axis for increasing loss.

We now present a simple analysis to understand when the metal losses dominate nonlocal effects in the MI waveguide. The back-bending occurs at the frequency Ω_{SP}, where the propagation constant is significantly larger than the free-space propagation constant. We can therefore justify to examine the simpler nonretarded dispersion relation given by Eq. (14) instead of the retarded dispersion relation [see Eq. (11)]. From Eq. (14), we see that nonlocality becomes negligible when $|\delta_{nl}^{nr}| \ll |1 + \varepsilon_m/\varepsilon_d|$. Evaluating this condition at the SPP frequency with $\varepsilon_d = 1$ (as in Fig. 2) for small Γ leads to the simple condition for loss-dominated behavior

$$\Gamma \gg \eta, \tag{21}$$

which is consistent with our numerical analysis. We point out that the loss parameter Γ is just one of several options for introducing an imaginary part to the metal permittivity. An alternative approach to introducing losses is by simply adding a constant imaginary part to the lossless free-electron Drude model. In either case, the metal permittivity becomes complex-valued. To bridge these different approaches, we can relate the condition in Eq. (21) to the imaginary part of the metal permittivity by noting that $\mathrm{Im}[\varepsilon_m(\Omega = \Omega_{SP})] = 2\sqrt{2}\Gamma/(1 + 2\Gamma^2)$ in which case Eq. (21) can be rewritten as

$$\mathrm{Im}(\varepsilon_m) \gg \frac{v_F}{c}. \tag{22}$$

In noble metals, the nonlocal parameter is of the order $v_F/c \approx 10^{-3}$ and the losses are of the order $\mathrm{Im}(\varepsilon_m) \approx 10^0$, which in general means that metal losses largely dominate nonlocal effects in the SPP mode of the MI waveguide.[54] In other words, in the MI waveguide, the spatial dispersion of the metal becomes invisible to the SPP mode in the limit of infinitely high absorption losses.

2. *MIM and IMI waveguides*

Figure 4 displays the effect of increasing losses on nonlocality for the fundamental modes of the MIM (first row) and IMI waveguides (second row) given by Eqs. (15a) and (18a), respectively. The normalized width of the waveguides is set to $W = 0.25$, which corresponds to a width of $w \approx 5$nm for Ag and Au ($\omega_p \approx 9$ eV). Considering the MIM waveguide first, we see that in the lossless case nonlocal response within the hydrodynamic model predicts a blueshift compared to the LRA (for a fixed K). As the losses in the metal increase ($\Gamma = 10^{-2}$), the local dispersion relation [$\mathrm{Re}(K)$] immediately bends back and the propagation length is significantly shorter than for the nonlocal case. Both of these effects are similar to those observed for the MI waveguide. When $\Gamma = 10^{-1}$ the nonlocal dispersion relation also bends back and the nonlocal propagation length becomes comparable to LRA, albeit for $\Omega < \Omega_{SP}$ nonlocal response gives rise to longer propagation lengths than in the LRA. Although the nonlocal dispersion relation bends back at these large losses, nonlocal response still reveals a blueshift and larger values of $\mathrm{Re}(K)$ than in the LRA.

The trend is very similar for the IMI waveguide (see second row of Fig. 4). In fact, in the LRA, the difference between the fundamental modes of the IMI and MIM waveguides is practically negligible. As for the nonlocal case, the biggest difference between the IMI and MIM waveguides is seen for $\Gamma = 10^{-1}$, where nonlocal response shows a slight increase in the maximum values of both the $\mathrm{Re}(K)$ and $\mathrm{Im}(K)$ for the IMI waveguide.

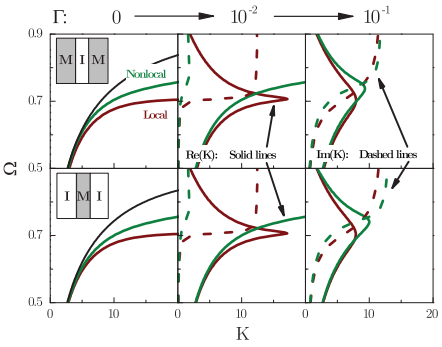

FIG. 4. (Color online) Local and nonlocal complex dispersion relations of the fundamental mode of the MIM (first row) and IMI (second row) waveguides, given by Eqs. (15a) and (18a), respectively, with $W = 0.25$, $\varepsilon_d = 1$, $\eta = 5 \times 10^{-3}$, and metal losses increasing from $\Gamma = 0$ to 10^{-1}. Local results are shown in red, while nonlocal are shown in green. Solid lines display the real part of the propagation constant $\mathrm{Re}(K)$, while the dashed lines display the imaginary part of the propagation constant $\mathrm{Im}(K)$. The black lines represent the approximate nonlocal dispersion relations given by Eqs. (17) and (20) for the MIM and IMI waveguides, respectively.

In Fig. 4, we have also examined the validity of the approximate relations for the nonlocal fundamental modes of the MIM and IMI waveguides given by Eqs. (17) and (20), respectively. They are plotted as black lines for the lossless case. We see that the approximate relations are in excellent agreement with the exact calculations when $KW \lesssim 1$.

The important feature for both waveguides is that even for large losses (of order $\Gamma = 10^{-1}$) the nonlocal and local dispersion relations are different, in stark contrast to the MI waveguide. The nonlocal dispersion relations show larger values of $\mathrm{Re}(K)$ than in the LRA for both waveguides. Thus the limitations and undesired properties of metal losses are counteracted by nonlocality, which gives rise to a shorter wavelength of the SPP mode and thereby an increase of the mode confinement. These interesting features arise due to the multiple reflections present in the IMI/MIM waveguides, introducing a new length scale given by the scaled width of the slab W. The importance of nonlocal effects increases with decreasing width (or, in general, size),[36] and it is clear from the nonlocal dispersion relations for the IMI and MIM waveguides that the strength of nonlocality is different in these two waveguide structures, as also observed in Fig. 4. This difference arises due to the presence of confined nonlocal pressure waves, which are naturally only present in the IMI waveguide.

B. Breaking of complementarity due to nonlocal response

It is well known that the LRA dispersion relations for the SPP modes of the MIM and IMI waveguides are identical in the nonretarded limit,[4,18] which is also clear from comparing Eqs. (16) to Eqs. (19) with $\delta_{\rm nl}^{\rm nr} = 0$. This property of identical surface modes in complementary waveguide structures, such as the MIM and IMI waveguides, is broken when retardation effects are included in the LRA, which become important for SPP propagation values K close to the light line $K_0 = \Omega$.[18] Here, we show explicitly that nonlocal response also breaks the symmetry by considering the SPP modes of the MIM and IMI waveguides in the nonretarded limit, i.e., in the limit where $K \gg K_0$. In the following, we divide the discussion of breaking of complementarity into two parts: one due to retardation effects alone in the LRA, and one solely due to nonlocal response in the nonretarded limit. For the latter, we consider the nonretarded limit to ensure that the breaking of complementarity is due to nonlocal response rather than being attributed to retardation.

Breaking of complementarity is illustrated in Fig. 5. In Fig. 5(a), we plot the SPP modes of the MIM and IMI waveguides only in the LRA, displaying the effect of retardation. First, we note, as already mentioned, that the SPP modes of the MIM and IMI modes in the nonretarded limit are completely identical and overlap in Fig. 5(a) (black lines). When retardation effects are included the MIM (green lines) and IMI (red lines) surface modes are no longer identical for K values close to the light line. The main consequence of properly taking retardation into account is that no guided modes exist above the light line (grey line). In Fig. 5(a), we clearly see that the retarded modes terminate at the light line, unlike the nonretarded modes.

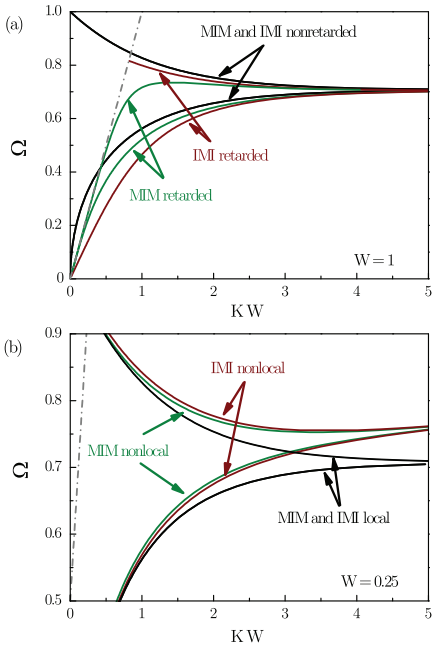

FIG. 5. (Color online) Plots of both surface modes of the lossless IMI and MIM waveguides (a) with and without retardation in the LRA and (b) with and without nonlocal response ($\eta = 5 \times 10^{-3}$) in the nonretarded limit. The light line is shown in grey. The widths of the waveguides are (a) $W = 1$ and (b) 0.25.

Figure 5(b) shows the nonlocal and local SPP modes of the MIM and IMI waveguides calculated in the nonretarded limit. We see clearly that nonlocal response distinguishes between the MIM and IMI waveguide modes, for both of the two surface modes. This effect was observed upon earlier,[55] but not elaborated on. As the propagation constant increases, both of the nonlocal modes of both waveguides converge towards the hydrodynamic nonlocal large-K limit $K = \Omega/\eta$, as for the MI waveguide,[24,26] and become indistinguishable. Finally, we also note the characteristic shift to higher frequencies of both nonlocal SPP modes compared to the LRA.

The breaking of the complementarity property of the MIM and IMI waveguides due to nonlocal response can of course be understood from the fact that the dispersion relations for the two waveguides are different even in the nonretarded limit, as seen by comparison of Eqs. (16) with Eqs. (19). We can quantify this difference for the fundamental mode of the two structures by considering the difference $\Delta k = k_{\rm MIM} - k_{\rm IMI}$, where $k_{\rm MIM}$ and $k_{\rm IMI}$ are given by the approximate relations in Eqs. (17) and (20), respectively. Using a Padé approximation, we find to the lowest order in w that

$$\Delta k \simeq -\frac{2\varepsilon_{\rm d}}{\varepsilon_{\rm m}} \frac{\Delta_{\rm IMI}^2}{w^3}. \tag{23}$$

From Eq. (23), we clearly see that in the absence of nonlocal response ($\Delta_{\rm IMI} = 0$), the difference between the fundamental modes of the MIM and IMI waveguides vanishes. Additionally, we observe that the dispersion-difference depends strongly on the width. At very narrow widths, we therefore expect a strong breaking of complementarity. Thus, in the presence of nonlocality, a thin film of electron gas embedded in an insulator behaves qualitatively different from a thin insulator gap embedded in an electron gas.

In an intuitive, but simplified picture of nonlocality, one could be inclined to attribute the complementarity breaking to the nonlocal smearing of the induced surface charge. In the nonlocal hydrodynamic model the induced surface charge is smeared over a length scale comparable to the Thomas-Fermi screening length, leading to an effective width increase (decrease) for the MIM (IMI) waveguide. In this picture, the dispersion relations of the nonlocal IMI and MIM SPP modes should then be below and above the local dispersion relations, respectively, which is not the case, see Fig. 5(b). In fact, the nonlocal IMI and MIM SPP modes are always above the local results, discrediting the simple interpretation of nonlocal response as local response with effective size parameters.

The complementarity breaking originates from the inclusion of pressure waves in the description of a metal with nonlocal response. More precisely, the breaking is due to the

confinement of these pressure waves in the IMI waveguide, which becomes more important for narrower widths. This confinement results in a significantly different description of the IMI waveguide compared to the MIM waveguide, where the pressure waves are not confined. For this reason, nonlocal effects are also stronger in the IMI waveguide, as can be seen from the presence of only the nonlocal IMI correction in Eq. (23). In contrast, in the nonretarded LRA, the absence of both retardation and the pressure waves leads to a faulty identical treatment of the MIM and IMI waveguides.

IV. CONCLUSIONS

The effects of nonlocal response, described by a linearized hydrodynamic model, on the waveguiding properties of the MI, MIM, and IMI waveguides have been investigated. The corresponding dispersion relations for the three waveguides have been derived, taking into account nonlocality, interband transitions, and retardation. The intriguing transition from nonlocal- to loss-dominated waveguiding behavior, which has not previously been studied extensively, was examined for the MI system, demonstrating that nonlocal response can counteract the effects of low metal losses. In the LRA, the presence of even minute losses drastically alters the dispersion relation of the SPP mode due the slow-light regime at the surface plasmon frequency Ω_{SP}. For larger losses, the effects of nonlocality in the MI structure is less important, and the difference between local and nonlocal response becomes negligible. In general, for the MI structure, the impact of metal losses is much more pronounced than that of nonlocal effects, partially due to the high losses in metals and partially due to the absence of any geometric length scale in the MI structure.

Conversely, for the MIM and IMI structures, the presence of an additional length scale, given by the geometric width of the waveguide, yields a comparative boost to the effect of nonlocality vis-à-vis the effect of metal losses. In turn, the increased strength of nonlocality gives rise to larger propagation constants and thereby an increased plasmonic confinement of the SPP modes. Nonlocal effects are shown to be slightly stronger in the IMI waveguide due to the presence of confined longitudinal pressure waves, which are absent in the MIM structure.

Lastly, we also examined the complementarity property of the MIM and IMI waveguides in the context of Babinet's principle. In the nonretarded limit of the LRA, the waveguide modes of the MIM and IMI modes are known to be identical. When retardation is taken into account, this symmetry is broken. In addition, we have shown that in the nonretarded limit the symmetry is also broken by the inclusion of nonlocal effects due to the presence of nonlocal pressure waves.

ACKNOWLEDGMENTS

The Center for Nanostructured Graphene is sponsored by the Danish National Research Foundation, Project DNRF58. The A. P. Møller and Chastine Mc-Kinney Møller Foundation is gratefully acknowledged for the contribution toward the establishment of the Center for Electron Nanoscopy.

*asger@mailaps.org

[1] R. Zia, J. A. Schuller, A. Chandran, and M. L. Brongersma, Mater. Today **9**, 20 (2006).
[2] P. Berini, Adv. Opt. Phot. **1**, 484 (2009).
[3] D. K. Gramotnev and S. I. Bozhevolnyi, Nat. Photon. **4**, 83 (2010).
[4] S. A. Maier, *Plasmonics: Fundamentals and Applications* (Springer, New York, 2007).
[5] S. Bozhevolnyi, Opt. Express **14**, 9467 (2006).
[6] D. Sarid, Phys. Rev. Lett. **47**, 1927 (1981).
[7] G. B. Hocker and W. K. Burns, Appl. Opt. **16**, 113 (1977).
[8] K. R. Welford and J. R. Sambles, J. Mod. Opt. **35**, 1467 (1988).
[9] S. I. Bozhevolnyi, V. S. Volkov, E. Devaux, and T. W. Ebbesen, Phys. Rev. Lett. **95**, 046802 (2005).
[10] J. A. Dionne, H. J. Lezec, and H. A. Atwater, Nano Lett. **6**, 1928 (2006).
[11] H. T. Miyazaki and Y. Kurokawa, Phys. Rev. Lett. **96**, 097401 (2006).
[12] S. I. Bozhevolnyi, V. S. Volkov, E. Devaux, J.-Y. Laluet, and T. W. Ebbesen, Nature (London) **440**, 508 (2006).
[13] J. J. Burke, G. I. Stegeman, and T. Tamir, Phys. Rev. B **33**, 5186 (1986).
[14] R. Zia, M. D. Selker, P. B. Catrysse, and M. L. Brongersma, J. Opt. Soc. Am. A **21**, 2442 (2004).
[15] P. Ginzburg, D. Arbel, and M. Orenstein, Opt. Lett. **31**, 3288 (2006).
[16] J. A. Dionne, L. A. Sweatlock, H. A. Atwater, and A. Polman, Phys. Rev. B **73**, 035407 (2006).
[17] E. N. Economou, Phys. Rev. **182**, 539 (1969).
[18] B. E. Sernelius, *Surface Modes in Physics* (Wiley-VCH, Berlin, 2001).
[19] M. Born and E. Wolf, *Principles of Optics*, 7th ed. (Cambridge University Press, Cambridge, 1999).
[20] B. Ögüt, R. Vogelgesang, W. Sigle, N. Talebi, C. T. Koch, and P. A. van Aken, ACS Nano **5**, 6701 (2011).
[21] D. Rossouw and G. A. Botton, Opt. Express **20**, 6968 (2012).
[22] S. I. Bozhevolnyi and J. Jung, Opt. Express **16**, 2676 (2008).
[23] T. Søndergaard, S. M. Novikov, T. Holmgaard, R. L. Eriksen, J. Beermann, Z. Han, K. Pedersen, and S. I. Bozhevolnyi, Nat. Commun. **3**, 969 (2012).
[24] A. D. Boardman, B. V. Paranjape, and Y. O. Nakamura, Phys. Status Solidi B **75**, 347 (1976).
[25] G. C. Aers, A. D. Boardman, and B. V. Paranjape, J. Phys. F: Met. Phys. **10**, 53 (1980).
[26] W. Yan, M. Wubs, and N. A. Mortensen, Phys. Rev. B **86**, 205429 (2012).
[27] R. Ruppin, Phys. Lett. A **340**, 299 (2005).
[28] A. Wiener, A. I. Fernández-Domínguez, A. P. Horsfield, J. B. Pendry, and S. A. Maier, Nano Lett. **12**, 3308 (2012).
[29] Q. Huang, F. Bao, and S. He, Opt. Express **21**, 1430 (2013).
[30] G. Toscano, S. Raza, W. Yan, C. Jeppesen, S. Xiao, M. Wubs, A.-P. Jauho, S. I. Bozhevolnyi, and N. A. Mortensen, Nanophotonics **2**, 161 (2013).
[31] R. Ruppin, J. Phys.: Condens. Matter **17**, 1803 (2005).
[32] K. Andersen, K. W. Jacobsen, and K. S. Thygesen, Phys. Rev. B **86**, 245129 (2012).

[33] A. Moreau, C. Ciracì, and D. R. Smith, Phys. Rev. B **87**, 045401 (2013).
[34] F. Bloch, Z. Phys. A **81**, 363 (1933).
[35] A. Boardman, *Electromagnetic Surface Modes* (Wiley, Chichester, 1982), Chap. 1, pp. 1–76.
[36] S. Raza, G. Toscano, A.-P. Jauho, M. Wubs, and N. A. Mortensen, Phys. Rev. B **84**, 121412(R) (2011).
[37] C. David and F. J. García de Abajo, J. Phys. Chem. C **115**, 19470 (2012).
[38] J. B. Pendry, A. Aubry, D. R. Smith, and S. A. Maier, Science **337**, 549 (2012).
[39] P. Ginzburg and A. V. Zayats, ACS Nano **7**, 4334 (2013).
[40] G. Toscano, S. Raza, A.-P. Jauho, N. A. Mortensen, and M. Wubs, Opt. Express **20**, 4176 (2012).
[41] A. I. Fernández-Domínguez, P. Zhang, Y. Luo, S. A. Maier, F. J. García-Vidal, and J. B. Pendry, Phys. Rev. B **86**, 241110 (2012).
[42] C. Ciracì, R. T. Hill, J. J. Mock, Y. Urzhumov, A. I. Fernández-Domínguez, S. A. Maier, J. B. Pendry, A. Chilkoti, and D. R. Smith, Science **337**, 1072 (2012).
[43] G. Toscano, S. Raza, S. Xiao, M. Wubs, A.-P. Jauho, S. I. Bozhevolnyi, and N. A. Mortensen, Opt. Lett. **37**, 2538 (2012).
[44] A. I. Fernández-Domínguez, A. Wiener, F. J. García-Vidal, S. A. Maier, and J. B. Pendry, Phys. Rev. Lett. **108**, 106802 (2012).
[45] A. D. Boardman and B. V. Paranjape, J. Phys. F: Met. Phys. **7**, 1935 (1977).
[46] P. Jewsbury, J. Phys. F: Met. Phys. **11**, 195 (1981).
[47] J. Zuloaga, E. Prodan, and P. Nordlander, Nano Lett. **9**, 887 (2009).
[48] R. Esteban, A. G. Borisov, P. Nordlander, and J. Aizpurua, Nat. Commun. **3**, 825 (2012).
[49] L. M. Delves and J. N. Lyness, Math. Comput. **21**, 543 (1967).
[50] C. Chen, P. Berini, D. Feng, S. Tanev, and V. P. Tzolov, Opt. Express **7**, 260 (2000).
[51] J. G. Pedersen, S. Xiao, and N. A. Mortensen, Phys. Rev. B **78**, 153101 (2008).
[52] L. Novotny and B. Hecht, *Principles of Nano-Optics*, 2nd ed. (Cambridge University Press, Cambridge, 2012).
[53] A. B. Yakovlev and G. W. Hanson, IEEE Trans. Microwave Theory Tech. **48**, 67 (2000).
[54] A. D. Rakić, A. B. Djurišić, J. M. Elazar, and M. L. Majewski, Appl. Opt. **37**, 5271 (1998).
[55] F. J. Garciá de Abajo, J. Phys. Chem. C **112**, 17983 (2008).

Paper H

S. Raza, G. Toscano, A.-P. Jauho, N. A. Mortensen, and M. Wubs

Refractive-index sensing with ultrathin plasmonic nanotubes

Plasmonics **8**, 193 (2013)

Author contributions
S. R. derived the equations, was the main author of the manuscript and created the figures. All authors were involved in discussing the obtained results and in correcting the manuscript.

Plasmonics (2013) 8:193–199
DOI 10.1007/s11468-012-9375-z

Refractive-Index Sensing with Ultrathin Plasmonic Nanotubes

Søren Raza · Giuseppe Toscano · Antti-Pekka Jauho · N. Asger Mortensen · Martijn Wubs

Received: 2 March 2012 / Accepted: 23 May 2012 / Published online: 7 June 2012

Abstract We study the refractive-index sensing properties of plasmonic nanotubes with a dielectric core and ultrathin metal shell. The few nanometer thin metal shell is described by both the usual Drude model and the nonlocal hydrodynamic model to investigate the effects of nonlocality. We derive an analytical expression for the extinction cross section and show how sensing of the refractive index of the surrounding medium and the figure of merit are affected by the shape and size of the nanotubes. Comparison with other localized surface plasmon resonance sensors reveals that the nanotube exhibits superior sensitivity and comparable figure of merit.

Keywords Refractive-index sensing · Nanoplasmonics · Hydrodynamic Drude model

Introduction

It is well known that metallic nanoparticles can sustain localized surface plasmon (LSP) oscillations, whose resonance frequencies in the quasistatic limit depend solely on the geometry of the nanoparticle, the permittivity of the metal, and the surrounding permittivity. The dependency of the LSP resonance (LSPR) on the surrounding medium makes metallic particles extremely good sensors, progressing towards the detection of single molecules [1]. However, the weak effect of retardation on the LSP resonance in nanosized metal particles leaves only one parameter to truly engineer: the geometry. By modifying the structure of the metal nanoparticle to have a dielectric core with a metal shell, an increased tunability is achieved due to the plasmon hybridization of the inner and outer surfaces of the metal [2]. Especially the spherical core–shell structure has received a considerable amount of attention in recent years [3–6] due to its excellent and tunable sensing properties, which show great promise in biological studies such as cancer therapy [7]. The plasmon hybridization allows one to position the LSP resonance of the nanoshell as desired by simply varying the core size r_1 and/or outer radius r_2 appropriately [8].

The hybridization of the inner and outer surface plasmons increases when the metal shell becomes thinner [8], which gives rise to significantly altered LSP resonances compared to usual homogeneous metal nanoparticles. Studies of the hybridization between two spherical [9] or cylindrical [10] metal nanoparticles in few nanometer proximity reveal that the effects of nonlocal response increase with increasing hybridization. Furthermore, nanosized metal particles [11–14] and metal films [15] are also strongly affected by nonlocal effects. The core–shell particle thus calls for a nonlocal description, since it features an ultrathin metallic shell with a resulting strong plasmon hybridization.

S. Raza · G. Toscano · N. A. Mortensen · M. Wubs
Department of Photonics Engineering, Technical University of Denmark, DK-2800 Kgs. Lyngby, Denmark

M. Wubs
e-mail: mwubs@fotonik.dtu.dk

S. Raza (✉)
Center for Electron Nanoscopy, Technical University of Denmark, DK-2800 Kgs. Lyngby, Denmark
e-mail: sraz@fotonik.dtu.dk

A.-P. Jauho
Department of Micro- and Nanotechnology, Technical University of Denmark, DK-2800 Kgs. Lyngby, Denmark

The use of arrays of nanotubes with high aspect ratio for biosensing [16] and hydrogen sensing [17] has yielded impressive results, yet only few theoretical studies have been performed on the nanotube [18, 19]. Schröter et al. investigate the plasmonic modes and dispersion relations of the nanotube [18], while Zhu et al. perform calculations using the discrete dipole approximation to discuss the changes of the resonance wavelength of the nanotube due to variations of the aspect ratio [19]. Thus, to our knowledge, no systematic study has yet been performed that addresses which parameters determine the LSPR refractive-index sensitivity of a nanotube-based sensor. In this paper, we fill this gap with a systematic study of the sensing and scattering properties of a single infinitely long cylindrical core–shell nanowire, see inset of Fig. 1, which is a good description of dilute arrays of noninteracting nanotubes with a high aspect ratio. On the basis of this study, we propose how to optimize a nanotube-based sensor to achieve the utmost sensitivity for the refractive-index sensing of both gases and liquids.

The outline of this paper is as follows. In the section "Theory," we discuss the physical principles of local and nonlocal response and introduce the sensitivity and figure of merit (FOM) as quantitative measures of the performance of a LSPR-based sensor. The section "Results and Discussion" is dedicated to the study of a nanotube with a silica core and gold shell. We determine the dependency of the sensitivity and FOM on the shape and size of the nanotube, using both local and nonlocal theory to model the response of the gold shell. Our conclusions and outlook on nanotube-based sensors is given in the section "Conclusions and Outlook," and details on the analytical calculations are in the Appendix.

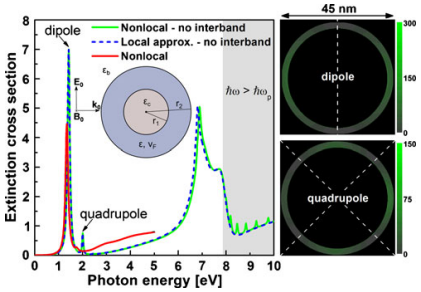

Fig. 1 Extinction cross sections as a function of incident photon energy for TM-polarized light normally incident on a $(r_1, r_2) = (40\,\text{nm}, 45\,\text{nm})$ silica–Au cylinder in vacuum. The three curves correspond to the nonlocal and local models without interband transitions (*solid green* and *dashed blue curves*, respectively) and the nonlocal model with interband transitions (*solid red curve*). Free-electron parameters for Au as in [20]: $\hbar\omega_p = 7.872\,\text{eV}$, $\hbar\gamma = 0.0530\,\text{eV}$, and $v_F = 1.39 \times 10^6\,\text{m/s}$. Interband parameters for Au are also as in [20] and valid up to 5 eV. The panel on the *right* shows the normalized intensity distributions $|\mathbf{E}|^2/|\mathbf{E_0}|^2$ in the nonlocal model without interband transitions at the dipole and quadrupole resonance frequencies. Here, $\mathbf{E_0}$ is the incident electric field. *Inset*: Schematic diagram of core–shell structure with relevant parameters

Theory

The ability of LSPR-based sensors to detect changes in the refractive index of their surrounding medium is usually quantified by the sensitivity and FOM [1]. The sensitivity $\partial\lambda/\partial n_b$ is determined as the shift in wavelength of the considered LSP resonance in the extinction spectrum of the sensor, when varying the background refractive index $n_b = \sqrt{\epsilon_b}$, while the FOM is given as

$$\text{FOM} = \frac{|\partial\lambda/\partial n_b|}{\Delta\lambda} \tag{1}$$

where $\Delta\lambda$ is the resonance linewidth, calculated as the FWHM of the considered LSP resonance in the extinction spectrum. Thus, to determine the performance of the nanotube as a LSPR sensor, we must calculate its extinction cross section, as this quantifies the extinction spectrum and therefore allows us to determine the sensitivity and FOM.

Predictions for the extinction cross section depend on how the optical response of electrons in the metal is modeled. The common approach to describe the response of metals is by making the local approximation which assumes that the response field at a certain position is proportional to the driving field at that position, with the proportionality function being a position- and frequency-dependent dielectric function. This approach has the rather unphysical consequence that all surface charges reside on an infinitely thin layer on the boundaries of the metal, thereby neglecting the actual extent (or wave nature) of the electrons. While the local approximation is justified as long as the metal boundaries are far apart such that the interaction between electrons due to their extent can be

neglected (i.e., large metallic structures), it cannot be safely assumed for nanosized metal particles where the wavelength of the electron becomes comparable in size to the metal particle. By describing the metal using the semiclassical hydrodynamic Drude model [14], we relax the local approximation by allowing the existence of local inhomogeneity in the density of the electron gas, which gives rise to pressure waves. The electron-gas pressure waves provide a means to transport energy in the metal in addition to the electromagnetic waves, which gives rise to nonlocal response: the response of the metal at a certain spatial point can depend on the driving field at other nearby points (on the length scale of the Fermi wavelength) in the metal.

In the Appendix, we provide an analytical expression for the extinction cross section in the cases of both nonlocal and local response, for a normally incident transverse magnetic (TM)-polarized wave (see the inset of Fig. 1). We have checked the analytical expression with our numerical implementation of the hydrodynamic Drude model [10], which showed a perfect agreement (not shown in this paper).

Results and Discussion

We consider the specific core–shell structure, where the core is silica (SiO_2) with dielectric constant $\epsilon_c = 1.5^2$ and the shell is gold (Au) modeled with the data by Rakić et al. [20]. To clearly show the difference in extinction cross section in local and nonlocal response, we start by examining the case where interband effects in Au are neglected. Figure 1 depicts the extinction cross section for a $(r_1, r_2) = (40\,\text{nm}, 45\,\text{nm})$ silica–Au cylinder in vacuum comparing the local and nonlocal model. The local approximation shows three distinct peaks, two at low frequencies (dipole and quadrupole peaks) and one at a high frequency (near 7 eV). These are due to the interaction between the localized plasmons at the inner and outer surface of the nanoshell or, equivalently, the interaction between a cavity mode and a cylinder mode [8]. The nonlocal description allows the same classification of peaks as the local approximation [10, 14], although the high-frequency peak is blueshifted compared to the local model. Since sensing depends on peak shifts, it is important to take possible nonlocal blueshifts into account. However, the low-frequency resonances show no noticeable blueshift because the strength of the nonlocal blueshift does not only increase with decreasing thickness of the metal layer [9, 13–15] but it also depends on the frequency, with a decreasing blueshift for lower frequencies. Thus, we find that there is an intricate interplay between plasmon hybridization and nonlocal response: Since a thinner metal shell produces stronger plasmon hybridization, the dipole and quadrupole peaks are pushed to such low frequencies that the nonlocal blueshift effect due to nanosized metallic features is counteracted by the low frequency of the resonances.

The panel on the right of Fig. 1 shows the nonlocal normalized intensity distribution in the metal at the dipole and quadrupole resonance frequencies, illustrating the expected dipole and quadrupole nature of the resonances. Above the plasma energy $\hbar\omega_p$, we see the characteristic additional resonances in the nonlocal model due to the excitation of longitudinal modes, as previously reported for different metal nanoparticles [13, 14, 21].

The difference between the red and green curves in Fig. 1 shows the importance of taking into account interband transitions in the response of the metal shell. The implications on the dipole and quadrupole resonances are that they are redshifted and damped due to interband transitions, with greatest impact on the quadrupole peak. In the remaining part of this paper, we will always use measured values for the dielectric function [20], i.e., we take interband transitions into account. We will concentrate on the dipole resonance, since this peak is the strongest, is close to visible and infrared frequencies, and can be affected by the shape and size of the cylinder and the background permittivity. Furthermore, the shift due to hybridization of the dipole resonance to lower energies is advantageous as it reduces the effects of Drude and interband damping.

There are two geometrical properties that can be modified in the nanotube structure: the first is the shape defined by the r_1/r_2 ratio and the second is the overall size, that is, varying the outer radius r_2 but keeping r_1/r_2 constant. In Fig. 2, we show the effect of shape variations of the nanotube on its sensing abilities, which is quantified through the change in the dipole resonance wavelength when the background refractive index is increased. We see that regardless of the shape, the dependency is always approximately linear. However, as shown in Fig. 2(i), there is no significant dependency on the background refractive index for low r_1/r_2 ratios, indicating the lack of ability to sense. Figure 2(i) illustrates that thicker tubes are less good as refractive-index sensors because the peak intensity is maximal near the inner rather than the outer surface. Only when the shell becomes thin ($r_1/r_2 \to 1$) does the resonance wavelength shift with the refractive index. The thinner

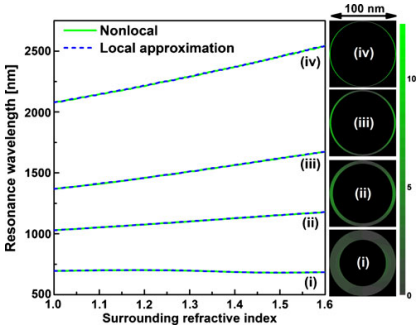

Fig. 2 The dipole resonance wavelength calculated with both local and nonlocal response taking into account interband transitions as a function of the background refractive index for four different r_1/r_2 ratios: (*i*) 0.7, (*ii*) 0.9, (*iii*) 0.95, and (*iv*) 0.98. The outer radius of the nanotube is kept constant at $r_2 = 100$ nm. The panel on the *right* shows the normalized intensity distribution $|\mathbf{E}|^2/|\mathbf{E_0}|^2$ in the nonlocal model at the vacuum dipole resonance wavelength for the corresponding four different shapes

the shell, the greater is the average slope of the curves. Relaxing the nonlocal description to a local one does not change this trend because the dipole resonances occur at too low energies for the nonlocal blueshift to kick in. Furthermore, the resonance wavelength shifts to higher wavelengths when the shell becomes thinner because the coupling between the cavity and cylinder modes increases. Thus, even though Fig. 2(iv) represents a nanotube with a 2-nm thin metal shell, where nonlocal blueshifts are expected to be very prominent, the local approximation predicts sensitivities that are almost identical to the nonlocal description. So, as in Fig. 1, here in Fig. 2 we see that for ultrathin nanotubes, the usual observation of larger nonlocal blueshifts for smaller structures does not occur. The nonlocal blueshift cancels out with the decrease of the resonance energy due to increased hybridization.

For a more quantitative description of the sensitivity of the nanotube, we present sensitivity and FOM calculations of the nanotube structures shown in Fig. 2 at the refractive index of air and water in Table 1. As in Fig. 2, it is again clear from Table 1 that increased sensitivity can be achieved for thinner metal shells. Comparing the sensitivity of the nanotube with other LSPR sensors based on different nanoparticle geometries [22, 23], where the sensitivity is in the range $90 - 801$ nm per refractive index unit (RIU), shows that the nanotube is comparable in sensitivity for ratios $r_1/r_2 > 0.7$, while it is superior for very high r_1/r_2 ratios. Comparison of the

Table 1 Sensitivity and figure of merit calculations (Eq. (1)) in the nonlocal description at the refractive index of air $n_b = 1$ (for gas sensing) and water $n_b = 1.333$ (for liquid sensing) for the four different shapes of Fig. 2

(r_1, r_2)	$\partial\lambda/\partial n_b$ (nm/RIU)		FOM	
	$n_b = 1$	$n_b = 1.333$	$n_b = 1$	$n_b = 1.333$
(70 nm, 100 nm)	58	−103	0.3	0.4
(90 nm, 100 nm)	298	261	1.6	1.2
(95 nm, 100 nm)	470	539	1.9	1.9
(98 nm, 100 nm)	790	788	2.4	2.2

FOM with other nanoparticle LSP sensors also shows equally good performance by the nanotube, although the FOM is mainly dependent on the properties of Au and not easily improved by changing the geometry [24]. The sensitivity values in Table 1 also reveal that the nanotube has a high sensitivity at both the refractive index of air and water, which shows the versatility of a nanotube-based sensor and its applicability as both a gas and liquid sensor.

Besides shape variations, we also varied the size r_2 of the nanotube while keeping r_1/r_2 constant. Figure 3 depicts the dipole resonance wavelength as a function of the background refractive index for three different sizes with $r_1/r_2 = 0.9$. The sensing ability of the nanotube is not as dependent on size as it is on shape, which can be seen by the three almost parallel lines in Fig. 3. Even though the sensitivity does not change much with

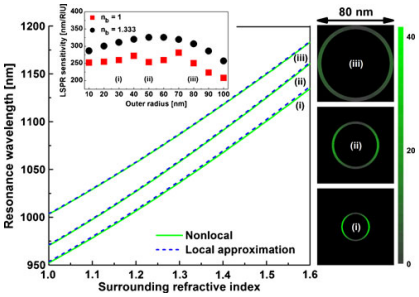

Fig. 3 The dipole resonance wavelength calculated with both local and nonlocal response taking into account interband transitions as a function of the background refractive index for three different r_2 values: (*i*) 30 nm, (*ii*) 50 nm, and (*iii*) 80 nm. The shape of the nanotube is kept constant by setting $r_1/r_2 = 0.9$. The panel on the *right* shows the normalized intensity distribution $|\mathbf{E}|^2/|\mathbf{E_0}|^2$ in the nonlocal model at the vacuum resonance wavelength for the corresponding three different sizes. *Inset*: The LSPR sensitivity at the refractive index of air ($n_b = 1$) and water ($n_b = 1.333$) calculated with the nonlocal model as a function of outer radius while keeping $r_1/r_2 = 0.9$

increasing size, there is still an optimum size which occurs at $r_2 = 50\,\text{nm}$ and $r_2 = 70\,\text{nm}$ for liquid and gas sensing, respectively, see the inset of Fig. 3. The fact that it is neither the smallest nor the biggest nanotube size that gives the highest sensitivity can be explained by a trade-off between the total structure size and the shell thickness. If the size of the structure is too small, then we have a weak LSP excitation and thereby poor sensing ability, but if the structure size is too big (with the shape kept constant), the absolute shell thickness increases, which also decreases the sensing ability, as we saw in Fig. 2. Therefore, for a larger r_1/r_2 value, the optimum size will also be larger.

In Fig. 3, we also show the calculations using the local approximation. As seen, effects are surprisingly well accounted for even with a local description, despite the fact that we actually consider very thin metallic shells, for instance a 3-nm shell in Fig. 3(iii), with concomitant strong plasmon hybridization. The strong hybridization in ultrathin metal shells shifts the dipole resonance to very low energies, where the nonlocal blueshift is weak. The sensitivity and consequently the FOM are therefore weakly influenced by nonlocal response. Although it is hardly visible in Fig. 3, the local resonances do in fact occur at slightly longer wavelengths than in the nonlocal description, revealing a small nonlocal blueshift.

Conclusions and Outlook

We have examined the infinite single dielectric-metal nanotube structure as an approximation for a dilute array of nanotubes with high aspect ratio. We calculate the extinction properties of a silica–gold nanotube analytically for both local and nonlocal response by extending the Mie theory for nanowires to nanotube geometries. Our investigation reveals that in contrast to the spherical nanoshell [6], the sensing ability of the nanotube is highly dependent on the shape of the structure, where few nanometer thin shells produce extreme sensitivities. The sensitivity is shown to be less dependent on the overall structure size. The sensitivity at the refractive index of air and water of ultrathin nanotubes is superior to other nanoparticle geometries, making nanotubes very promising for both gas and liquid sensing.

Our results also show unexpectedly that nonlocal response has a negligible influence on the extinction and sensing properties of the nanotube, even though the metal shell is ultrathin (a few nanometer) because the hybridization in the nanotube is so strong that the dipole resonance is pushed to very low energies. The strength of the nonlocal blueshift is an interplay between the metal thickness and the resonance energy, where a thinner shell produces a stronger blueshift while a lower energy produces a weaker blueshift. This interplay is surprisingly well balanced in the nanotube structure because a thinner shell gives rise to lower resonance energies.

With the high sensitivity and good FOM of the nanotube geometry, we propose a sensor based on ultrathin nanotubes. The robustness of the sensitivity of the nanotube to size variations provides desirable advantages, since fluctuations in size due to imperfect fabrication will have a less impact. In the special case of gas sensing, the sensitivity may be further improved by a factor of 2 by designing the nanotube to have a hollow core. With a hollow core, the inner surface of the metal shell is also exposed to the surrounding medium, which significantly improves the sensitivity. However, mechanical stability is sacrificed with a hollow core if for instance the nanotubes are to stand vertically on a substrate.

Appendix

The nonlocal optical properties of the nanotube are determined by solving Maxwell's wave equation coupled to the hydrodynamic equation for the current [14]. We solve the coupled set of equations by extending the Mie theory for wires of Ref. [25] to core–shell structures. By expanding the electromagnetic fields in the dielectric core, metal shell, and surrounding medium in cylindrical Bessel functions, we can most easily take into account Maxwell's boundary conditions along with the additional boundary condition of a vanishing normal component of the current in the nonlocal case [14]. Although quantum tunneling is not taken into account with this treatment, we do not expect any such effects to be important in this structure [26, 27].

To determine the extinction property of the infinite cylindrical nanotube we calculate the extinction cross section [28]

$$\sigma_{\text{ext}} = -\frac{2}{k_0 r_2} \sum_{n=-\infty}^{\infty} \text{Re}\{a_n\}, \tag{2}$$

where $k_0 = \sqrt{\epsilon_b}\omega/c$ is the background wave vector, ϵ_b is the background permittivity, and a_n is a cylindrical Bessel-function expansion coefficient for the scattered electromagnetic field. We consider a normally incident

electric-field polarization perpendicular to the cylinder axis (TM), as sketched in the inset of Fig. 1. The nonlocal-response scattering coefficient is calculated analytically as

$$a_n = -\frac{\sqrt{\epsilon_b}J_n(k_0r_2)\left[C_n + J'_nP_n - H'_nQ_n\right] - \sqrt{\epsilon}J'_n(k_0r_2)\left[J_nP_n - H_nQ_n\right]}{\sqrt{\epsilon_b}H_n(k_0r_2)\left[C_n + J'_nP_n - H'_nQ_n\right] - \sqrt{\epsilon}H'_n(k_0r_2)\left[J_nP_n - H_nQ_n\right]}. \tag{3}$$

Here, J_n and H_n are the Bessel and Hankel functions of the first kind, $k_t = \sqrt{\epsilon}\omega/c$, and $\epsilon(\omega) = \epsilon_{other}(\omega) - \omega_p^2/(\omega[\omega + i\gamma])$ is the Drude local-response function that includes interband effects through $\epsilon_{other}(\omega)$. The arguments of the Bessel and Hankel functions are k_tr_2 unless written explicitly otherwise.

The coefficients P_n, Q_n, and C_n are given by

$$P_n = p_n\alpha_n + J_n(k_cr_1)\left[H_n(k_tr_1)\delta_n + H_n\tau_n\right], \tag{4}$$

$$Q_n = q_n\alpha_n + J_n(k_cr_1)\left[J_n(k_tr_1)\delta_n + J_n\tau_n\right], \tag{5}$$

$$C_n = \frac{in}{k_0r_2}\left[H_n(k_lr_2)c_n - J_n(k_lr_2)d_n\right], \tag{6}$$

where $k_c = \sqrt{\epsilon_c}\omega/c$ and ϵ_c is the dielectric constant of the core. Furthermore, $k_l^2 = (\omega^2 + i\omega\gamma - \omega_p^2/\epsilon_{other})/\beta^2$ and $\beta^2 = 3v_F^2/5$ with v_F being the Fermi velocity of the metal shell. The coefficients p_n, q_n, α_n, δ_n and τ_n of Eqs. (4–5) are given as

$$p_n = \sqrt{\epsilon}J'_n(k_cr_1)H_n(k_tr_1) - \sqrt{\epsilon_c}J_n(k_cr_1)H'_n(k_tr_1), \tag{7}$$

$$q_n = \sqrt{\epsilon}J'_n(k_cr_1)J_n(k_tr_1) - \sqrt{\epsilon_c}J_n(k_cr_1)J'_n(k_tr_1). \tag{8}$$

$$\alpha_n = \left(\frac{k_l\epsilon_{other}}{k_0}\right)^2 \times\left[J'_n(k_lr_2)H'_n(k_lr_1) - H'_n(k_lr_2)J'_n(k_lr_1)\right], \tag{9}$$

$$\delta_n = -\frac{k_ln^2\sqrt{\epsilon_c}\epsilon_{other}(\epsilon - \epsilon_{other})}{k_tk_0^2r_1^2} \times\left[J'_n(k_lr_2)H_n(k_lr_1) - H'_n(k_lr_2)J_n(k_lr_1)\right], \tag{10}$$

$$\tau_n = -\frac{k_ln^2\sqrt{\epsilon_c}\epsilon_{other}(\epsilon - \epsilon_{other})}{k_tk_0^2r_1r_2} \times\left[H'_n(k_lr_1)J_n(k_lr_1) - J'_n(k_lr_1)H_n(k_lr_1)\right], \tag{11}$$

while the coefficients c_n and d_n of Eq. (6) are given as

$$c_n = f_n\left[J'_n(k_lr_2)\eta_n + J_n(k_lr_1)\kappa_n\right] + J'_n(k_lr_1)g_n\left[J_np_n - H_nq_n\right], \tag{12}$$

$$d_n = f_n\left[H'_n(k_lr_2)\eta_n + H_n(k_lr_1)\kappa_n\right] + H'_n(k_lr_1)g_n\left[J_np_n - H_nq_n\right], \tag{13}$$

where

$$g_n = \frac{ink_l\epsilon_{other}(\epsilon - \epsilon_{other})}{k_0k_tr_2}, \tag{14}$$

$$f_n = \frac{in\sqrt{\epsilon_c}(\epsilon - \epsilon_{other})}{k_0k_tr_1}J_n(k_tr_1), \tag{15}$$

$$\eta_n = k_l\left[J_n(k_tr_1)H'_n(k_tr_1) - H_n(k_tr_1)J'_n(k_tr_1)\right], \tag{16}$$

$$\kappa_n = \frac{n^2(\epsilon - \epsilon_{other})}{k_tr_2r_1}\left[J_n(k_tr_1)H_n - H_n(k_tr_1)J_n\right]. \tag{17}$$

The local-response result can be retrieved in the limit of a vanishing Fermi velocity for which $P_n = p_n$, $Q_n = q_n$, and $C_n = 0$.

References

1. Anker JN, Hall WP, Lyandres O, Shah NC, Zhao J, van Duyne RP (2008) Nat Mater 7:442
2. Prodan E, Radloff C, Halas NJ, Nordlander P (2003) Science 302:419
3. Brongersma ML (2003) Nat Mater 2:296
4. Raschke G, Brogl S, Susha AS, Rogach AL, Klar TA, Feldmann J, Fieres B, Petkov N, Bein T, Nichtl A, Kürzinger K (2004) Nano Lett 4:1853
5. Nehl CL, Grady NK, Goodrich GP, Tam F, Halas NJ, Hafner JH (2004) Nano Lett 4:2355
6. Tam F, Moran C, Halas NJ (2004) J Phys Chem B 108:17290
7. Bardhan R, Lal S, Joshi A, Halas NJ (2011) Acc Chem Res 44:936
8. Prodan E, Nordlander P (2004) J Chem Phys 120:5444
9. David C, García de Abajo FJ (2011) J Phys Chem C 115:19470
10. Toscano G, Raza S, Jauho A-P, Mortensen NA, Wubs M (2012) Opt Express 20:4176
11. Boardman AD, Paranjape BV (1977) J Phys F: Met Phys 7:1935
12. Dasgupta BB, Fuchs R (1981) Phys Rev B 24:554
13. Ruppin R (1973) Phys Rev Lett 31:1434
14. Raza S, Toscano G, Jauho A-P, Wubs M, Mortensen NA (2011) Phys Rev B 84:121412(R)
15. Jones WE, Kliewer KL, Fuchs R (1969) Phys Rev 178:1201
16. McPhillips J, Murphy A, Jonsson MP, Hendren WR, Atkinson R, Höök F, Zayats AV, Pollard RJ (2010) ACS Nano 4:2210
17. Lim MA, Kim DH, Park CO, Lee YW, Han SW, Li Z, Williams RS, Park I (2012) ACS Nano 6:598

18. Schröter U, Dereux A (2001) Phys Rev B 64:125420
19. Zhu J, Li KF (2011) Eur Phys J B 80:83
20. Rakić AD, Djurišić AB, Elazar JM, Majewski ML (1998) Appl Opt 37:5271
21. Fuchs R, Claro F (1987) Phys Rev B 35:3722
22. Mayer KM, Hafner JH (2011) Chem Rev 111:3828
23. Mahmoud MA, El-Sayed MA (2010) J Am Chem Soc 132:12704
24. Jeppesen C, Xiao S, Mortensen NA, Kristensen A (2010) Opt Express 18:25075
25. Ruppin R (2001) Opt Commun 190:205
26. Zuloaga J, Prodan E, Nordlander P (2009) Nano Lett 9:887
27. Öztürk ZF, Xiao S, Yan M, Wubs M, Jauho A-P, Mortensen NA (2011) J Nanophotonics 5:051602
28. van de Hulst H (1957) Light scattering by small particles. Wiley, New York

Paper I

S. Raza, N. Stenger, S. Kadkhodazadeh, S. V. Fischer, N. Kostesha, A.-P. Jauho, A. Burrows, M. Wubs, and N. A. Mortensen

Blueshift of the surface plasmon resonance in silver nanoparticles studied with EELS

Nanophotonics **2**, 131 (2013)

Author contributions
S. R., N. S. and S. K. conducted the experimental electron energy-loss spectroscopy measurements. S. R. and N. S. performed the analysis of the measurements. S. R. performed the theoretical modeling. S. V. F. and N. K. synthesized the silver nanoparticles. S. R. and N. S. wrote the paper. All authors were involved in discussing the obtained results and in correcting the manuscript.

 DOI 10.1515/nanoph-2012-0032 — Nanophotonics 2013; 2(2): 131–138

Søren Raza[a], Nicolas Stenger[a], Shima Kadkhodazadeh, Søren V. Fischer, Natalie Kostesha, Antti-Pekka Jauho, Andrew Burrows, Martijn Wubs and N. Asger Mortensen*

Blueshift of the surface plasmon resonance in silver nanoparticles studied with EELS

Abstract: We study the surface plasmon (SP) resonance energy of isolated spherical Ag nanoparticles dispersed on a silicon nitride substrate in the diameter range 3.5–26 nm with monochromated electron energy-loss spectroscopy. A significant blueshift of the SP resonance energy of 0.5 eV is measured when the particle size decreases from 26 down to 3.5 nm. We interpret the observed blueshift using three models for a metallic sphere embedded in homogeneous background material: a classical Drude model with a homogeneous electron density profile in the metal, a semiclassical model corrected for an inhomogeneous electron density associated with quantum confinement, and a semiclassical nonlocal hydrodynamic description of the electron density. We find that the latter two models provide a qualitative explanation for the observed blueshift, but the theoretical predictions show smaller blueshifts than observed experimentally.

Keywords: Electron energy loss spectroscopy; nonlocal response; plasmonics.

[a]Both authors contributed equally.
***Corresponding author: N. Asger Mortensen,** Department of Photonics Engineering, Technical University of Denmark, DK-2800 Kgs. Lyngby, Denmark; and Center for Nanostructured Graphene (CNG), Technical University of Denmark, DK-2800 Kgs. Lyngby, Denmark, e-mail: asger@mailaps.org
Søren Raza, Nicolas Stenger and Martijn Wubs: Department of Photonics Engineering, Technical University of Denmark, DK-2800 Kgs. Lyngby, Denmark
Søren Raza, Shima Kadkhodazadeh and Andrew Burrows: Center for Electron Nanoscopy, Technical University of Denmark, DK-2800 Kgs. Lyngby, Denmark
Nicolas Stenger and Antti-Pekka Jauho: Center for Nanostructured Graphene (CNG), Technical University of Denmark, DK-2800 Kgs. Lyngby, Denmark
Søren V. Fischer, Natalie Kostesha and Antti-Pekka Jauho: Department of Micro and Nanotechnology, Technical University of Denmark, DK-2800 Kgs. Lyngby, Denmark

Edited by Javier Garcia de Abajo

1 Introduction

Surface plasmons are collective excitations of the electron gas in metallic structures at the metal/dielectric interface [1]. The ability to concentrate light with SPs [2] and to enhance light-matter interaction on a subwavelength scale enables few and even single-molecule spectroscopy when the size of the metallic structures is decreased to a few nanometers [3]. These collective excitations are usually well-described by the classical Drude model for nanoparticles with dimensions of tens of nanometer and larger [1]. In the quasistatic limit, i.e., when the wavelength of the exciting electromagnetic wave considerably exceeds the dimensions of the structure, the local-response Drude theory predicts that the resonance energy of localized SPs is independent of the size of the nanostructure [4], and that the field enhancement created in the gap between two metallic nanostructures diverges for vanishing gap size [5]. These predictions are however in conflict both with earlier [6–9] and with more recent experimental results, which have shown a size dependency of the localized SP resonance in noble metal nanoparticles in the size range of 1–10 nm [10] and pronounced deviations for dimer geometries [11, 12].

This dependence of the SP resonance on the size of noble metal nanostructures is believed to be a signature of quantum properties of the free-electron gas. With decreasing sizes of the nanoparticles, the quantum wave nature of the electrons is theoretically expected to manifest itself in the optical response due to the effects of quantum confinement [13–17], quantum tunneling [17–20], as well as nonlocal response [21–27]. Nonlocal effects are a direct consequence of the inhomogeneity of the electron gas, which arises due to the quantum wave nature and the many-body properties of the electron gas.

The recent developments in analytical scanning transmission electron microscopes (STEM) equipped with a monochromator and electron energy-loss spectroscopy (EELS) [28] give the possibility of accessing the near-field energy distribution of the plasmon resonance of individual nanoparticles on a subnanometer scale with an energy resolution better than 0.2 eV. This method has

been used for the imaging of surface plasmons in many different metallic nanostructures [10, 29–32]. With STEM EELS it is possible to correlate the structural and chemical information on the nanometer scale, such as the shape and the presence of organic ligands, with the spectral information of the SP resonance of single isolated nanoparticles. STEM EELS is thus perfectly suited to probe and access plasmonic nanostructures and SP resonances at length scales where quantum mechanics is anticipated to become important.

In this paper we report the experimental study of the SP resonance of chemically grown single Ag nanoparticles dispersed on 10 nm thick Si_3N_4 membranes with STEM EELS. Our measurements present a significant blueshift of the SP resonance energy from 3.2 to 3.7 eV for particle diameters ranging from 26 down to 3.5 nm. Our results also confirm very recent experiments made with Ag nanoparticles on different substrates using different STEM operating conditions [10], thereby strengthening the interpretation that the blueshift is predominantly associated with the tight confinement of the plasma and the intrinsic quantum properties of the electron gas itself rather than having an extrinsic cause.

We compare our experimental data to three different models: a purely classical local-response Drude model which assumes a constant electron density profile in the metal nanoparticle, a semiclassical local-response Drude model where the electron density is determined from the quantum mechanical problem of electrons moving in an infinite spherical potential well [16], and finally, a semiclassical model based on the hydrodynamic description of the motion of the electron gas which takes into account nonlocal response through the internal quantum kinetics of the electron gas in the Thomas-Fermi (TF) approximation [33, 34]. We find good qualitative agreement between our experimental data and the two semiclassical models, thus supporting the anticipated nonlocal nature of SPs of Ag nanoparticles in the 1–10 nm size regime. The experimentally observed blueshift is however significantly larger than the predictions by the two semiclassical models.

2 Materials and methods

The nanoparticles are grown chemically following the method described in Ref. [35] and subsequently stabilized in an aqueous solution with borohydride ions. The mean size of the nanoparticles is 12 nm with a very broad size distribution ranging from 3 to 30 nm. The nanoparticle solution is dispersed on a 10 nm thick commercially available Si_3N_4 membrane (TEMwindows.com), which has a refractive index of approximately $n \approx 2.1$ [36]. To characterize our nanoparticles we have used an aberration-corrected STEM FEI Titan (www.FEI.com) operated at 120 kV with a probe diameter of approximately 0.5 nm, and convergence and collection angles of 15 mrads and 17 mrads, respectively. The Titan is equipped with a monochromator allowing us to perform EELS with an energy resolution of 0.15±0.05 eV. We systematically performed EELS measurements at the surface and in the middle of each nanoparticle. The EELS spectra were taken with an exposure time of 90 ms to avoid beam damage as much as possible. To improve the signal-to-noise ratio we accumulated 10–15 spectra for each measurement point. We observed no evidence of damage after each measurement.

The experimental data were analyzed with the aid of commercially available software (Digital Micrograph) and three different methods were used to reconstruct and remove the zero-loss peak (ZLP): the first method is the reflected tail (RT) method, where the negative-energy half part of the ZLP is reflected about the zero-energy axis to approximate the ZLP at positive energies, while the second method is based on fitting the ZLP to the sum of a Gaussian and a Lorentzian functions. The third method is to prerecord the ZLP prior to each set of EELS measurements. All three methods yielded consistent results.

The energies of the SP resonance peaks were determined by using a nonlinear least-squares fit of our data to Gaussian functions. The error in the resonance energy is given by the 95 % confidence interval for the estimate of the position of the center of the Gaussian peak. Nanoparticle diameters were determined by calculating the area of the imaged particle and assigning to the area an effective diameter by assuming a perfect circular shape. The error bars in the size therefore correspond to the deviation from the assumption of a circular shape, which is estimated as the difference between the largest and smallest diameter of the particle.

3 Theory

In the following theoretical analysis our hypothesis is that the blueshift of the SP resonance energy is related to the properties of the electron density profile in the metal nanoparticle. Therefore, we use three different approaches to model the electron density of the Ag nanoparticle. In all three approaches, we calculate the optical response and thereby also the resonance energies of the nanoparticle through the quasistatic polarizability α of a sphere embedded in a homogeneous background dielectric with

permittivity ε_B. With this approach, we make two implicit assumptions: the first is that we can neglect retardation effects and the second is that we can neglect the symmetry-breaking effect of the substrate. We have validated the quasistatic approach by comparing to fully retarded calculations [37], which shows excellent agreement in the particle size range we consider. The effect of the substrate will be taken into account indirectly by determining an effective homogeneous background permittivity ε_B using the average resonance frequency of the largest particles ($2R$>20 nm) as the classical limit.

The first, and simplest, approach is to assume a constant free-electron density n_0 in the metal particle, which drops abruptly to zero outside the particle. This assumption is the starting point of the classical local-response Drude model for the response of the Ag nanoparticle, where the polarizability is given by the Clausius-Mossotti relation, which is well-known to be size independent for subwavelength particles. The classical local-response polarizability α_L is [1]

$$\alpha_L(\omega)=4\pi R^3\frac{\varepsilon_D(\omega)-\varepsilon_B}{\varepsilon_D(\omega)+2\varepsilon_B}, \tag{1}$$

where R is the radius of the particle and $\varepsilon_D(\omega)=\varepsilon_\infty(\omega)-\omega_p^2/(\omega^2+i\gamma\omega)$ is the classical Drude permittivity taking additional frequency-dependent polarization effects such as interband transitions into account through $\varepsilon_\infty(\omega)$, not included in the plasma response of the free-electron gas itself.

The second approach is to correct the standard approximation in local-response theory of a homogeneous electron density profile by using insight from the quantum wave nature of electrons to model the electron density profile and take into account the quantum confinement of the electrons. For nanometer-sized spheres, the classical polarizability given by the Clausius-Mossotti relation must be altered to take into account an inhomogeneous electron density. In Ref. [16], it is shown that in general the local-response polarizability for a sphere embedded in a homogeneous material is given as

$$\alpha_{LQC}(\omega)=12\pi\int_0^R r^2 dr\frac{\varepsilon(r,\omega)-\varepsilon_B}{\varepsilon(r,\omega)+2\varepsilon_B}, \tag{2}$$

now with a spatially varying Drude permittivity [16, 17]

$$\varepsilon(r,\omega)=\varepsilon_\infty(\omega)-\frac{\omega_p^2}{\omega(\omega+i\gamma)}\frac{n(r)}{n_0}. \tag{3}$$

Here, $n(r)$ is the electron density in the metal nanoparticle. Clearly, if $n(r)=n_0$ we arrive at the classical Clausius-Mossotti relation Eq. (1) as expected. To determine the density profile in this local-response model, we follow the approach of Ref. [16] and assume that the free electrons move in an infinite spherical potential well. The approach just outlined of a local-response theory with an inhomogeneous electron density is very similar to the theoretical model used in Ref. [10] for explaining their experimental results. It should be noted that any effects due to electron spill-out and quantum tunneling are neglected in all of the approaches that we consider.

The third and final approach is to compare our experimental data with a linearized nonlocal hydrodynamic model in which the electron density is allowed to deviate slightly from the constant electron density used in classical local-response theories [22, 38–40]. The dynamics of the electron gas is governed by the semiclassical hydrodynamic equation of motion [25, 26, 34], which results in an inhomogeneous electron density profile. The nonlocal hydrodynamic polarizability $\alpha_{NL}(\omega)$ is exactly given as

$$\alpha_{NL}(\omega)=4\pi R^3\frac{\varepsilon_D(\omega)-\varepsilon_B(1+\delta_{NL})}{\varepsilon_D(\omega)+2\varepsilon_B(1+\delta_{NL})}, \tag{4}$$

$$\delta_{NL}=\frac{\varepsilon_D(\omega)-\varepsilon_\infty(\omega)}{\varepsilon_\infty(\omega)}\frac{j_1(k_LR)}{k_LRj_1'(k_LR)}, \tag{5}$$

and these results constitute our nonlocal-response generalization of the Clausius-Mossotti relation of classical optics. Here, $k_L=\sqrt{\omega^2+i\omega\gamma-\omega_p^2/\varepsilon_\infty}/\beta$ is the wave vector of the additional longitudinal wave allowed to be excited in the hydrodynamic nonlocal theory [25, 34], and j_1 is the spherical Bessel function of first order. Finally, within TF theory $\beta^2=3/5v_F^2$, where v_F is the Fermi velocity [34]. We emphasize that for $\beta\to0$, the local-response Drude result is retrieved, since $\delta_{NL}\to0$ and Eq. (4) simplifies to the classical Clausius-Mossotti relation Eq. (1).

The SP resonance energy follows theoretically from the Fröhlich condition, i.e., we must consider the poles of Eq. (4). For sufficiently small blueshifts and neglecting damping, the resonance frequency can be approximated by

$$\omega=\frac{\omega_P}{\sqrt{\mathrm{Re}[\varepsilon_\infty(\omega)]+2\varepsilon_B}}+\sqrt{\frac{2\varepsilon_B}{\mathrm{Re}[\varepsilon_\infty(\omega)]}}\frac{\beta}{2R}+O\left(\frac{1}{R^2}\right), \tag{6}$$

where the first term is the common size-independent local-response Drude result for the SP resonance that also follows from Eq. (1), and the second term gives the size-dependent blueshift due to nonlocal corrections. At this stage, we note that a $1/(2R)$ dependence was experimentally observed in Refs. [6, 7] using optical spectroscopy. However, Eq. (6) reveals, besides a $1/(2R)$ dependence, that there is a delicate interplay in the blueshift between the material parameters of the metal, through $\varepsilon_\infty(\omega)$ and

β, and the background medium ε_B. Furthermore, Eq. (6) shows that the blueshift can be enhanced with a large-permittivity background medium.

4 Results

Figures 1(A–C) display STEM images of Ag nanoparticles with diameters of 15.5, 10.0, and 5.5 nm, respectively. The images show that no chemical residue is left from the synthesis and that the particles are faceted. We find that approximately 70% of the studied nanoparticles have a relative size error (i.e., the ratio of the size error bar to the particle diameter) below 20% (determined from the 2D STEM images), verifying that the shape of the nanoparticles is to a first approximation overall spherical (see Supplementary Figure 1). On a subset of the particles, thickness measurements using image recordings at different tilt angles were performed, revealing information about the shape of the nanoparticle in the third dimension. Such 3D investigations confirmed that the shape is overall spherical, but however could not be completed for all particles due to stability issues: the positions of tiny nanoparticles fluctuate under too long exposure of the electron beam, thus preventing accurate determination of the shape of the nanoparticle in the third dimension perpendicular to the substrate.

Figures 1(D–F) display raw normalized EELS data, acquired on Ag nanoparticles with diameters 14.1, 9.8, and 6.6 nm, respectively. The peaks correspond to the excitation of the SP. When the diameter of the nanoparticle decreases, the SP resonance clearly shifts progressively to higher energies. Figures 1(D–F) also display that the amplitude and linewidth of the SP resonances can vary from particle to particle (with the same size) and at times show narrowing instead of the expected broadening of the resonance for decreasing nanoparticle sizes [6, 13, 14]. This is for example seen in the linewidths in Figures 1(D–F) which seem to decrease with size. However, as will be explained in more detail in the next paragraph, we did not find a systematic trend of the linewidths in our EELS measurements probably due to the shape variations in our ensemble of nanoparticles.

Figure 2 displays the resonance energy of the SP as a function of the diameter of the nanoparticles. A significant blueshift of the SP resonance of 0.5 eV is observed when

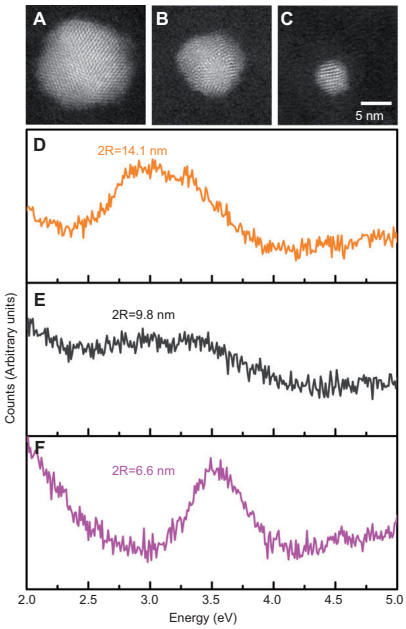

Figure 1 Aberration-corrected STEM images of Ag nanoparticles with diameters (A) 15.5 nm, (B) 10 nm, and (C) 5.5 nm, and normalized raw EELS spectra of similar-sized Ag nanoparticles (D-F). The EELS measurements are acquired by directing the electron beam to the surface of the particle.

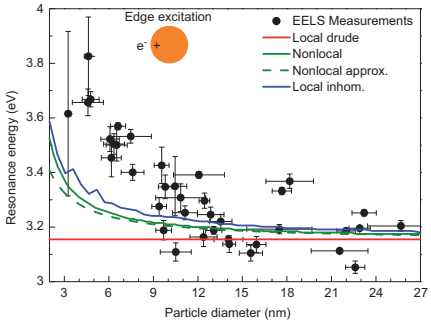

Figure 2 Nanoparticle SP resonance energy as a function of the particle diameter. The dots are EELS measurements taken at the surface of the particle and analyzed using the RT method, and the lines are theoretical predictions. We use parameters from Ref. [41]: $\hbar\omega_p$=8.282 eV, $\hbar\gamma$=0.048 eV, n_0=5.9×10^{28} m^{-3} and v_F=1.39×10^6 m/s. From the average large-particle ($2R>20$ nm) resonances we determine ε_B=1.53.

the nanoparticle diameter decreases from 26 to 3.5 nm. This trend is in good agreement with the results shown in Ref. [10], despite the difference in the substrate and the STEM operating conditions, a strong indication that the blueshift of Ag nanoparticles is robust to extrinsic variations. Another prominent feature in Figure 2 is the scatter of resonance energies at a fixed particle diameter. We mainly attribute the spread in resonance energies at a given particle size to shape variations in our ensemble of nanoparticles (see Supplementary Material). Slight deviations from perfect circular shape in the STEM images will result in a delicate dependency on the location of the electron probe and give rise to splitting of SP resonance energies due to degeneracy lifting. In this regard, we also note that even a perfectly circular particle on a 2D STEM image may still possess some weak prolate or oblate deformation in the third dimension, resulting in a departure from spherical shape. Calculations using the local response model show that a 20% deformation of a sphere into an oblate or prolate spheroid results in a 0.4 eV spread in resonance energy (see Supplementary Figure 2), which is approximately the spread in resonance energy we observe for particles larger than 10 nm. Furthermore, shape deviations may also impact the linewidth of the SP resonance, since the electron probe can excite the closely-spaced non-degenerate resonance energies simultaneously, which may appear as a single broadened peak. This broadening mechanism could explain the apparent linewidth narrowing for decreasing particle size seen in Figures 1(D–F). However, we cannot rule out that other effects beyond shape deviations contribute to the spread of resonance energies and impact the SP resonance linewidth. These could for example be the facets or the particle-to-substrate interface [42].

Along with the EELS measurements in Figure 2, we show Eq. (1) for the local-response Drude model (red line) and the semiclassical local-response model Eq. (3) (blue line). Furthermore, the nonlocal relation of Eq. (3) (green solid line) and the approximate nonlocal relation of Eq. (6) (green dashed line) are also depicted, and we see that Eq. (6) is accurate for particle sizes $2R \gtrsim 10$ nm.

Due to the narrow energy range in consideration (~3.0–3.9 eV), we approximate $\varepsilon_\infty(\omega)$ as a second-order Taylor polynomial based on the frequency-dependent values given for Ag in Ref. [41]. We find $\varepsilon_\infty(\omega)=(59.8+i55.1)(\omega/\omega_p)^2-(40.3+i42.4)(\omega/\omega_p)+(10.5+i8.6)$. Since the refractive index of the Si_3N_4 substrate varies hardly ($n\approx2.1$) in the narrow energy range we consider [36], we assume that the background permittivity ε_B is constant and determine it by approximating the average resonance energy of the largest particles ($2R>20$ nm) as the classical limit, i.e., the first term of Eq. (6).

It is known that local Drude theory produces size-independent resonance frequencies of subwavelength particles, but this theory is clearly inadequate to describe the measurements of Figure 2. The nonlocal quasistatic hydrodynamic model predicts a blueshift in agreement with the experimental EELS measurements. Interestingly, the measured blueshift is even larger than predicted. We also see that the local-response model with an inhomogeneous electron density profile shows a similar trend as the nonlocal hydrodynamic model, indicating that these two different models describe very similar physical effects. The oscillations in the resonance energy in the inhomogeneous local-response model seen for small particle diameter are due to small variations in the density profile with decreasing size (i.e., discrete changes in the number of electrons), as also stated in Ref. [10].

The inhomogeneous local-response model and the nonlocal hydrodynamic model, when applied to a sphere in a homogeneous background medium, agree qualitatively with the EELS measurements. However, they do not provide the full picture. One of the probable issues arising is that the substrate is taken into account indirectly through a homogeneous background medium, a state-of-the-art procedure [10] which however may not be adequate to describe the effects of the presence of a dielectric substrate. It has been shown that the dielectric substrate modifies the absorption spectrum of an isolated sphere [43] and also the waveguiding properties of nanowires [31, 44, 45]. In an attempt to include the symmetry breaking effect of the substrate in our theoretical analysis, we apply a simple image charge model. The main effect of the substrate in this picture stems from the interaction of the dipole mode of the nanoparticle with the induced dipole mode in the substrate [46–48]. However, we find that such a dipole-dipole model for the substrate is inadequate to describe the large blueshift observed experimentally (see Supplementary Material). Indeed, it has been shown that the induced image charges in the substrate can make the contributions of higher order multipoles in the nanoparticle important [49], and it has also been observed theoretically that higher order multipoles produce larger blueshifts in the nonlocal hydrodynamic model (Figure 2 in Ref. [50]). The impact of the substrate on the electron density inhomogeneity and thereby the SP resonance energy depends on the thickness and refractive index of the substrate, which may explain the quantitative agreement between theory and experiment reported in Ref. [10], since thinner substrates with smaller refractive indexes were used in their experiments. In order to completely address this issue, one would need to go beyond the dipole-dipole model for the substrate, thus future 3D EELS simulations taking nonlocal effects

and/or inhomogeneous electron densities into account would be needed.

Another complementary explanation in the context of the inhomogeneity of the free-electron density could be the combined contribution of both the inhomogeneous static equilibrium electron density and nonlocality. It is well-known that the static equilibrium electron density is inhomogeneous, even in a semi-infinite metal [51], due to Friedel oscillations and the electron spill-out effect at the metal surface. The Friedel oscillations are modeled in the local quantum-confined model given by Eq. (3) while nonlocality is neglected, and *vice versa* in the nonlocal hydrodynamic model given by Eq. (3). As seen in Figure 2, the two effects separately give rise to similar-sized blueshifts, suggesting that the contribution of both effects simultaneously could add up to the significantly larger experimentally observed blueshift. Simply put, an extension of the nonlocal hydrodynamic model to include an inhomogeneous equilibrium free-electron density could produce a larger blueshift, which may be in accordance with the experimental observations. Furthermore, such a model could also take into account the electron spill-out effect, which in free-electron models has been argued to produce a redshift of the SP resonance [21, 50, 52–54], describing adequately simple metals. In contrast, it has also been shown that the spill-out effect in combination with the screening from the *d* electrons gives rise to the blueshift seen in Ag nanoparticles [55].

Additional size effects such as changes of the electronic band structure of the smallest nanoparticles, which are considerably more difficult to take into account, also impact the shift in SP resonance energy [6].

5 Conclusion

We have investigated the surface plasmon resonance of spherical silver nanoparticles ranging from 26 down to 3.5 nm in size with STEM EELS and observed a significant blueshift of 0.5 eV of the resonance energy. We have compared our experimental data with three different models based on the quasistatic optical polarizability of a sphere embedded in a homogeneous material. Two of the models, a nonlocal hydrodynamic model and a generalized local model, incorporate an inhomogeneity of the electron density induced by the quantum wave nature of the electrons. These two different models produce similar results in the SP resonance energy and describe qualitatively the blueshift observed in our measurements. Although our exact hydrodynamic generalization of the Clausius-Mossotti relation predicts a nonlocal blueshift that grows fast [as $1/(2R)$] when decreasing the diameter and increases even faster for the smallest particles ($2R<10$ nm), the observed blueshifts are nevertheless larger than predicted.

The quantitative agreement between the two different theoretical models and the discrepancy with the larger observed blueshift suggest that a more detailed theoretical description of the system is needed to fully understand the influence of the substrate and the effect of the confinement of free electrons on the SP resonance shift in silver nanoparticles. On the experimental side, further EELS studies of other metallic materials and on different substrates could unveil the mechanism behind the size dependency of the SP resonance of nanometer scale particles.

Acknowledgments: We thank S. I. Bozhevolnyi for directing our attention to the theoretical model in Ref. [16] and G. Toscano for fruitful discussions. The Center for Nanostructured Graphene is sponsored by the Danish National Research Foundation, Project DNRF58. The A. P. Møller and Chastine Mc-Kinney Møller Foundation is gratefully acknowledged for the contribution toward the establishment of the Center for Electron Nanoscopy. N. Stenger acknowledges financial support by a Lundbeck Foundation Grant Nbr. R95-A10663.

Received October 9, 2012; accepted February 19, 2013; previously published online March 23, 2013

References

[1] Maier SA. Plasmonics: fundamentals and applications. New York: Springer; 2007.
[2] Schuller JA, Barnard ES, Cai W, Jun YC, White JS, Brongersma ML. Plasmonics for extreme light concentration and manipulation. Nat Mater 2010;9:193–204.
[3] Kneipp K. Surface-enhanced Raman scattering. Phys Today 2007;60:40–6.
[4] Wang F, Shen YR. General properties of local plasmons in metal nanostructures. Phys Rev Lett 2006;97:206806.
[5] Romero I, Aizpurua J, Bryant GW, García de Abajo FJ. Plasmons in nearly touching metallic nanoparticles: singular response in the limit of touching dimers. Opt Express 2006;14:9988–99.
[6] Kreibig U, Genzel L. Optical absorption of small metallic particles. Surf Sci 1985;156:678–700.

[7] Charlé K-P, Schulze W, Winter B. The size dependent shift of the surface-plasmon absorption-band of small spherical metal particles. Z Phys D 1989;12:471–5.

[8] Ouyang F, Batson P, Isaacson M. Quantum size effects in the surface-plasmon excitation of small metallic particles by electron-energy-loss spectroscopy. Phys Rev B 1992;46:15421–5.

[9] Berciaud S, Cognet L, Tamarat P, Lounis B. Observation of intrinsic size effects in the optical response of individual gold nanoparticles. Nano Lett 2005;5:515–8.

[10] Scholl JA, Koh AL, Dionne JA. Quantum plasmon resonances of individual metallic nanoparticles. Nature 2012;483:421–7.

[11] Ciracì C, Hill RT, Mock JJ, Urzhumov Y, Fernández-Domínguez AI, Maier SA, Pendry JB, Chilkoti A, Smith DR. Probing the ultimate limits of plasmonic enhancement. Science 2012;337:1072–4.

[12] Kern J, Grossmann S, Tarakina NV, Häckel T, Emmerling M, Kamp M, Huang J-S, Biagioni P, Prangsma J, Hecht B. Atomic-scale confinement of resonant optical fields. Nano Lett 2012;12:5504–9.

[13] Genzel L, Martin TP, Kreibig U, Dielectric function and plasma resonance of small metal particles. Z Phys B 1975;21:339–46.

[14] Kraus WA, Schatz GC. Plasmon resonance broadening in small metal particles. J Chem Phys 1983;79:6130.

[15] Halperin WP, Quantum size effects in metal particles. Rev Mod Phys 1986;58:533–606.

[16] Keller O, Xiao M, Bozhevolnyi S. Optical diamagnetic polarizability of a mesoscopic metallic sphere: transverse self-field approach. Opt Comm 1993;102:238–44.

[17] Öztürk ZF, Xiao S, Yan M, Wubs M, Jauho A-P, Mortensen NA. Field enhancement at metallic interfaces due to quantum confinement. J Nanophot 2011;5:051602.

[18] Zuloaga J, Prodan E, Nordlander P. Quantum description of the plasmon resonances of a nanoparticle dimer. Nano Lett 2009;9:887–91.

[19] Mao L, Li Z, Wu B, Xu H. Effects of quantum tunneling in metal nanogap on surface-enhanced Raman scattering. Appl Phys Lett 2009;94:243102.

[20] Esteban R, Borisov AG, Nordlander P, Aizpurua J. Bridging quantum and classical plasmonics with a quantum-corrected model. Nat Commun 2012;3:825.

[21] Ljungbert A, Lundqvist S. Non-local effects in the optical absorption of small metallic particles. Phys Rev Lett 1985;156:839–44.

[22] García de Abajo FJ. Nonlocal effects in the plasmons of strongly interacting nanoparticles, dimers, and waveguides. J Phys Chem C 2008;112:17983–7.

[23] David C, García de Abajo FJ. Spatial nonlocality in the optical response of metal nanoparticles. J Phys Chem C 2012;115:19470–5.

[24] Aizpurua J, Rivacoba A. Nonlocal effects in the plasmons of nanowires and nanocavities excited by fast electron beams. Phys Rev B 2008;78:035404.

[25] Raza S, Toscano G, Jauho A-P, Wubs M, Mortensen NA. Unusual resonances in nanoplasmonic structures due to nonlocal response. Phys Rev B 2011;84:121412(R).

[26] Toscano G, Raza S, Jauho A-P, Mortensen NA, Wubs M. Modified field enhancement and extinction in plasmonic nanowire dimers due to nonlocal response. Opt Express 2012;20:4176.

[27] Fernández-Domínguez AI, Wiener A, García-Vidal FJ, Maier SA, Pendry JB. Transformation-optics description of nonlocal effects in plasmonic nanostructures. Phys Rev Lett 2012;108:106802.

[28] García de Abajo FJ. Optical excitations in electron microscopy. Rev Mod Phys 2010;82:209–75.

[29] Nelayah J, Kociak M, Stephan O, García de Abajo FJ, Tence M, Henrard L, Taverna D, Pastoriza-Santos I, Liz-Marzan LM, Colliex C. Mapping surface plasmons on a single metallic nanoparticle. Nat Phys 2007;3:348–53.

[30] Koh AL, Bao K, Khan I, Smith WE, Kothleitner G, Nordlander P, Maier SA, McComb DW. Electron energy-loss spectroscopy (EELS) of surface plasmons in single silver nanoparticles and dimers: influence of beam damage and mapping of dark modes. ACS Nano 2009;3:3015–22.

[31] Nicoletti O, Wubs M, Mortensen NA, Sigle W, van Aken PA, Midgley PA. Surface plasmon modes of a single silver nanorod: an electron energy loss study. Opt Express 2011;19:15371.

[32] Koh AL, Fernández-Domínguez AI, McComb DW, Maier SA, Yang JKW. High-resolution mapping of electron-beam-excited plasmon modes in lithographically defined gold nanostructures. Nano Lett 2011;11:1323–30.

[33] Bloch F. Bremsvermögen von Atomen mit mehreren Elektronen. Z Phys A 1933;81:363–76.

[34] Boardman A. Electromagnetic surface modes. Hydrodynamic theory of plasmon-polaritons on plane surfaces. Chichester: John Wiley and Sons; 1982.

[35] Mulfinger L, Solomon SD, Bahadory M, Jeyarajasingam A, Rutkowsky SA, Boritz C. Synthesis and study of silver nanoparticles. J Chem Educ 2007;84:322–5.

[36] Bååk T. Silicon oxynitride; a material for GRIN optics. Appl Opt 1982;21:1069–72.

[37] Ruppin R. Optical properties of a plasma sphere. Phys Rev Lett 1973;31:1434–7.

[38] Pendry JB, Aubry A, Smith DR, Maier SA. Transformation optics and subwavelength control of light. Science 2012;337:549–52.

[39] Dasgupta BB, Fuchs R. Polarizability of a small sphere including nonlocal effects. Phys Rev B 1981;24:554–61.

[40] Fuchs R, Claro F. Multipolar response of small metallic spheres: nonlocal theory. Phys Rev B 1987;35:3722–7.

[41] Rakić AD, Djurišić AB, Elazar JM, Majewski ML. Optical properties of metallic films for vertical-cavity optoelectronic devices. Appl Opt 1998;37:5271–83.

[42] Noguez C. Surface plasmons on metal nanoparticles: the influence of shape and physical environment. J Phys Chem C 2007;111:3806–19.

[43] Ruppin R. Optical absorption by a small sphere above a substrate with inclusion of nonlocal effects. Phys Rev B 1992;45:11209–15.

[44] Li Z, Bao K, Fang Y, Guan Z, Halas NJ, Nordlander P, Xu H. Effect of a proximal substrate on plasmon propagation in silver nanowires. Phys Rev B 2010;82:1.

[45] Zhang S, Xu H. Optimizing substrate-mediated plasmon coupling toward high-performance plasmonic nanowire waveguides. ACS Nano 2012;6:8128–35.

[46] Yamaguchi T, Yoshida S, Kinbara A. Optical effect of the substrate on the anomalous absorption of aggregated silver films. Thin Solid Films 1974;21:173–87.

[47] Jain PK, Huang W, El-Sayed MA. On the universal scaling behavior of the distance decay of plasmon coupling in metal

nanoparticle pairs: a plasmon ruler equation. Nano Lett 2007;7:2080–8.
[48] Novotny L, Hecht B. Principles of nano-optics. New York: Cambridge; 2006.
[49] Ruppin R. Surface modes and optical absorption of a small sphere above a substrate. Surf Sci 1983;127:108–18.
[50] Boardman AD, Paranjape BV. The optical surface modes of metal spheres. J Phys F Met Phys 1977;7:1935.
[51] Lang ND, Kohn W. Theory of metal surfaces: charge density and surface energy. Phys Rev B 1970;1:4555–68.
[52] Ascarelli P, Cini M. "Red shift" of the surface plasmon resonance absorption by fine metal particles. Solid State Commun 1976;18:385–8.
[53] Ruppin R. Plasmon frequencies of small metal spheres. J Phys Chem Solids 1978;39:233–7.
[54] Apell P, Ljungbert Å. Red shift of surface plasmons in small metal particles. Solid State Commun 1982;44:1367–9.
[55] Liebsch A. Surface-plasmon dispersion and size dependence of Mie resonance: silver versus simple metals. Phys Rev B 1993;48:11317–28.

 DOI 10.1515/nanoph-2012-0032SUP — Nanophotonics 2013; 2(2): Ad1–Ad3

Søren Raza[a], Nicolas Stenger[a], Shima Kadkhodazadeh, Søren V. Fischer, Natalie Kostesha, Antti-Pekka Jauho, Andrew Burrows, Martijn Wubs and N. Asger Mortensen*

Supplemental data

1 Shape analysis

The diameters of our nanoparticles are determined by using the free online image analysis tool ImageJ [1] which includes a particle analysis package. We use the 2D images taken in STEM mode to measure the surface area A of the nanoparticle, whereafter we determine the mean nanoparticle diameter D using the relation $A=\pi(D/2)^2$. The particle analysis tool also evaluates the maximum D_{max} and minimum D_{min} diameters of the nanoparticle and the difference between these two diameters, i.e., $\Delta D=D_{max}-D_{min}$ provides us a measure for error in the nanoparticle diameter (shown as the error bar in Article Figure 2). The relative size error ($\Delta D/D$) then represents the deviation of the shape of the particles from a perfect circle.

Supplementary Figure 1 displays a histogram with the number of particles as function of the relative size error (5% interval between each bar). The first observation is that the relative error in the diameter is spread from 5% to 50% with a maximum of counts centered on 15% deviation. We also see that more than 70% of the particles have an error smaller than 20%, thus giving us confidence that assuming the particles to be spherical is justified. We also emphasize that this analysis was made on 2D images which are the projections of the 3D shapes of the nanoparticles onto the plane parallel to the substrate. This lack of information in the third dimension leaves indeterminacy of the exact shape of the particle. However, since the nanoparticles are fabricated in a liquid phase suspension [2], i.e., growing identically in three dimensions, we can to a first approximation infer that we have the same relative size error distribution in the third dimension perpendicular to the substrate, thus assuming that particle orientation is independent of its shape deformation.

In order to understand the scattering of the SP resonance energies observed in Article Figure 2, we model the deviation from the perfect spherical shape as an ellipsoidal particle with minor and major axes. We calculate the optical polarizability of two different types of ellipsoids: the prolate spheroid (one major and two equal minor axes) and the oblate spheroid (two equal major and one minor axes). The polarizability is calculated within the local Drude theory under two different polarizations of the incident electric field, parallel to the major axis or parallel to the minor axis [3]. The perfect spherical sphere is deformed while keeping the volume constant. We use a relative deformation of the major (minor) axis of 20%

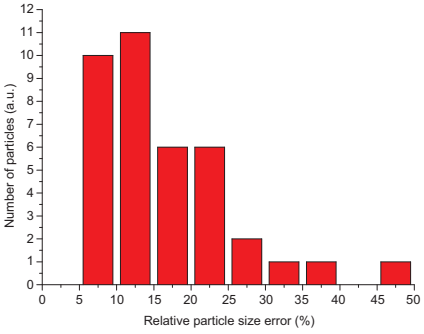

Supplementary Figure 1 Histogram showing the distribution of relative size error $\Delta D/D$. The relative size error represents the shape deviation of the nanoparticle from a perfect circle in the 2D STEM image.

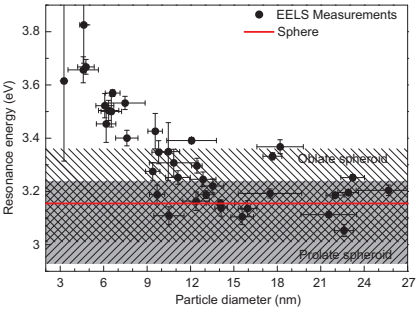

Supplementary Figure 2 Local-response calculations of the SP resonance for perfectly spherical (red line), oblate (white patterned) and prolate (gray patterned) particles under excitation of different polarizations.

for the prolate (oblate) particles which corresponds to the deviation of the majority of the nanoparticles studied.

The results are shown in Supplementary Figure 2. The red line represents the local Drude calculation for a perfect sphere (same as Article Figure 2). The gray patterned area corresponds to the span of resonance energies for the prolate particles, when a relative deviation of the major axis of 20% is allowed. The part of the area that is above the red line (i.e., blueshifted with respect to the perfect sphere) corresponds to a polarization along the minor axis, while the part below the red line (i.e., redshifted with respect to the perfect sphere) is due a polarization along the major axis. For the polarization along the minor axis, we see a blueshift of approximately 0.1 eV of the SP resonance while we obtain a redshift of approximately 0.2 eV for the polarization along the major axis. The increased redshift observed for the polarization along the major axis is due to the fact that a size increase of 20% on the major axis will give only a size decrease of 9% on the minor axis (scales as $1/a_{major}^2$, where a_{major} is the length of the major axis) for a constant volume. The same arguments are valid for the oblate case with the exception that here the blueshift is higher than the redshift (major and minor axes are inverted). However, the overall span of resonance energies considering both type of spheroids is approximately 0.4 eV. Interestingly, this interval is similar to the scattering of the resonance energy observed in Article Figure 2 for particles above 10 nm, where the local theory is still valid. However, we emphasize that the measured resonance energies for the smallest particles (below 10 nm) exceeds this span of resonance energies, and thus the observed blueshift cannot be explained by a simple shape deviation argument.

In conclusion, we see that the deviation from the spherical shape into ellipsoid-like particles and the thereby prompted dependency on the location of the EELS probe when measuring the SP resonance gives a reasonable and probable explanation for the spread but not for the magnitude of SP resonance energies observed in our measurements.

2 Substrate effects: dipole-dipole interaction

The optical polarizability α of a single sphere in a homogeneous background ε_B can be modified to take into account the presence of a semi-infinite substrate with permittivity ε_S using a simple image charge model. In this picture, the coupling between the sphere and the substrate is based on a dipole-dipole interaction between the dipole moment of the sphere and the weaker dipole moment of the image charges in the substrate. Taking only dipole moments into account is an approximation. Due to the symmetry-breaking presence of the substrate, there are two separate cases to be treated for the direction of the incident field: one when the incident electric field is parallel to the substrate, the other when the incident field is perpendicular to the substrate. It has been shown that the altered polarizability α_{sub} in the presence of the semi-infinite substrate is [4–6]

$$\alpha_{sub}=\alpha\left[1-\frac{\kappa\alpha}{4\pi(2R)^3}\frac{\varepsilon_S-\varepsilon_B}{\varepsilon_S+\varepsilon_B}\right]^{-1}, \quad \text{(S1)}$$

where κ=-1 for a parallel incident electric field while κ=2 for a perpendicular electric field. The interesting case for our EELS measurements is when κ=2, since the electric field produced by a swift electron is predominantly in the same direction as the movement of the electron, i.e., perpendicular to the substrate.

Supplementary Figure 3 shows calculations on the SP resonance energy performed using Eq. (S1) with $\varepsilon_S=2.08^2$ and $\varepsilon_B=1$. Ellipsometry measurements of the complex refractive index $n=n'+in''$ on the Si_3N_4 substrate has been provided by the manufacturer of the TEM membranes (TEMwindows.com), showing an almost constant index of refraction of $n'\approx 2.08$ and a negligible extinction coefficient $n''\approx 0$ in the energy range we consider (3.0–3.9 eV). The provided measurements are very similar to that of Ref. [7]. We emphasize that with the dipole-dipole model for the substrate no fitting of the background permittivity has been done.

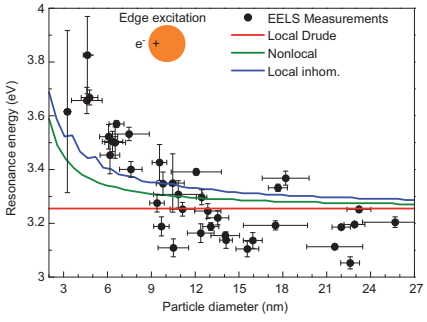

Supplementary Figure 3 The same as Article Figure 2, but calculated using Eq. (S1) with κ=2, $\varepsilon_S=2.08^2$ and ε_B=1.

Supplementary Figure 3 shows that the dipole-dipole interaction predicts a slightly larger resonance energy in the classical limit (i.e., for the largest particles) compared to the fitted homogeneous background permittivity approach used for Article Figure 2. However, the blueshift in the resonance energy for decreasing particle size in the two semiclassical models is very similar to the effective homogeneous background approach, and thus the dipole-dipole model for the substrate cannot fully account for the significantly larger experimental blueshift. We also see that many of the EELS measurements of the larger particles ($2R$>10 nm) lie at lower resonance energies than predicted by any of the theoretical substrate models. These discrepancies suggest that the simple dipole-dipole model for the substrate is inadequate to describe our experimental observations, and that a complete understanding of the effect of the substrate requires the inclusion of higher-order multipoles and the finite thickness of the substrate [8, 9].

References

[1] Available at: http://imagej.nih.gov/ij/.
[2] Mulfinger L, Solomon SD, Bahadory M, Jeyarajasingam A, Rutkowsky SA, Boritz C. Synthesis and study of silver nanoparticles. J Chem Educ 2007;84:322–5.
[3] Maier SA. Plasmonics: fundamentals and applications. New York: Springer; 2007.
[4] Yamaguchi T, Yoshida S, Kinbara A. Optical effect of the substrate on the anomalous absorption of aggregated silver films. Thin Solid Films 1974;21:173–87.
[5] Jain PK, Huang W, El-Sayed MA. On the universal scaling behavior of the distance decay of plasmon coupling in metal nanoparticle pairs: a plasmon ruler equation. Nano Lett 2007;7:2080–8.
[6] Novotny L, Hecht B. Principles of nano-optics. New York: Cambridge; 2006.
[7] Bååk T. Silicon oxynitride; a material for GRIN optics. Appl Opt 1982;21:1069–72.
[8] Boardman AD, Paranjape BV. The optical surface modes of metal spheres. J Phys F Met Phys 1977;7:1935.
[9] Ruppin R. Surface modes and optical absorption of a small sphere above a substrate. Surf Sci 1983;127: 108–18.

Paper L

S. Raza, G. Toscano, A.-P. Jauho, M. Wubs, and N. A. Mortensen

Unusual resonances in nanoplasmonic structures due to nonlocal response

Phys. Rev. B **84**, 121412(R) (2011)

Author contributions
S. R. and G. T. performed the theoretical and numerical modeling. S. R. wrote the first draft of the paper and created the figures. All authors were involved in discussing the obtained results and in the writing of the paper.

RAPID COMMUNICATIONS

PHYSICAL REVIEW B 84, 121412(R) (2011)

Unusual resonances in nanoplasmonic structures due to nonlocal response

Søren Raza,[1] Giuseppe Toscano,[1] Antti-Pekka Jauho,[2] Martijn Wubs,[1,*] and N. Asger Mortensen[1,†]
[1]*Department of Photonics Engineering, Technical University of Denmark, DK-2800 Kgs. Lyngby, Denmark*
[2]*Department of Micro and Nanotechnology, Technical University of Denmark, DK-2800 Kgs. Lyngby, Denmark*
(Received 6 July 2011; published 29 September 2011)

We study the nonlocal response of a confined electron gas within the hydrodynamical Drude model. We address the question as to whether plasmonic nanostructures exhibit nonlocal resonances that have no counterpart in the local-response Drude model. Avoiding the usual quasistatic approximation, we find that such resonances do indeed occur, but only above the plasma frequency. Thus the recently found nonlocal resonances at optical frequencies for very small structures, obtained within quasistatic approximation, are unphysical. As a specific example we consider nanosized metallic cylinders, for which extinction cross sections and field distributions can be calculated analytically.

DOI: 10.1103/PhysRevB.84.121412 PACS number(s): 78.67.Uh, 71.45.Gm, 71.45.Lr, 78.67.Bf

Nanoplasmonics[1,2] is presently entering an era where the metallic structures offer nanoscale features that will eventually allow both photons and electrons to exhibit their full wave nature. This regime challenges the existing theoretical framework resting on a local-response picture using bulk-material parameters. In tiny metallic nanostructures, quantum confinement[3–7] and nonlocal response[8–18] are believed to change the collective plasmonic behavior with resulting strong optical fingerprints and far-reaching consequences for, e.g., field enhancement and extinction cross sections. Within nonlocal response, Maxwell's constitutive relation between the displacement and the electric fields reads

$$\boldsymbol{D}(\boldsymbol{r},\omega) = \varepsilon_0 \int d\boldsymbol{r}'\, \boldsymbol{\varepsilon}(\boldsymbol{r},\boldsymbol{r}',\omega)\cdot \boldsymbol{E}(\boldsymbol{r}',\omega). \tag{1}$$

The dielectric tensor $\boldsymbol{\varepsilon}(\boldsymbol{r},\boldsymbol{r}',\omega)$ reduces to $\varepsilon(\boldsymbol{r},\omega)\delta(\boldsymbol{r}-\boldsymbol{r}')$ in the local-response limit. Historically, there has been a strong emphasis on nonlocal response in extended systems with translational invariance (TI),[10] where a k-space representation is useful. However, for the present problem of metallic nanostructures, TI is broken and a real-space description is called for.

Recent theoretical studies of nanoscale plasmonic structures have predicted considerable differences in the field distributions and scattering cross sections between local and nonlocal response theories, both in numerical implementations of a simplified hydrodynamic Drude model,[14–18] and in corresponding analytical calculations.[15] Importantly, additional resonances of the free-electron plasma were found, also at optical frequencies, which have no counterparts in local-response theories. Such resonances have already gained interest both from a fundamental[7] and an applied[19] perspective. At present, the status of these optical nonlocal resonances is unclear, since in Ref. 13 the same nonlocal model was used as in Refs. 14–18, and yet no corresponding modes were found at visible frequencies. Resolving this issue is important for the engineering of ultrasmall plasmonic structures with optimized functionalities.[19–21]

In this Rapid Communication we report that unusual resonances due to nonlocal response do exist in nanoplasmonic structures, but only above the plasma frequency, not in the visible. We illustrate this property of arbitrary plasmonic structures by exact calculations for metallic cylinders. We also clarify that different implementations of the common quasistatic approximation[9,11] are the reason for the conflicting results in Refs. 13–18. Here we refrain from making this approximation altogether, and by comparison analyze the validity and implementation of the quasistatic approximation in the hydrodynamic model.

The hydrodynamic Drude model. We express the collective motion of electrons in an inhomogeneous medium in terms of the electron density $n(\boldsymbol{r},t)$ and the hydrodynamical velocity $\boldsymbol{v}(\boldsymbol{r},t)$.[8] Under the influence of macroscopic electromagnetic fields $\boldsymbol{E}(\boldsymbol{r},t)$ and $\boldsymbol{B}(\boldsymbol{r},t)$, the hydrodynamic model is defined via[10]

$$[\partial_t + \boldsymbol{v}\cdot\nabla]\,\boldsymbol{v} = -\gamma\boldsymbol{v} - \frac{e}{m}[\boldsymbol{E} + \boldsymbol{v}\times\boldsymbol{B}] - \frac{\beta^2}{n}\nabla n, \tag{2}$$

along with the continuity equation $\partial_t n = -\nabla\cdot(n\boldsymbol{v})$, expressing charge conservation. In the right-hand side of Eq. (2), the γ term represents damping, the second term is the Lorentz force, while the third term is due to the internal kinetic energy of the electron gas, here described within the Thomas-Fermi model, with β proportional to the Fermi velocity v_{F}. In analogy with hydrodynamics, the third term represents a pressure that gives rise to a nonlocal dielectric tensor, since energy may be transported by mechanisms other than electromagnetic waves.

We follow the usual approach[11] to solve Eq. (2) and the continuity equation, by expanding the physical fields in a zeroth-order static term, where, e.g., n_0 is the homogeneous static electron density, and a small (by assumption) first-order dynamic term, thereby linearizing the equations. In the frequency domain, we obtain

$$\beta^2\nabla[\nabla\cdot\boldsymbol{J}] + \omega(\omega+i\gamma)\boldsymbol{J} = i\omega\omega_{\mathrm{p}}^2\varepsilon_0\boldsymbol{E} \tag{3a}$$

for a homogeneous medium, where $\boldsymbol{J}(\boldsymbol{r}) = -en_0\boldsymbol{v}(\boldsymbol{r})$ is the current density, and ω_{p} is the plasma frequency which also enters the Drude local-response function $\varepsilon(\omega) = 1 - \omega_{\mathrm{p}}^2/[\omega(\omega+i\gamma)]$. We focus on the plasma, leaving out bulk interband effects present in real metals that could be easily taken into account,[14,22] as well as band-bending effects at the metal surface.

The electromagnetic wave equation. The retarded linearized hydrodynamic model is then fully described by Eq. (3a), together with the Maxwell wave equation

$$\nabla \times \nabla \times \boldsymbol{E} = \frac{\omega^2}{c^2}\boldsymbol{E} + i\omega\mu_0 \boldsymbol{J}. \tag{3b}$$

In order to see that these coupled equations (3) indeed describe a nonlocal dielectric response, one can in Eq. (3b) rewrite the current density $\boldsymbol{J}$ as an integral over the Green's tensor of Eq. (3a) and the electric field, whereby the nonlocal dielectric tensor of Eq. (1) can be identified.

In a local-response description it is commonplace to introduce the quasistatic or curl-free assumption that $\nabla \times \boldsymbol{E} = 0$.[23] This well-established approximation lies at the heart of most treatments and interpretations of electromagnetic wave interactions with subwavelength structures. Intuitively, one might expect that it can be extended to the nonlocal case and indeed several nonlocal treatments use this assumption.[9,11,13–17] However, as we shall demonstrate, one should proceed with care.

Three models. Here we solve Eqs. (3) directly, without further assumptions or approximations. We also compare the *nonlocal model* with two other models obtained by further assumptions. The *curl-free nonlocal model* enforces the condition $\nabla \times \boldsymbol{E} = 0$, which with Eq. (3a) implies that also $\nabla \times \boldsymbol{J} = 0$ in the medium. For the differential-operator term in Eq. (3a), from now on denoted $\hat{L}_J$, this has the consequence that $\nabla[\nabla\cdot]$ simplifies to the Laplace operator ∇^2, which gives the model used by Ruppin in the context of exciton physics in Ref. 27, and recently in plasmonics by McMahon *et al.*[14–17] and also by ourselves.[18] Finally, by assuming $\hat{L}_J = 0$ in the hydrodynamic treatment (3a), the familiar *local model* is obtained, with $\boldsymbol{J}$ and $\boldsymbol{E}$ related by Ohm's law.

We assume that the static density of electrons n_0 vanishes outside the metal of volume V, while it is constant and equal to the bulk value inside V, thus neglecting tunneling effects and inhomogeneous electron distributions associated with quantum confinement.[3,6] As a consequence, $\boldsymbol{J} = 0$ outside V for all three models.

Boundary conditions. In the local model the current $\boldsymbol{J}$ has the same the spatial dependence as the $\boldsymbol{E}$ field. Thus, in this case there are no additional boundary conditions (ABCs) to those already used in Maxwell's equations. For the nonlocal-response models, on the other hand, ABCs are in general needed.[10,16,24–26] From discussions in the literature it might appear that the number of necessary ABCs is a subtle issue, but we emphasize that there should be no ambiguity. The crucial point is that the required number of ABCs depends on the assumed static electron density profile at the boundaries.[26] For the present problem with the electron density vanishing identically outside the metal, only one ABC is needed in the nonlocal model to obtain unique solutions,[26] and it is readily found from the continuity equation and Gauss' theorem: $\hat{\boldsymbol{n}} \cdot \boldsymbol{J} = 0$ on the boundary, where $\hat{\boldsymbol{n}}$ is a normal vector to the surface, i.e., the normal-component of the current vanishes,[10,24,26] for all three models. On the other hand, in general, the tangential current $\hat{\boldsymbol{n}} \times \boldsymbol{J}$ is nonzero. This "slip" of the current is not surprising, since the hydrodynamic equation (2) describes the plasma as a nonviscous fluid.

TABLE I. Summary of the three different response models. V is the volume of the nanostructure, and ∂V its boundary.

	$\boldsymbol{r} \in V$		$\boldsymbol{r} \in \partial V$		$\boldsymbol{r} \notin V$
	$\nabla \times \boldsymbol{J}$	$\hat{L}_J$	$\hat{\boldsymbol{n}} \cdot \boldsymbol{J}$	$\hat{\boldsymbol{n}} \times \boldsymbol{J}$	$\boldsymbol{J}$
Local	$\neq 0$	0	0	$\neq 0$	0
Nonlocal	$\neq 0$	$\beta^2\nabla[\nabla\cdot]$	0	$\neq 0$	0
Nonlocal (curl-free)	0	$\beta^2\nabla^2$	0	0	0

Likewise, in several implementations of the quasistatic approximation, no further ABCs are needed to uniquely determine the electric field and current density.[11,13] In contrast, in the curl-free nonlocal model of Refs. 14–18 and 27, one more ABC *is* needed. It is assumed that the tangential components of $\boldsymbol{J}$ vanish at the boundary ($\hat{\boldsymbol{n}} \times \boldsymbol{J} = 0$), so that both normal and tangential components of the current field vanish on the boundary. In the different context of exciton physics[27] these are often referred to as Pekar's additional boundary conditions. There, the vanishing of the tangential boundary currents is motivated by the physical assumption that exciton wave functions vanish on the boundary.[27,28] Instead, in the hydrodynamical theory of metals, the ABC $\hat{\boldsymbol{n}} \times \boldsymbol{J} = 0$ seems more *ad hoc*: not a direct consequence of the quasi-static approximation, and not correct if that approximation is not made. The different boundary conditions are summarized in Table I.

Extinction cross section of metallic nanowires. To illustrate the surprisingly different physical consequences of the three models, we consider light scattering by a nanowire. Rather than solving Eqs. (3) numerically for a general cross-sectional geometry, we here limit our analysis to cylindrical wires whereby significant analytical progress is possible. We use an extended Mie theory, developed by Ruppin,[27,29] to calculate the extinction cross section σ_{ext} of an infinitely long spatially dispersive cylindrical metal nanowire in vacuum. Outside the wire there are incoming and scattered fields (both divergence free), whereas inside the wire both divergence-free and curl-free modes can be excited, the latter type only in the case of nonlocal response. The cross section is[30]

$$\sigma_{\text{ext}} = -\frac{2}{k_0 a}\sum_{n=-\infty}^{\infty} \text{Re}\{a_n\}, \tag{4}$$

where a is the radius, $k_0 = \omega/c$ is the vacuum wave vector, and a_n is a cylindrical Bessel-function expansion coefficient for the scattered fields. We consider a normally incident plane wave with the electric-field polarization perpendicular to the cylinder axis (TM). The expression for the coefficients a_n depends on the particular response model and the associated ABCs. For the curl-free nonlocal model, the a_n are known.[27] For the full hydrodynamic model we follow the approach of Ref. 29, where the ABC of Ref. 25 is employed. This ABC is for metals in free space equivalent to $\hat{\boldsymbol{n}} \cdot \boldsymbol{J} = 0$. We obtain

$$a_n = -\frac{\left[d_n + J_n'(\kappa_t a)\right] J_n(k_0 a) - \sqrt{\varepsilon} J_n(\kappa_t a) J_n'(k_0 a)}{\left[d_n + J_n'(\kappa_t a)\right] H_n(k_0 a) - \sqrt{\varepsilon} J_n(\kappa_t a) H_n'(k_0 a)}, \tag{5}$$

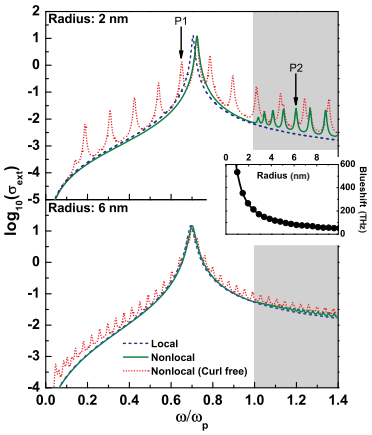

FIG. 1. (Color online) Extinction cross sections $\sigma_{\rm ext}$ as a function of frequency for TM-polarized light normally incident on a metallic cylinder in vacuum. Parameters for Au as in Ref. 14: $\hbar\omega_{\rm p} = 8.812$ eV, $\hbar\gamma = 0.0752$ eV, and $v_{\rm F} = 1.39 \times 10^6$ m/s. Inset: Frequency shift of the maximum $\sigma_{\rm ext}(\omega)$ for nonlocal against local response, as a function of radius.

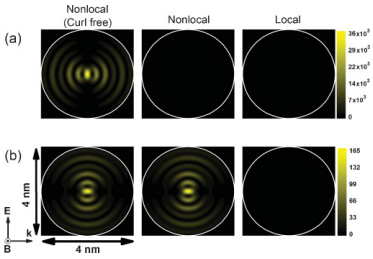

FIG. 2. (Color online) Field distributions in the three different models, for TM-polarized light normally incident on a cylinder of radius $a = 2$ nm. (a) Normalized displacement field $|\boldsymbol{D}|^2/|\boldsymbol{D}_{\rm in}|^2$ at the frequency $\omega = 0.6503\omega_{\rm p}$ (P1 in Fig. 1). $\boldsymbol{D}_{\rm in} = \varepsilon_0\boldsymbol{E}_{\rm in}$ and $\boldsymbol{E}_{\rm in}$ is the incident electric field. (b) Analogous plots of $|\boldsymbol{E}|^2/|\boldsymbol{E}_{\rm in}|^2$ for $\omega = 1.1963\omega_{\rm p}$ (P2 in Fig. 1).

where J_n and H_n are Bessel and Hankel functions of the first kind and $\kappa_t^2 = \varepsilon(\omega)k_0^2$. The d_n coefficients are

$$d_n = \frac{n^2}{\kappa_t a}\frac{J_n(\kappa_t a)}{J_n'(\kappa_t a)}\frac{J_n(\kappa_t a)}{\kappa_t a}\,[\varepsilon(\omega) - 1]\,, \tag{6}$$

where $\kappa_t^2 = (\omega^2 + i\omega\gamma - \omega_{\rm p}^2)/\beta^2$. In the limit $\beta \to 0$, the d_n vanish and the a_n of Eq. (5) reduce to the local Drude scattering coefficients,[30] which confirms that the nonlocal response in our model requires moving charges.

Are there nonlocal resonances? Figure 1 depicts the extinction cross section of Eq. (4) for two cylinder radii, comparing the nonlocal models with the local Drude model. The main surface-plasmon resonance peak at $\omega_{\rm p}/\sqrt{2}$ is blueshifted as compared to the local model, and more so for smaller radii. Similar blueshifts have been reported for other geometries[12] and in the curl-free nonlocal model.[14,27]

Figure 1 shows the unusual resonances mentioned in the title of this Rapid Communication: Additional peaks *do* appear in the nonlocal theory but only for frequencies *above* the plasma frequency $\omega_{\rm p}$ ($\hbar\omega_{\rm p} = 8.9$ eV for Ag and Au; 1.5–3 eV is visible). These peaks (such as P2 in Fig. 1) are due to the excitation of confined longitudinal modes, which are bulk-plasmon states with discrete energies above $\hbar\omega_{\rm p}$ due to confinement in the cylinder.[13] These peaks are analogous to discrete absorption lines above the band gap in quantum-confined semiconductor structures. Interestingly, contrary to the common belief that light does not scatter off bulk plasmons, which is correct in the local theory (i.e., no peak around $\omega_{\rm p}$ in Fig. 1), here in the nonlocal model we do find such a coupling to longitudinal modes. The corresponding resonances could therefore be observed with electron loss spectroscopy but also with extreme UV light. The curl-free model also exhibits these resonances.

The striking difference between the two nonlocal-response models is that the curl-free nonlocal model shows additional stronger resonances, both above and below the plasma frequency, such as P1 in Fig. 1, in particular also at optical frequencies. These peaks do not show up in the full hydrodynamical model, and thus originate from a mathematical approximation rather than a physical mechanism. It would, however, be premature to conclude that the quasistatic approximation breaks down, because in Ref. 13 the modes of cylinders in the hydrodynamical Drude model were found after making the quasistatic approximation, and the only different modes found were the confined bulk plasmon modes above $\omega_{\rm p}$. Figure 1 also illustrates that for increasing radii, $\sigma_{\rm ext}$ in the two nonlocal models converges toward the local-response value. This convergence is slower for the curl-free model.

In Fig. 2(a) we depict the scaled *displacement*-field distributions for the three models at the frequency marked P1 in Fig. 1, where only the curl-free nonlocal model has a (spurious) resonance. Correspondingly, in Fig. 2(a) we find a standing-wave pattern only in that model. Its appearance in the displacement field illustrates that the spurious resonance is a transverse resonance, i.e., occurring in the divergence-free components of $\boldsymbol{E}$ and $\boldsymbol{J}$. Figure 2(b), on the other hand, shows the normalized *electric*-field intensity for a true resonant mode at the frequency P2 of Fig. 1. Only the two nonlocal models give rise to resonant electric-field patterns. These confined bulk plasmon modes are longitudinal and would not produce standing waves in the displacement field.

Origin of spurious resonances. By eliminating the electric field from Eqs. (3), it follows that the exact hydrodynamic current satisfies the pair of third-order equations

$$\left(\beta^2\nabla^2+\omega^2+i\omega\gamma-\omega_p^2\right)\nabla\cdot\boldsymbol{J}=0, \tag{7a}$$

$$[c^2\nabla^2+\omega^2\varepsilon(\omega)]\nabla\times\boldsymbol{J}=0, \tag{7b}$$

which reduce to the more symmetric Boardman equations[31] in the absence of damping. For arbitrary geometry, Eq. (7a) has damped solutions of $\nabla\cdot\boldsymbol{J}$ for $\omega<\omega_p$ and finite-width resonances for $\omega>\omega_p$, as seen in Fig. 1. Both solutions can be consistent with the quasistatic approximation $\nabla\times\boldsymbol{J}=0$ that trivially solves Eq. (7b). On the other hand, we find that the spurious resonances have resonant divergence-free components of $\mathbf{E}$ and $\mathbf{J}$. However, these cannot at the same time be curl free. Thus the curl-free nonlocal model has resonant solutions with nonvanishing curl, which is logically inconsistent. But how could this arise? Once the $\nabla\times\boldsymbol{J}=0$ assumption has been invoked to simplify the differential operator into $\hat{L}_J=\beta^2\nabla^2$, the resulting Laplacian equation analogous to (3a) carries no information that the resulting solution should also be curl free. Thus, the solutions found for this equation are not necessarily self-consistent.

Conclusions. We have shown that plasmonic nanostructures exhibit unique resonances due to nonlocal response in the hydrodynamic Drude model, but only above the plasma frequency. The recently reported nonlocal resonances in the visible[14–18] agree with older work,[27] but are a surprisingly pronounced consequence of an implementation of the quasistatic approximation that is not self-consistent. For nanowires, we find extinction resonances without making the quasistatic approximation that agree with the quasistatic modes of Ref. 13, so we do not claim a general breakdown of the approximation itself. Even though there are no nonlocal resonances in the visible, plasmonic field enhancements are affected by nonlocal response. For arbitrary geometries, numerical methods must be used to quantitatively assess their importance. Self-consistent versions of the versatile time-domain[14–17] and frequency-domain[18] implementations of the hydrodynamical model can do just that.

This work was financially supported by Danish Research Council for Technology and Production Sciences (Grant No. 274-07-0080), and by the FiDiPro program of the Finnish Academy.

*mwubs@fotonik.dtu.dk
†asger@mailaps.org

[1] D. K. Gramotnev and S. I. Bozhevolnyi, Nat. Photon. **4**, 83 (2010).
[2] J. A. Schuller, E. S. Barnard, W. Cai, Y. C. Jun, J. S. White, and M. L. Brongersma, Nat. Mater. **9**, 193 (2010).
[3] N. D. Lang and W. Kohn, Phys. Rev. B **1**, 4555 (1970).
[4] J. Zuloaga, E. Prodan, and P. Nordlander, Nano Lett. **9**, 887 (2009).
[5] O. Pérez-González, N. Zabala, A. G. Borisov, N. J. Halas, P. Nordlander, and J. Aizpurua, Nano Lett. **10**, 3090 (2010).
[6] Z. F. Öztürk, S. Xiao, M. Yan, M. Wubs, and N. A. Mortensen, J. Nanophoton. **5**, 051602 (2011).
[7] M. Wand, A. Schindlmayr, T. Meier, and J. Förstner, Phys. Status Solidi B **248**, 887 (2011).
[8] F. Bloch, Z. Phys. A **81**, 363 (1933).
[9] G. Barton, Rep. Prog. Phys. **42**, 963 (1979).
[10] A. D. Boardman, *Electromagnetic Surface Modes* (Wiley, New York, 1982).
[11] J. M. Pitarke, V. M. Silkin, E. V. Chulkov, and P. M. Echenique, Rep. Prog. Phys. **70**, 1 (2007).
[12] F. J. García de Abajo, J. Phys. Chem. C **112**, 17983 (2008).
[13] I. Villó-Pérez and N. R. Arista, Surf. Sci. **603**, 1 (2009).
[14] J. M. McMahon, S. K. Gray, and G. C. Schatz, Phys. Rev. Lett. **103**, 097403 (2009).
[15] J. M. McMahon, S. K. Gray, and G. C. Schatz, Phys. Rev. B **82**, 035423 (2010).
[16] J. M. McMahon, S. K. Gray, and G. C. Schatz, Nano Lett. **10**, 3473 (2010).
[17] J. M. McMahon, S. K. Gray, and G. C. Schatz, J. Phys. Chem. C **114**, 15903 (2010).
[18] G. Toscano, M. Wubs, S. Xiao, M. Yan, Z. F. Öztürk, A.-P. Jauho, and N. A. Mortensen, Proc. SPIE **7757**, 77571T (2010).
[19] R. Marty, A. Arbouet, C. Girard, J. Margueritat, J. Gonzalo, and C. N. Afonso, J. Chem. Phys. **131**, 224707 (2009).
[20] Y. Xia, Y. Xiong, B. Lim, and S. E. Skrabalak, Angew. Chem. Int. Ed. **48**, 60 (2009).
[21] S. Peng, J. M. McMahon, G. C. Schatz, S. K. Gray, and Y. Sun, Proc. Natl. Acad. Sci. USA **107**, 14530 (2010).
[22] S. A. Maier, *Plasmonics: Fundamentals and Applications* (Springer, New York, 2007).
[23] J. D. Jackson, *Classical Electrodynamics*, 3rd ed. (Wiley, Hoboken, NJ, 1999).
[24] F. Sauter, Z. Phys. **203**, 488 (1967).
[25] A. R. Melnyk and M. J. Harrison, Phys. Rev. B **2**, 835 (1970).
[26] P. Jewsbury, J. Phys. F **11**, 195 (1981).
[27] R. Ruppin, J. Opt. Soc. Am. B **6**, 1559 (1989).
[28] S. Pekar, J. Phys. Chem. Solids **5**, 11 (1958).
[29] R. Ruppin, Opt. Commun. **190**, 205 (2001).
[30] H. van de Hulst, *Light Scattering by Small Particles* (Wiley, New York, 1957).
[31] A. D. Boardman and B. V. Paranjape, J. Phys. F **7**, 1935 (1977).